

VYSOKÉ UČENÍ TECHNICKÉ V BRNĚ

BRNO UNIVERSITY OF TECHNOLOGY

FAKULTA STROJNÍHO INŽENÝRSTVÍ

FACULTY OF MECHANICAL ENGINEERING

INFLUENCE OF MICROSTRUCTURE ON THE FATIGUE RESPONSE OF NONFERROUS METALS AND THEIR ALLOYS

VLIV MIKROSTRUKTURY NA ÚNAVOVOU ODEZVU NEŽELEZNÝCH KOVŮ A JEJÍCH SLITIN

HABILITAČNÍ PRÁCE

HABILITATION THESIS

AUTOR PRÁCE

Ing. Stanislava Fintová, Ph.D.

AUTHOR

BRNO 2018

Vysoké učení technické v Brně

Fakulta strojního inženýrství



a

Ústav fyziky materiálů

Akademie věd České republiky, v. v. i.



Influence of microstructure on the fatigue response of nonferrous metals and their alloys

Ing. Stanislava Fintová, Ph.D.

Habilitační práce

Brno 2018

**Poděkování:**

*Tato habilitační práce by nemohla vzniknout bez vedení a podpory prof. RNDr. Ludvíka Kunze, CSc., dr. h. c. a bez přispění řady kolegů z Ústavu fyziky materiálů AV ČR v Brně a Fakulty strojního inženýrství Vysokého učení technického v Brně.*

© Stanislava Fintová, 2018

Vysoké učení technické v Brně  
Fakulta strojního inženýrství  
Technická 2896/2, 616 69 Brno

a

Ústav fyziky materiálů  
Akademie věd české republiky v. v. i.  
Žižkova 22, 616 62 Brno

Tel.: (+420) 532 290 301  
e-mail: fintova@ipm.cz

**Content**

1 INTRODUCTION.....4

2 INFLUENCE OF THE GRAIN SIZE ON FATIGUE CRACK INITIATION ..... 9

    2.1 AZ91 magnesium alloy ..... 9

    2.2 AW 6082-T561 aluminum alloy ..... 14

    2.3 AW 7075-T6511 aluminum alloy ..... 17

3 INFLUENCE OF THE GRAIN SIZE ON THE FATIGUE CRACK GROWTH..... 20

    3.1 Pure copper ..... 20

    3.2 Commercially pure titanium grade 4 ..... 23

4 INFLUENCE OF CASTING DEFECTS ..... 28

    4.1 AlSi7Mg aluminum alloy..... 28

    4.2 IN 713LC nickel alloy..... 34

    4.3 MAR-M-247 nickel alloy..... 36

5 CONCLUSIONS ..... 39

6 REFERENCES ..... 42

7 AUTHOR’S OWN REFERED WORKS ..... 46



## **1 INTRODUCTION**

Fatigue life of metallic materials is known to be mainly predetermined by the localization of the cyclic plastic deformation resulting in the fatigue crack initiation and propagation except the component design and processing. The initiation of fatigue cracks and primary crack growth represent a major part of the fatigue lifetime of engineering components exposed to the cyclic loading. In homogenous materials, the localization of the plastic deformation in slip bands (SBs) results in the fatigue crack initiation in places on the material surface where slip markings (SMs) develop. In the case of inhomogeneous materials, the stress concentration at inclusions, intermetallic phases, defects, grain boundaries etc. usually play a decisive role and these locations are then preferable fatigue crack initiation sites.

In homogeneous materials, the material response to the cyclic loading lies in the localization of the cyclic plastic deformation resulting in the formation of SBs or persistent slip bands (PSBs) which manifests themselves on material surface in a form of SMs [1, 2]. Several theories explaining the SBs formation, connected with a surface relief formation, were proposed and are available in the literature. SMs observed on the material surface as a result of the intersection of SB and specimen surface generally consist of extrusions and intrusions or extrusion-intrusion pairs representing preferential fatigue crack initiation sites. The latest models of PSBs/SMs formation can be divided into three categories: i) surface stress assisted models [3, 4]; ii) vacancy models [5, 6]; and iii) micromechanical models [7]. Polák's vacancy-based model, [5, 8-10], well applicable for low cycle fatigue and high cycle fatigue regions, is based on the ladder-like arrangement of dislocations in the PSB undergoing high plastic strain amplitude. The model assumes that the material (matrix) around the PSB is deformed only elastically and all the plastic strain is concentrated in PSBs. Development of point defects (vacancies) is a result of the annihilation of two opposite edge dislocations. The vacancies are continuously generated in the channels of the ladder-like structure and migrate to the material volume, which is the mechanism of material redistribution between the PSBs and the matrix. Migration of vacancies from the PSBs to the matrix is compensated by the migration of material atoms from the matrix to PSBs. This process results in the creation of compressive and tensile stresses in PSBs and in the matrix, respectively. While the relaxation of the accumulated compressive stress is possible only in the direction of active Burgers vector, this leads to extrusion growth on the material surface in this direction. Due to the fact that the matrix is harder than PSB, the tensile stress relaxation is more difficult when compared to the relaxation of the compressive stresses. Therefore the relaxation of the tensile stresses, resulting in the formation of intrusions on the material surface, starts later. As a result,

the intrusions start growing at both sides of the extrusion with a delay to the extrusion growth. Due to the development of intrusions on the material surface, a very sharp surface defect localized in high slip activity area is created. A fatigue crack initiates at the tip of the intrusion and starts to grow initially along the PSB. When the fatigue crack leaves the PSB, it usually grows perpendicularly to the maximum of the applied stress. The model is supported by wide experimental measurements especially in LCF region, however, the studies were performed mainly on model materials like copper or relatively simple alloys like austenitic stainless steels i.e. materials with predominantly cubic crystallographic structure [8, 11, 12].

In a contrast to the cubic crystallographic structures, the signs of the localization of the plastic deformation, observable on the material surface in a form of SMs, are strongly limited in materials with the hexagonal structure (hcp). The reason is the low deformation characteristics of these types of materials due to a small number of independent active slip systems. So it is not surprising that the mechanisms of the localization of the cyclic plasticity and formation of SBs and SMs were studied less extensively on hcp structures and are only rarely described in the literature from the fatigue crack initiation point of view.

Creation of the SB and their manifestation on the surface in a form of the SM is limited with material deformation characteristics (primarily resulting from the crystallographic lattice) influenced also by material strengthening (solid solution strengthening, grain boundary strengthening, precipitation strengthening, etc.).

Besides the crystallographic lattice, the grain size is another factor strongly influencing the mechanical properties of materials. Usually, smaller grain size corresponds to the higher tensile strength and yield stress. This phenomenon can be quantified by the Hall-Petch relationship, [13], which is, however, applicable only to the threshold grain size. When the grain size decreases and the fraction volume of the grain boundaries become comparable or even higher than the fraction volume of the material in the grain interior, the Hall-Petch relationship is not valid anymore.

Significant grain refinement via severe plastic deformation (SPD) techniques resulting in a positive effect on the strength of materials due to the grain boundary strengthening was clearly demonstrated [14-19]. However, the extent of the improvement is dependent on the particular material and the used SPD technique and processing details, e.g. number of passes, temperature, route, etc. [20, 21]. Decreasing grain size and increasing fraction of grain boundaries make the fatigue crack initiation and early crack propagation more difficult. Materials with an ultra-fine grained (UFG) microstructure reached mostly higher fatigue endurance limit when compared to the initial coarse-grained materials (i.e. as-received materials before application of SPD).

On the other hand, the UFG microstructure generally exhibits lower threshold of the stress intensity factor for the growth of long fatigue cracks and higher crack rates when compared to the coarse-grained materials.

In the last decades the fatigue response of the UFG materials having fcc, bcc and hcp lattice was broadly investigated, however, the studies do not offer a sufficiently detailed information about the fatigue crack initiation and fatigue crack growth mechanisms. The decisive majority of studies is focused on the material properties and behavior only and, particularly, the knowledge of the localization of the cyclic plasticity in UFG materials with hcp lattice is rare [14, 15, 17, 22, 23].

In inhomogeneous materials containing secondary phases with different mechanical properties (inclusions, intermetallic phases, etc.), the secondary phases can act as stress concentrators. Cyclic loading can cause initiation of cracks in the phase/matrix interface or particles cracking. The crack initiation can move from the surface to the material bulk, which is more dangerous from the point of view of the safe operation of the component. The stress concentrators and the inhomogeneous stress field (often rapidly decreasing with the distance from the defect) limit the formation of the SBs due to the cyclic loading. Therefore there is a lack of SM on the free surface and thus the inhomogeneities act as the preferable fatigue crack initiation sites.

Many engineering materials contain inhomogeneities not only in the form of microstructural features such as inclusions but also processing defects as pores and voids. Typical example is casting, a conventional method for production of engineering parts used for many decades. The casting process is advantageous due to the quite simple production of components with complicated shape. Possibilities to modify microstructure in the wide range via thermal and/or mechanical treatment is another benefit. However, cast materials contain very often processing defects in the form of voids, gas pores and/or shrinkage cavities. Formation of voids is connected not only with casting but it is an important issue also in advanced technologies like 3D printing or other powder metallurgy techniques. Basic knowledge of the influence of these defects on fatigue behavior is still insufficient and is currently intensively discussed within the scientific community. The same holds for the mechanisms of the localization of plastic deformation in the defects vicinity and for the influence on the crack initiation and the fatigue life.

One of the statistical methods for the prediction of the fatigue life of components is LEVD (Largest Extreme Distribution Theory) proposed by Murakami [24]. Statistical evaluation of the largest defects present at 2D area of the metallographic specimen can be extrapolated to the area of the cross-section or to the volume of a real component. The method offers a potential

---

to predict the size of the possible largest defect for example in a cast component and finally to predict the fatigue life under given type of loading.

The fact that not all defects are dangerous and negatively influence the fatigue life was well established and documented in the literature. Small defects can be considered non-damaging and harmless. For example, based on the experimental data and numerical simulations of the stress concentration, it has been shown that the threshold defect size of AlSi7Mg – T6 alloy is in the range from 25 to 50  $\mu\text{m}$  [25]. The defects below this size are too small to act as the crack initiation sites. Defects with the size above this range are sufficient to concentrate enough of stress during the cyclic loading to initiate the fatigue crack independently on their shape and localization. Estimation of the largest possible defect size in the real component-based on the statistical analysis can be used for prediction of the stress concentration or stress fields during loading and prediction of the fatigue life. However, the further improvement of the prediction of the fatigue life of components with defects needs the detailed knowledge of the mechanism of the crack initiation, which is closely related to the problem of localization of cyclic plasticity. This issue is still not sufficiently elucidated, particularly in materials with hcp crystallographic structure. Simultaneously, it is important to note, that many non-ferrous engineering alloys, applied in the top industry are alloys just of this type.

The rapidly developing advanced experimental methods of observation of material surface and microstructure enable more detailed investigation of localization of the cyclic plasticity, crack initiation and cyclic plasticity in the plastic zone at the crack tip. Detailed surface inspection using scanning electron microscopy (SEM) allows much more detailed observation and an analysis of the formation and evolution of the surface relief. In combination with the focused ion beam (FIB) method, the advanced electron microscopy offers detailed observation of material microstructure just below the surface or in the crack vicinity. The FIB technique allows also extraction of the thin sections (lamellae) from the exactly defined location which is suitable for the transmission electron microscopy (TEM) observations of the dislocation structures. The information on the structure and surface relief across the SM or in the crack vicinity can be obtained and compared to the material bulk. Atomic force microscopy (AFM) and lithography measurements are other advanced methods allowing the analysis of the evolution of the surface relief and characterization of the conditions suitable for the fatigue crack initiation. Further, an analysis of the grain orientation and texture by electron backscatter diffraction (EBSD) enables to get comprehensive information about the changes of microstructure due to the applied cyclic loading and about the preferential sites of the specific dislocation structures creation resulting in the SBs formation.

Application of the knowledge base, in combination with the advanced methods for characterization of the material microstructure and its changes due to the cyclic loading, brings a new opportunity to describe better and understand deeper the mechanisms of material response to the cyclic loading and localization of the cyclic plastic deformation. This can further bring extra knowledge on the fatigue crack initiation mechanism in materials that have not been studied yet for the experimental limitations. The new information obtained by advanced methods brings a possibility to confirm or disprove some of the existing theories. An analysis performed on the nonferrous engineering materials with hcp structure will contribute to the knowledge base beneficial for both the academic and engineering field.

The present thesis summarizes author's previous and current contribution to the topic and puts the results in the context of current knowledge on the localization of cyclic plasticity during fatigue loading. The benefit lies in the broadening of the basic knowledge on the formation of SBs in the bulk and SMs on the surface together with microstructural changes both at the fatigue crack tip and in the crack vicinity. The investigation was mainly focused on the materials which are utilized in the engineering practice. Specific microstructure of the advanced materials resulting from their specific production, processing and/or treatment, results in specific properties. The current knowledge about the behavior of conventional microstructures is often inapplicable or applicable only partially. Therefore, the presented work outlines possible solutions for selected materials with hcp structure enabling accurate and reliable predictions of the fatigue life.

## 2 INFLUENCE OF THE GRAIN SIZE ON FATIGUE CRACK INITIATION

A fatigue crack initiation is a factor predetermining material lifetime and its effect is even more pronounced in the high cycle fatigue region. Localization of the cyclic plastic deformation due to the cyclic loading is in terms of the material surface influenced by both the surface roughness and the grain size. Those characteristics are the main factors influencing the fatigue crack initiation in homogeneous materials without internal defects.

The influence of the grain size in material bulk and on the surface processed by severe plastic deformation on the fatigue crack initiation was the main topic of authors' recent research work. The results contribute to deeper knowledge on the fatigue crack initiation mechanism in nonferrous engineering alloys.

### 2.1 AZ91 magnesium alloy

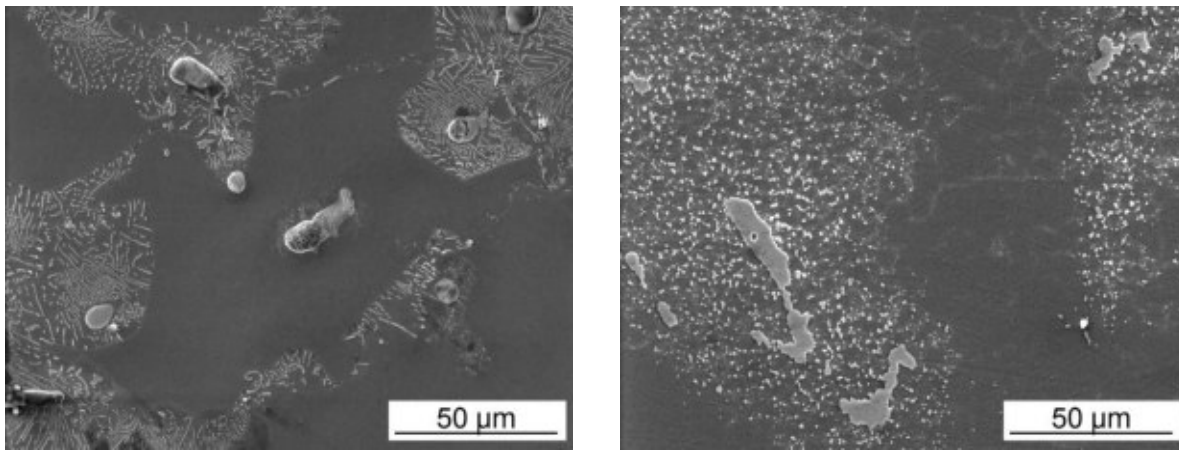
Low weight in combination with good mechanical properties, which can be easily tailored via chemical composition and material processing, is the main reason for a wide range of applications of magnesium-based alloys. Magnesium and most of its alloys have also good biocompatibility and besides the engineering applications also the biomedical field offers a large spectrum of material utilization. The main limiting factor for magnesium exploitation is its high reactivity resulting in low resistance to the corrosion.

Fatigue properties of AZ91 magnesium alloy (hcp crystallographic lattice) processed by ECAP (Equal Channel Angular Pressing) were examined in terms of fatigue tests in [25-30]. Advanced FIB cutting technique extending a conventional SEM observation was adopted to analyze the character of the surface relief created due to the localization of the cyclic plastic deformation and its relation to the fatigue crack initiation. The obtained results were compared with the behavior of a die-cast AZ91 magnesium alloy serving as the basic material for the SPD processing. The ECAP treatment of the alloy was performed at 300 °C. The cast semi-products were extruded through the ECAP die (die angle 120°) in BC route for 6 passes. The treatment resulted in a bimodal material structure. Fatigue tests were performed on a servohydraulic system Shimadzu at the stress ratio  $R = -1$  ( $R =$  ratio of minimum to a maximum stress of the loading cycle) at frequency  $f = 10$  Hz in the air at room temperature.

The cast microstructure consisted of areas of the solid solution of alloying elements (mainly Al and Zn) in Mg, eutectics (Mg solid solution +  $Mg_{17}Al_{12}$ ),  $Mg_{17}Al_{12}$  discontinuous precipitate particles, large particles of  $Mg_{17}Al_{12}$  intermetallic phase and AlMn based particles, Fig. 1a. The ECAPed AZ91 microstructure consisted of fine grain areas with the average grain size

of  $3.3 \pm 0.5 \mu\text{m}$  where the particles of individual phases present in the cast structure were localized in the grains as well as on the grain boundaries. Except for fine grain areas, regions with larger grains with the average grain size of  $9.9 \pm 5.5 \mu\text{m}$  and with particles present only on the grain boundaries, Fig. 1b, were present in the microstructure. The particles were smaller when compared to the cast structure, which is a result of the ECAP treatment.

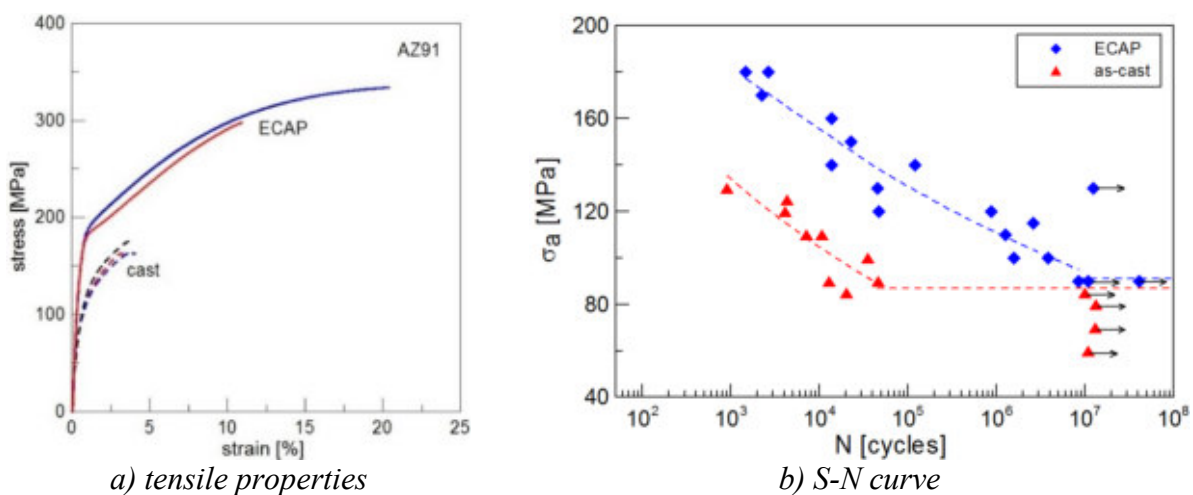
A significant increase of the ultimate tensile strength and yield stress from  $167 \pm 8 \text{ MPa}$  and  $87 \pm 7 \text{ MPa}$  for the as-cast state, to  $321 \pm 21 \text{ MPa}$  and  $160 \pm 4 \text{ MPa}$  for the ECAPed material, respectively, was found due to the grain refinement. An increase of ductility from  $3.1 \pm 0.4 \%$  obtained for the as-cast state to  $15.4 \pm 4.7 \%$  determined for the ECAPed material was connected with the bimodal microstructure of the material due to the SPD processing, Fig. 2a.



a) as-cast state

b) ECAPed state

Fig. 1 Microstructure of AZ91 magnesium alloy, etched by 5% Nital, SEM, [25].



a) tensile properties

b) S-N curve

Fig. 2 AZ91 magnesium alloy tensile and fatigue properties, [25-30].

Even though a positive influence of the grain refinement on the tensile properties and on the shift of the S-N curve to the higher number of cycles was reached, the fatigue endurance limit of the cast AZ91 magnesium alloy (80 MPa) was changed only slightly for the ECAPed structure (85 MPa), Fig. 2b [25].

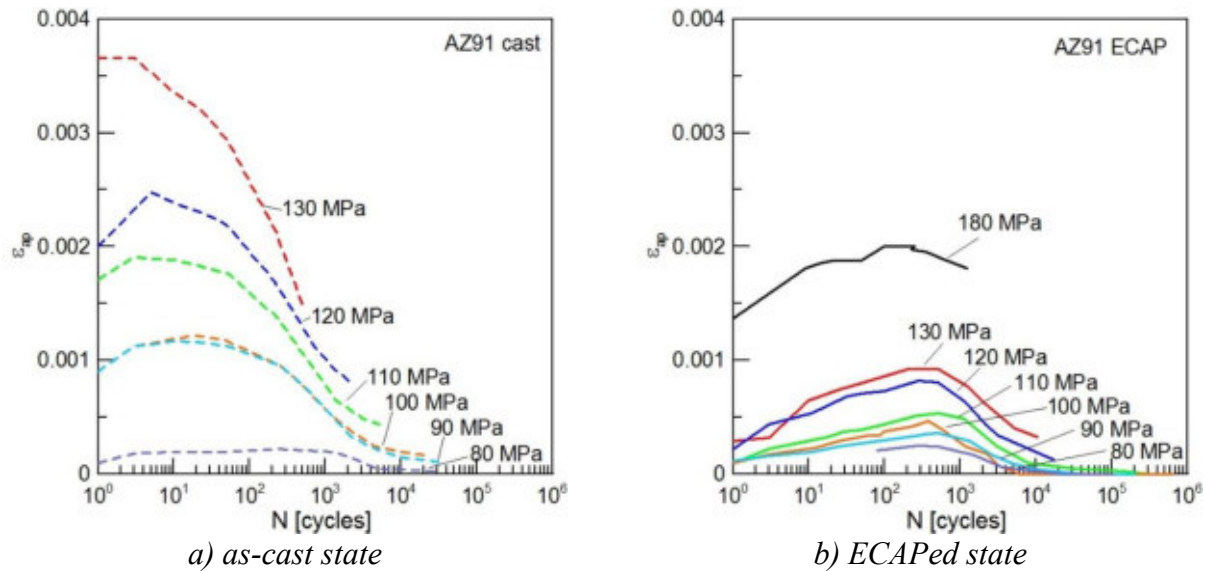
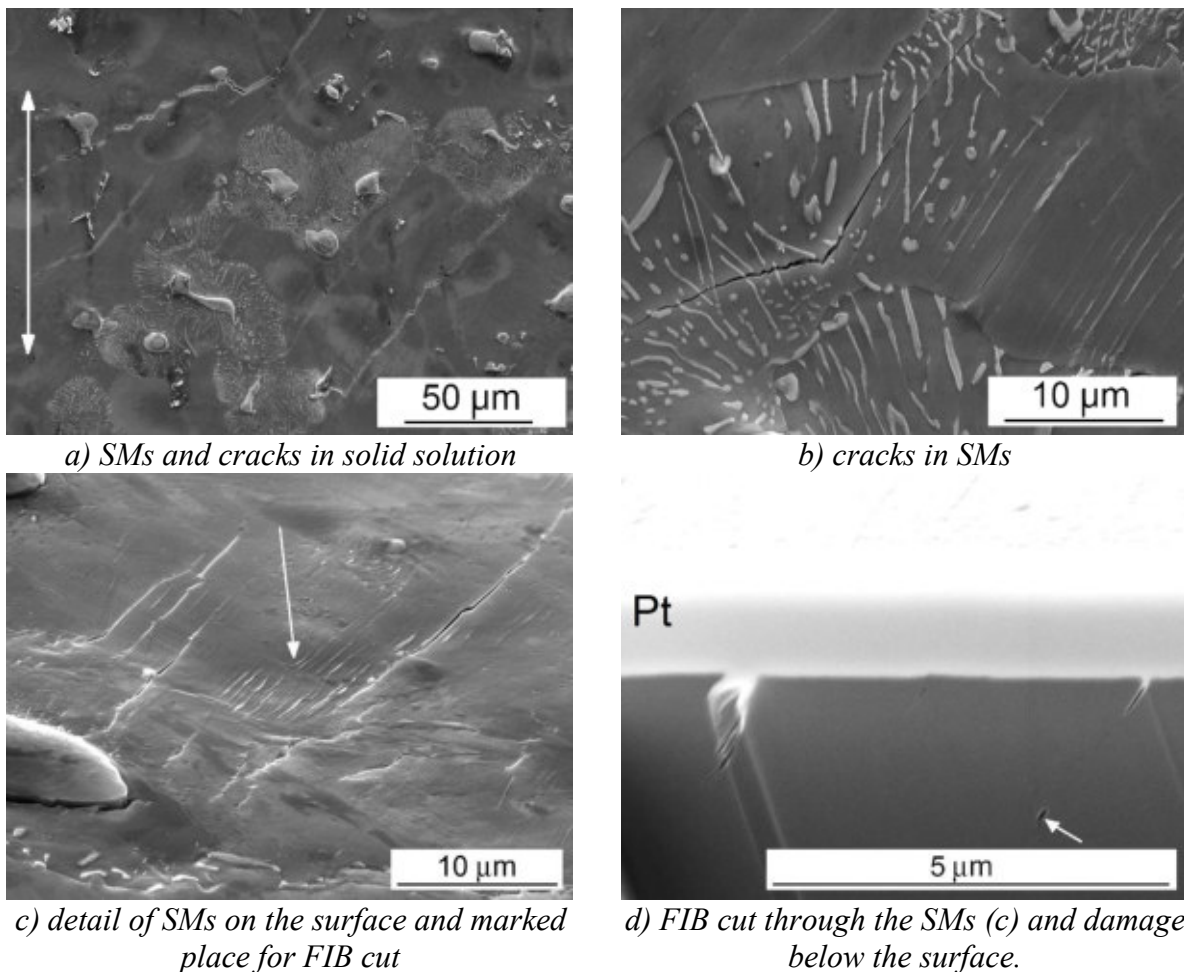


Fig. 3 Cyclic deformation curves for AZ91 magnesium alloy, [26].

The response to the cyclic loading was determined via hysteresis loops analysis [26]. The cyclic softening at the beginning of the cyclic loading was a characteristic feature for both material states. Subsequent cyclic hardening for the rest of the fatigue lifetime was observed. Primary cyclic softening up to 100 of cycles was characteristic for the as-cast state of AZ91 while in the case of the ECAPed material it was up to 1000 of cycles, see Fig. 3.

The creation of SMs on the polished surface in the whole stress amplitudes range for the cast alloy was observed. Fig. 4 shows SMs developed in the areas of the Mg solid solution. The SMs act as the fatigue crack initiation sites and were responsible for the failure of all tested specimens. The decrease of the stress amplitude resulted in the decrease of the amount and the size (length) of created SMs. Detailed SEM analysis of the FIB cuts performed through the SMs observed on the specimen surface, Fig. 4c, revealed a crack initiation and material damage in a form of voids and cavities, Fig. 4d. Observation of the FIB cuts indicated, that there is no direct relation between the height of extrusions and the damage along the slip plane below the surface. This means that for this type of materials, the models proposed for fcc metals are apparently not directly applicable.





*Fig. 4 Fatigue crack initiation analysis on the as-cast AZ91 material, 120 MPa, 4 088 cycles, mechanically polished and etched by 5% Nital before testing, SEM, FIB, [25].*

Two different mechanisms of the fatigue crack initiation were observed for the bimodal structure of the SPD treated material. In the case of the stress amplitudes above 120 MPa, the formation of the SM in the large grains of the bimodal structure and sometimes also the cracking of the grain boundaries in the small grain areas were observed, Fig. 5a-b. A limited number of SMs was observed also in the fine grains; however, the SMs created in the large grains were preferable sites for the fatigue crack initiation, Fig. 5a. Very sporadic development of SMs in the small grains of the bimodal structure indicates their minor contribution to the plastic deformation and consequently to the plastic strain amplitude. The initiation of cracks was entirely related to the cracking of the grain boundaries in the fine grain areas when SMs were not created, Fig. 5b.

The analysis of the FIB cuts performed through the SMs revealed the damage of the material below the surface and proved that the initiation of the fatigue cracks starts on the SMs, Fig. 5c. It seems that there is no relation between the height of extrusions on the material surface and the extent of the damage in the material interior, Fig. 5d.

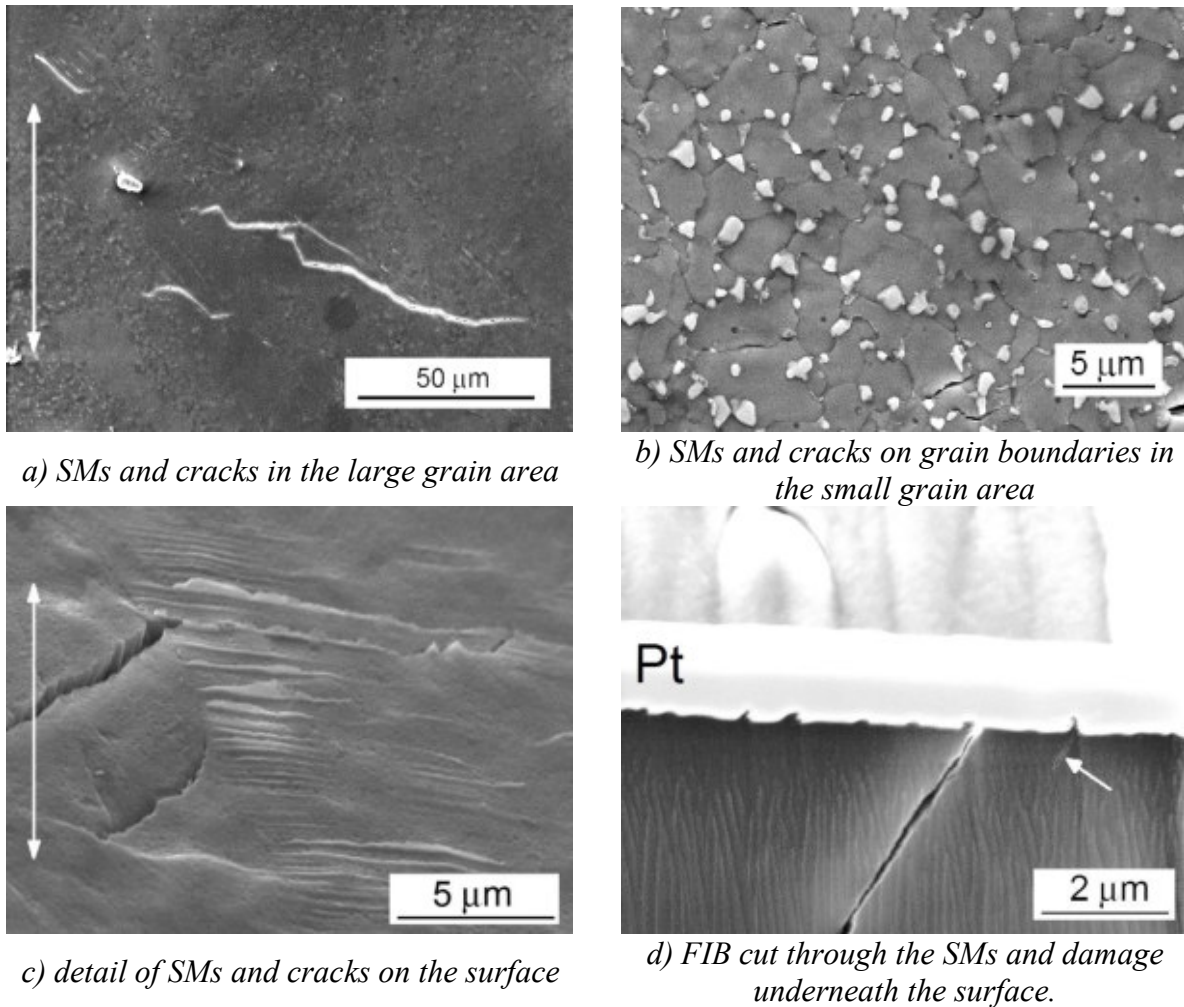


*Fig. 5 Fatigue crack initiation analysis on the ECAPed material, 180 MPa, 1 473 cycles, mechanically polished and etched by 5% Nital before testing, SEM, FIB, [25].*

Detailed analysis of the AZ91 magnesium alloy response on the cyclic loading using the advanced microscopic methods revealed differences in the behavior of the cast and ECAPed material. While the creation of SMs on the material surface due to the localization of the plastic deformation was a characteristic feature of the as-cast microstructure, the combination of SMs formation in a limited extent and the grain boundary cracking were two mechanisms responsible for the failure of the ECAPed material. The grain refinement resulted in a decrease of the ability of the material to be plastically deformed under the cyclic loading, therefore, only limited number of SMs in the case of ECAPed material exposed to higher stress amplitudes was observed. Decreasing stress amplitude resulted in the fatigue cracks initiation on the grain boundaries. No relation between the height of extrusions on the material surface (SM size) and the extension of the damage below the surface was observed for both material types. However, besides the cracks initiated on the SMs also cavities below the surface localized in the slip planes were observed in the case of the cast material.

The observation and interpretation of the results published in [25-30] contributed to the discussion about the mechanisms of the localization of the cyclic plastic deformation in UFG hcp materials.

## **2.2 AW 6082-T561 aluminum alloy**

Besides the grain refinement in the whole material volume, the surface grain refinement by means of various techniques is another way how to improve fatigue resistance. The effect is related to retarding of the fatigue crack initiation on the surface. One of the often applied approach for the surface grain refinement and the surface, strengthening is shot peening (SP).

The surface of specimens of the wrought AW 6082-T561 aluminum alloy (fcc crystallographic lattice) was treated by an air blast shot peening with Almen intensity 6 N and coverage of 100 %, [31]. Almen intensity represents the SP intensity defined as the arc height of an Almen test strip measured at a saturation point by using an Almen gauge. The coverage means the percentage of the surface actually impacted by the shot peening process (dimpled or obliterated surface). Resulting material structure analyzed in terms of light microscopy (LM) can be characterized as having elongated grains of the solid solution of Zn and alloying elements present in alloy and small intermetallic phase particles present on grain boundaries, Fig. 6. The fatigue tests of specimens with non-treated (as received), SP and SP+anodizing treated surface were performed at  $f = 20$  kHz,  $R = -1$  at laboratory air and temperature.

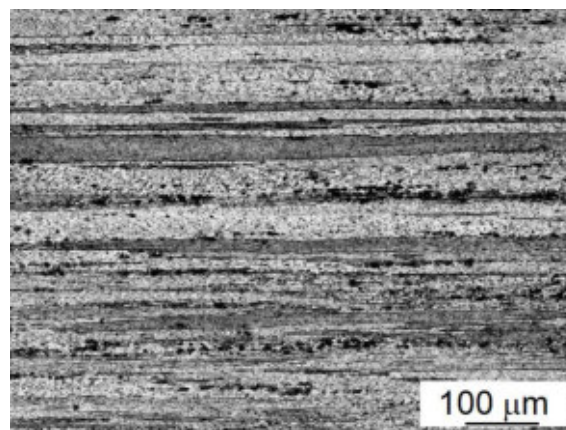
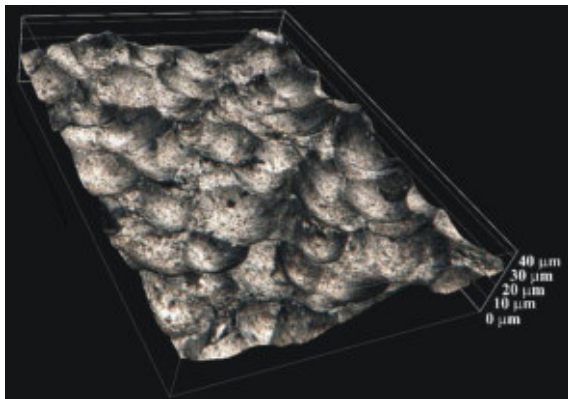


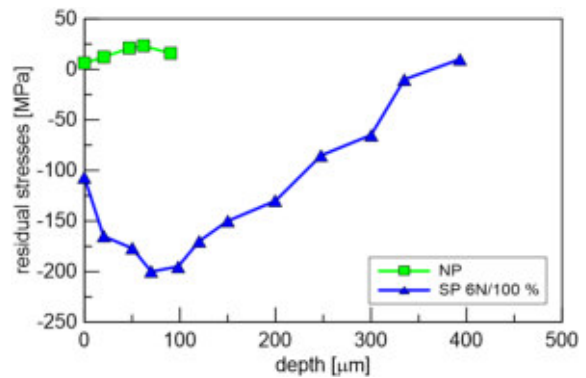
*Fig. 6 Microstructure of SP AW 6082-T561 in the longitudinal cut, etched with Tucker, LM, [31].*

The SP usually generates compressive residual stress field in the surface layer accompanied by the grain refinement and increased surface roughness, Fig. 7. Compressive residual stresses at the surface have generally positive effect from the point of view of fatigue life, contrary to the increasing surface roughness. Higher surface roughness is, usually, connected with shorter

fatigue life, because the stress concentration due to the notch effect promotes the initiation of cracks and decreases the fatigue strength.



a) morphology of the surface after SP, 3D reconstruction LM



b) residual stress profiles

Fig. 7 Surface roughness and residual stress profiles of AW 6082-T561, [31].

The results of the fatigue tests, Fig. 8, revealed a positive influence of the surface treatment performed by SP comparing to the non-peened (NP) material in the low, high and even in the ultra-high cycle fatigue region. The results indicate that the negative effect of the surface roughness is weaker than the positive effect of the compressive residual stresses reaching the maximum of 205 MPa, Fig. 7b. While the stress amplitude of 110 MPa can be considered as the conventional fatigue endurance limit (specimens not broken for  $10^7$  cycles) for the NP material, SP of the surface resulted in the increase of the endurance limit to the value of 140 MPa. The increase of the fatigue endurance limit in the ultra-high cycle fatigue region due to the SP surface was observed as well (to be from 85 to 115 MPa). Additional anodic oxidation of the SP surface, which is performed with the aim to improve material corrosion resistance, resulted in a decrease of the fatigue life in both the low and high cycle fatigue regions. However, better fatigue properties in the ultra-high cycle fatigue region were reached when compared to the only SP material.

Improvement of the fatigue properties of the AW 6082-T561 aluminum alloy after SP can be attributed to the strengthening of the surface layer due to the presence of compressive residual stresses and the grain refinement. These effects led to the improvement of material surface layer resistance against crack initiation and propagation.

While the machining caused a formation of a short-range tensile residual stress field (maximum value of 25 MPa up to 100  $\mu\text{m}$  below the surface) in the case of NP specimens, the SP generated the compressive residual stress field with a maximum of 205 MPa, Fig. 7b, [31]. Even though the depth of the compressive residual stress field was approximately 350  $\mu\text{m}$ , the maximum value



was reached at a distance of about 100  $\mu\text{m}$  below the surface, which corresponds to the change of the crack path observed on the fracture surface of fatigued specimens in Fig. 9.

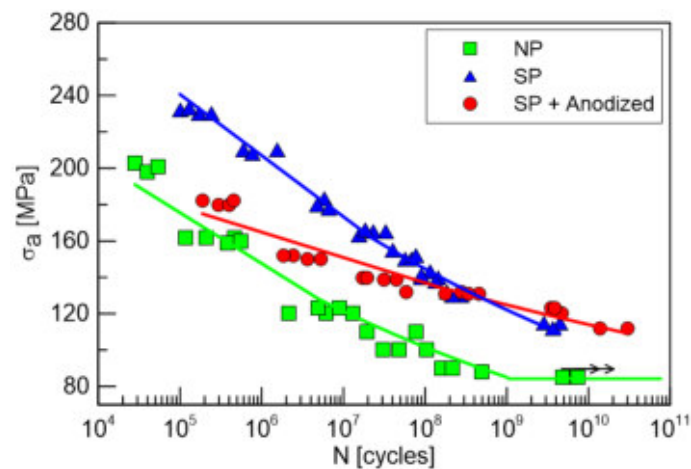
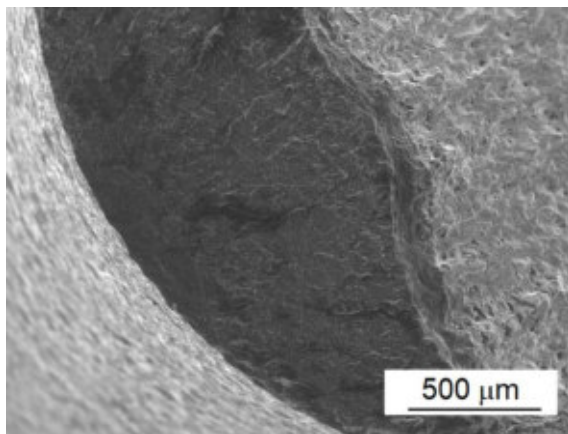
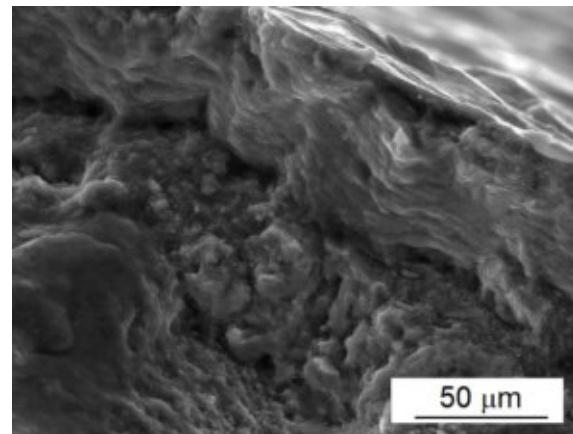


*Fig. 8 S-N curves of AW 6082-T561 with different surface treatment; NP – non-peened, SP – shot peened, SP+Anodized – shot peened + anodized surface, [31].*



*a) fracture surface*



*b) initiation site + crack path change*

*Fig. 9 Fatigue crack initiation in AW 60-82-T561, SEM, [31].*

Obviously, the compressive residual stress field in combination with the fine-grained structure eliminate the negative effect of the increased surface roughness created during the SP. Even though a large number of cracks on the rough SP surface was observed, the surface SP layer resistance to the short crack growth was responsible for the higher lifetime compared to the NP material.

Anodizing performed after SP resulted in the creation of a brittle oxide layer on the material surface including defects, which have acted as fatigue crack initiation sites. Moreover, the easy initiation of the cracks in the brittle  $\text{Al}_2\text{O}_3$  layer due to the cyclic loading resulted in reduced fatigue strength when compared to SP specimens.

### 2.3 AW 7075-T6511 aluminum alloy

Individual parameters of the SP treatment can strongly influence surface characteristics such as roughness, residual stresses, compactness, etc. Properties of the surface layer is an important feature regards to the fatigue crack initiation, therefore an analysis of the influence of the SP parameters on the character of the fracture surface of AW 7075-T6511 aluminum alloy was performed in [32].

Parameters of the SP such as Almen intensity and coverage are the important factors influencing the character of the surface layer of the SP material. Variation of SP parameters results in a different thickness of the deformed layer, different level of deformation and different surface roughness. Specimens with the surface peened using a various set of parameters were subjected to the fatigue tests on the ultrasonic device under the frequency of 20 kHz.

The dependence of the fatigue life of AW7075 aluminum alloy on applied SP parameters is shown in Fig. 10. A significant differences in the fatigue life of the specimens with different SP treatment parameters were observed.

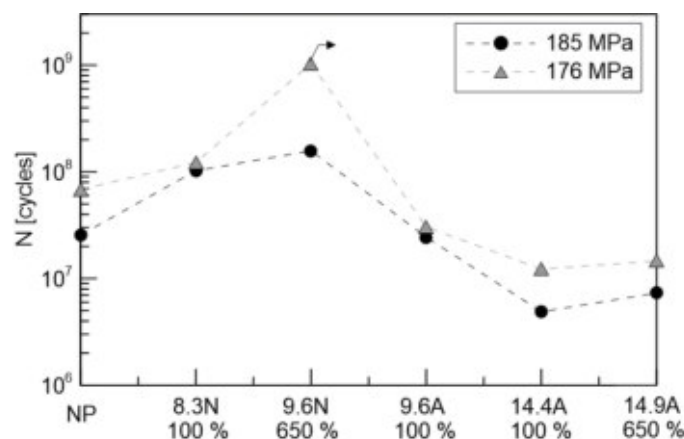
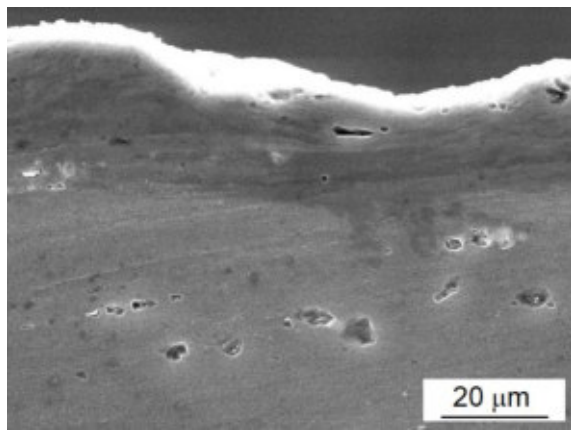
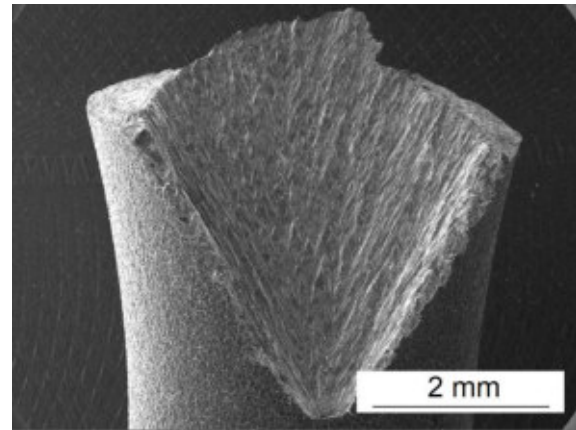


Fig. 10 Dependence of fatigue life on the shot peening intensity and coverage of AW7075 aluminum alloy, [32].

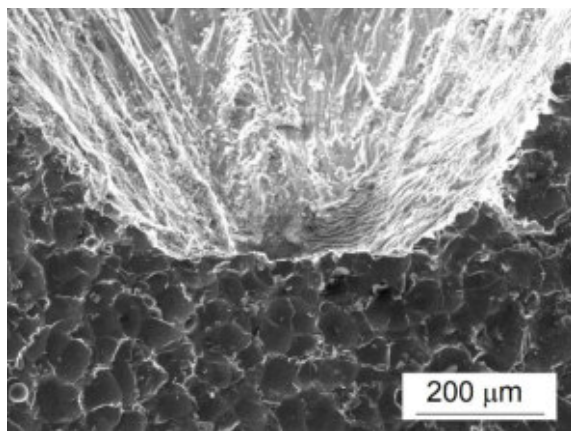
Detailed analysis of the surface layer revealed the differences in the thickness and character of the SP layer on the material surface. While appropriate SP parameters resulted in a quite compact deformed layer, Fig. 11a, the overpeening resulted in defects and microcracks formation in the SP layer, Fig. 12a. The defects act as fatigue crack initiation sites during the cyclic loading. Surface roughness increased due to the SP treatment, represents larger number of stress concentrators. An increased number of the fatigue secondary cracks on the specimen surface was observed after cycling. On fracture surfaces of all SP specimens the change of the crack path was observed. As the fatigue crack which initiated on the specimen surface reached the SP layer/bulk material interface, the crack path direction changed, Fig. 11d and Fig. 12d.



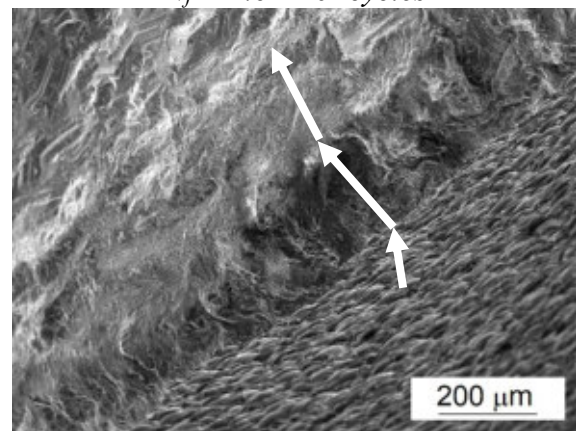
*a) surface SP layer, etched with Fuss*



*b)  $\sigma_a = 185 \text{ MPa}$ ,  
 $N_f = 1.6 \times 10^8 \text{ cycles}$*



*c) fatigue crack initiation site + surface morphology*

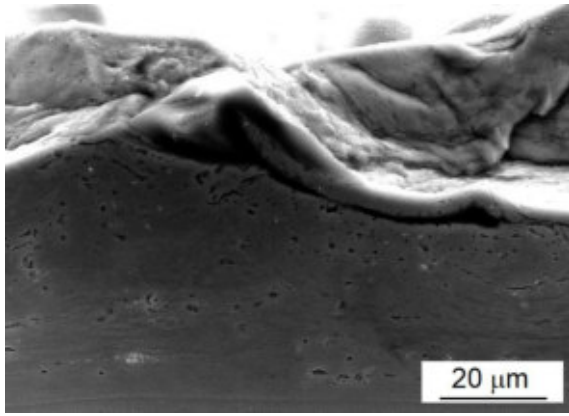


*d) change in the crack growth path – SP surface layer*

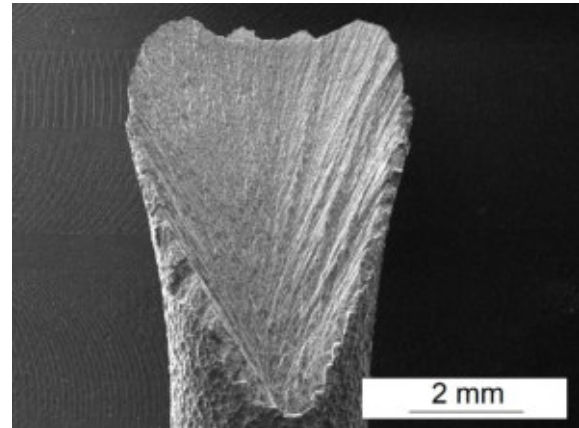
*Fig. 11 Characterization of the surface and fatigue fracture mechanism of the specimen with SP treatment at 9.6 N/650 %, SEM, [32].*

Defects and cracks in the SP layer created using the overpeening parameters resulted besides the cracks initiation also in the layer peeling off during the cycling, Fig. 12e.

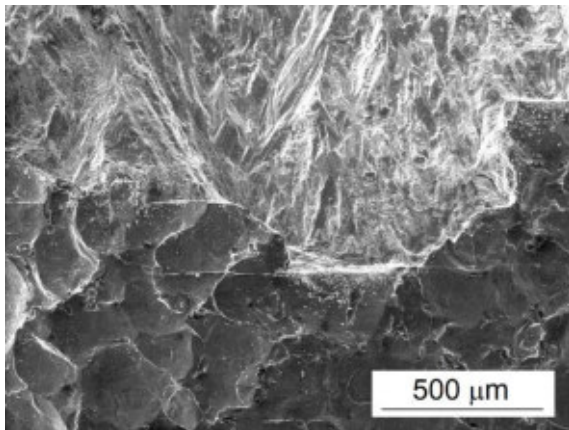
The investigation has shown that under appropriate SP parameters which did not result in the creation of a layer full of defects and cracks (as overpeened layer), the fatigue life can be significantly improved when compared to the NP specimens [32]. Layer deformed by the SP treatment, usually consisting of fine grains and containing compressive residual stresses, is more resistant to the crack initiation and to the short cracks growth when compared to the material without surface deformation. However, the SP parameters and the quality of the SP layer have to be thoroughly examined/checked, since the overpeening and inappropriately chosen processing parameters can have a detrimental effect on the treated material fatigue life.



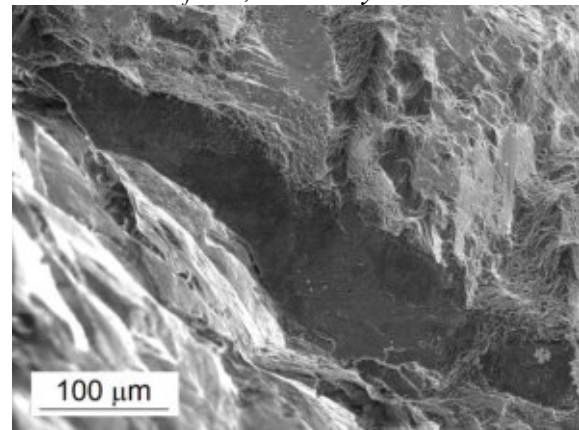
a) surface SP layer, etched with Fuss



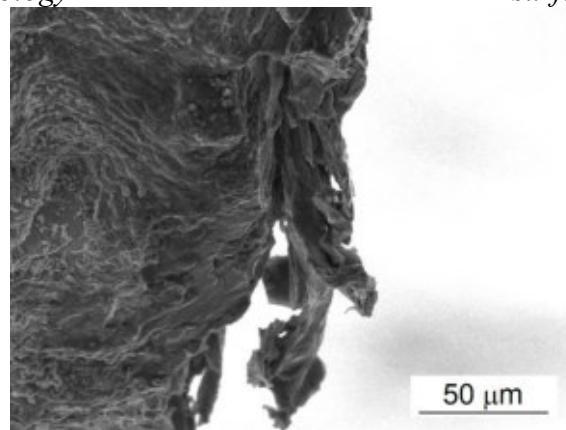
b)  $\sigma_a = 185 \text{ MPa}$ ,  
 $N_f = 7,3 \times 10^6 \text{ cycles}$



c) fatigue crack initiation site + surface morphology



d) change in the crack growth path – SP surface layer



e) peeling off of the surface layer

Fig. 12 Characterization of the surface and fatigue fracture mechanism of the specimen with SP treatment at 14.9 N/650 %, SEM, [32].



### 3 INFLUENCE OF THE GRAIN SIZE ON THE FATIGUE CRACK GROWTH

The cyclic stress-strain response and fatigue crack growth in metallic materials is influenced by the grain size. The UFG microstructure, prepared by the SPD may not be stable under the cyclic loading, particularly under loading with higher plastic strain amplitudes. Such conditions are characteristic for propagating long cracks in their plastic zone, particularly at higher crack growth rates. The influence of cyclic plasticity on the UFG microstructure at the crack tip has been studied up to now rarely in just a few works.

Author's contribution to the investigation of this topic can be seen in a study dealing with the crack growth in the threshold region and the effect of cyclic plasticity on the UFG microstructure stability.

#### 3.1 Pure copper

The identification of the influence of the grain size on the fatigue crack growth rate and its mechanisms in pure copper (fcc crystallographic lattice) was the aim of the work [33].

A servohydraulic testing device for the fatigue tests at  $R = 0.1$  and  $f = 20$  Hz at laboratory temperature was used. Experiments in vacuum and for comparison also in the air were performed. The research effort was also paid to the identification of the effective part of the stress intensity factor and to the problem of the crack closure. Standardized polished CT specimens with dimensions of  $19 \times 19 \times 5$  mm for the crack growth tests were used. The UFG material was processed by ECAP treatment by 5 passes through the ECAP die at the BC route, resulting in the grain size below  $1 \mu\text{m}$ .

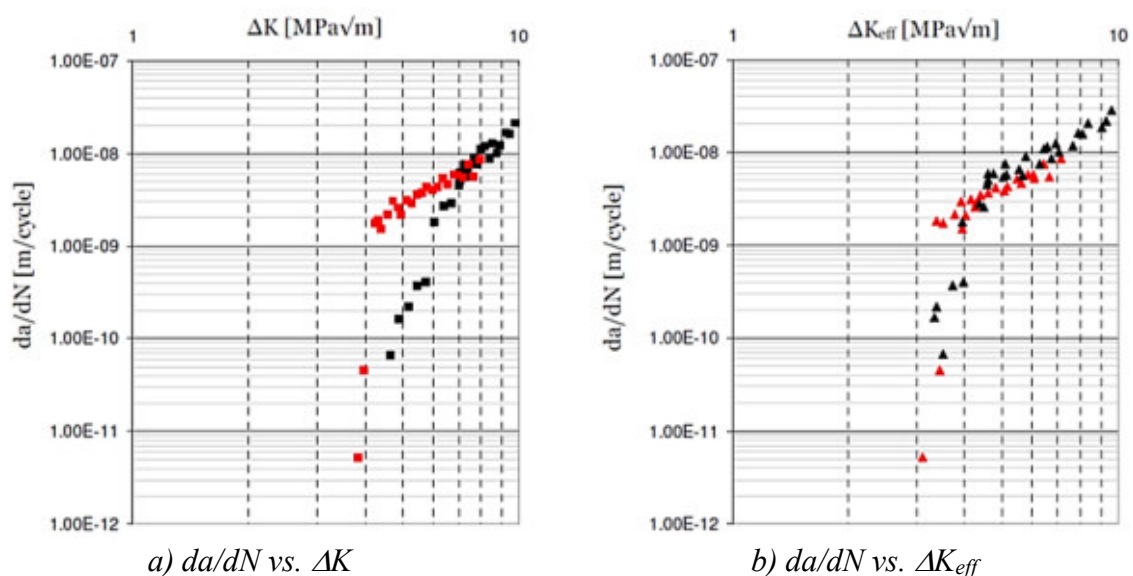


Fig. 13 Crack growth test results for pure Cu, CG – black, UFG – red, air,  $R = 0.1$ , [33].

The UFG Cu exhibited higher crack growth rates in the near threshold region, specifically below the stress intensity factor range  $\Delta K$  of  $7 \text{ MPa}\cdot\text{m}^{1/2}$  when compared to the coarse-grained (CG) Cu (average grain size of  $50 \text{ }\mu\text{m}$ ). Correspondingly, the threshold of the stress intensity factor for the UFG Cu was lower. However, taking into account the effective value of the stress intensity factor,  $K_{eff}$ , identical crack growth rates and threshold stress intensity factor values were found for both the UFG and the CG material, Fig. 13.

Different response of the UFG material on the cyclic loading in vacuum was observed when compared to the testing in air. The crack path change accompanied with lower crack growth rates and more pronounced SM creation on the specimen surface were characteristic features when the testing environment was changed from air to vacuum, Fig. 14. The change of the atmosphere influences the crack growth character and the threshold stress intensity factor which is lower for vacuum when compared to the UFG specimen tested in air.

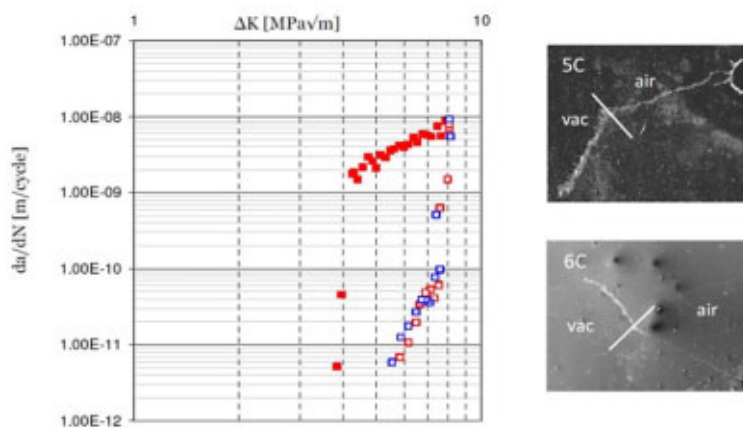
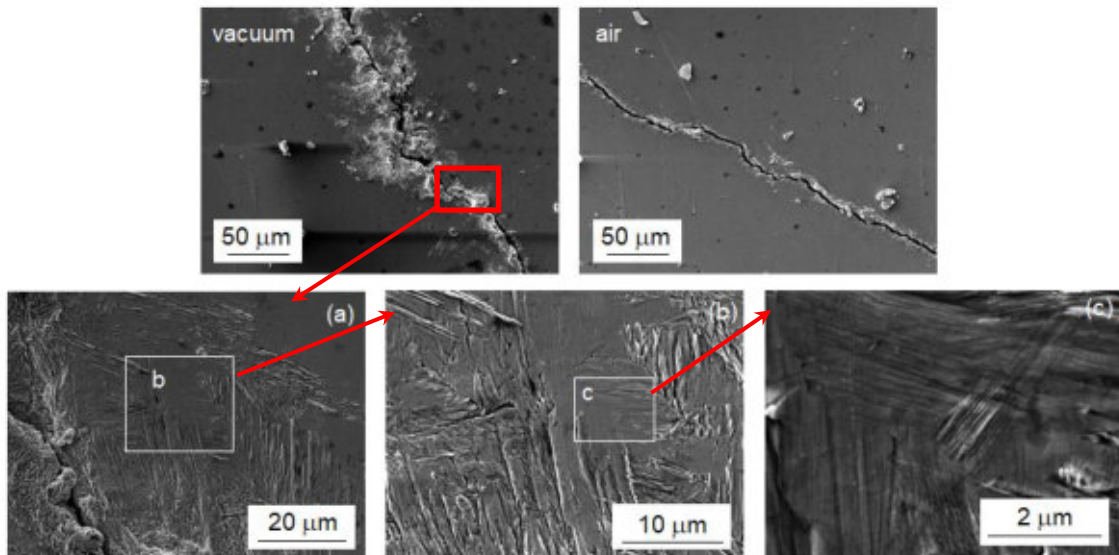


Fig. 14  $da/dN$  vs.  $\Delta K$  curves for UFG specimens tested in the air (full red symbols) and under the vacuum (5C red empty symbols, 6C blue empty symbols), [33].

In the case of the CG Cu tested in the air the SMs in the vicinity of the crack and in the plastic zone at the crack tip were observed. Similar behaviour in the case of the UFG Cu processed by the ECAP with the average grain size smaller than  $1 \text{ }\mu\text{m}$  was also found. Even though the grain refinement resulted in the significant improvement of mechanical properties, the SMs created due to the localization of the cyclic plastic deformation were present in the vicinity of the crack and at the crack tip. The similar character of the material response and an evolution of the surface relief in the crack vicinity for the specimens tested in air and also in vacuum was observed, however, the intensity of the slip activity and the number of the created SMs were higher for the UFG material tested in vacuum when compared to the specimen tested in air, Fig. 15.



*Fig. 15 Surface of UFG specimen tested in air and under the vacuum with details of the slip activity in the vicinity of the crack tip (a-c), SEM, [33].*

Adopting FIB technique, the changes of the UFG microstructure in the vicinity of the crack path were observed and analyzed. The FIB cuts performed transversely to the crack and in the plastic zone of the crack tip revealed grain coarsening caused by the cyclic loading at nearly the same  $\Delta K$ . The extent of the grain growth was dependent on the testing environment used (air or vacuum), Fig. 16.

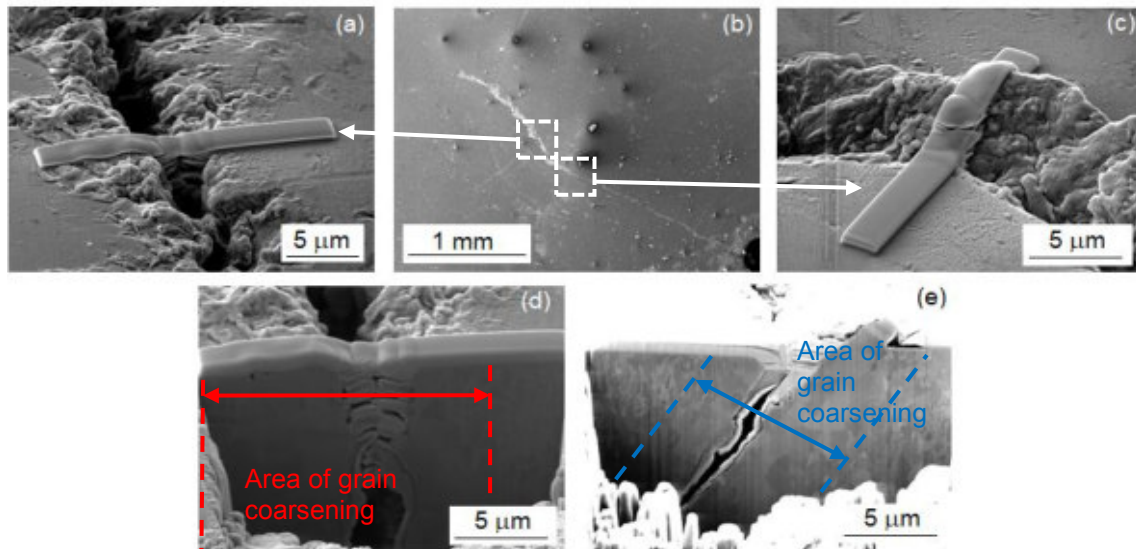


*Fig. 16 FIB observation of the UFG microstructure evolution in the crack vicinity in air (a, d) and in vacuum (c, e), SEM, FIB, [33].*

The larger area of the grain coarsening was observed in the case of testing in the air when compared to the testing in the vacuum. The extent of grain coarsening was explained by the dynamic recrystallization of the UFG material caused by the stress field at the crack tip. The observed grain

coarsening was correlated to the development of the plastic zone size created at the crack tip during the crack growth.

The fracture surface relief was more pronounced for the CG material when compared to the UFG Cu, however, no influence of the crack growth rate or the applied loading on the fracture surface morphology was observed for both material states.

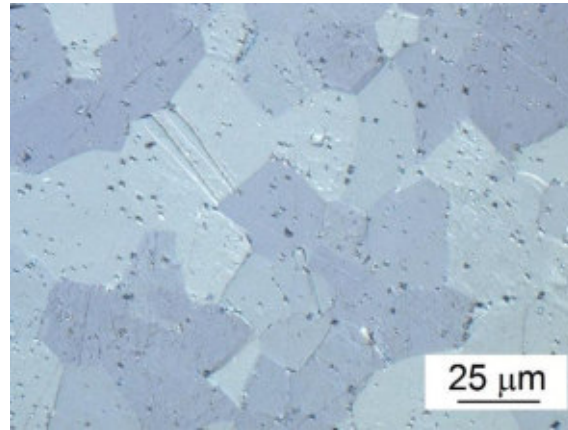
Application of advanced experimental methods for the microstructure observation and the analysis brought a new piece of knowledge on differences between fatigue behavior of the CG and UFG copper; the results are in detail discussed in [33]. Moreover, it was found and discussed that taking into account effective values of the stress intensity factor,  $K_{eff}$ , the same fatigue crack growth curve for both material states was obtained in air. However, tests performed on the UFG Cu, consequent analysis of obtained data and observation of specimens revealed different response of the material in terms of the more pronounced SMs formation and the smaller extent of grain coarsening in the vacuum when compared to the results obtained in air.

### 3.2 Commercially pure titanium grade 4

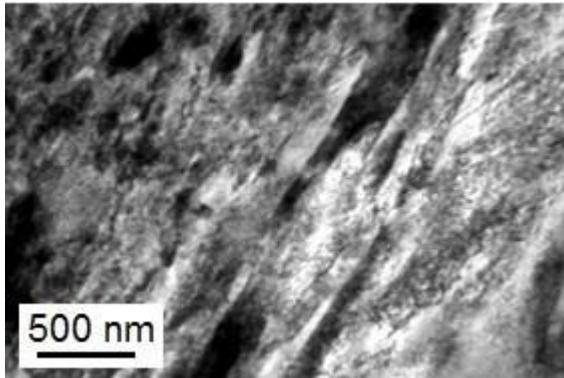
The influence of the grain size on the fatigue crack growth rate and the crack growth mechanism in conventionally pure (CP) titanium grade 4 was studied in [34]. The CG material with the average grain size of  $16.3 \pm 1.0 \mu\text{m}$  processed by ECAP (BC route, 250 °C, 4 passes) followed by cold drawing (at temperature 200 °C) was used in this study. Elongated grains with the average minor axis of 250 nm and the major axis of 1.5  $\mu\text{m}$  were characteristic for the UFG material, Fig. 17. The microstructure of CG and UFG materials was analyzed by light optical microscopy (LM) The microstructure of the UFG state was observed by TEM.

Fatigue crack growth tests utilizing a servohydraulic testing device at  $R = 0.1$ ,  $f = 20 \text{ Hz}$  in laboratory air and temperature were performed. Non-standardized single edge notched specimens (length 70 mm, 5 mm width and 2 mm thickness) with an extensometer placed on the specimen (on the notch side) were used for the crack growth rate and for the crack closure measurements.

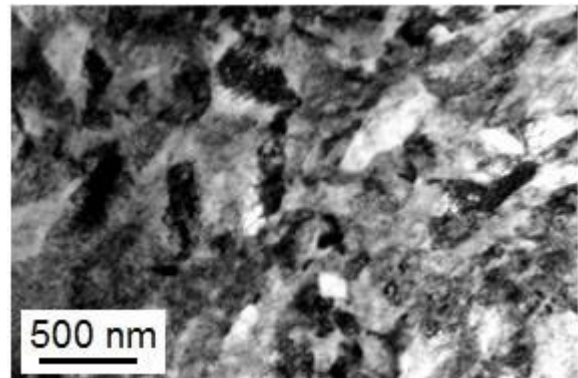
The UFG material exhibited higher fatigue crack growth rates in the Paris region and in the threshold region comparing to the CG Ti, Fig. 18a. A lower value of the threshold stress intensity factor for the UFG material ( $2.5 \text{ MPa m}^{1/2}$ ) comparing to the CG material ( $4.7 \text{ MPa m}^{1/2}$ ) was found. However, taking into account the effective value of the stress intensity factor, identical fatigue crack growth curves were determined for both material states, Fig. 18b.



a) basic CG state, LM, etched with 50 ml H<sub>2</sub>O + 30 ml HNO<sub>3</sub> + 15 ml HF, LM

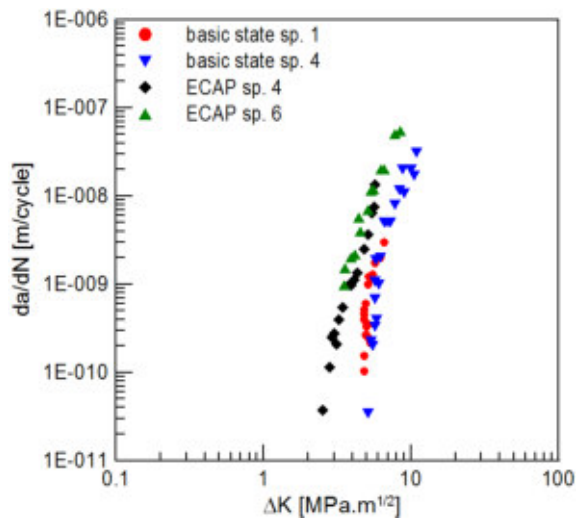


b) UFG state, longitudinal direction, TEM

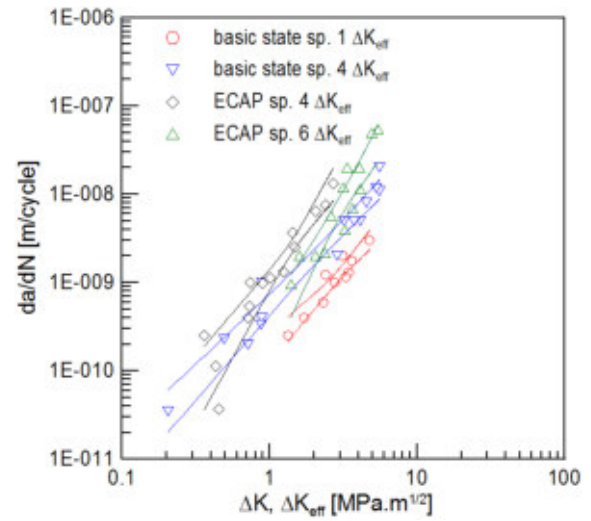


c) UFG state, transversal direction, TEM

Fig. 17 The microstructure of CP Ti grade 4, [34].



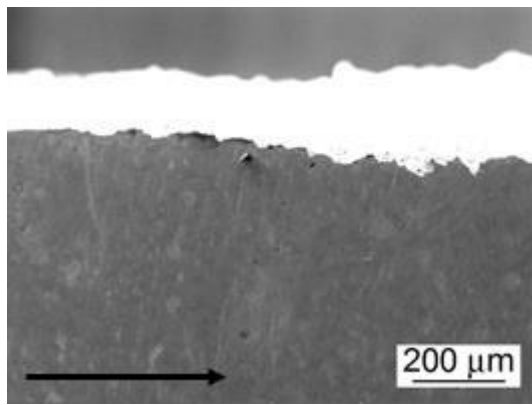
a)  $da/dN$  vs.  $\Delta K$



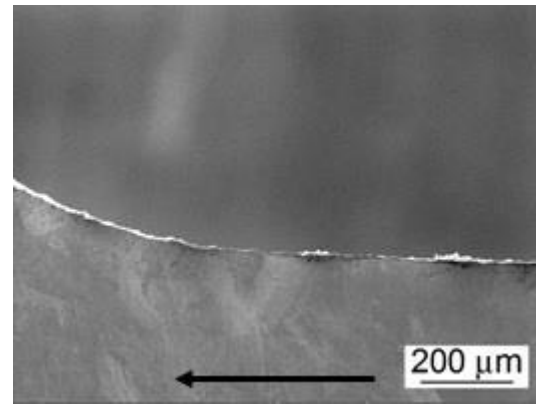
b)  $da/dN$  vs.  $\Delta K_{eff}$

Fig. 18 Fatigue crack growth curves, [34].

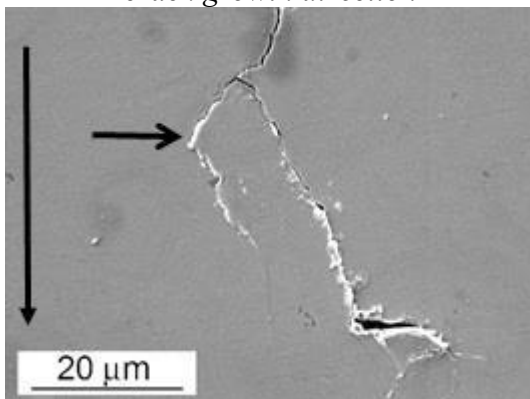




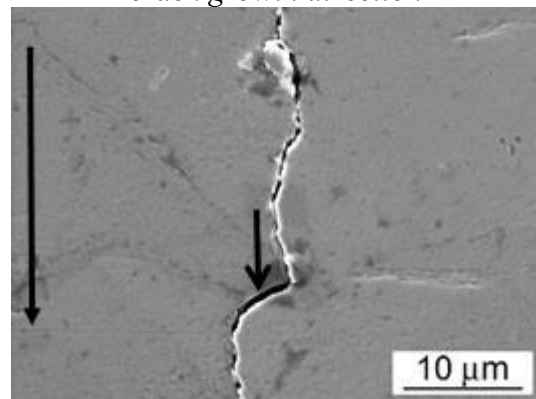
a) crack path, CG state; arrow indicates crack growth direction



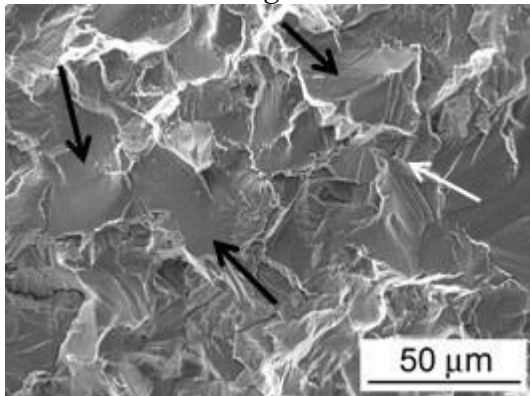
b) crack path, UFG state; arrow indicates crack growth direction



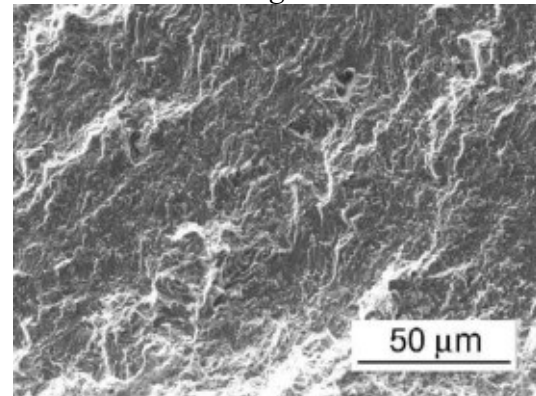
c) crack character, CG state; arrow indicates crack growth direction



d) crack character, UFG state; arrow indicates crack growth direction



e) crack growth rate  $1 \times 10^{-9}$  m/cycle, CG state



f) crack growth rate  $1.76 \times 10^{-9}$  m/cycle, UFG state

Fig. 19 CP Ti grade 4, crack growth character, SEM, [34].

While the material has a good corrosion resistivity and no damage of the fracture surfaces due to the roughness induced closure on fracture surfaces was observed, the plasticity induced closure was assumed to be absolutely decisive for the crack closure. Taking this into account, the crack closure was calculated according to the model proposed by Newman. Because the results of numerical calculations and the experimentally determined values were in good agreement it was concluded that besides the plastic closure the other closure mechanisms are insignificant in this case.

The fracture surface of the CG material exhibited higher roughness comparing to the fracture surface of the UFG material. While the same intensity of the plasticity induced closure for both the states of the same material are assumed, the shift of the threshold stress intensity factor (Fig. 18) to the higher values for the CG Ti could be attributed to the roughness induced closure.

No influence of the crack growth rate or of the applied loading on the fracture mechanism was observed in the case of both material states.

Although the incorporation of the effect of plasticity induced closure on the fatigue crack propagation describes quite well the differences in the crack growth rate curves of UFG and CG materials and although this type of closure is evidently dominant, a classical manifestation of the cyclic plasticity was not observed. No signs of the localization of the plastic deformation in the crack vicinity were observed, neither in the vicinity of the crack tip, Fig 19a-d.

The fracture surface of Ti in the CG state, Fig. 19e, was characteristic with a combination of the inter-granular and the trans-granular quasi-cleavage areas (examples shown in Fig. 19e with arrows; black – trans-crystalline, white – inter-crystalline fracture surface). Primary crack branching and presence of secondary cracks were often found on the CG specimen surface, Fig. 19c.

The fracture surface appearance of the UFG Ti was substantially different from the appearance of the CG material. The fracture surface of the UFG Ti seems to have a transcrystalline character, Fig. 19c. No signs of the intercrystalline fracture were observed in this case. Similarly to the case of CG material no difference in the fracture surface and thus the crack growth mechanism for the crack rates ranging from  $10^{-8}$  m·cycle<sup>-1</sup> to the threshold was observed.

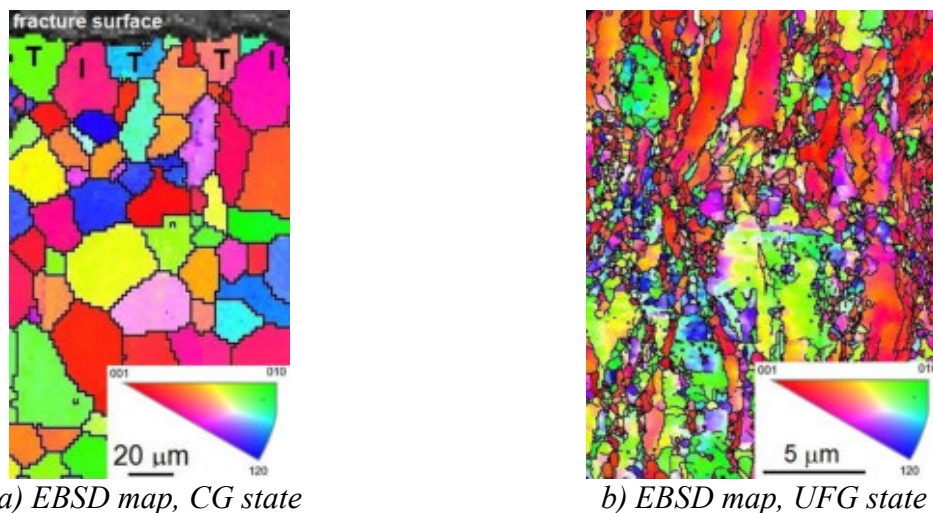


*Fig. 20 CP Ti grade 4 EBSD maps in the crack vicinity, [34].*

The analysis of the cross-cuts prepared by the FIB method did not provide any information about the UFG material microstructure. Based on the results of the EBSD mapping, Fig. 20,

of the broken specimen surface, no significant grain coarsening in the case of the UFG material was observed.

The main conclusion of the investigation of the influence of the grain size on the fatigue crack growth in CG and UFG Ti grade 4, is following: different crack growth curves and threshold values were experimentally determined when the stress intensity factor range is used as a crack growth criterion [34]. However, taking into account only the effective part of the threshold stress intensity factor, the same fatigue crack growth behavior for both material states was observed. No signs of localization of the cyclic plastic deformation were observed for both the material states, even though the cyclic plasticity is apparently decisive for the crack growth mechanism.



## **4 INFLUENCE OF CASTING DEFECTS**

Microstructural inhomogeneities, when they are large enough, act as stress concentration sites where the localized cyclic plastic deformation results in the crack initiation during the fatigue loading. Casting defects, which belong to the inevitable defects in cast engineering materials, are the most dangerous sites from the fatigue crack initiation point of view of conventionally produced and commercially used materials.

Adopting a statistical method for the evaluation of casting defects in both aluminum alloys and nickel-based superalloys and the fatigue life prediction was the topic of authors study. The main aim of the analysis was to specify the influence of microstructural defects on the fatigue crack initiation.

### **4.1 AlSi7Mg aluminum alloy**

Cast aluminum alloys are materials used in industry for their good strength to weight ratio and for the reasonable price. On the other hand, the disadvantage of all cast materials lies in the unavoidable presence of casting defects. They limit the mechanical and, particularly, fatigue properties of cast components. It is well documented, that the fatigue properties of cast Al-Si alloys depend primarily on the casting defects which act as the stress concentrators and/or fatigue crack initiation sites.

The AlSi7Mg cast alloy after T6 heat treatment was subjected to the metallographic analysis using the Largest Extreme Value Distribution (LEVD) statistical method for the prediction of the largest defect size [35-39]. It is assumed that the largest defect, resp. the defect with the highest stress concentration is a critical site for the initiation of fatigue cracks and thus for the fatigue life. One of the most difficult issues is a characterization of the defect size and its shape. Usually, the square root area ( $\text{area}^{1/2}$ ) as the characteristic defect size is used, [35-41], however, due to the complicated shape of some casting defects (shrinkage pores) also other parameters for the LEVD statistical analysis of material structure such as equivalent diameter or Feret diameter were used [35, 39-41]. An x-ray computed tomography for detailed inspection of the real shape and size of the present casting defects was used in [39, 42], where also the Feret diameter for the defect size description instead of conventional  $\text{area}^{1/2}$  was used.

The microstructure of the cast AlSi7Mg – T6 alloy, which was investigated in [35-41] consisted of dendrites of a solid solution of the alloying elements in Al and eutectics which was formed by a solid solution and almost pure Si crystals, Fig. 21a. Due to the casting process, the defects were inevitable in the AlSi7Mg microstructure. Two types of casting defects usually appeared: (i) gas pores and (ii) shrinkage pores, Fig. 21b-c.

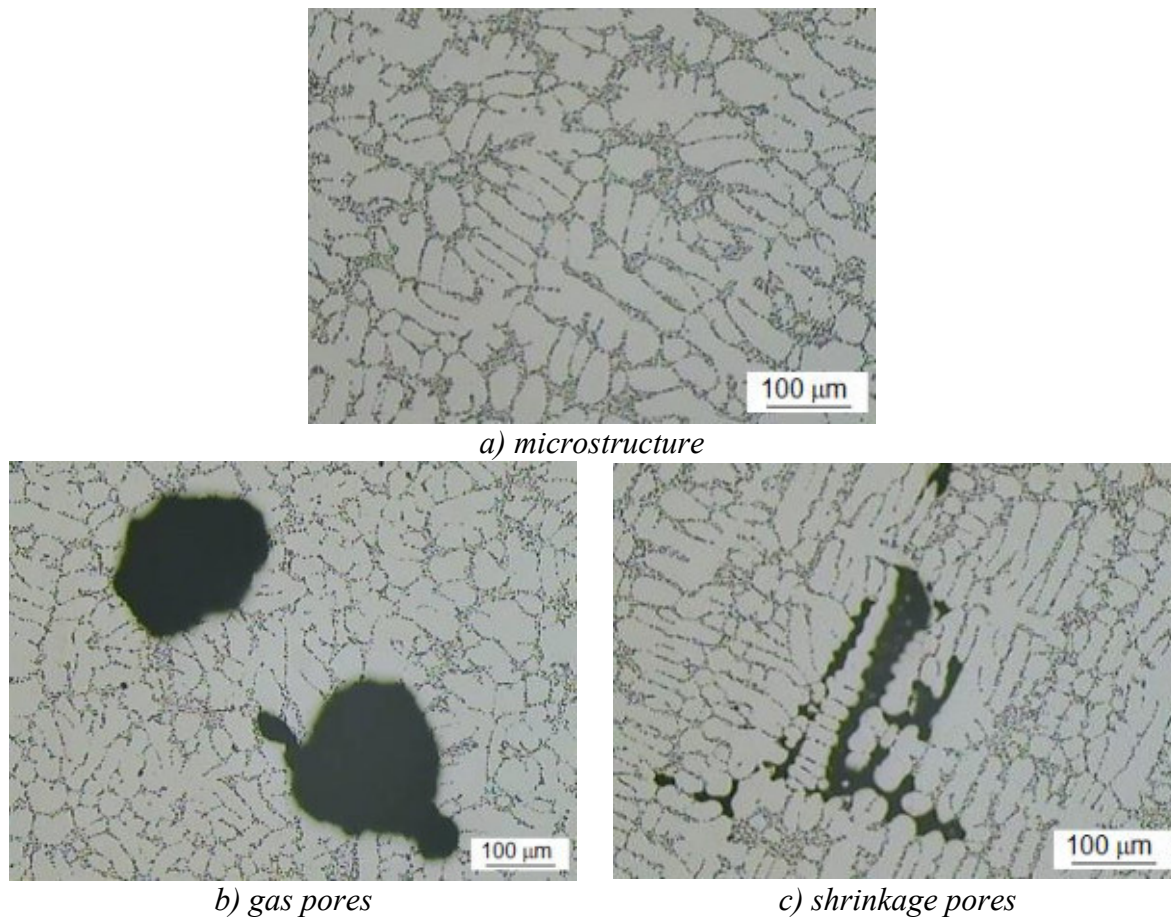


*Fig. 21 Microstructure and casting defects character in AlSi7Mg – T6, LM, etched with 0.5% HF solution, LM, [40].*

The role of the casting defects in terms of the stress concentration was discussed in [39, 42], Fig. 22. The results show that the average stress concentration factor of the realistic pore was higher than that for an idealized spherical pore geometry and lower for the metallographic 2D pore cross-section. Authors studied the real shape of the present casting defects and their distribution within the bulk volume and used the numerical simulation for the analysis of the stress distribution in the vicinity of the defect surface as is documented in Fig. 22. Numerical simulations show substantially different stress fields around spherical and around shrinkage defects. It has been proposed that the application of the morphology-dependent defect size correction factor for the defect-based lifetime prediction should be used. However, it has been reported that simple application of the LEVD statistical approach using only data obtained from the metallographic cross-sections yields adequately precise results of the lifetime prediction. Even though the morphology-dependent pore size correction factor was not incorporated.

Sophisticated methods such as RTG or CT (computed tomography) which can provide information about the real shape and size of casting defects are nowadays available, however, their application is difficult and too expensive in real engineering practice. Moreover, the size

of the inspected specimens is very limited. Another limitation is in a quite small size of potentially dangerous defects, which can be detected only by an equipment with high resolution. On the other hand, it is quite easy to prepare the metallographic specimen, even though the cross-section of the micro-shrinkage pore observed on the metallographic specimen provide only limited information about the shape of the defect, Fig. 23. This fact has to be taken into account while performing the metallographic analysis and applying such data for statistical analysis of defects and the component fatigue life prediction.

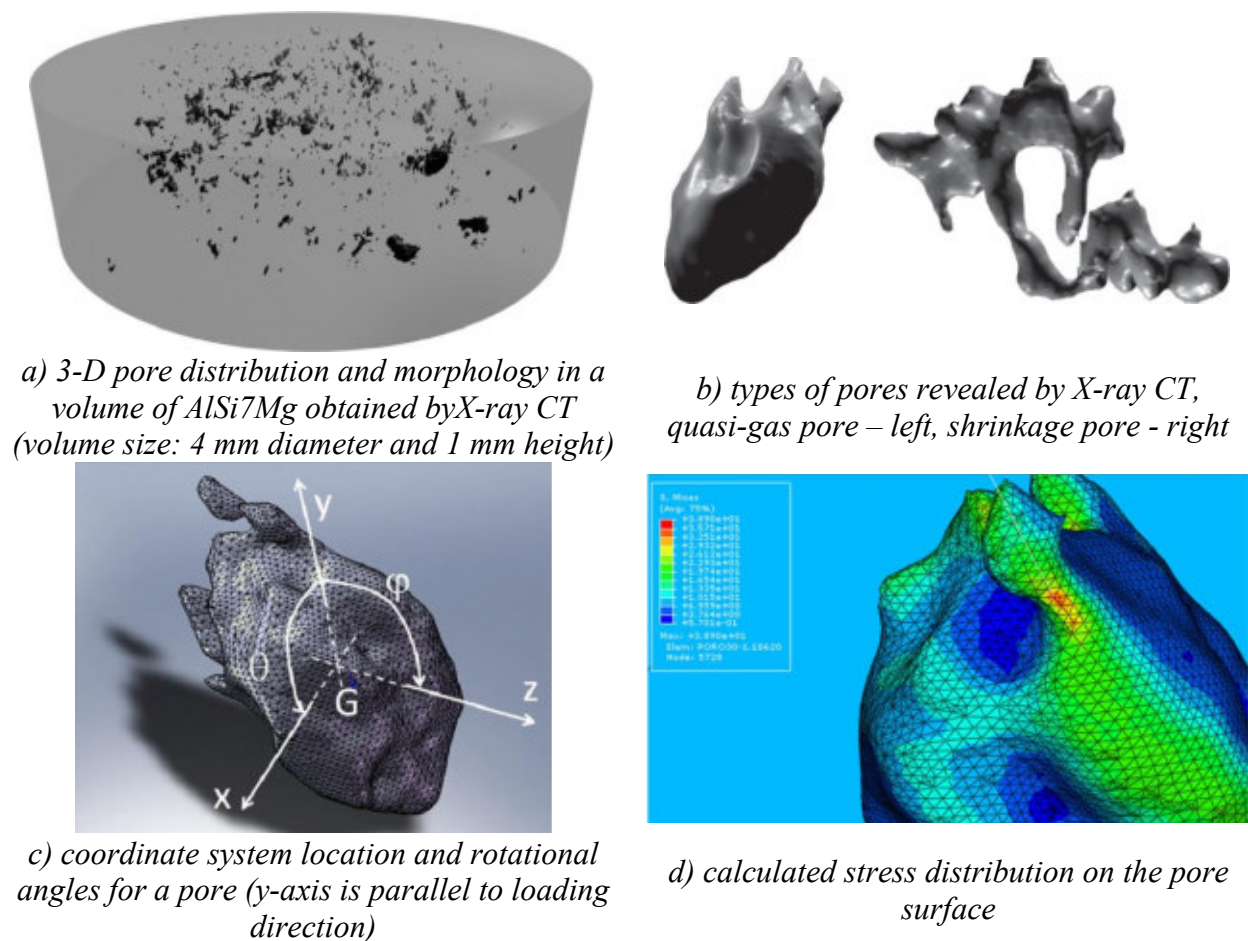
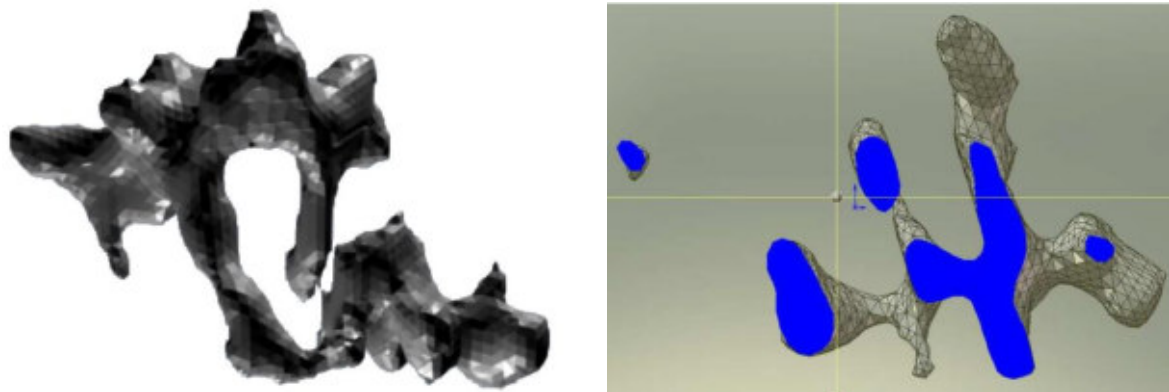


*Fig. 22 X-ray and finite element method analysis of the casting defects present in AlSi7Mg – T6, [39].*

Even when no morphology-dependent pore size correction factor for the statistical prediction of the largest defect size was used, a good correlation between the predicted largest defect size and the number of cycles to the fracture for the AlSi7Mg alloy was reported in [35-39]. The LEVD statistical method was applied for different batches of the cast material with various modifiers, which resulted in the different porosity of the castings. Fatigue properties of the examined batches were correlated with the LEVD predictions. The amount and localization of casting defects within

material volume were shown to influence the fatigue crack initiation; however, the shape of the present defects did not have any significant influence on the fatigue lifetime [35, 37, 40].



a) 3D reconstruction of a shrinkage pore using X-ray computed tomography

b) random section through a shrinkage pore and resulting 2D porosity

Fig. 23 Casting defect character in 3D and 2D, [35].

Discussing the characteristic defect size, authors in [41] used the area<sup>1/2</sup> and maximum Feret diameter (Fig. 24a) as the characteristic parameters of the defect for the LEVD analysis performed on three batches (set A, set B, set C, see Table 1) of the AlSi7Mg cast alloy with slightly different microstructure and porosity due to the modifier used. After the metallographic analysis of the experimental material, statistical evaluation of the obtained data according to the LEVD theory was performed. Using the data available in the literature the analyzed specimens lifetime was predicted adopting the AFGROW, [41], structural life prediction program, Fig. 24b and Table 1.

Table 1

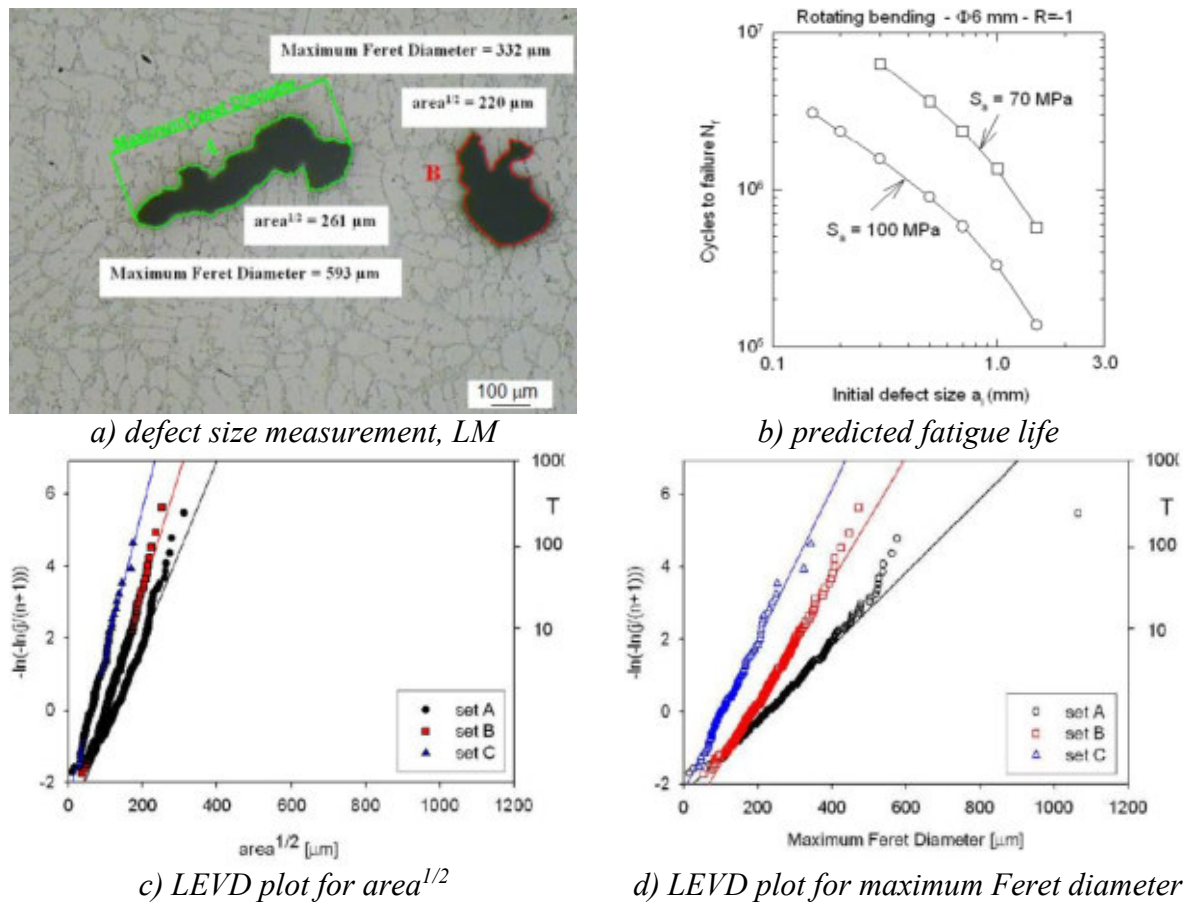
Prediction of the largest defect size and number of cycles to the fracture, [41].

batch	SDAS	D <sub>a</sub> [μm]	N <sub>f</sub> [cycles]	D <sub>F</sub> [μm]	N <sub>f</sub> [cycles]
A	32	186	2.3×10 <sup>6</sup>	377	1.1×10 <sup>6</sup>
B	30	148	3×10 <sup>6</sup>	279	1.6×10 <sup>6</sup>
C	40	99	4×10 <sup>6</sup>	180	2.3×10 <sup>6</sup>

D<sub>a</sub> - prediction of the largest defect size for S = 10 mm<sup>2</sup>; T = S/S<sub>0</sub>; area<sup>1/2</sup>

N<sub>f</sub> - predicted number of cycles to the fracture;

D<sub>F</sub> - prediction of the largest defect size for S = 10 mm<sup>2</sup>; T = S/S<sub>0</sub>; Max Feret diameter



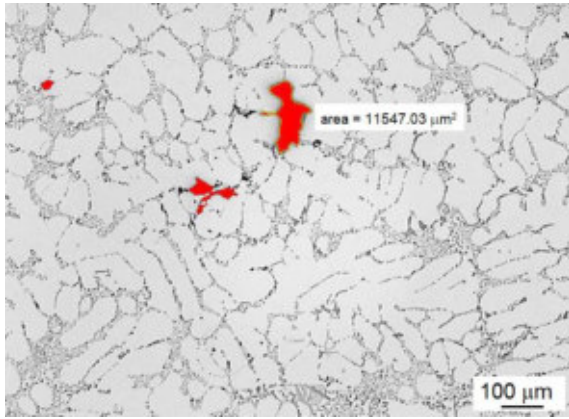
a) defect size measurement, LM  
 b) predicted fatigue life  
 c) LEVD plot for  $area^{1/2}$   
 d) LEVD plot for maximum Feret diameter  
 Fig. 24 Prediction of the largest defect size and comparison of the predictions with the fatigue life, [41].

The predicted lifetime was found to be in correlation to the predicted largest defect sizes for the examined material, however, the predicted fatigue lifetimes, based on the maximum Feret diameter were larger than those predicted based on the  $area^{1/2}$  parameter.

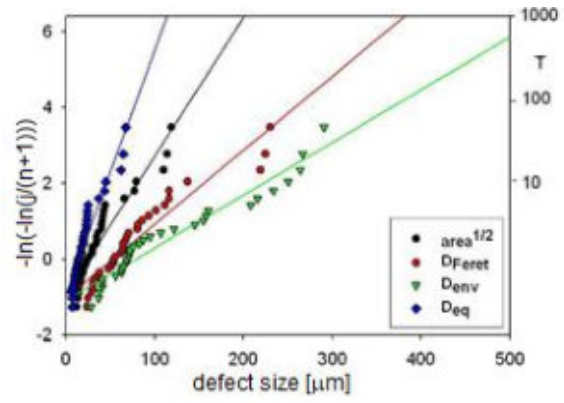
Besides the  $area^{1/2}$  and maximum Feret diameter parameters, also the equivalent diameter,  $D_{eq}$ , and multiple pores envelop size,  $D_{env}$ , for the pore size characterization were used by authors in [35]. The results of the rotating bending fatigue tests performed on the AlSi7Mg-T6 alloy showed a good correlation of lifetime with the predicted largest defect sizes. The 2D inspection of the metallographic specimens used for the LEVD statistical analysis revealed quite good agreement for all parameters used for the defect size approximation, Fig. 25, [35].

Detailed analysis of the influence of the casting defects on the fatigue life of the AlSi7Mg cast alloy performed in [35-42] using the LEVD theory for the defects characterization and the fatigue life prediction showed that the method proposed by Murakami is suitable for the fatigue life prediction.

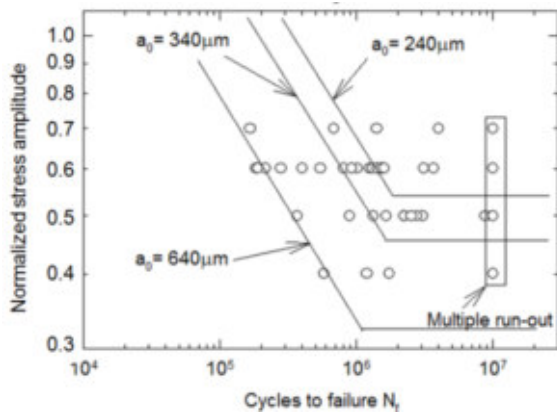




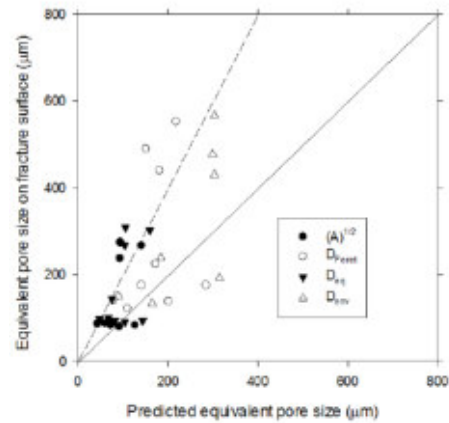
a) typical microstructure and casting defects, LM



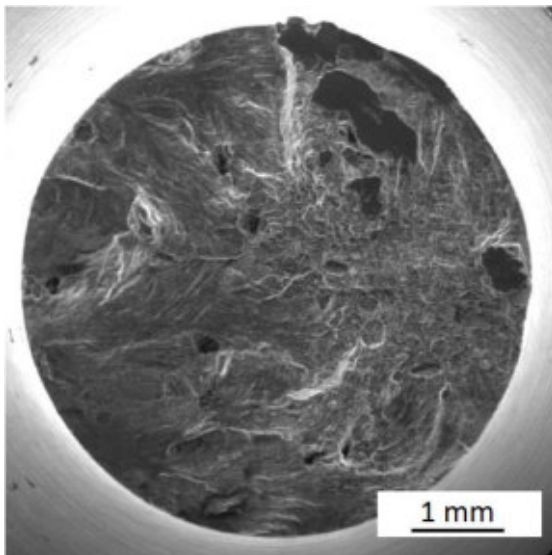
b) LEVD plot



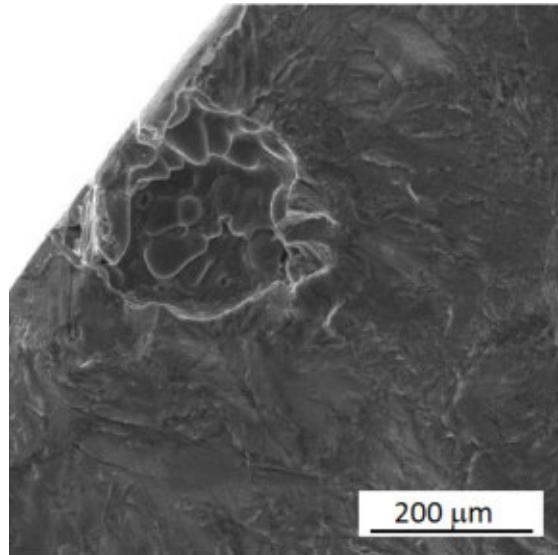
c) rotating bending fatigue test results



d) predicted vs. observed equivalent pore sizes.



e) fracture surface of a broken specimen, multiple crack initiation, SEM



f) casting defect in a fatigue crack initiation site, SEM

Fig. 25 Casting defect analysis and correlation with the fatigue life for AlSi7Mg alloy, [35].

Even though the morphology of the present casting defects is not included in the model, the predicted largest defect size correlated with the defects observed on the fracture surface of broken specimens during the rotating bending fatigue test corresponds well.

On the other hand, including the morphology of the defects via a characteristic defect size parameter (Feret diameter,  $D_{eq}$ ,  $D_{env}$ , ...) or the defects localization in clusters, and precise extrapolation of the data (presuming linearity of the data) will provide a more accurate prediction of the material fatigue life.

## **4.2 IN 713LC nickel alloy**

Nickel-based superalloys which are predetermined for the high-temperature applications represent another group of commercial materials often used in a cast state.

The low carbon IN 713LC nickel alloy is due to its good casting properties, excellent high-temperature mechanical properties and relatively low price, one of the most applied nickel-based superalloys. No additional heat treatment is required for the alloy after casting. The castings are characteristic with a large grain size and sometimes with a texture which is dependent on the casting process. Since the casting defects act as the fatigue crack initiation sites their elimination is required. Hot isostatic pressing (HIP) is one of the methods applicable for casting defects reduction.

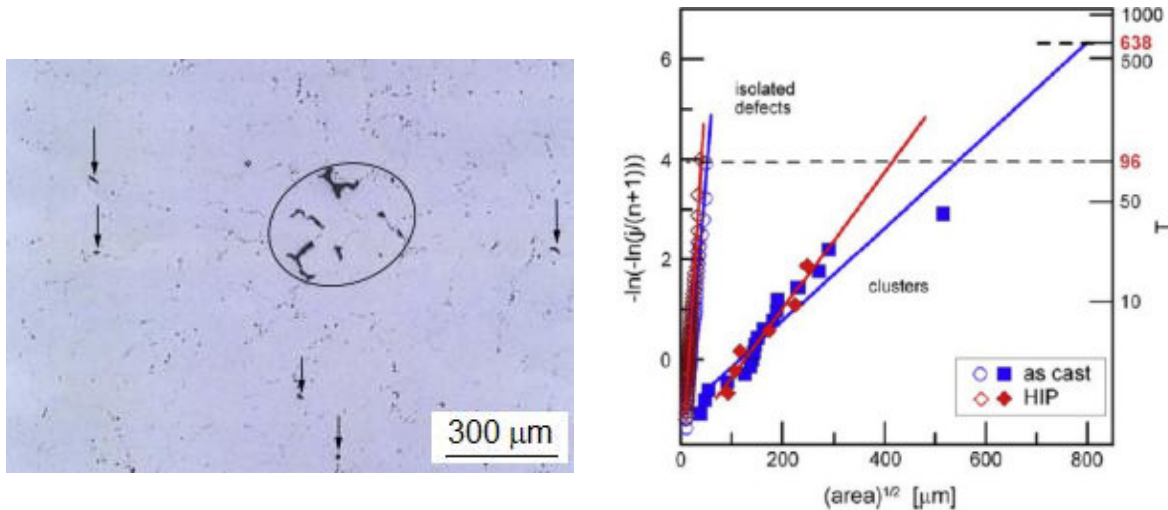
Due to the pressing at elevated temperatures closure of the casting defects and an improvement of the fatigue properties of the nickel alloys castings can be achieved.

Influence of casting defects on the fatigue properties of the IN 713LC alloy in a cast and HIP processed state was analyzed in [43]. The microstructure of the material consists of  $\gamma$  matrix strengthened by coherently embedded  $\gamma'$  precipitates and carbides.

The testing temperature of 800°C, and the mean stress of 0 and 300 MPa were applied during the cycling. The testing frequency was approximately 115 Hz at  $R = -1$ . The LEVD theory was applied for the statistical analysis of the casting defects present in the microstructure and for the prediction of the fatigue life of the cast and HIPed material. The analysis was performed on 25 areas of the metallographic specimens cut in the direction perpendicular and longitudinal to the loading direction extracted from the gauge length of the fatigue specimens. The inspected area was  $S_0 = 1.83 \text{ mm}^2$ , while the  $\text{area}^{1/2}$  was used as the characteristic defect size. Due to the character of material porosity, the defects were characterized individually as well as in clusters, Fig. 26.

Fatigue test results corresponded to the predictions based on both the microstructural and the LEVD statistical analysis of defects. The HIPed material contained smaller defects in terms of size as well as of amount. The smaller porosity of HIPed material resulted in the fatigue endurance

limit increase from 167 MPa for the cast alloy to 216 MPa under the mean stress of 0 MPa at 800 °C for cast material. When the mean stress of 300 MPa at 800 °C was applied, the fatigue endurance limits of 84 MPa and 151 MPa were determined for the cast and the HIPed material, respectively.



a) individual defects and cluster in cast specimen, LM

b) LEVD plots – largest defect size prediction

Fig. 26 Casting defects and LEVD plot for IN 713LC superalloy, [43].

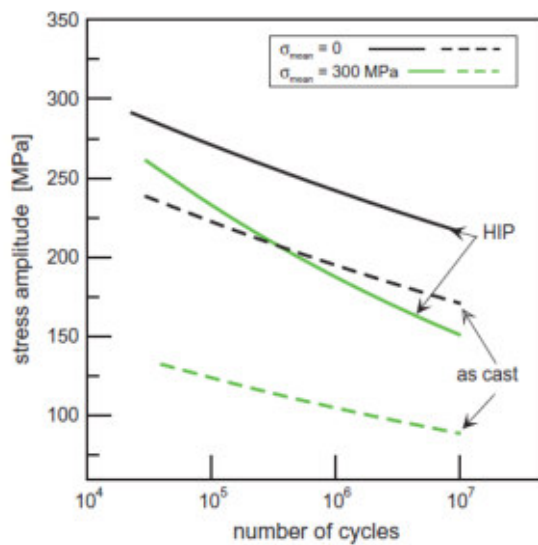
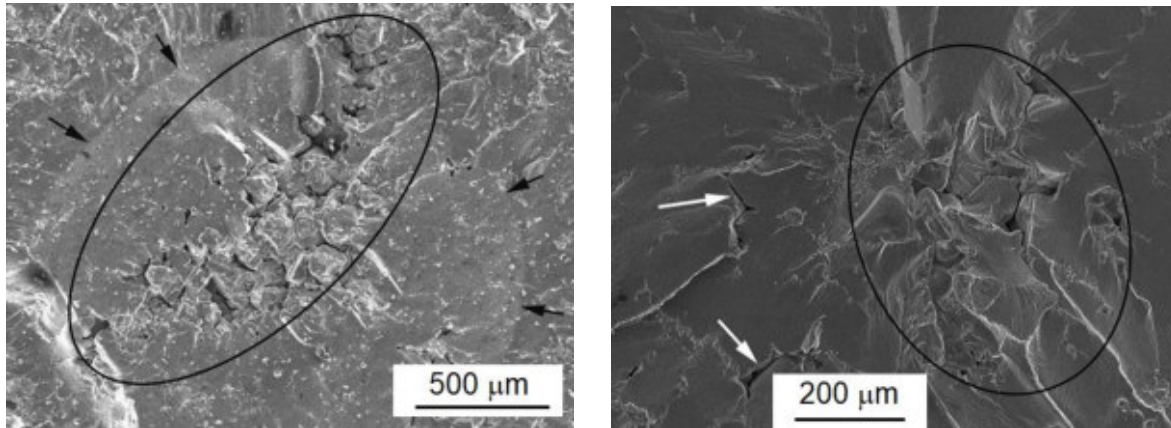


Fig. 27 Fatigue test results for IN 713LC superalloy, [43].

Based on the metallographic analysis of the material porosity, the size of the largest defect in the specimen gauge length volume was predicted. Fractographic analysis of the fracture surface of failed specimens revealed clusters of defects, Fig. 28, responsible for the specimen fatigue fracture.





*a) cluster of defects on the fatigue fracture surface of cast specimen*

*b) cluster of defects on the fatigue fracture surface of the HIPed specimen*

*Fig. 28 Casting defects on the IN 713LC specimens fatigue fracture surface, SEM, [43].*

The comparison of the LEVD predicted largest defect sizes (clusters sizes) and dimensions of defects (clusters of defects) observed on the fracture surfaces were found to be in reasonable agreement [43]. In other words, a prediction of the fatigue life of materials containing casting defects can be performed using the LEVD theory. Not only the size of the largest defect but also the size of clusters of casting defects have to be considered during the statistical analysis. A cluster of small defects can be more dangerous from the fatigue crack initiation point of view due to the larger stress concentration during cycling when compared to the individual defect with a larger size than the size of the defects in the cluster.

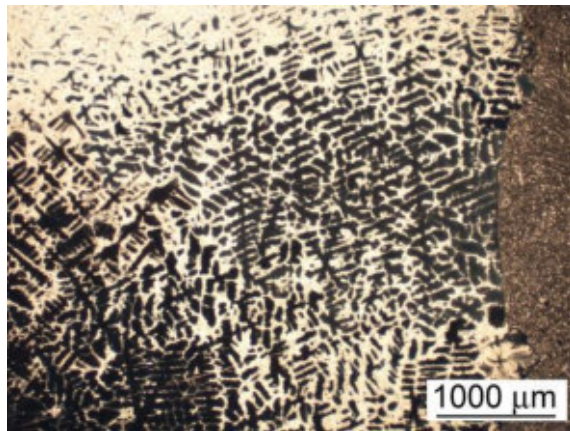
### **4.3 MAR-M-247 nickel alloy**

Another type of often used nickel-based superalloy is the advanced MAR-M-247. Typical  $\gamma$  matrix –  $\gamma'$  precipitates microstructure containing also carbide particles predetermines the alloy for applications at elevated temperatures, Fig. 29a-b. Thanks to the content of Hf the MAR-M-247 superalloy is resistant to higher temperatures when compared to the IN 713LC superalloy. However, to keep the good mechanical properties at elevated temperatures, the casting defects have to be again eliminated. The HIP process is generally used to seal/eliminate the present casting defects, however, some porosity still remains in the microstructure, Fig. 29c-d.

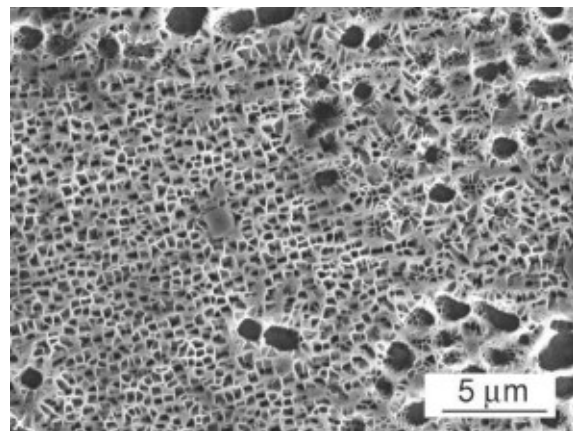
The influence of the casting defects on fatigue life using the LEVD theory was studied in [44,45]. The fatigue tests at two testing temperatures, namely 650 °C and 800 °C were performed.

The LEVD theory for the largest extreme defect size prediction and the prediction of the fatigue life of the MAR-M-247 superalloy was applied. Resulting plots from the LEVD analysis provided

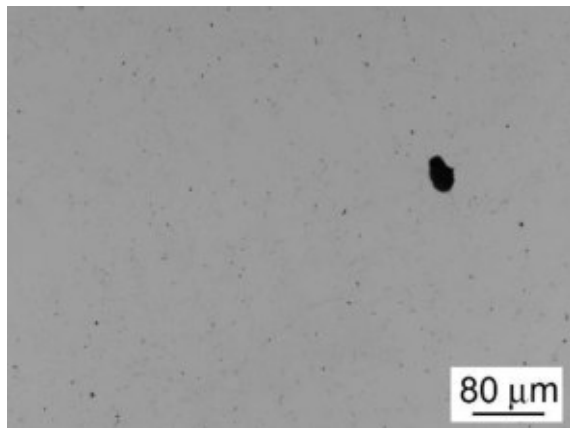
in Fig. 30 were used for prediction of the fatigue life of individual specimens via prediction of the largest defect size for the area equal to the specimen cross-section.



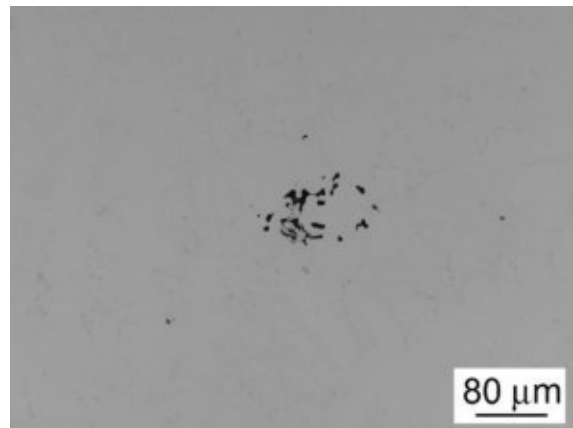
a) typical microstructure, LM, etched with 40 ml  $\text{HNO}_3$  + 30 ml HF, LM - dark field



b) size and shape of the strengthening  $\gamma'$  precipitates, SEM, etched with 40 ml  $\text{HNO}_3$  + 30 ml HF



c) rounded defects



d) shrinkage defects

Fig. 29 Typical microstructure and casting defects in MAR-M-247 superalloy, LM, [45].

Due to the observed size of casting defects, a modified approach of the data extrapolation was applied. The model proposed by Murakami assumes linear dependence on the size of the defect, which was not the case, as can be seen in Fig. 30. In some specimens, two different groups of defects were observed from the size point of view. Since two different slopes of the obtained data were observed, two lines for the more precise data extrapolation and the largest extreme defect size prediction were used. Predicted largest defect size using the approach of data extrapolation by bi-linear approach exhibited better correlation with the size of real defects observed on the fracture surfaces when compared to the linear extrapolation. The predicted and observed real defect size on the fracture surface is given in Table 2.

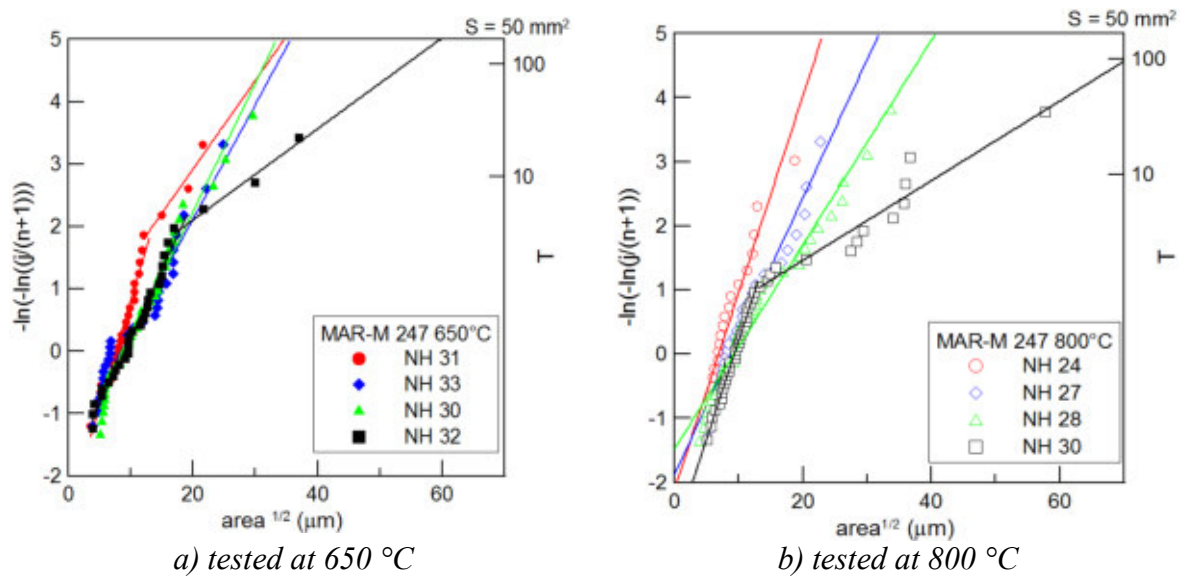


Fig. 30 LEVD plots for analyzed specimens of the MAR-M-247 superalloy, [45].

Table 2  
Values of the average defects size, the predicted largest defect size and real defect size observed on the fatigue fracture surface, [45].

specimen	650 °C				800 °C				
	average defect size [ $\mu\text{m}^2$ ]	predicted largest defect size [ $\mu\text{m}^2$ ]	real defect size on the fracture surface [ $\mu\text{m}^2$ ]	$N_f$ [cycles] at $\sigma_a = 240$ MPa	average defect size [ $\mu\text{m}^2$ ]	predicted largest defect size [ $\mu\text{m}^2$ ]	real defect size on the fracture surface [ $\mu\text{m}^2$ ]	$N_f$ [cycles] at $\sigma_a = 240$ MPa	
NH 31	107	1 100	1 200	1 301 000	NH 24	84	550	560	8 309 000
NH 33	162	1 142	740	1 132 000	NH 27	149	1 044	3 940	1 991 000
NH 30	169	1 145	490	987 000	NH 28	211	1 700	1 160	1 078 000
NH 32	199	3 884	40	783 000	NH 34	342	5 608	4 870	465 000

Even though the predictions were not always in absolutely perfect correlation with the obtained data, the explanation lies in the rough cast structure characteristic for nickel-based superalloys produced by conventional methods and preferable crystallographic fatigue crack orientation via slip.

Similarly to the investigation performed on the IN 713LC alloy it has been found that the LEVD theory used for the prediction of the largest defect size corresponds well with the size of the real defects observed on the fracture surfaces of fatigued specimens. The fatigue life at the same stress amplitude corresponded to the predicted size of the largest defect. The size of defects responsible for the fatigue crack initiation correlates well to the predicted size of the largest defects [44,45].

## 5 CONCLUSIONS

The thesis brings a summary of the results and findings presented in author's papers and contributions at international conferences and a brief discussion of the results in light of the current trends in research of mechanisms of material fatigue. The set of works is designed to show the contribution to the current state of knowledge in the field of fatigue of nonferrous metals and alloys. Two phenomena of the material structure were analyzed while describing the relation of structure and the fatigue response, namely the grain size and casting defects.

Considering the influence of the grain size on the fatigue crack initiation studied on AZ91 magnesium alloy the following conclusions can be drawn:

- Formation of the SMs due to the cyclic loading was observed in the AZ91 cast alloy. The surface relief in the form of extrusions and intrusions in the solid solution grain areas of microstructure acts as the crack initiation site. The size and the amount of the SMs were decreasing with decreasing stress amplitude. This observation corresponds to the general knowledge on the fatigue crack initiation which was based mainly on the metal with fcc structure.
- In the case of the bimodal UFG structure produced via ECAP, only limited amount of tiny SMs created in the larger grains was observed. The SMs act as the crack initiation sites. The decrease of the stress amplitude resulted in the reduction of the SMs formation. Simultaneously, boundary cracking at small grains becomes a decisive mechanism which causes the final fatigue failure.
- The limited slip in the hcp structure in combination with the ultra-fine grain microstructure resulted in a progressive decrease of SMs formation with decreasing stress amplitude. The grain boundary cracking mechanism becomes prevailing in this case.

Adopting the SP treatment on AW 6082-T561 and AW 7075-T6511 aluminum alloys, the fine-grained microstructure was generated in a thin surface layer.

- Even though the SP treatment is connected with surface roughness increase, internal compressive stresses induced due to the SP treatment and grain refinement resulted in higher fatigue life when compared to the non-treated material. This effect overbalances the fact that small internal defects and cracks in the SP surface layer were generated.

- Fatigue crack initiation on the SP surface and its shift into the SP layer/basic material interface was a characteristic feature observed on the fatigue fracture surfaces of both treated alloys.

The grain size was identified as a factor having a significant influence on the crack growth parameters. The analysis of the grain size effect on the fatigue crack growth rate and its mechanisms was conducted using pure copper (fcc) and CP Ti grade 4 (hcp) materials.

- Higher crack growth rates and lower values of the threshold stress intensity factor were determined for the UFG copper and CP Ti grade 4 when compared to the CG material states. This finding is in agreement with data published in the literature. However, taking into account only the effective value of the stress intensity factor, similar behavior for CG and UFG state of the materials was observed.
- In the case of pure copper, a large number of SMs in the crack vicinity as well as in front of the crack tip for both material states was observed, while the SMs creation was less pronounced in the air when compared to the testing in the vacuum.
- Grain coarsening in the crack vicinity, indicating dynamic grain recrystallization in the area of the cyclic plastic deformation localization was a characteristic feature for the UFG copper. In contrast to the size and amount of the SMs observed on the tested specimen surfaces, the larger grain coarsening area was observed in the case of the crack grown in the air when compared to the vacuum.
- In the case of CP Ti grade 4, no signs of the localization of the plastic deformation on the surface of CG and UFG materials in terms of SMs formation were observed. Similarly, no grain coarsening takes place in the UFG CP Ti grade 4 alloy.

The influence of the casting defects on the fatigue crack initiation in AlSi7Mg aluminum alloy was investigated. Further, the application of the statistical method for the prediction of the fatigue lifetime of two Ni-based superalloys brought the following results.

- In agreement with the literature, the casting defects were shown to be responsible for the fatigue crack initiation under the cyclic loading regardless the studied material and loading conditions.
- Not the shape of the casting defects, as it was assumed, but their size was shown to play the major role in the case of the fatigue crack initiation.

- 
- Specification of the size of the defect using different characteristic parameters for their description was demonstrated. The goal was to make the statistical analysis and defect size prediction more precise. It was found that there is no need to use the morphology-dependent pore size correction factor for the statistical analysis of the metallographic cross-sections used for the LEVD analysis. The results obtained using the defect size only were found to be in good agreement with the results of fatigue tests accompanied by the fractographic analysis.
  - It was observed that due to the character of porosity of individual castings the size of clusters of defects has to be taken into account (simple extrapolation of single defects results in an overestimation of the lifetime). The defects cluster size used for the LEVD statistical analysis of the Ni-based superalloys was shown to be more precisely correlating with the experimentally determined fatigue life of materials and results from the fractographic analysis when compared to the conventional approach taking into account only the size of the largest defects.

Published papers brought a contribution to the knowledge on the localization of the cyclic plasticity during the fatigue loading, particularly, on the formation of SMs and their role in the fatigue crack initiation in the case of homogeneous UFG materials. The presented results show that the theory used for the conventionally grained materials is not directly applicable to the fine-grained nonferrous materials.

In materials with casting defects, their size is a major factor influencing the fatigue crack initiation. The morphology-dependent pore size correction factor can be used for the statistical analysis of the defects and prediction of the material's fatigue life, however, even without application of the correction factor the data obtained using the LEVD theory were shown to be in good agreement with the experimentally acquired data.

## 6 REFERENCES

- [1] M. Klesnil, P. Lukáš, *Fatigue of Metallic Materials*, Academia, 1992.
- [2] P. Lukáš, L. Kunz, Role of persistent slip bands in fatigue, *Philosophical Magazine*, 84 (2004) 317-330.
- [3] J.G. Antonopoulos, L.M. Brown, A.T. Winter, Vacancy dipoles in fatigued copper, *Philosophical Magazine*, 34 (1976) 549-563.
- [4] G.A.D. Briggs, T. Zhai, J.W. Martin, Fatigue damage in aluminium single crystals. I. On the surface containing the slip Burgers vector, *International Journal of Fatigue*, 18 (1996) 606.
- [5] J. Polák, *Cyclic plasticity and low cycle fatigue life of metals*, Elsevier, 1991.
- [6] U. Essmann, U. Gösele, H. Mughrabi, A model of extrusions and intrusions in fatigued metals I. Point-defect production and the growth of extrusions, *Philosophical Magazine A*, 44 (1981) 405-426.
- [7] T.H. Lin, S.R. Lin, Micromechanical theory of fatigue crack initiation applied to time-dependent fatigue, in: F.J. T. (Ed.) *Fatigue Mechanisms*, ASTM International, 1979, pp. 707.
- [8] J. Polák, J. Man, Initiation of Stage I Fatigue Cracks – Experiments and Models, *Procedia Engineering*, 101 (2015) 386-394.
- [9] J. Polák, J. Man, Fatigue crack initiation – The role of point defects, *International Journal of Fatigue*, 65 (2014) 18-27.
- [10] J. Polák, J. Man, Mechanisms of extrusion and intrusion formation in fatigued crystalline materials, *Materials Science and Engineering: A*, 596 (2014) 15-24.
- [11] J. Man, M. Valtr, M. Petrevec, J. Dluhoš, I. Kuběna, K. Obrtlík, J. Polák, AFM and SEM-FEG study on fundamental mechanisms leading to fatigue crack initiation, *International Journal of Fatigue*, 76 (2015) 11-18.
- [12] H. Mughrabi, *Damage Mechanisms and Fatigue Lives: From the Low to the Very High Cycle Regime*, *Procedia Engineering*, 55 (2013) 636-644.
- [13] R.W. Armstrong, The influence of polycrystal grain size on several mechanical properties of materials, *Metallurgical and Materials Transactions B*, 1 (1970) 1169-1176.
- [14] Y. Estrin, A. Vinogradov, Fatigue behaviour of light alloys with ultrafine grain structure produced by severe plastic deformation: An overview, *International Journal of Fatigue*, 32 (2010) 898-907.
- [15] A.Y. Vinogradov, V.V. Stolyarov, S. Hashimoto, R.Z. Valiev, Cyclic behavior of ultrafine-grain titanium produced by severe plastic deformation, *Materials Science and Engineering: A*, 318 (2001) 163-173.

- [16] V.V. Stolyarov, L. Zeipper, B. Mingler, M. Zehetbauer, Influence of post-deformation on CP-Ti processed by equal channel angular pressing, *Materials Science and Engineering: A*, 476 (2008) 98-105.
- [17] P. Cavaliere, Fatigue properties and crack behavior of ultra-fine and nanocrystalline pure metals, *International Journal of Fatigue*, 31 (2009) 1476-1489.
- [18] C.W. Chung, R.G. Ding, Y.L. Chiu, M.A. Hodgson, W. Gao, Microstructure and Mechanical Properties of an As-Cast AZ91 Mg Alloy Processed by Equal Channel Angular Pressing, in, 2009.
- [19] B. Chen, D.-L. Lin, L. Jin, X.-Q. Zeng, C. Lu, Equal-channel angular pressing of magnesium alloy AZ91 and its effects on microstructure and mechanical properties, *Materials Science and Engineering: A*, 483–484 (2008) 113-116.
- [20] C.-S. Chung, D.-K. Chun, H. Kim, Fatigue properties of fine grained magnesium alloys after severe plastic deformation, *Journal of Mechanical Science and Technology*, 19 (2005) 1441-1448.
- [21] C.W. Chung, R.G. Ding, Y.L. Chiu, W. Gao, Effect of ECAP on microstructure and mechanical properties of cast AZ91 magnesium alloy, in, 2010.
- [22] I.P. Semenova, G.K. Salimgareeva, V.V. Latysh, T. Lowe, R.Z. Valiev, Enhanced fatigue strength of commercially pure Ti processed by severe plastic deformation, *Materials Science and Engineering: A*, 503 (2009) 92-95.
- [23] H.-K. Kim, Y.-I. Lee, C.-S. Chung, Fatigue properties of a fine-grained magnesium alloy produced by equal channel angular pressing, *Scripta Materialia*, 52 (2005) 473-477.
- [24] Y. Murakami, *Metal Fatigue: Effects of Small Defects and Nonmetallic Inclusions*, Elsevier Science, 2002.
- [25] S. Fintová, L. Kunz, Fatigue properties of magnesium alloy AZ91 processed by severe plastic deformation, *Journal of the Mechanical Behavior of Biomedical Materials*, 42 (2015) 219-228.
- [26] S. Fintová, L. Kunz, Cyclic plastic behavior and fatigue life of AZ91 alloy in as-cast and ultrafine-grained state, *Materials Engineering - Materiálové inžinierstvo*, 21 (2014) 109-115.
- [27] S.F.a.L. Kunz, Initiation of fatigue cracks in AZ91 Mg alloy processed by ECAP, *IOP Conference Series: Materials Science and Engineering*, 63 (2014) 012159.
- [28] S. Fintova, L. Pantelejev, L. Kunz, Microstructure and Mechanical Properties of Ultrafine-Grained Magnesium AZ91 Alloy, *Metallography Xv*, 782 (2014) 384-389.
- [29] L. Kunz, S. Fintova, Fatigue behaviour of AZ91 magnesium alloy in as-cast and severe plastic deformed conditions, 11th International Fatigue Congress, Pts 1 and 2, 891-892 (2014) 397-402.
- [30] S. Fintová, L. Kunz, Initiation of fatigue cracks in AZ91 Mg alloy processed by ECAP, *IOP Conference Series: Materials Science and Engineering*, 63 (2014) 012159.



- [31] B. Hadzima, F. Nový, L. Trško, F. Pastorek, M. Jambor, S. Fintová, Shot peening as a pre-treatment to anodic oxidation coating process of AW 6082 aluminum for fatigue life improvement, *The International Journal of Advanced Manufacturing Technology*, 93 (2017) 3315-3323.
- [32] L. Trško, S. Fintová, F. Nový, O. Bokůvka, M. Jambor, F. Pastorek, Z. Florková, M. Oravcová, Study of Relation between Shot Peening Parameters and Fatigue Fracture Surface Character of an AW 7075 Aluminium Alloy, *Metals*, 8 (2018) 111.
- [33] M. Arzaghi, S. Fintová, C. Sarrazin-Baudoux, L. Kunz, J. Petit, Near threshold fatigue crack growth in ultrafinegrained copper, *IOP Conference Series: Materials Science and Engineering*, 63 (2014) 012158.
- [34] S. Fintová, M. Arzaghi, I. Kuběna, L. Kunz, C. Sarrazin-Baudoux, Fatigue crack propagation in UFG Ti grade 4 processed by severe plastic deformation, *International Journal of Fatigue*, 98 (2017) 187-194.
- [35] R. Konecna, S. Fintova, G. Nicoletto, Shrinkage pores and fatigue behavior of cast Al-Si alloys, *Materials Structure & Micromechanics of Fracture*, 465 (2011) 354-357.
- [36] R. Konecna, G. Nicoletto, S. Fintova, Statistical description of largest pore sizes in cast Al-Si alloys, *25th Danubia-Adria Symposium on Advances in Experimental Mechanics*, (2008) 123-124.
- [37] S. Fintova, R. Konecna, G. Nicoletto, Influence of shrinkage porosity on the behavior of cast AlSi7Mg, *Metal 2010: 19th International Metallurgical and Materials Conference*, (2010) 690-695.
- [38] S. Fintova, R. Konecna, G. Nicoletto, Largest defect sizes distribution application in the Al-Si alloys, *Metal 2009, Conference Proceedings*, (2009) 428-434.
- [39] G. Nicoletto, R. Konecna, S. Fintova, Characterization of microshrinkage casting defects of Al-Si alloys by X-ray computed tomography and metallography, *International Journal of Fatigue*, 41 (2012) 39-46.
- [40] S. Fintová, R. Konečná, G. Nicoletto, Microstructure, defects and fatigue behavior of cast AlSi7Mg alloy, in, 2013, pp. 223-231.
- [41] F. Stanislava, K. Radomila, ná, N. Gianni, Statistical description of largest pore size in modifies Al-Si alloys, *Materiálové Inžinierstvo*, 16 (2009) 24-28.
- [42] S. Fintová, G. Anzelotti, R. Konečná, G. Nicoletto, Casting Pore Characterization by X-Ray Computed Tomography and Metallography, in: *Archive of Mechanical Engineering*, 2010, pp. 263.
- [43] L. Kunz, P. Lukáš, R. Konečná, S. Fintová, Casting defects and high temperature fatigue life of IN 713LC superalloy, *International Journal of Fatigue*, 41 (2012) 47-51.
- [44] M. Šmíd, S. Fintová, L. Kunz, P. Hutař, Role of defects in fatigue damage mechanisms of cast polycrystalline superalloy MAR-M 247, *MATEC Web of Conferences*, 12 (2014) 03005.

[45] M. Šmíd, S. Fintová, L. Kunz, P. Hutař, K. Hrbáček, Prediction of maximum casting defect size in MAR-M 247 alloy processed by hot isostatic pressing, *Materials Engineering - Materiálové inžinierstvo*, 22 (2015).

## **7 AUTHOR'S OWN REFERED WORKS**

- I. [25] S. Fintová, L. Kunz, Fatigue properties of magnesium alloy AZ91 processed by severe plastic deformation, *Journal of the Mechanical Behavior of Biomedical Materials*, 42 (2015) 219-228.
- II. [26] S. Fintová, L. Kunz, Cyclic plastic behavior and fatigue life of AZ91 alloy in as-cast and ultrafine-grained state, *Materials Engineering - Materiálové inžinierstvo*, 21 (2014) 109-115.
- III. [27] S. Fintová, L. Kunz, Initiation of fatigue cracks in AZ91 Mg alloy processed by ECAP, *IOP Conference Series: Materials Science and Engineering*, 63 (2014) 012159.
- IV. [28] S. Fintova, L. Pantelejev, L. Kunz, Microstructure and Mechanical Properties of Ultrafine-Grained Magnesium AZ91 Alloy, *Metallography Xv*, 782 (2014) 384-389.
- V. [29] L. Kunz, S. Fintova, Fatigue behaviour of AZ91 magnesium alloy in as-cast and severe plastic deformed conditions, 11th International Fatigue Congress, Pts 1 and 2, 891-892 (2014) 397-402.
- VI. [30] S. Fintová, L. Kunz, Initiation of fatigue cracks in AZ91 Mg alloy processed by ECAP, *IOP Conference Series: Materials Science and Engineering*, 63 (2014) 012159.
- VII. [31] B. Hadzima, F. Nový, L. Trško, F. Pastorek, M. Jambor, S. Fintová, Shot peening as a pre-treatment to anodic oxidation coating process of AW 6082 aluminum for fatigue life improvement, *The International Journal of Advanced Manufacturing Technology*, 93 (2017) 3315-3323.
- VIII. [32] L. Trško, S. Fintová, F. Nový, O. Bokůvka, M. Jambor, F. Pastorek, Z. Florková, M. Oravcová, Study of Relation between Shot Peening Parameters and Fatigue Fracture Surface Character of an AW 7075 Aluminium Alloy, *Metals*, 8 (2018) 111.
- IX. [33] M. Arzaghi, S. Fintová, C. Sarrazin-Baudoux, L. Kunz, J. Petit, Near threshold fatigue crack growth in ultrafinegrained copper, *IOP Conference Series: Materials Science and Engineering*, 63 (2014) 012158.
- X. [34] S. Fintová, M. Arzaghi, I. Kuběna, L. Kunz, C. Sarrazin-Baudoux, Fatigue crack propagation in UFG Ti grade 4 processed by severe plastic deformation, *International Journal of Fatigue*, 98 (2017) 187-194.
- XI. [35] R. Konecna, S. Fintova, G. Nicoletto, P. Sandera, Shrinkage pores and fatigue behavior of cast Al-Si alloys, *Materials Structure & Micromechanics of Fracture*, 465 (2011) 354-357.

- 
- XII. [36] R. Konecna, G. Nicoletto, S. Fintova, Statistical description of largest pore sizes in cast Al-Si alloys, 25th Danubia-Adria Symposium on Advances in Experimental Mechanics, (2008) 123-124.
- XIII. [37] S. Fintova, R. Konecna, G. Nicoletto, Influence of shrinkage porosity on the fatigue behaviour of cast AlSi7Mg, Metal 2010: 19th International Metallurgical and Materials Conference, (2010) 690-695.
- XIV. [38] S. Fintova, R. Konecna, G. Nicoletto, Largest defect sizes distribution application to the Al-Si alloys, Metal 2009, Conference Proceedings, (2009) 428-434.
- XV. [39] G. Nicoletto, R. Konecna, S. Fintova, Characterization of microshrinkage casting defects of Al-Si alloys by X-ray computed tomography and metallography, International Journal of Fatigue, 41 (2012) 39-46.
- XVI. [40] S. Fintová, R. Konečná, G. Nicoletto, Microstructure, defects and fatigue behavior of cast AlSi7Mg alloy, in, 2013, pp. 223-231.
- XVII. [41] F. Stanislava, K. Radomila, ná, N. Gianni, Statistical description of largest pore size in midified Al-Si alloys, Materiálové Inžinierstvo, 16 (2009) 24-28.
- XVIII. [42] S. Fintová, G. Anzelotti, R. Konečná, G. Nicoletto, Casting Pore Characterization by X-Ray Computed Tomography and Metallography, in: Archive of Mechanical Engineering, 2010, pp. 263.
- XIX. [43] L. Kunz, P. Lukáš, R. Konečná, S. Fintová, Casting defects and high temperature fatigue life of IN 713LC superalloy, International Journal of Fatigue, 41 (2012) 47-51.
- XX. [44] M. Šmíd, S. Fintová, L. Kunz, P. Hutař, Role of defects in fatigue damage mechanisms of cast polycrystalline superalloy MAR-M 247, MATEC Web of Conferences, 12 (2014) 03005.
- XXI. [45] M. Šmíd, S. Fintová, L. Kunz, P. Hutař, K. Hrbáček, Prediction of maximum casting defect size in MAR-M 247 alloy processed by hot isostatic pressing, Materials Engineering - Materiálové inžinierstvo, 22 (2015).

- I. [25] S. Fintová, L. Kunz, Fatigue properties of magnesium alloy AZ91 processed by severe plastic deformation, *Journal of the Mechanical Behavior of Biomedical Materials*, 42 (2015) 219-228.

Available online at [www.sciencedirect.com](http://www.sciencedirect.com)

ScienceDirect

[www.elsevier.com/locate/jmbbm](http://www.elsevier.com/locate/jmbbm)

## Research Paper

# Fatigue properties of magnesium alloy AZ91 processed by severe plastic deformation

Stanislava Fintová<sup>a,b,\*</sup>, Ludvík Kunz<sup>b</sup><sup>a</sup>Brno University of Technology, CEITEC BUT—Central European Institute of Technology, Technická 3058/10, 616 00 Brno, Czech Republic<sup>b</sup>Institute of Physics of Materials AS CR, Žitkova 22, 616 62 Brno, Czech Republic

## ARTICLE INFO

## Article history:

Received 24 September 2014

Received in revised form

21 November 2014

Accepted 23 November 2014

Available online 29 November 2014

## Keywords:

AZ91 magnesium alloy

ECAP

Fatigue

Crack initiation

## ABSTRACT

Fatigue properties of cast AZ91 magnesium alloy processed by severe plastic deformation were investigated and compared with the properties of the initial cast state. The severe plastic deformation was carried out by equal channel angular pressing (ECAP). The ECAP treatment resulted in a bimodal structure. The bimodality consists in a coexistence of fine grained areas with higher content of Mg<sub>17</sub>Al<sub>12</sub> particles and areas exhibiting larger grains and lower density of Mg<sub>17</sub>Al<sub>12</sub> particles.

Improvement of the basic mechanical properties of AZ91 (yield stress, tensile strength and ductility) by ECAP was significant. Also the improvement of the fatigue life in the low-cycle fatigue region was substantial. However the improvement of the fatigue strength in the high-cycle fatigue region was found to be negligible. The endurance limit based on 10<sup>7</sup> cycles for the cast alloy was 80 MPa and for the alloy processed by ECAP 85 MPa. The cyclic plastic response in both states was qualitatively similar; initial softening was followed by a long cyclic hardening.

Fatigue cracks in cast alloy initiate in cyclic slip bands which were formed in areas of solid solution. In the case of severe plastic deformed material with bimodal structure two substantially different mechanisms of crack initiation were observed. Crack initiation in slip bands was a preferred process in the areas with large grains whereas the grain boundaries cracking was a characteristic mechanism in the fine grained regions.

© 2014 Elsevier Ltd. All rights reserved.

## 1. Introduction

Magnesium alloys are traditionally used materials for applications in many engineering fields mainly in automotive, aerospace and electronic (Gupta and Sharon, 2011). Recently,

their importance markedly increased also in medical applications. The large spectrum of their utilization is based on their low weight but still good mechanical properties, which can be influenced in broad range by changes of chemical composition (Gupta and Sharon, 2011; Altwicker et al., 1939; Němcová

\*Corresponding author at: Brno University of Technology, CEITEC BUT—Central European Institute of Technology, Technická 3058/10, 616 00 Brno, Czech Republic. Tel.: +420 532 290 301; fax: +420 541 218 657.

E-mail address: [fintova@ipm.cz](mailto:fintova@ipm.cz) (S. Fintová).



et al., 2009; Eisenmeier et al., 2001; Chung et al., 2010; Ebel-Wolf et al., 2008; Yamashita et al., 2001; Chen et al., 2014). Moreover, they exhibit biodegradable properties. They are still innovative materials, particularly due to their application as temporary implants into human body (Choudhary and Singh, 2012; Chen et al., 2014; Witte et al., 2006). Magnesium is not only biocompatible, but also essential to human metabolism as a co-factor of many enzymes (Choudhary and Singh, 2012; Wolf and Cittadini, 2003; Saris et al., 2000), and its degradation products are not toxic. For utilization as temporary implants both the corrosion resistance and the mechanical properties are important factors. The corrosion resistance can be controlled by alloying and surface treatment (Gupta and Sharon, 2011) and the mechanical properties are closely related to the grain size. Chemical composition has to be chosen very carefully because some of the elements improving corrosion resistance and mechanical properties can be toxic. From this point of view the mechanical processing seems to be a very promising way how to make magnesium alloys viable biomaterials (Wang et al., 2007; Hadzima et al., 2008).

One of the most often used magnesium alloys from the AZ group is AZ91, which exhibits perfect castability and good mechanical properties combined with good corrosion resistance (for high purity version of the alloy) and low production costs (Altwicker et al., 1939; Němcová et al., 2009; Eisenmeier et al., 2001; Chung et al., 2010; Ebel-Wolf et al., 2008).

Even though the mechanical and corrosion properties of AZ91 alloy are due to its chemical composition in the best ratio from the AZ group of Mg alloys, new ways for their improvement are still a discussed issue, permanently activated by engineering practice and industrial demands.

Within the last some years AZ magnesium alloys, primarily intended for castings, have been investigated with the aim to answer the question if severe plastic deformation (SPD) can influence its tensile strength ( $\sigma_{UTS}$ ), yield stress ( $\sigma_{0.2}$ ) and improve ductility due to the grain refinement. One of the most popular SPD techniques is ECAP. AZ91 contains relatively high volume of alloying elements; high volume of Al results in larger amount of  $Mg_{17}Al_{12}$  intermetallic particles, which can be exploited in material hardening due to the ECAP treatment (Chung et al., 2010). It has been shown that resulting influence of ECAP strongly depends on the details of the process (temperature, type and number of passes and pressing rate) and also on the structure of the initial material.

In the case of magnesium alloys the ECAP treatment has to be done at elevated temperatures to activate more slip systems in the hcp structure. Otherwise cracks appear in the processed material. It was proved that ECAP treatment performed at elevated temperatures can improve tensile properties of magnesium alloys, corrosion properties and also fatigue strength (Chung et al., 2009; Chen et al., 2008; Vrátná et al., 2013).

ECAP process can raise the yield stress,  $\sigma_{0.2}$ , and the ultimate tensile strength,  $\sigma_{UTS}$ , (almost 100% improvement), and, particularly, improve the ductility (A) (almost 500% improvement) due to the substantial grain refinement (Chung et al., 2010; Yamashita et al., 2001; Chen et al., 2008). On the other hand lowering of  $\sigma_{UTS}$  and fatigue strength were reported for wrought Mg alloys processed by ECAP (Brazzcyńska-Malik, 2011; Chung et al., 2005; Kim et al., 2005).

It has been also proved that suitable solution heat treatment of the initial cast alloy before ECAP promotes formation of more homogenous and finer structure. When a proper heat treatment is applied before ECAP, only 2 passes through ECAP die are sufficient to refine the structure and significantly improve the yield stress and tensile strength. Following passes through ECAP die homogenize the structure whereas the influence on mechanical properties of treated material is weak (Chung et al., 2010; Yamashita et al., 2001; Chen et al., 2008).

The structure of ultrafine-grained materials prepared by any method utilizing SPD techniques is inherently unstable at increasing temperature due to high stored energy. Grain coarsening throughout the whole volume of the material or a specific bimodal structure creation takes place during thermal exposure (Štěpánek et al., 2013; Molodova et al., 2007; Korn et al., 2011; Höppel et al., 2010). In the case of AZ91 alloy the structure obtained by ECAP is stable below 300 °C while increased temperatures (350 °C and 400 °C) result in gradual grain coarsening (Štěpánek et al., 2013).

Fatigue behavior of the cast AZ91 magnesium alloy was studied by many investigators, e.g. (Altwicker et al., 1939; Eisenmeier et al., 2001; Wolf et al., 2004; Gu et al., 2010; Murugan et al., 2009). The S–N curves exhibit a sharp knee. The slope of the S–N curve in the region of high number of cycles to failure is extremely low and the fatigue limit is in the range from 60 to 85 MPa, according to the details of chemical composition and casting process.

Fatigue crack initiation in the cast alloy was observed both at the casting defects or pores. Some investigations (Wolf et al., 2004; Gu et al., 2010; Murugan et al., 2009) show that casting defects are preferable sites for crack initiation. On the other hand, in the case of absence of defects of critical size, it has been reported e.g. (Eisenmeier et al., 2001; Wolf et al., 2004; Gu et al., 2010; Murugan et al., 2009) that the crack initiation takes place due to localization of cyclic plastic deformation in slip bands which are formed in areas of solid solution. Fatigue cracks initiate at the surface micro-relief at in-/extrusions and on interfaces between brittle  $Mg_{17}Al_{12}$  intermetallic particles and ductile solid solution matrix. Also an  $Mg_{17}Al_{12}$  intermetallic particle cracking was observed. The initiation mechanism is often reported as quasicleavage. Contrary to the cast AZ91 the knowledge on the mechanism of fatigue crack initiation in the alloy processed by SPD is entirely missing. The same holds for the cyclic plastic response to the fatigue loading. The cyclic deformation of the cast material (Wolf et al., 2004) exhibits a weak cyclic softening at the beginning (for some tens to hundreds of loading cycles), which is followed by cyclic hardening. In the case of higher applied stress amplitudes the maximum on the cyclic softening/hardening curves disappears and the cyclic hardening is characteristic response for the whole fatigue life.

The present study is focused on fatigue behavior, fatigue crack initiation mechanism and early crack growth in relation to structure of AZ91 magnesium alloy processed by ECAP. The motivation was a response to the missing data in the open literature and the extension of knowledge on the mechanisms of fatigue crack initiation in SPD processed hcp structures.

**Table 1 – Chemical composition of tested AZ91 in wt%.**

Elements	Al	Zn	Mn	Si	Fe	Be	Ni	Cu	Mg
wt%	87	0.65	0.25	0.006	0.003	0.0008	0.0006	0.0005	Rest

## 2. Experimental material and procedures

### 2.1. Experimental material

AZ91 magnesium alloy in cast state and after ECAP was investigated. Chemical composition given by producer is shown in Table 1.

The cast alloy was processed by ECAP under the following conditions. The temperature was 300 °C to prevent material cracking due to the plastic deformation. The pressing route Bc was repeated 6 times. The angle of the die channels was 120°. The semi-products for specimen machining were cylindrical rods of 15 mm in diameter and 80 mm length.

### 2.2. Structural analysis

Examination of structure and observation of the surface relief produced by fatigue on the specimen gauge length was performed in scanning electron microscope (SEM) Tescan LYRA 3 XMU FEG/SEM x FIB. Focused ion beam (FIB) technique was applied to perform cuts through the places of interest and to investigate the characteristic features of the structure and its relation to the surface relief, fatigue slip markings and cracks.

### 2.3. Tensile testing

Tensile tests were conducted on cylindrical specimens with gauge length of 30 mm. The diameter of the gauge length was 6 mm. The tests were performed on testing machine ZWICK Z020 with a crossbeam rate of 1 mm/min. The basic tensile properties were determined on three specimens from the cast material and on three specimens from the material after ECAP. Tensile tests were conducted at room temperature in laboratory air.

### 2.4. Fatigue test specimens preparation

Cylindrical specimens with 4 mm diameter and 15 mm gauge length and thread heads were machined for fatigue tests. With the aim to observe the development of the surface relief, fatigue crack initiation and their relation to the structure the gauge length of the specimens was polished and etched before fatigue testing. The polishing consisted of mechanical grinding (SiC papers no. 800, 1200 and 2500) and mechanical polishing (1 µm diamond paste). Finally, the gauge length was spread with 2% Nital etchant to make the AZ91 structure visible.

### 2.5. Fatigue testing

Fatigue tests were performed under load control in symmetrical tension–compression (load ratio  $R = -1$ ). Shimadzu EHF-F1 servohydraulic system was used for the testing up to  $1 \times 10^6$  cycles. The loading frequency was in the range from 0.1 to 10 Hz (Fintová and Kunz, 2014a, 2014b). The cyclic plastic response was monitored by a clip gauge extensometer and by recording of hysteresis loops for selected number of cycles. Amsler HFP 5100 resonant fatigue machine was used for the continuation of testing in high-cycle fatigue region, i.e. above  $1 \times 10^6$  cycles. In this case the loading frequency was of about 60 Hz. The hysteresis loops were not measured at this high frequency. Fatigue tests were conducted at room temperature in laboratory air.

## 3. Results

### 3.1. Structural analysis

A comparison of structure of cast alloy and alloy processed by ECAP is shown in Fig. 1. The cast structure, Fig. 1a, consists of solid solution of alloying elements in magnesium, eutectic and discontinuous precipitates and  $Mg_{17}Al_{12}$  and AlMn based intermetallic particles. The average grain size is  $185 \pm 70$  µm. The structure of AZ91 processed by ECAP, Fig. 1b, consists of grains of solid solution of alloying elements in magnesium,  $Mg_{17}Al_{12}$  intermetallic particles and AlMn based intermetallic particles. From the macroscopic point of view the structure can be characterized as bimodal. There are areas with larger grains there and areas with smaller grains containing large amount of intermetallic particles. The average grain size of grains characterized as large was  $9.9 \pm 4.5$  µm and the density of small  $Mg_{17}Al_{12}$  particles is here markedly lower when compared to the small grained areas. The average grain size of the small grains was of  $3.3 \pm 0.5$  µm and in these areas large amount of fine  $Mg_{17}Al_{12}$  can be observed. Besides small intermetallic particles also large primary  $Mg_{17}Al_{12}$  intermetallic particles are present in small grained areas.

### 3.2. Tensile properties

Fig. 2 compares the stress–strain curves of three cast and three specimens from material processed by ECAP. Substantial improvement of tensile properties due to ECAP is obvious. The tensile strength of the cast material is  $\sigma_{UTS} = 167 \pm 8$  MPa, the yield stress  $\sigma_{0.2} = 87 \pm 8$  MPa and ductility  $3.1 \pm 0.4\%$ . The values for alloy after ECAP are  $\sigma_{UTS} = 321 \pm 21$  MPa, the  $\sigma_{0.2} = 160 \pm 4$  MPa and the ductility is  $15.4 \pm 4.7\%$ .

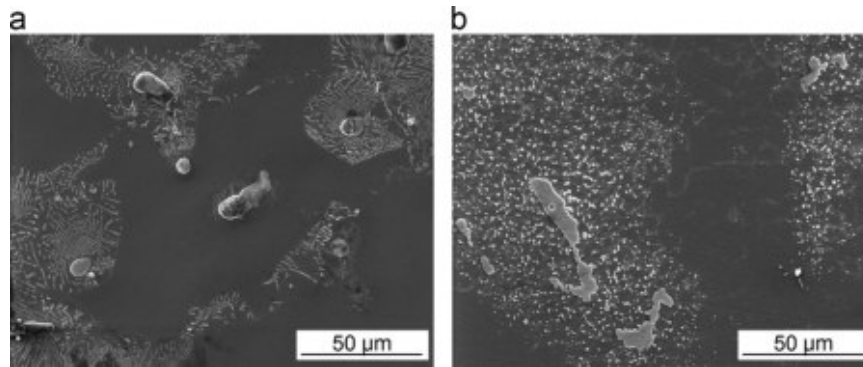


Fig. 1 – Characteristic structure of AZ91 magnesium alloy, etched by 2% Nital, SEM. (a) Structure of cast state, (b) structure after ECAP.

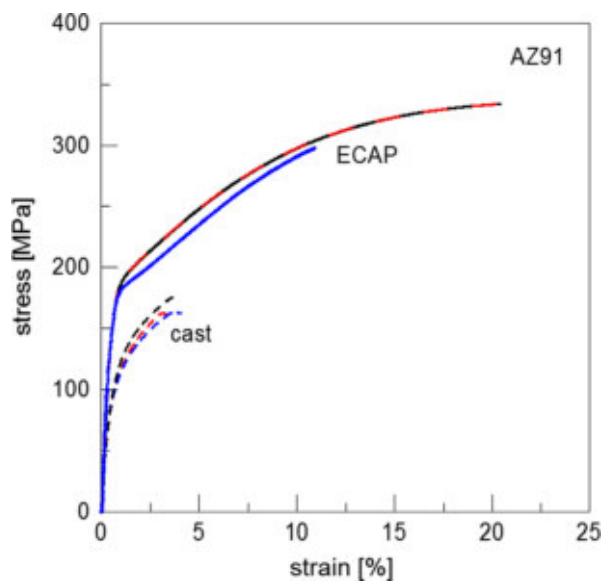


Fig. 2 – Stress–strain curves for material in cast state and after ECAP (Fintová and Kunz, 2014a, 2014b).

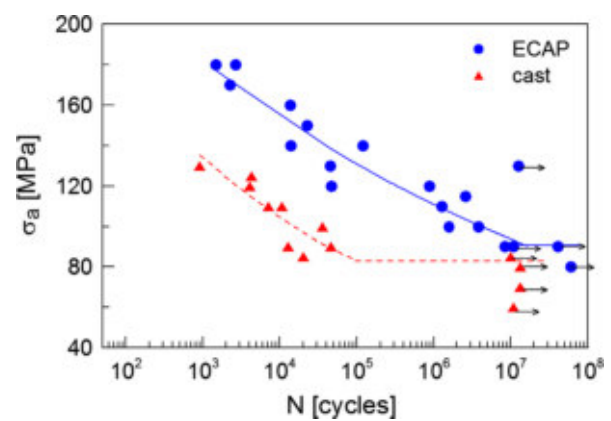


Fig. 3 – AZ91 S–N curves of cast AZ91 and AZ91 processed by ECAP.

### 3.3. Fatigue strength

S–N curves presented in Fig. 3 prove an increase of the fatigue life by factor of two orders of magnitude due to ECAP treatment.

The S–N curve of the cast alloy exhibits a typical sharp knee. Stress amplitude,  $\sigma_a$ , of 80 MPa can be considered as the endurance limit (based on  $10^7$  cycles). All the cast specimens tested at the stress amplitude higher than 80 MPa were broken before they reached  $10^5$  cycles. All the cast specimens tested at the stress amplitude below 80 MPa exceeded  $N=10^7$  cycles and were considered as run-outs. The points corresponding to the run-out specimens are denoted by arrows in Fig. 3. The decreasing part of the S–N curve for cast AZ91 alloy in the interval from  $10^3$  to  $10^5$  cycles can be well fitted by the power law dependence

$$\sigma_a = 282 N_f^{-0.11}, \quad (1)$$

where  $N_f$  is a number of cycles to failure. Eq. (1) is based only on the data corresponding to the broken specimens.

The S–N curve of the alloy processed by ECAP decreases continuously with increasing number of cycles in the broad interval from  $10^3$  to  $10^7$  cycles and can be well approximated by the equation.

$$\sigma_a = 300 N_f^{-0.07}. \quad (2)$$

The curve does not exhibit any knee in the investigated interval of the applied stress amplitudes and number of cycles.

In contrast to the significant improvement of fatigue strength in low and middle range of number of cycles, the endurance limit of both materials is similar. The experimental results clearly indicate that the ECAP of cast AZ91 does not bring a benefit as regards the high cycle fatigue strength. The endurance limit based on  $10^7$  cycles for the cast alloy is 80 MPa and for the alloy processed by ECAP is 85 MPa.

### 3.4. Cyclic plastic response

AZ91 cast magnesium alloy exhibit a short stage of cyclic softening at the beginning of cycling, Fig. 4a. Initial cyclic softening lasts typically some hundreds of cycles. The softening is followed by a pronounced cyclic hardening. Cyclic hardening is characteristic for almost all the fatigue life of tested specimens. By decreasing the stress amplitude,  $\varepsilon_{ap}$ , the

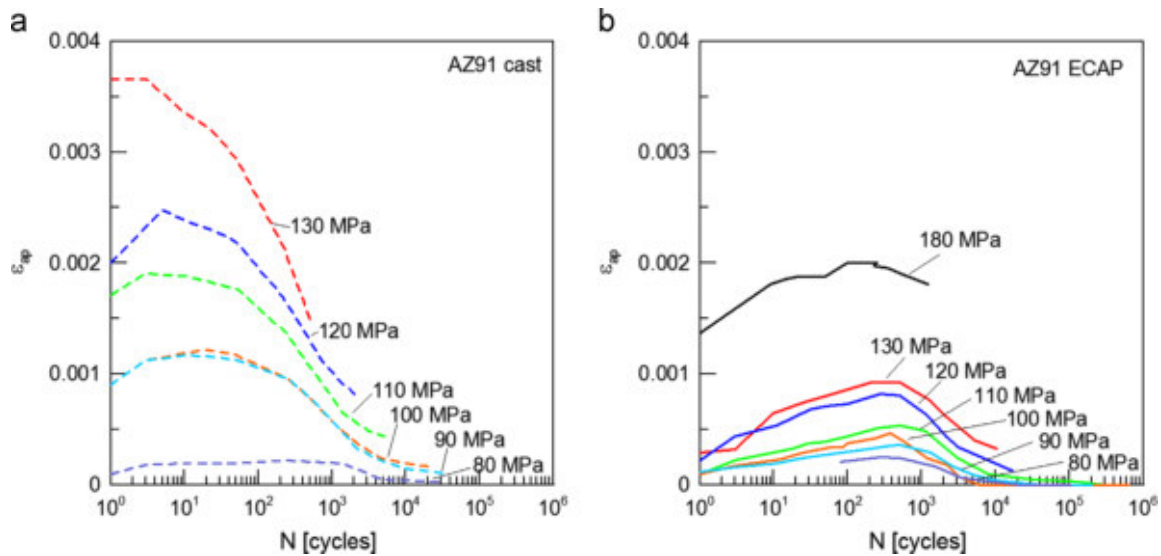


Fig. 4 – Cyclic deformation curves of AZ91 alloy of cast alloy and alloy processed by ECAP. (a) Cast material, (b) ECAPed specimens.

maximum on the softening/hardening curves is shifted to higher number of cycles,  $N$ , and became less expressive.

The cyclic deformation curves of material processed by ECAP are qualitatively similar to those of the cast alloy. However, the initial cyclic softening stage is substantially longer when compared to the cast material. Similarly to the cast material after the maximum on the curves is reached, a cyclic hardening appears, Fig. 4b. The transition between cyclic softening/hardening appears after elapsing of some hundreds of cycles. Observed cyclic hardening is not as strong as in the case of the cast material. The effect of hardening/softening also becomes less intense with decreasing amplitude.

### 3.5. Fatigue crack initiation

Cyclic plastic deformation takes place in the solid solution areas in both material states. The cyclic plasticity manifests itself by formation of slip bands on the surface. Fig. 5 shows a typical example of slip bands and fatigue crack initiation in cast alloy and alloy processed by ECAP. The slip bands are inclined mostly at the angle of nearly  $45^\circ$  to the loading direction, Fig. 5, which is marked by arrows in Fig. 5a and c.

Fatigue cracks initiate in slip bands which form prevalently in the solid solution in cast structure, Fig. 5a. Multiple crack initiation was characteristic for high stress amplitudes. In some cases the slip bands were formed also in areas of mixture of solid solution and  $Mg_{17}Al_{12}$  discontinuous precipitates Fig. 5b. With decreasing stress amplitude the length and the number of created slip bands decreases. In the cast alloy no slip bands were found on the run-out specimens.

The slip bands form also in the alloy processed by ECAP. Similarly to the cast state the solid solution is the preferential region for their development. Due to the bimodal structure and the distribution of  $Mg_{17}Al_{12}$  particles the larger grains are preferential sites for this process. Fatigue cracks initiate in the slip bands. Similarly to the fatigue crack initiation in the

cast material multiple crack initiation is characteristic at high stress amplitudes. The crack initiation is similar to that which takes place in the cast material, only the length of the slip bands and initiated cracks is substantially shorter due to the small grain size. In the small grained areas of the bimodal structure the formation of slip bands is very rare, Fig. 6a. On the other hand, the grain boundary cracking appears here, Fig. 6b. The occurrence of the slip bands and their frequency strongly depends on the stress amplitude. In the ECAP processed alloy no slip bands were observed below the stress amplitude of 120 MPa. At very high stress amplitudes cracking of large primary particles was observed, however, these cracks did not usually propagate into the surrounding matrix.

Surface relief evolution, during cycling, slip bands and crack initiation sites including the structure in the vicinity of early cracks were studied by means of FIB technique. Fig. 7a shows the slip bands and cracks initiated on the surface of a cast specimen. Beyond the cracks which form in slip bands, cracks appear also at the boundaries of  $Mg_{17}Al_{12}$  particles and matrix. Also broken particles can be often found at higher stress amplitudes. In both the latter cases, however, these cracks do not propagate into the matrix. The initiation in slip bands is decisive for final damage and development of long cracks resulting in final fatigue failure. The area which was investigated by FIB is in Fig. 7a marked by an arrow. The FIB cut was performed perpendicularly to the short (on SEM images not apparently cracked) slip bands and to the specimen surface. The surface relief and the structure underneath are shown in Fig. 7b. The protective Pt layer covering the surface appears as white band, above which the surface with slip bands (under high angle) can be seen. Fatigue damage below the surface related to the surface slip bands is clearly seen on the FIB section. The damage is located along the slip planes in which the bands form. The damage consists of elongated material discontinuities connected with the surface (see the band on the left hand side of the figure) or from elongated voids or cavities. Some of them are situated deep in



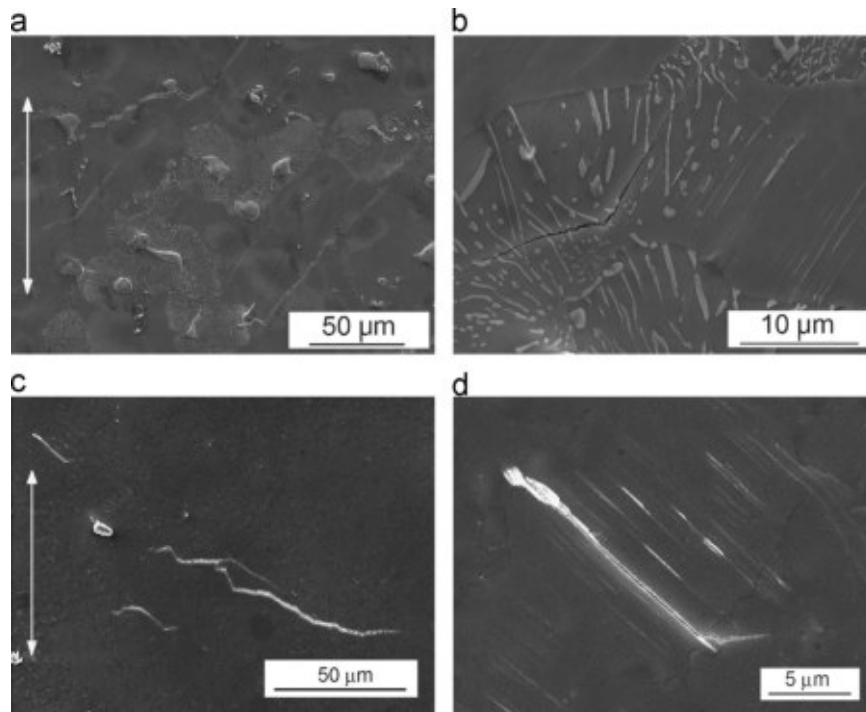


**Fig. 5 – Crack initiation in the structure of cast alloy and alloy processed by ECAP. (a) Slip bands and cracks in solid solution, cast specimen, 120 MPa, 4 088 cycles, (b) cracks in slip bands, cast specimen, 120 MPa, 4 088 cycles, (c) cracks and slip bands in large grains, ECAP processed alloy, 180 MPa, 1 473 cycles, (d) cracks initiated in slip bands, ECAP processed alloy, 180 MPa, 1 473 cycles.**

the material and are located along the slip planes. An example of such cavity is in Fig. 7b marked by the arrow.

Observation of surface relief morphology and subsurface damage in material processed by ECAP can be seen in Fig. 8. The slip bands with extrusions appear only in suitably oriented grains, whereas neighboring grains do not exhibit any apparent slip activity in terms of slip band formation. Grain boundary cracks are often observed. The detail of material damage and crack initiation as observed by FIB is shown in Fig. 8b. The well developed crack is running crystallographically along the slip plane into material interior. The crack is opened along the whole length displayed in the figure. The damage marked by the arrow in Fig. 8b is similarly located along the slip plane, however, is only very short. The subsurface damage is related to the extrusions on the surface. It seems that there is no relation of the height of the extrusions and the extent of the damage below them.

#### 4. Discussion

The improvement of the fatigue life of AZ91 alloy processed by ECAP is a consequence of bimodal structure created due to severe plastic deformation and different conditions for fatigue crack initiation. In the low- and medium-cycle fatigue region the lifetime is increased by two orders of magnitude. This is a natural effect of substantially higher strength and ductility of the processed alloy, which is related to the bimodal structure.

The structure of AZ91 magnesium alloy processed by ECAP depends on the initial structure of the cast alloy. The bimodality observed in this study is caused by missing heat pre-treatment of the cast semiproducts before ECAP. Usually applied heat treatment should make the cast structure homogenous and the following ECAP procedure refines the structure. Chen et al. (2008) found that the suitable heat treatment before ECAP resulted in creation of well developed homogeneous ultrafine structure after only two ECAP passes. The following passes brought only homogenization. Results of the present work document that when the adequate heat pre-treatment is missing the structure of AZ91 even after six ECAP passes by the route Bc remains heterogeneous.

ECAP treatment increases the mechanical properties, strength and also deformation properties, of AZ91 alloy (Chung et al., 2010, 2009; Yamashita et al., 2001; Chen et al., 2008; Valiev and Alexandrov, 2002). The improvement which can be reached depends strongly on the details of the process. The strengthening due to severe plastic deformation of AZ91 is caused by an increase of grain boundaries related to the decrease of the grain size and by the formation and distribution of small  $Mg_{17}Al_{12}$  particles (Chen et al., 2008). The effect of ECAP on the improvement of tensile properties and ductility of AZ91 was found to be more expressive than in the case of other AZ magnesium alloys (Chung et al., 2009; Hadzima et al., 2008; Chen et al., 2008). The reason is first of all substantially higher content of small  $Mg_{17}Al_{12}$  particles (Chung et al., 2010). The values of the yield stress and strength obtained by direct ECAP of cast AZ91 alloy are somewhat lower than the parameters which were reported for fully homogeneous structure observed after ECAP of the hot-rolled AZ91

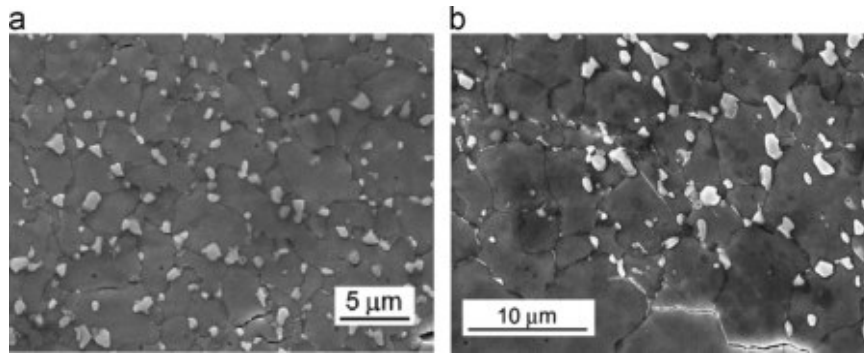


Fig. 6 – Slip bands and cracks in small grained area, ECAP processed alloy, 180 MPa, 1 473 cycles. (a) Cracks on grain boundaries in small grained area, (b) cracks on grain boundaries and slip bands in small grained area.

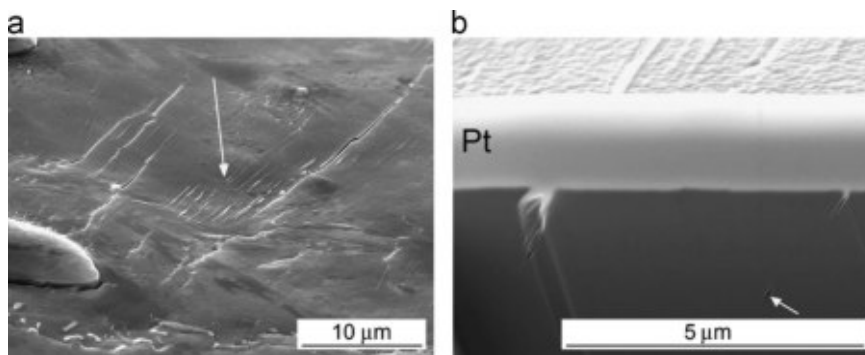


Fig. 7 – SEM image of a surface and FIB cut through slip bands and initiated cracks in cast specimen; 120 MPa, 4 088 cycles. (a) Surface of cycled cast specimen, (b) detail of slip bands and damage below the surface.

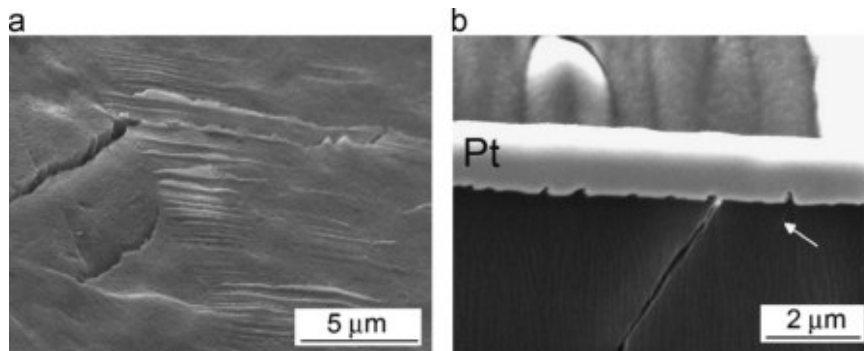


Fig. 8 – FIB cut through slip bands and initiated cracks in ECAPed specimen; 180 MPa, 1 473 cycles. (a) Slip bands, cracks on grain boundaries, (b) detail of surface relief and material below the slip bands.

alloy (Chen et al., 2008). This can be explained by the degree of strengthening by the grain boundaries and small  $Mg_{17}Al_{12}$  particles amount, which is higher in the small grained areas. The large grained areas of lower strength are responsible for higher plasticity of the bulk and thus for substantially higher ductility with relatively low decrease of tensile strength. Indeed, the  $\sigma_{UTS}=321\pm 21$  MPa of the bimodal structure is lower than  $\sigma_{UTS}=417$  MPa determined in Chen et al. (2008) for fully homogeneous structure, however the ductility is substantially better. The 100% increase of the yield stress and tensile strength and above all the fivefold increase of ductility of cast AZ91 processed

by ECAP determined in this work indicate that the bimodal structure provides a favorable combination of strength and ductility.

From the comparison of S–N curves of cast and by ECAP treated alloy it is obvious that the ECAP improves the fatigue life only in the low- and medium-cycle fatigue region. There is no benefit of ECAP as regards the high-cycle fatigue strength. The endurance limit based on  $10^7$  cycles is 85 MPa which is very close to endurance limit of cast material.

The S–N curve of cast AZ91 alloy exhibits a typical knee. All the specimens tested at stress amplitudes higher than 80 MPa

failed before they reached  $10^5$  cycles. Specimens tested at the stress amplitudes below 80 MPa exceeded  $10^7$  cycles without failure and were taken as run-outs (marked by arrows in Fig. 3). The stress amplitude 80 MPa was thus considered to be the endurance limit. This value is somewhat higher than values published in Wolf et al. (2004), Gu et al. (2010), Murugan et al. (2009). From the summary of results of Wolf et al. (2004), Gu et al. (2010), Murugan et al. (2009) it follows that the average value of the endurance limit of cast AZ91D alloy is of about 50 MPa. The explanation of this difference can be sought in differences in the examined alloy structure. While in the present study the cast structure does not contain any casting defects, in the mentioned studies the fatigue cracks very often initiated on the casting defects or pores. Endurance limit determined in this work fits well with the average value of the endurance limit of 80–90 MPa of cast AZ91 alloy determined on the basis of many sources and published in Altwicker et al. (1939).

Fine bimodal structure obtained after ECAP is obviously more resistant against the slip band formation and fatigue crack initiation than the cast structure. The cracks were observed to initiate preferentially in the large grained areas. The length of slip bands and their development is restricted by the grain size. High angle boundaries are generally unfavorable for induced initiation and growth of slip bands in neighboring grains. Thorough observation of the specimen gauge length by SEM led to the conclusion that the number of slip bands decreases rapidly with decreasing stress amplitude. No slip bands were observed in bimodal structure below 120 MPa and this amplitude can be considered the threshold amplitude for slip band formation in the large grained structure. Simultaneously, the plastic strain amplitude in high-cycle region had become non-measurable (below  $10^{-6}$ ). The characteristic features of crack initiation resemble the mechanism known for cast AZ91 alloy. The cracks, which initiate along the slip bands, later on tend to propagate by the opening mode macroscopically perpendicularly to the principal stress. The slip band formation in small grained areas was very rare and was observed only at high stress amplitudes (above 180 MPa). Sporadically broken large particles or cracks on the particle/matrix interfaces were observed in the bimodal structure. These cracks, however, did not propagate further and it was not observed that they were responsible for development of a major fatigue crack. On the other hand, in small grain areas cracks on grain boundaries were observed, Fig. 6b. These cracks seem to be responsible for continuous decrease of the S–N curve below the threshold for slip band formation. It can be even speculated, that in gigacycle region the fatigue strength of material processed by ECAP can be even worse than that of the cast alloy.

The fatigue life of alloy processed by ECAP continuously increases with decreasing stress amplitude. There is no a knee in the investigated interval of the stress amplitudes and number of cycles to failure, contrary to the S–N curve of the cast material. Here the slip bands form in the large solid solution areas. Very often are oriented at the angle of nearly  $45^\circ$  to the loading direction. The length of formed slip bands is limited by the solid solution areas and the particles located in the structure. The cracks initiated in long slip bands later on grow perpendicularly to the loading direction. This observation is in full agreement with Wolf et al. (2004), Gu et al. (2010) who observed the crack initiation on slip bands formed

in the solid solution areas and on structural defects which were present in the structure. In the alloy studied in this work no structural defects were observed. In some cases the slip bands formation occur also in the areas of discontinuous precipitates, where the slip bands were formed in the solid solution and they broke the small  $Mg_{17}Al_{12}$  particles, Fig. 5b. In some cases also broken intermetallic particles and eutectic can be observed in the structure; nevertheless in this case initiated cracks stopped and did not propagate further. No connection between slip bands formation and large particles cracking was observed in this study. Similarly to the bimodal structure no slip bands were found on the run-out specimens. The stress amplitude 80 MPa can be thus taken as the limit for the slip bands formation and crack initiation in the cast alloy.

Fatigue cracks in both states of the alloy initiate in the slip bands, which express themselves by extrusions on the surface. FIB observation indicates that there is no direct relation among the height of extrusions and the damage along the slip plane below the surface. This seems to be in contradiction with the observation performed on f.c.c. materials by Polák and Man (2014). On the other hand, the damage in form of voids and cavities, which can be seen in Fig. 7b, witnesses for an important role of point defects in the crack initiation mechanism.

Cyclic plastic response of the cast AZ91 alloy, Fig. 4a, consists in a short initial softening for  $10^2$  cycles followed by hardening which is characteristic for the largest part of the fatigue life. This finding is in full agreement with the results published by Wolf et al. (2004), our previous results (Fintová and Kunz, 2014a, 2014b) and results of Horynová et al. (2013) on AZ31. The maximum on the cyclic hardening/softening curve is located in the range  $1\text{--}2 \times 10^3$  cycles, which corresponds also to the observation published in Ebel-Wolf et al. (2008) for experiments under total strain control.

ECAP treatment results in structure refinement but it also induce internal stresses to the treated structure. Relaxation of the stresses in the heavily deformed structure is suggested to be responsible for the initial softening of AZ91 after ECAP. The following cyclic hardening, Fig. 4b, is related mainly to the cyclic slip activity within the large grain areas. These areas exhibit similar behavior as the solid solution areas in the cast material. Similar behavior was mentioned by Chung et al. (2009) for unidirectional loading of bimodal structure of AZ91 alloy. They observed formation of slip bands at the beginning of loading in large favorably oriented grains and later on onset of plastic deformation of grains in small grained areas. In agreement with Chung et al. (2009) only limited number of slip bands was observed in small grained areas however no crack initiation was observed. In the case of small grained areas the hardening due to grain boundaries and small particles presence prevent to plastic deformation (Wolf et al., 2004). In the small grain areas grain boundaries cracking was observed.

## 5. Conclusions

The structure of AZ91 magnesium alloy processed by six ECAP passes by route Bc at  $300^\circ\text{C}$  is bimodal. It consists of



areas of small grains (average grain size of  $3.3 \pm 0.5 \mu\text{m}$ ) with large amount of small  $\text{Mg}_{17}\text{Al}_{12}$  particles and of areas of large grains (average grain size of  $9.9 \pm 4.5 \mu\text{m}$ ) with substantially smaller amount of  $\text{Mg}_{17}\text{Al}_{12}$  particles when compared to the small grained areas. In the structure also primary large particles were observed.

ECAP treatment increases the tensile properties of the cast alloy by the factor of two. Particularly, the yield stress increases from 87 to 160 MPa and the tensile strength from 167 to 321 MPa. The ductility increases from 3.1 to 15.4%.

The endurance limit based on  $10^7$  cycles remains practically unaffected by ECAP. It is 80 MPa for the cast alloy and 85 MPa for the alloy processed by ECAP. Contrary to this, the fatigue lifetime in the low-cycle fatigue region is substantially improved. The  $S$ - $N$  curve is shifted by two orders of magnitude to higher fatigue lives.

Cyclic hardening during load controlled test is the characteristic feature for the decisive part of the lifetime of cast alloy, whereas the material after ECAP exhibits expressive initial cyclic softening followed by hardening which is representative for the major part of the fatigue life.

Cyclic slip bands which develop during fatigue loading are the preferable sites of the fatigue crack initiation in both states of the alloy. They are formed in the large grained areas in the alloy processed by ECAP and in the areas of solid solution in the cast material. In the fine grained areas of the severe plastic deformed alloy grain boundary cracking was observed.

## Acknowledgments

The Czech Science Foundation under the contract 108/10/2001 and Ministry of Education of the Czech Republic under the project CZ.1.07/2.3.00/30.0039 supported this work.

## REFERENCES

- Altwicker, H., et al., 1939. *Magnesium und seine Legierungen*. J. Springer Verlag, Berlin.
- Braszczyńska-Malik, K.N., 2011. Precipitates of  $\gamma$ - $\text{Mg}_{17}\text{Al}_{12}$  Phase in AZ91 Alloy. In: ([http://cdn.intechopen.com/pdfs/12741/InTech-Precipitates\\_of\\_gamma\\_mg17al12\\_phase\\_in\\_mg\\_al\\_alloys.pdf](http://cdn.intechopen.com/pdfs/12741/InTech-Precipitates_of_gamma_mg17al12_phase_in_mg_al_alloys.pdf)).
- Chen, B., Lin, D.L., Jin, L., Zeng, X.Q., Lu, Ch., 2008. Equal-channel angular pressing of magnesium alloy AZ91 and its effects on microstructure and mechanical properties. *Mater. Sci. Eng., A* 483–484, 113–116.
- Chen, Y., Xu, Z., Smith, Ch., Sankr, J., 2014. Recent advances on the development of magnesium alloys for biodegradable implants. *Acta Biomater.* 10, 4561–4573.
- Choudhary, R.K., Singh, R., 2012. Magnesium alloys as body implants: fracture mechanism under dynamic and static loadings in a physiological environment. *Acta Biomater.* 8, 916–923.
- Chung, C.W., Ding, R.G., Chiu, Y.L., Gao, W., 2010. Effect of ECAP on microstructure and mechanical properties of cast AZ91 magnesium alloy. *J. Phys.: Conf. Ser.* 241, 012101.
- Chung, C.W., Ding, R.G., Chiu, Y.L., Hodgson, M.A., Gao, W., 2009. Microstructure and mechanical properties of an as-cast AZ91 Mg alloy processed by equal channel angular pressing. *IOP Conf. Ser.: Mater. Sci. Eng.* 4, 012012.
- Chung, Ch-S., Chun, D-K, Kim, H.K., 2005. Fatigue properties of fine grained magnesium alloys after severe plastic deformation. *J Mech. Sci. Technol.* 19, 1441–1448.
- Ebel-Wolf, B., Walther, F., Eifler, D., 2008. Influence of elevated temperatures on the cyclic deformation behaviour of the magnesium die-cast alloys AZ91D and MRI 230D. *Mater. Sci. Eng., A* 486, 634–640.
- Eisenmeier, G., Holzwarth, B., Höppel, H.W., Mughrabi, H., 2001. Cyclic deformation and fatigue behaviour of the magnesium alloy AZ91. *Mater. Sci. Eng., A* 319–321, 578–582.
- Fintová, S., Kunz, L., 2014a. Cyclic plastic behavior and fatigue life of AZ91 alloy in as-cast and ultrafine-grained state. *Mater. Eng.—Mater. Inž.* 21, 109–115.
- Fintová, S., Pantělejev, L., Kunz, L., 2014b. Microstructure and mechanical properties of ultrafine-grained magnesium AZ91 alloy. *Mater. Sci. Forum* 782, 384–389.
- Gu, X.N., Zhou, W.R., Zheng, Y.F., Cheng, Y., Wei, S.C., Zhong, S.P., Xi, T.F., Chen, L.J., 2010. Corrosion fatigue behaviors of two biomedical Mg alloys-AZ91D and WE43-in simulated body fluid. *Acta Biomater.* 6, 4605–4613.
- Gupta, M., Sharon, N.M.L., 2011. *Magnesium, Magnesium Alloys, and Magnesium Composites*. John Wiley & Sons 257.
- Hadzima, B., Janeček, M., Suchý, P., Müller, J., Wagner, L., 2008. Microstructure and corrosion properties of fine-grained Mg-based alloys. *Mater. Sci. Forum* 584–586, 994–999.
- Horynová, M., Zapletal, J., Doležal, P., Gejdoš, P., 2013. Evaluation of fatigue life of AZ31 magnesium alloy fabricated by squeeze casting. *Mater. Des.* 45, 253–264.
- Höppel, H.W., Korn, M., Lapovok, R., Mughrabi, H., 2010. Bimodal grain size distribution in UFG materials produced by SPD: their evolution and effect on mechanical properties. *J. Phys.: Conf. Ser.* 240, 012147.
- Kim, H.K., Lee, Y.-I., Chung, Ch-S., 2005. Fatigue properties of a fine-grained magnesium alloy produced by equal channel angular pressing. *Scr. Mater.* 52, 473–477.
- Korn, M., Lapovok, R., Böhner, A., Höppel, H.W., Mughrabi, H., 2011. Bimodal grain size distribution in UFG materials produced by SPD—their evolution and effect on the fatigue and monotonic strength properties. *Kovove Mater.* 49, 51–63.
- Molodova, X., Gottstein, G., Hellmig, R.J., 2007. On the thermal stability of ECAP deformed FCC metals. *Mater. Sci. Forum* 558–559, 259–264.
- Murugan, G., Raghukandan, K., Pillai, U.T.S., Pai, B.C., Mahadevan, K., 2009. High cyclic fatigue characteristics of gravity cast AZ91 magnesium alloy subjected to transverse load. *Mater. Des.* 30, 2636–2641.
- Němcová, A., Zapletal, J., Juliš, M., Podrábský, T., 2009. Cyclic fatigue resistance of AZ91 magnesium alloy. *Mater. Inž.* 16, 5–10.
- Polák, J., Man, J., 2014. Mechanisms of extrusion and intrusion formation in fatigued crystalline materials. *Mater. Sci. Eng., A* 596, 15–24.
- Saris, N-EL, Mervaala, E., Karppanen, H., Khawaja, J.A., Lewenstam, A., 2000. Magnesium: an update on physiological, clinical and analytical aspects. *Clin. Chim. Acta* 294, 1–26.
- Štěpánek, R., Pantělejev, L., Man, O., 2013. Thermal stability of magnesium alloy AZ91 prepared by severe plastic deformation. *Mater. Eng.—Mater. Inž.* 20, 160–166.
- Valiev, R.Y., Alexandrov, I.V., 2002. Paradox of strength and ductility in metals processed by severe plastic deformation. *J. Mater. Res.* 17, 5–8.
- Vrátná, J., Hadzima, B., Bukovina, M., Janeček, M., 2013. Room temperature corrosion properties of AZ31 magnesium alloy processed by extrusion and equal channel angular pressing. *J. Mater. Sci.* 48, 4510–4516.

- Wang, H., Estrin, Y., Fu, H.M., Song, G.L., Zúberová, Z., 2007. The effect of pre-processing and grain structure on the bio-corrosion and fatigue resistance of magnesium alloy AZ31. *Adv. Eng. Mater.* 11, 967–972.
- Witte, F., Fischer, J., Nellesen, J., Crostack, H.A., Kaese, V., Pisch, A., et al., 2006. In vitro and in vivo corrosion measurements of magnesium alloys. *Biomaterials* 27, 1013–1018.
- Wolf, B., Fleck, C., Eifler, D., 2004. Characterization of the fatigue behaviour of the magnesium alloy AZ91D by means of mechanical hysteresis and temperature measurements. *Int. J. Fatigue* 26, 1357–1363.
- Wolf, F.I., Cittadini, A., 2003. Chemistry and biochemistry of magnesium. *Mol. Aspect Med.* 24, 3–9.
- Yamashita, A., Horita, Z., Langdon, T.G., 2001. Improving the mechanical properties of magnesium and a magnesium alloy through severe plastic deformation. *Mater. Sci. Eng., A* 300, 142–147.

- II. [26] S. Fintová, L. Kunz, Cyclic plastic behavior and fatigue life of AZ91 alloy in as-cast and ultrafine-grained state, *Materials Engineering - Materiálové inžinierstvo*, 21 (2014) 109-115.



# CYCLIC PLASTIC BEHAVIOR AND FATIGUE LIFE OF AZ91 ALLOY IN AS-CAST AND ULTRAFINE-GRAINED STATE

Stanislava Fintová<sup>1, 2, 3, \*</sup>, Ludvík Kunz<sup>2</sup>

<sup>1</sup> CEITEC – Central European Institute of Technology, Brno University of Technology, Technická 3058/10, 61600 Brno, Czech Republic

<sup>2</sup> Institute of Physics of Materials Academy of Sciences of the Czech Republic, v. v. i., Žitkova 22, 616 62 Brno, Czech Republic

<sup>3</sup> University of Žilina, Faculty of Mechanical Engineering, Univerzitná 1, 010 26 Žilina, Slovak Republic

\* corresponding author: tel: +420 541 212 301, e-mail: fintova@ipm.cz.

## Resume

Fatigue properties of magnesium alloy AZ91 in as-cast and in ultrafine-grained state prepared by equal channel angular pressing were investigated. The fatigue strength in the low-cycle fatigue region was found to be substantially improved by the severe plastic deformation, whereas the improvement in the high-cycle fatigue region is negligible. The cyclic plastic response in both states is qualitatively similar; short initial softening is followed by a long cyclic hardening. The observed fatigue behavior was discussed in terms of specific microstructural features of both states and on the basis of cyclic slip localization and fatigue crack initiation.

## Article info

### Article history:

Received 22 December 2013

Accepted 23 February 2014

Online 15 September 2014

### Keywords:

AZ91;

ECAP;

Bimodal structure;

Fatigue;

Plastic deformation;

Crack initiation.

Available online: <http://fstroj.uniza.sk/journal-mi/PDF/2014/16-2014.pdf>

ISSN 1335-0803 (print version)

ISSN 1338-6174 (online version)

## 1. Introduction

AZ91 magnesium alloy, the most popular magnesium alloy from AZ group, exhibits perfect castability and good mechanical properties combined with good corrosion resistance (for high purity version of the alloy) and low production costs. Because this alloy has been used in industry since more than eighty years [1] its mechanical and corrosion behaviour has been thoroughly investigated in the past and the results can be found in plenty of papers, e.g. [2 - 6] Beyond the favourable properties the alloy has also some disadvantages consisting mainly in its poor formability and limited ductility at room temperature. This is a natural consequence of its hexagonal close packed (hcp) structure with restricted number of available slip systems and presence of an intermetallic phase Mg<sub>17</sub>Al<sub>12</sub> [2 - 4, 7 - 10].

Within the last some years the alloy, primarily intended for castings, has been investigated with the aim to answer the question if severe plastic deformation (SPD) can influence its tensile strength,  $\sigma_{UTS}$ , yield stress,  $\sigma_y$ , and, particularly, improve the ductility due to the grain refinement. One of the most popular SPD techniques is equal channel angular pressing (ECAP). In the case of magnesium alloys the ECAP treatment has to be done at elevated temperatures by reason of activation of more slip systems in the hcp structure. Otherwise undesirable cracks appear in the processed material. It has been shown that the ultimate strength and ductility of AZ91 alloy can be significantly improved by ECAP treatment. The improvement of  $\sigma_{UTS}$ ,  $\sigma_y$  and ductility of AZ91 is more significant when compared to the other AZ magnesium alloys.

This is a consequence of high amount of small  $Mg_{17}Al_{12}$  particles after ECAP [7, 11]. Besides the mechanical properties also corrosion resistance of magnesium alloys can be improved by ECAP treatment [3, 8].

The fatigue life of the cast AZ91 alloy expressed in terms of S-N curve can be found in literature, e.g. [4, 12] and the same holds for its cyclic stress-strain behaviour expressed in terms of cyclic softening/hardening curves. The S-N curve exhibits a sharp knee. The slope of the S-N curve in the region of high number of cycles to failure is extremely low and the fatigue limit is in the range from 60 to 85 MPa, according to the details of chemical composition and casting process. The cyclic stress-strain behaviour of the cast material [12] exhibits at the beginning a weak cyclic softening (for some tens to hundreds of loading cycles), which is followed by cyclic hardening. In the case of higher applied stress amplitudes the maximum on the cyclic softening/hardening curves is missing and the cyclic hardening is characteristic response for the whole fatigue life.

As far as to the authors' knowledge no experimental data on the fatigue strength and the stress-strain response of the AZ91 after ECAP are available. The main aim of this study was to experimentally determine the S-N curve and the cyclic stress-strain response and to compare them with the behaviour of as-cast alloy. Simultaneously the influence of ECAP treatment on the microstructure was examined. The manifestation of localization of cyclic plasticity and formation of early fatigue cracks on the surface was examined by scanning electron microscopy (SEM).

## 2. Material and experiments

Fatigue behavior and the response of the material to the cyclic deformation were investigated on AZ91 alloy in as-cast and in ultrafine-grained (UFG) state, which was prepared by severe plastic deformation by ECAP. The severe plastic deformation was

conducted at temperature 573 K. The intersecting angle of the die channels was 120°. The processing route was Bc. The billets were manufactured by 6 passes. Final semi-products for machining of specimens for fatigue tests were cylindrical rods of 80 mm length and 15 mm in diameter. ECAP treatment was applied directly to the material in as-cast state.

The basic mechanical properties of the cast and UFG material are the following:  $\sigma_{UTS} = 167 \pm 8$  MPa, the yield stress  $\sigma_{0.2} = 87 \pm 8$  MPa and ductility  $3.1 \pm 0.4$  % for material in as-cast state and  $\sigma_{UTS} = 321 \pm 21$  MPa,  $\sigma_{0.2} = 160 \pm 4$  MPa and the ductility  $5.4 \pm 4.7$  % for the material after several plastic deformation by ECAP. Chemical composition of the AZ91 magnesium alloy is shown in Table 1.

Cylindrical specimens, Fig. 1, with the gauge length 15 mm and the gauge length diameter 4 mm were used for fatigue tests. The specimen gauge length was carefully ground and subsequently polished to get smooth surface for the observation by SEM with the aim to reveal the development of slip bands and cracks.

Fatigue testing was performed under controlled load in symmetrical tension-compression (load ratio R -1). The direction of the loading of UFG material coincided with the extrusion direction. For the fatigue tests servohydraulic testing system Shimadzu EHF-F1 was used. During the first 50 cycles the test frequency was 0.1 Hz. Then it was increased to 1 Hz until 100 cycles were reached. After 500 cycles the test frequency was increased to 5 Hz. After elapsed 3000 cycles the frequency was increased to 10 Hz. At the pre-defined number of cycles the hysteresis loops were recorded; for this purpose during the recording procedure the loading frequency was reduced to 0.1 Hz. When the specimen lifetime exceeded  $1 \times 10^6$  cycles, the specimen was moved to a resonant fatigue machine Amsler HFP 5100 and the loading was continued with a frequency of about 60 Hz. Tests were conducted at room temperature in laboratory air.

Table 1

*Chemical composition of AZ91 magnesium alloy (in wt. %).*

elements	Al	Zn	Mn	Si	Fe	Be	Ni	Cu	Mg
wt. %	8.7	0.65	0.25	0.006	0.003	0.0008	0.0006	0.0005	Rest

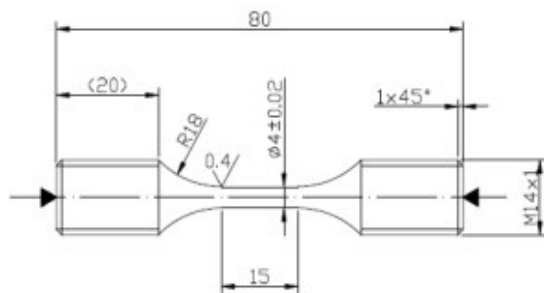


Fig. 1. Geometry of specimen for the fatigue tests.

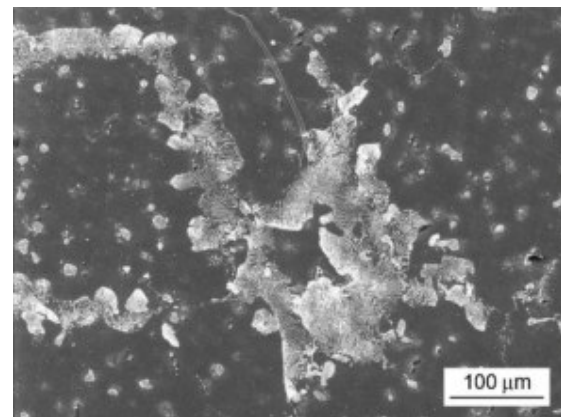
Microstructure and the specimen surface were examined by SEM Tescan LYRA 3 XMU FEG/SEM x FIB.

### 3. Results

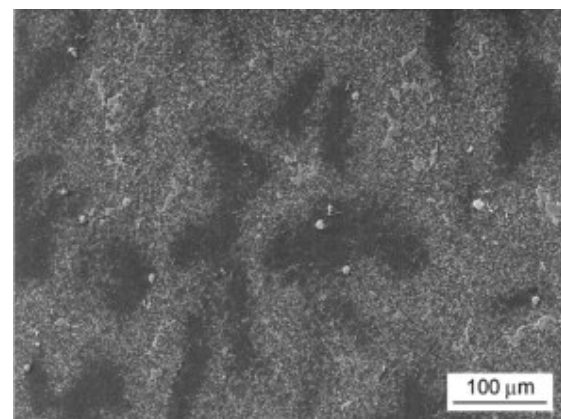
The microstructure of AZ91 magnesium alloy in as-cast state consists of a solid solution of alloying elements in magnesium and eutectic. Eutectic consists of the solid solution and particles of intermetallic phase  $Mg_{17}Al_{12}$  in a plate like shape. Furthermore, large primary  $Mg_{17}Al_{12}$  and AlMn based particles are present in the structure, Fig. 2a.

The structure after ECAP processing by 6 passes by the route Bc is not fully homogenous from the macroscopic point of view. It can be characterized as bimodal. There are areas with small grains with the average grain size of  $3.3 \pm 0.5 \mu m$  with large amount of small  $Mg_{17}Al_{12}$  particles, and areas with larger grains, with the average grain size of  $9.9 \pm 4.5 \mu m$  where the density of small  $Mg_{17}Al_{12}$  particles is low. Some large primary  $Mg_{17}Al_{12}$  particles and AlMn based particles remained in the heavily deformed structure, Fig. 2b. The grain size deviates from the convention that as UFG materials are considered those ones having the grain size in the range from 1000 to 100 nm. On the other

hand, materials prepared by ECAP are generally denoted as UFG. In the case of Mg alloys ECAP produces substantially smaller grain size as can be reached by conventional deformation techniques like rolling etc. That is why in this work the authors stick on the description of the microstructure as UFG.



a) Microstructure of cast AZ91 alloy



b) Microstructure of AZ91 after ECAP

Fig. 2. Microstructure of cast AZ91 alloy and after ECAP. SEM, etched by 2% Nital.

Results of the experimental determination of the fatigue life of AZ91 in the as-cast state and after ECAP are shown in Fig. 3. Obviously, there is a strong influence of ECAP procedure on the S-N curves. Cast AZ91 magnesium alloy exhibits typical knee in the S-N curve. Stress amplitude 80 MPa can be considered to be the



endurance limit (based on  $10^7$  cycles) for the cast alloy. Below this stress amplitude the fatigue life of all specimens tested exceeded  $10^7$  cycles. All the specimens loaded at higher stress amplitudes than 80 MPa failed before they reached  $10^5$  cycles. The decreasing part of the S-N curve can be well fitted by the power law dependence

$$\sigma_a = 282 N_f^{-0.11} \quad (1)$$

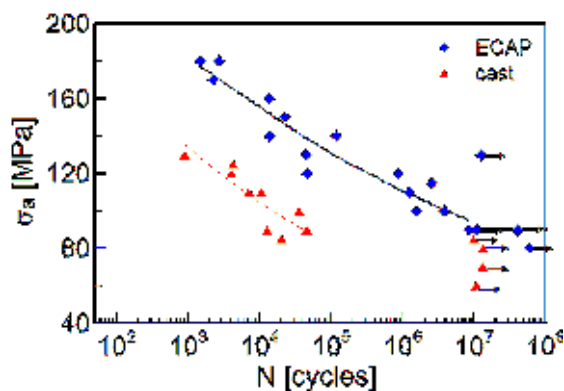


Fig. 3. S-N curves of cast AZ91 alloy and after ECAP.  
(full colour version available online)

The S-N curve of the UFG alloy is shifted to the higher lifetimes at the same stress amplitudes when compared to the cast alloy. It decreases linearly with the increasing number of cycles in the log-log plot and can be well approximated by the following equation

$$\sigma_a = 300 N_f^{-0.07} \quad (2)$$

There is no knee on the S-N curve of the UFG material. From the comparison of both curves it is obvious that the improvement of the fatigue properties by ECAP is substantial only in the low-cycle fatigue region. The endurance limit based on  $10^7$  cycles for the alloy processed by ECAP is 90 MPa, which is very close to the endurance limit of the cast alloy.

The cyclic deformation curves determined under load control are shown in Fig. 4. At the beginning of cycling the AZ91 in the as-cast

state exhibits a short stage of the cyclic softening during a few of cycles. The softening is followed by a pronounced cyclic hardening, which is characteristic for the decisive part of the fatigue life. The effect of initial cyclic softening is more apparent at low stress amplitudes. With increasing stress amplitudes the maximum on the softening/hardening curves is shifted towards lower number of cycles and became less expressive.

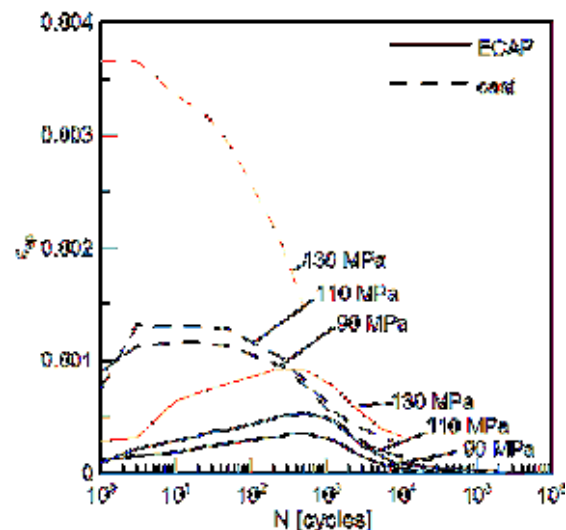


Fig. 4. Cyclic deformation curves of cast AZ91 alloy and after ECAP.  
(full colour version available online)

The cyclic deformation curves of UFG material are qualitatively similar to those of the cast alloy. The length of the initial cyclic softening stage of UFG structure is somewhat longer than that of the cast alloy and makes typically some hundreds of cycles. After the maximum is reached, a long stage of the cyclic hardening represents the characteristic stress-strain response. In the case of material treated by ECAP cyclic softening was typical for the beginning period up to approximately  $10^3$  cycles. This period was followed by cyclic hardening, which was not as strong as in the case of the cast material. The effect of cyclic softening was largest for the specimen tested at 130 MPa. Also in this case the cyclic hardening represents the largest part of the ECAPed material fatigue life.



#### 4. Discussion

The structure of AZ91 alloy processed by ECAP was found to be bimodal even after 6 passes of ECAP. The bimodality could be caused by missing pretreatment of the alloy before severe plastic deformation. A heat treatment is usually applied before the ECAP process. It makes the structure homogeneous and the following ECAP processing then refines the structure. Chen et al. [11] found that the heat treatment and subsequent ECAP resulted in creation of well-developed UFG structure after 2 ECAP passes. The following passes caused than only homogenization of the UFG structure. In the case when the pretreatment is missing the structure obtained by six ECAP passes by the route Bc can remain heterogeneous as observed in this study.

The effect of ECAP on the improvement of tensile properties and ductility of AZ91 was found to be more expressive than in the case of other AZ magnesium alloys [3, 7, 8, 11]. The explanation is sought in dominantly larger amount of small  $Mg_{17}Al_{12}$  particles and also in the strengthening role of the fine grain structure [5]. Gubicza et al. [13], observed significant improvement of strength and ductility of AZ91 alloy after only 2 ECAP passes at 543 K despite of not homogeneous final microstructure. The explanation is based on the evolution of precipitates during ECAP. Following ECAP passes led to little or no additional improvement of material strength. The results of this work and published data indicate that also the bimodal structure results in serious improvement of tensile properties, which is comparable with the fully homogenous UFG microstructure. The improvement of ultimate stress  $\sigma_{UTS}$  observed in this study for the bimodal structure of AZ91 alloy obtained by ECAP, was 100% when compared to the as-cast state. Chung et al. [5, 7] observed 100% improvement of tensile strength of AZ 91 processed by ECAP. In their case the obtained microstructure after 6 passes through the die at

593 K [7] and 573 K [5] was homogenous with  $8 \mu m$  [7] and  $6 \mu m$  [5] the average grain size.

Fatigue strength of AZ91 was substantially improved by ECAP in the low-cycle fatigue region, Fig. 3. This is obviously related to the high  $\sigma_{UTS}$  and  $\sigma_y$  of the bimodal structure. Contrary to the low-cycle fatigue region the fatigue strength improvement in the high-cycle fatigue region is negligible. There is no significant difference in the endurance limit of the cast alloy and the alloy after ECAP. The S-N curve of the cast alloy has the typical knee at  $10^5$  cycles. Observation of surface relief development during cycling implies the following explanation. The cracks initiate mainly on slip bands created due to the cyclic plastic deformation in softer solid solution areas. Fatigue cracks which were found in eutectics apparently grew into these regions from the solid solution. Sometimes broken intermetallic  $Mg_{17}Al_{12}$  particles were observed, however the cracks did not propagate further into their surroundings. With decreasing stress amplitude the percent occurrence of created slip bands rapidly decreases. At the stress amplitude of about 85 MPa the slip band formation in softer solid solution areas ceases entirely and the lifetime exceeds  $10^7$  cycles. On run-out specimens no slip bands were observed. The stress amplitude of 85 MPa can be considered as threshold amplitude for slip band formation. This conclusion was supported by SEM observation of specimens gauge length prepared by polishing and etching.

In the case of ECAPed alloy two mechanisms of fatigue crack initiation were observed. Slip bands in large grains of the bimodal structure were preferable places for crack initiation. The process has the same features as in the cast material; only the scale is smaller. Besides this mechanism crack initiation at grains boundaries in small grained areas was observed, particularly at lower stress amplitudes. However, the decisive majority of the investigated fracture surfaces bear witness

for initiation of fatal fatigue cracks in large grains of the bimodal structure. Nevertheless, it can be expected, that with decreasing stress amplitude the transition from initiation at slip bands to initiation on grain boundaries and on cracked large precipitates can take place. The confirmation of this idea needs further experimental evidence.

The experimentally determined response of the cast AZ91 alloy on the cyclic deformation, Fig. 4, consists in a short initial softening followed by continuous cyclic hardening. This is in full agreement with the results published by Wolf et al. [12], who observed cyclic softening for  $10^2$  cycles and following cyclic hardening which was typical for the largest part of the fatigue life. When the experiments are performed under total strain control [6], the cyclic hardening follows the preliminary softening which lasts typically  $1 - 2 \times 10^3$  cycles. Plastic deformation of cast material occurs mainly in softer solid solution dendrites where slip bands were observed. The length of the observed slip bands is limited only by areas of solid solution. The cracks initiated in slip bands later grow perpendicularly to the loading direction. Slip bands were not observed in the eutectic hardened by the intermetallic phase  $Mg_{17}Al_{12}$  in a plate like shape. In the eutectic areas only cracked intermetallic  $Mg_{17}Al_{12}$  particles were observed, however, these cracks did not grow further into the dendrite areas. This observation is in agreement with Wolf et al. [12] who observed the crack initiation on slip bands formed in the solid solution areas and on structural defects which were present in the structure. In the alloy studied in this work no structural defects were observed.

The short initial softening of AZ91 after ECAP can be attributed to a relaxation of stresses in the heavily deformed structure. The following cyclic hardening, Fig 4, is related mainly with the cyclic slip activity within the large grained areas of the bimodal structure with the average grain size of  $9.9 \pm 4.5 \mu m$  where the

density of small  $Mg_{17}Al_{12}$  particles is low. These areas exhibit similar behavior as the solid solution areas in cast material; only their dimension is substantially smaller. SEM observation reveals development of slip bands during cycling, inherently at higher stress amplitudes. Similar behavior was mentioned by Chung et al. [5] for unidirectional loading of bimodal structure of AZ91 alloy. They observed formation of slip bands at the beginning of loading in large favorably oriented grains and later on onset of plastic deformation of grains in small grained areas. Cyclic plastic deformation of large grains was proved in the present study by development of slip bands on which cracks were initiated, Fig. 5b. With decreasing stress amplitude the number of slip bands decreases. Below 120 MPa no slip band formation was observed on specimen gauge length. Simultaneously, the plastic strain amplitude in high-cycle region had become non-measurable (below  $10^{-6}$ ).

The slip activity in the small grained areas manifests itself by formation of slip bands very sporadically. This indicates that the contribution of small grained areas to the plastic strain amplitude and its changes during cycling seems to be very low.

## 5. Conclusions

ECAP treatment of cast AZ91 improves its mechanical properties and fatigue strength in low-cycle fatigue region. The improvement in high-cycle fatigue region is negligible and the fatigue strength is similar to that of the cast material. Cyclic stress-strain response of ECAPed alloy is qualitatively the same as the response of cast alloy, namely short initial cyclic softening followed by long cyclic hardening.

The microstructure of AZ91 alloy processed by ECAP by 6 Bc passes is bimodal. The cyclic slip activity manifests itself mainly in the coarse grained areas of the structure, where long slip bands and later fatigue cracks form. The role and contribution of coarse grained areas to the

fatigue damage is decisive in the low-cycle region. Its cyclic plasticity resembles that of as cast material. With increasing number of cycles and exhausting of cyclic hardening in coarse grained regions the cyclic deformation in fine grained areas becomes important.

They are later on sites of initiation of fatigue cracks. With decreasing stress amplitude the slip activity in grain boundary crack initiation mechanism starts to play the dominant role.

### **Acknowledgment**

*The Czech Science Foundation under the contract 108/10/2001 and Ministry of Education of the Czech Republic under the projects CZ.1.07/2.3.00/30.0039 and 7AMB14SK064 supported this work. The research is supported by European regional development fund and Slovak state budget by the project ITMS 26220220121 (50%).*

### **References**

- [1] H. Altwicker et al.: Magnesium und seine Legierungen, J. Springer Verlag, Berlin, 1939.
- [2] A. Němcová, J. Zapletal, M. Juliš, T. Podrábský: Mat. Eng. Vol. 16 (4) (2009) 5-10.
- [3] L. Bukovinová, B. Hadzima: Corr. Eng. Sci. Technol. 47(5) (2012) 352-357
- [4] G. Eisenmeier, B. Holzwarth, H.W. Höppel, H. Mughrabi: Mat. Sci. Eng. A319-321 (2001) 578-582.
- [5] C.W. Chung, R.G. Ding, Y.L. Chiu, W. Gao: J. Phys.: Conf. Ser. 241 (2010) 012101.
- [6] B. Ebel-Wolf, F. Walther, D. Eifler: Mat. Sci. and Eng. A 486 (2008) 634-640.
- [7] C.W. Chung, R.G. Ding, Y.L. Chiu, M.A. Hodgson, W. Gao: IOP Conf. Series: Mat. Sci. and Eng. 4 (2009) doi:10.1088/1757-899X/4/1/012012.
- [8] B. Hadzima, M. Janeček, P. Suchý, J. Müller, L. Wagner: Mat. Sci. Forum 584-586 (2008) 994-999.
- [9] B. L. Mordike, T. Ebert: Mat. Sci. Eng. A302 (2001) 37-45.
- [10] K.N. Braszczyńska-Malik, Precipitates of  $\gamma$ -Mg<sub>17</sub>Al<sub>12</sub> Phase in AZ91 Alloy, In: [http://cdn.intechopen.com/pdfs/12741/InTech-Precipitates\\_of\\_gamma\\_mg17al12\\_phase\\_in\\_mg\\_al\\_alloys.pdf](http://cdn.intechopen.com/pdfs/12741/InTech-Precipitates_of_gamma_mg17al12_phase_in_mg_al_alloys.pdf)
- [11] B. Chen, D.L. Lin, L. Jin, X.Q. Zeng, Ch. Lu: Mat. Sci. Eng. A483-484 (2008) 113-116.
- [12] B. Wolf, C. Fleck, D. Eifler.: Int. J. Fat 26 (2007) 1357-1363.
- [13] J. Gubicza, K. Máthis, Z. Hege: J. of Alloys and Compounds 492 (2010) 166-172.

- III. [27] S.Fintová, L. Kunz, Initiation of fatigue cracks in AZ91 Mg alloy processed by ECAP, IOP Conference Series: Materials Science and Engineering, 63 (2014) 012159.

# Initiation of fatigue cracks in AZ91 Mg alloy processed by ECAP

S Fintová<sup>1</sup> and L Kunz<sup>2</sup>

<sup>1</sup> Brno University of Technology, CEITEC BUT – Central European Institute of Technology, Technická 3058/10, 616 00 Brno, CZ, e-mail: [stanislava.fintova@ceitec.vutbr.cz](mailto:stanislava.fintova@ceitec.vutbr.cz)

<sup>2</sup> Institute of Physics of Materials AS CR, Žitkova 22, 616 62 Brno, CZ, e-mail: [kunz@ipm.cz](mailto:kunz@ipm.cz)

**Abstract.** Mechanism of fatigue crack initiation was investigated in ultrafine-grained (UFG) magnesium alloy AZ91 processed by equal channel angular pressing (ECAP). Fatigue behaviour of UFG material was compared to the behaviour of material in an initial as-cast state. Focused ion beam technique (FIB) was applied to reveal the surface relief and early fatigue cracks. Two substantially different mechanisms of crack initiation were observed in UFG structure, which can be characterized as bimodal even after 6 ECAP passes by route Bc. The bimodality consists in a coexistence of very fine grained areas with higher content of Mg<sub>17</sub>Al<sub>12</sub> particles and areas exhibiting somewhat larger grains and lower density of particles. The fatigue cracks which initiate in areas of larger grains are related to the cyclic slip bands; this initiation mechanism is similar to that observed in cast alloy. The second initiation mechanism is related to the grain boundary cracking which takes place predominantly in the fine grained areas.

## 1. Introduction

Magnesium alloys are used especially because of their low weight but still good mechanical properties. Based on the chemical composition and resulting microstructure, different ratio among individual material properties can be reached [1 – 7].

Though there is a relatively extensive knowledge on relation of microstructure and mechanical properties of Mg alloys, methods of further improvement of the mechanical properties is still a discussed issue, permanently activated by engineering practice and industrial demands. One of the ways how to improve mechanical properties is application of severe plastic deformation (SPD). Equal channel angular pressing (ECAP) is one of the most studied and explored techniques. ECAP treatment performed at elevated temperatures can improve tensile properties of magnesium alloys, corrosion properties and also fatigue strength [8, 9]. On the other hand also lowering of tensile and fatigue strength were reported for wrought Mg alloys processed by ECAP [10, 11, 12]. Elevated temperatures under which the SPD is applied are necessary for activation of sufficient amount of slip systems in magnesium hcp crystallographic lattice. It has been shown that suitable heat treatment of the initial cast alloy before ECAP promotes formation of more homogenous structure and the ECAP refines than the structure more effectively. When a proper heat treatment is applied before ECAP, only 2 passes through ECAP die are sufficient to refine the structure and significantly improve the yield stress and tensile strength. Following passes through ECAP die homogenize the structure whereas the influence on mechanical properties of treated material is weak [5, 7, 8].

AZ91 magnesium alloy is one of the most often used magnesium alloys from AZ group. It contains relatively high volume of alloying elements; high volume of Al results in larger amount of Mg<sub>17</sub>Al<sub>12</sub> intermetallic particles, which can be exploited in material hardening due to the treatment by ECAP [5]. ECAP process rises the yield stress ( $\sigma_{0.2}$ ) and ultimate tensile strength ( $\sigma_{UTS}$ ) (almost 100 % improvement), and, particularly, improves the ductility (A) (almost 500 % improvement) due to the substantial grain refinement [5, 7, 13].

The AZ91 alloy is primarily intended and used for fabrication of cast components. The fatigue behaviour of AZ91 in cast state was examined in [4, 14]. It has been shown that the endurance limit is of about 80 MPa. Wolf et al. [4] studied the fatigue behavior and the



mechanism of fatigue crack initiation and growth. They reported that the initiation of fatigue cracks takes place due to localization of the cyclic plastic deformation in slip bands which are formed in solid solution areas. Fatigue cracks initiate at the surface micro-relief at in-/extrusions and on interfaces between brittle  $Mg_{17}Al_{12}$  intermetallic particles and ductile solid solution matrix. Also an  $Mg_{17}Al_{12}$  intermetallic particle cracking was observed. The authors draw also the attention to the role of pores present in the material which can be sites of fatigue crack initiation.

The studies dealing with fatigue behaviour, crack initiation and growth in ECAPed AZ91 magnesium alloy are very rare. That is why this study was focused on the experimental determination of the S-N curve, investigation of mechanisms of fatigue crack initiation in UFG AZ91 processed by ECAP and comparison with the behaviour of the as-cast state.

## 2. Material and experiments

AZ91 magnesium alloy with chemical composition given in Table 1 was investigated. Cast billets were used with no preliminary heat treatment for ECAP. The processing temperature  $300^{\circ}C$  was sufficient to perform the severe plastic deformation without cracking. Bc route was applied and the intersecting angle of the die channels was  $120^{\circ}$ . The billets were treated by 6 passes.

Table 1. Chemical composition of AZ91 magnesium alloy, wt. %.

elements	Al	Zn	Mn	Si	Fe	Be	Ni	Cu	Mg
wt. %	8.7	0.65	0.25	0.006	0.003	0.0008	0.0006	0.0005	rest

The semi-products used for machining of the fatigue specimens were cylindrical rods of 80 mm length and 15 mm in diameter. The specimen geometry is shown in Fig. 1. Gauge length of the specimens was carefully polished for the following inspection with the aim to reveal the development of slip bands and cracks. The procedure of gauge length preparation consisted of mechanical grinding (SiC papers. No. 800, 1200 and 2500) and mechanical polishing ( $1\ \mu m$  diamond paste). In some cases also electrolytic polishing or etching before the testing was applied. Due to the reaction of the chemical solutions with the surface the microstructure was visible and the relationship of the structural features and the crack initiation can be examined.

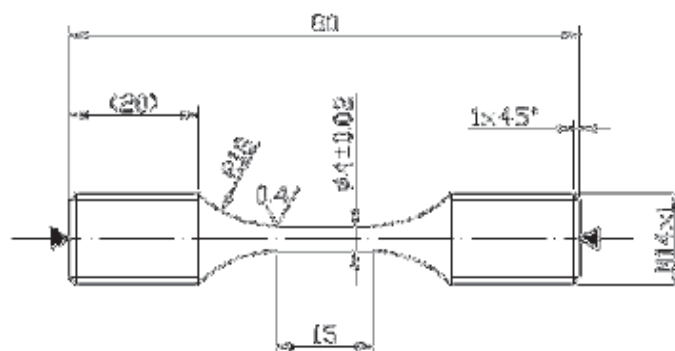


Fig. 1. Fatigue test specimen geometry.

Load controlled cycling in symmetrical tension-compression (load ratio  $R = -1$ ) was used for fatigue testing in the Shimadzu EHF-F1 servo-hydraulic system. The loading frequency was in the range 0.1 to 10 Hz in the low-cycle fatigue region. When the specimen lifetime exceeded  $1 \times 10^6$  cycles, the specimen was moved to the Amsler HFP 5100 resonant fatigue

machine and the loading was continued with a frequency of about 60 Hz. Tests were conducted at room temperature in laboratory air.

Tescan LYRA 3 XMU FEG/SEM x FIB scanning electron microscope (SEM) was used for observation and analysis of microstructure and the examination of specimen gauge length surface after fatigue tests. Focused ion beam (FIB) technique was applied to examine the characteristic features of microstructure and formation of surface relief and early cracks.

### 3. Results and discussion

#### 3.1. Structure

The structure of cast specimens consists of solid solution of alloying elements in magnesium, eutectic (solid solution of alloying elements in magnesium +  $Mg_{17}Al_{12}$  particles) and discontinuous precipitates and intermetallic particles. The solid solution consists of grains with the average grain size of  $185 \pm 70 \mu m$ . The characteristic structure of AZ91 in cast state is shown in Fig. 2a.

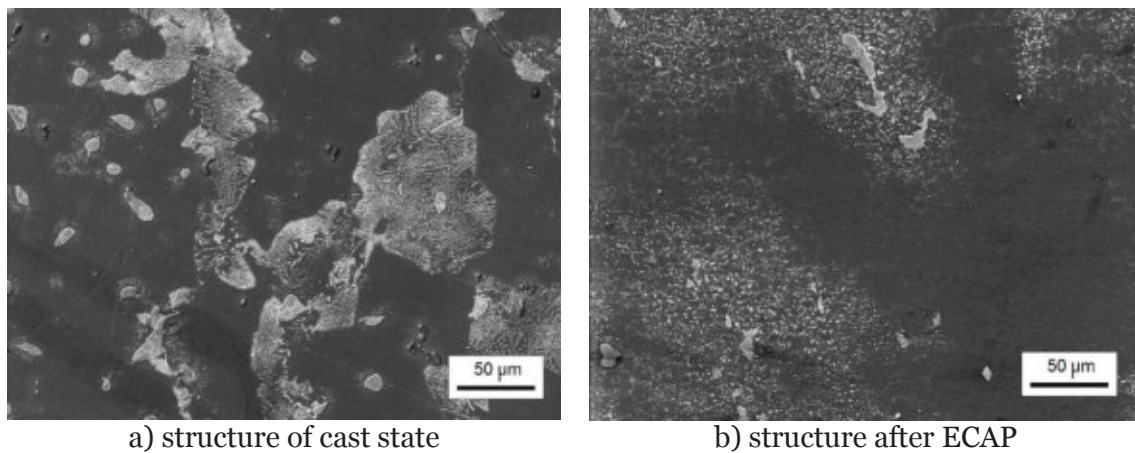


Fig. 2. Characteristic structure of AZ91 magnesium alloy, etched by Nital, SEM.

The structure of specimens treated by 6 passes of ECAP consists of grains of solid solution of alloying elements in magnesium,  $Mg_{17}Al_{12}$  intermetallic particles and AlMn based intermetallic particles. The structure can be characterized as bimodal from the macroscopic point of view. There are areas with small grains there with the average grain size of  $3.3 \pm 0.5 \mu m$  with large amount of small  $Mg_{17}Al_{12}$  particles. Besides these fine grained areas there are also areas with larger grains, with the average grain size of  $9.9 \pm 4.5 \mu m$  where the density of small  $Mg_{17}Al_{12}$  particles is markedly lower. A typical example of the bimodal structure of AZ91 after ECAP is shown in Fig. 2b. It can be seen that some amount of large primary  $Mg_{17}Al_{12}$  particles and AlMn based intermetallic particles remained in the ECAPed structure.

The observed bimodality of structure after ECAP can be explained by missing heat pretreatment of cast material before ECAP. According to the observation by Chen et al. [15] the microstructure of AZ91 magnesium alloy after ECAP looks to be strongly influenced by the structure before ECAP treatment. When the heat pretreatment is optimal, the ECAP results in creation of fine grained structure as early as after 2 passes. Following passes cause only homogenization of the structure, without any important influence on the grain size. In the case of missing heat pretreatment the structure obtained after 6 passes can remain bimodal as in the present study. Simultaneously, the tensile properties and ductility of bimodal structure are substantially improved when compared to the cast state [5, 7, 8, 13].





gauge length were observed even after  $10^7$  cycles. Thus the stress amplitude 85 MPa can be considered a threshold for slip band formation in as cast structure.

In the material after ECAP the mechanism of the fatigue crack initiation in the large grain areas of the bimodal structure (grain size about  $10\ \mu\text{m}$ ) was found to be qualitatively the same as observed in the cast material. The grains formed by solid solution with low density of  $\text{Mg}_{17}\text{Al}_{12}$  particles were predominant places of slip band formation, Fig. 4b. The slip bands are, due to small grain size, much shorter than in the cast material. Also the distance between parallel slip bands in the ECAPed material is smaller. The whole process is substantially scaled down when compared to the cast state. Also the transition to the crack propagation perpendicularly to the loading axis starts much earlier, i.e. for quite short cracks developed in slip bands. This is shown in Fig. 4b, where the cracks macroscopically propagate perpendicularly to the loading axis (marked by arrows in Fig. 4b). The crack initiation in a slip band requires a definite amount of cyclic plasticity to produce the necessary material damage. This is in agreement with observations of Chung et al. [8]. It is obvious, that the crack initiation and early crack growth in a fine grained structure are more difficult than in the coarse grained case due to higher number of barriers.

Similarly to the cast state, with decreasing stress amplitude the number of slip bands rapidly decreases. The multiple crack initiation ceases quickly and single crack initiation becomes decisive. Below 120 MPa no slip bands on the polished and etched specimen gauge lengths were observed. Consequently, this stress amplitude can be considered a threshold for formation of the slip bands in the fine-grained structure. Simultaneously, the stress amplitude 130 MPa is a level, at which a run-out specimen was found, Fig. 3. Nevertheless, some specimens failed also below this stress level. This means that at least one crack had to initiate on the specimen gauge length and this crack caused the fatigue failure. Detailed inspection of the fracture surfaces of specimens which failed below 130 MPa together with observation of microstructure gave evidence that the initiation took place in the large grained area.

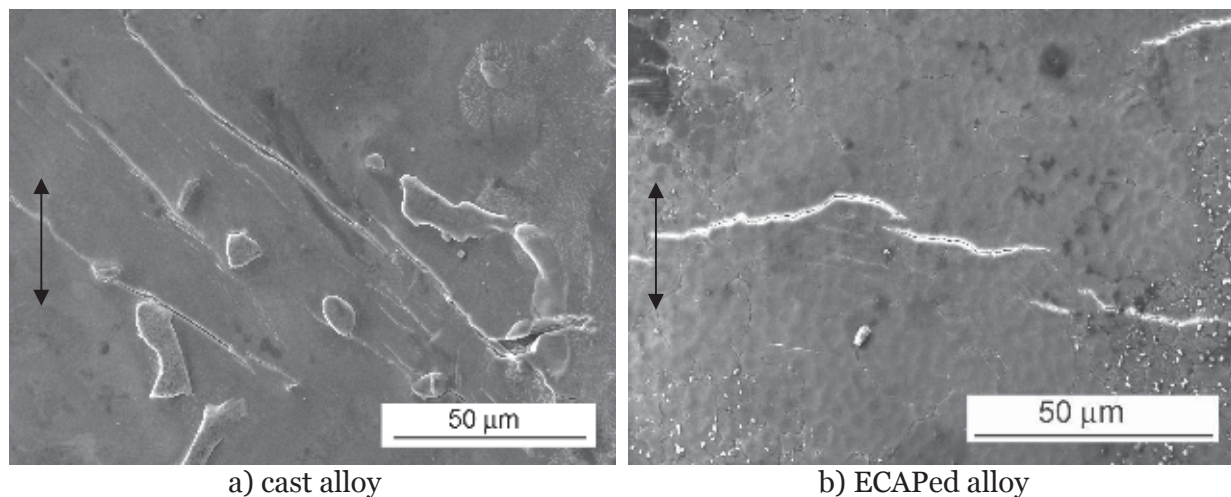


Fig. 4. Slip bands and fatigue cracks on the specimen surface after fatigue loading.

Results of the examination of the surface relief and microstructure in the vicinity of early cracks by FIB are shown in Fig. 5 and 6. A set of slip bands in cast material can be seen in Fig. 5a. This set was covered by protective platinum layer for the FIB cutting and following surface relief observation. Fig. 5b documents high extrusions above the plain surface which correspond to the slip bands visible in the Fig. 5a. Intrusions are inexpressive; however material damage along the straight slip planes below them can be seen. In the case of long slip bands the well developed straight cracks along these planes are visible. The initiation of

fatigue cracks in Mg alloys is often described in literature as quasi-cleavage [16], without detailed description of the inherent mechanism. The existence of well-developed extrusions witnesses for severe concentration of the cyclic plasticity and slip activity within the slip bands. From this aspect the mechanism of crack initiation resembles that known from f.c.c. metals.

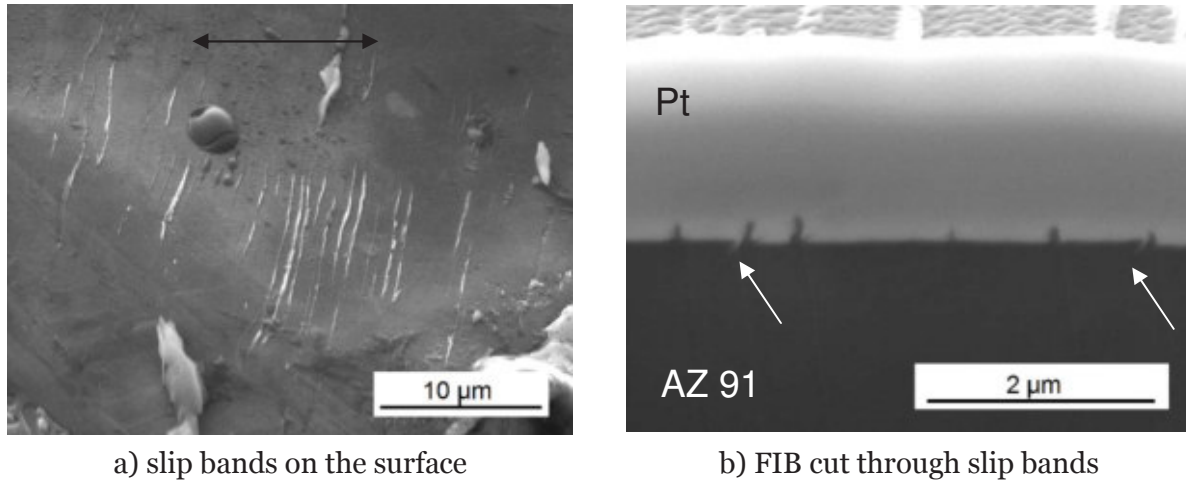


Fig. 5. Slip bands in cast alloy, specimen tested at  $\sigma_a = 120$  MPa,  $N_f = 4\ 088$  cycles.

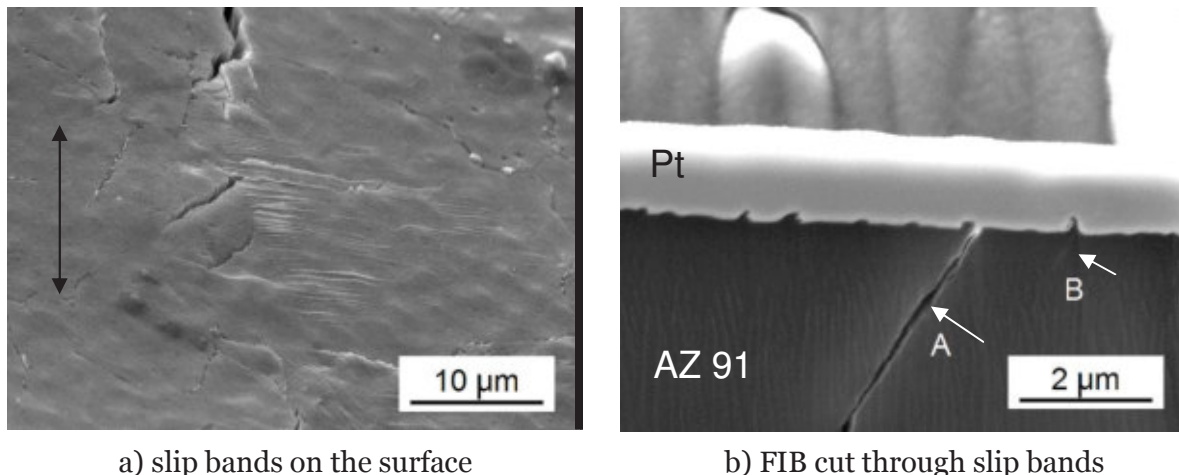


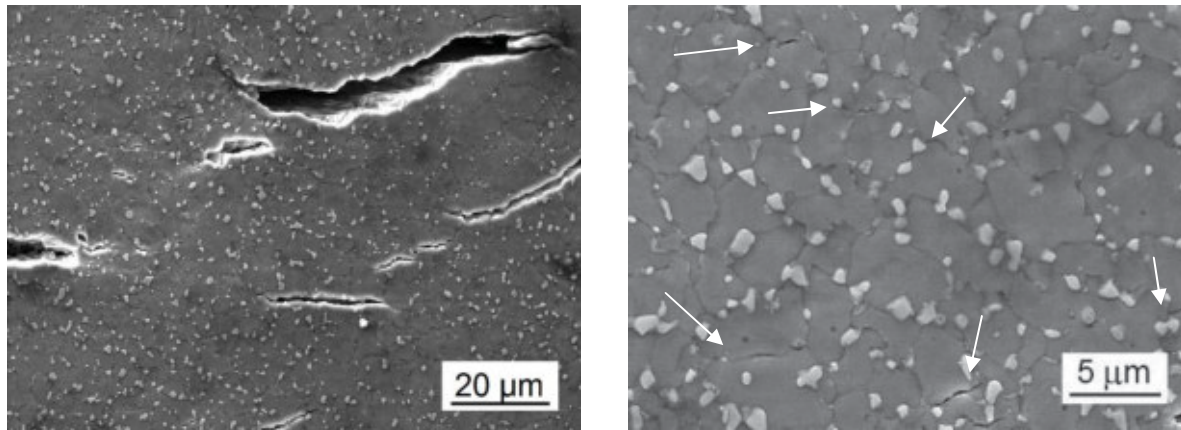
Fig. 6. Slip bands in alloy after ECAP, specimen tested at  $\sigma_a = 180$  MPa,  $N_f = 1\ 473$  cycles.

An example of the surface of large grained area of the bimodal structure after fatigue loading can be seen in Fig. 6a. The slip bands with clear extrusions appear only in suitably oriented grains, whereas neighboring grains does not exhibit any apparent slip activity in terms of slip band formation. Fig. 6b shows the FIB cut perpendicular to the surface and nearly perpendicular to the slip bands. Similarly to the cast material the extrusion profile is visible on the surface. Some of extrusions are related to cracks. The crack denoted by A is well developed, running crystallographically along the slip plane into material interior. The fracture surfaces are clearly separated and the crack runs across the whole grain. The crack denoted by B, which is also related to the extrusion on the surface is short (about 1  $\mu\text{m}$ ) and does not represent fully separated material. It is worthwhile to mention that there seems not to be any relation between the height of extrusions and the length of a related crack.

From Fig. 6a it is evident that besides the slip bands, grain boundary cracks appear in the structure. An example of this type of cracking in fine grained area is shown in Fig. 7. In the



neighbouring grains no apparent signs of cyclic plasticity in terms of slip bands can be detected. This type of crack initiation was not observed in the cast material.



a) cracks in area with small grains

b) detail of grain boundary cracks

Fig. 7. Grain boundary cracks in alloy after ECAP, specimen tested at  $\sigma_a = 180$  MPa,  $N_f = 1\,473$  cycles.

### 3.4. Fatigue life

ECAP treatment obviously improves fatigue strength in the low-cycle fatigue region. This effect is related to substantially higher  $\sigma_{UTS}$  and  $\sigma_{0.2}$  of the alloy after SPD treatment, which is connected with microstructural changes and strengthening due to the ECAP [5, 13]. However, no significant difference in the endurance limit based on  $10^7$  cycles of the cast alloy and the alloy after ECAP follows from the experimental data shown in Fig. 3. For both tested material states, similar stress amplitude can be considered as the endurance limit; 80 MPa for as-cast state and 90 MPa for ECAPed alloy. The value for cast material corresponds well with the average value of the endurance limit 80 - 90 MPa of cast AZ91 alloy based on large set of literature data [1]. Simultaneously this amplitude is the threshold amplitude for development of slip bands which are sites of initiation of fatigue cracks. In material processed by ECAP the development of slip bands which are responsible for initiation of fatigue cracks ceases when the stress amplitude decreases below 120 MPa. However, due to the existence of simultaneous crack initiation mechanism related to the grain boundary cracking the endurance limit further decreases. The number of experimental S-N points presented in Fig. 3 in the region of endurance limit is not very high. It would be worthwhile to determine experimentally the endurance limit for ECAPed material by stair case method and to evaluate statistically the scatter of data for both states of material. However, this task is beyond the range of this work.

## 4. Conclusions

- ECAP treatment improves the fatigue strength of AZ91 alloy. The S-N curve is shifted by two orders of magnitude towards higher number of cycles to failure when compared to the cast alloy. The endurance limit for  $10^7$  cycles of cast and ECAPed alloy is nearly the same.
- Two types of the fatigue crack initiation were observed. In the cast material the cracks initiate exclusively in the cyclic slip bands. They are formed in solid solution areas with low density of  $Mg_{17}Al_{12}$  particles. In the alloy processed by ECAP identical mechanism operates, however due to small grain size the lengths of slip bands in which cracks develop is substantially smaller. Besides initiation in slip bands grain boundary cracking was observed in ECAPed alloy.

## Acknowledgments

The Czech Science Foundation under the contract 108/10/2001 and Ministry of Education of the Czech Republic under the project CZ.1.07/2.3.00/30.0039 supported this work.

## References

- [1] Altwicker H et al 1939 *Magnesium und seine Legierungen* (Berlin: J. Springer Verlag)
- [2] Němcová A et al 2009 *Mat. Eng.* **16** (4) pp 5-10
- [3] Bukovina M, Škorík V, Hadzima B *Proc. TRANSCOM 2009* (University of Žilina) pp 37-42.
- [4] Eisenmeier G 2001 *Mat. Sci. and Eng. A* **319-321** pp 578-582
- [5] Chung C W et al 2010 *J. Phys.: Conf. Ser.* **241** 012101
- [6] Ebel-Wolf B, Walther F, Eifler D 2008 *Mat. Sci. and Eng. A* **486** pp 634-640
- [7] Yamashita A, Horita Z, Langdon T G 2001 *Mater. Sci. and Eng. A* **300** pp 142-147
- [8] Chung C W et al 2009 *IOP Conf. Series: Mat. Sci. and Eng.* **4** doi:10.1088/1757-899X/4/1/012012
- [9] Chen B et al 2008 *Mat. Sci. Eng. A* **483-484** pp 113-116
- [10] Chung Ch S, Chun D K, Kim H K 2005 *J. of Mech. Sci. and Technol.* **7** pp 1441-1448
- [11] Kim H K, Lee Y I, Chung Ch S 2005 *Scripta Mater.* **52** pp 473-477
- [12] Zúberová Z et al 2007 *Met. Mat. Trans.* **38A** pp 1934-1940
- [13] Chen B et al 2008 *Mat. Sci. and Eng. A* **483-484** pp 113-116
- [14] Wolf B, Fleck C, Eifler D 2004 *Int. J. Fat* **26** pp 1357-1363
- [15] Chen B et al 2008 *Mat. Sci. and Eng. A* **483-484** pp 113-116
- [16] *Fatigue and Fracture* 1996 ASTM Handbook vol.19 (ASTM Int. Materials Park, OH., U.S.A.) p.875.

- IV. [28] S. Fintova, L. Pantelejev, L. Kunz, Microstructure and Mechanical Properties of Ultrafine-Grained Magnesium AZ91 Alloy, *Metallography* Xv, 782 (2014) 384-389.

## Microstructure and Mechanical Properties of Ultrafine-Grained Magnesium AZ91 Alloy

Stanislava Fintová<sup>1, a</sup>, Libor Pantělejev<sup>2, b</sup> and Ludvík Kunz<sup>1, c</sup>

<sup>1</sup>Institute of Physics of Materials, AS CR Brno, Czech Republic

<sup>2</sup>Brno University of Technology, Brno, Czech Republic

<sup>a</sup>fintova@ipm.cz, <sup>b</sup>pantelejev@fme.vutbr.cz, <sup>c</sup>kunz@ipm.cz

**Keywords:** AZ91, ECAP, microstructure, mechanical properties, cyclic plastic deformation, fatigue crack initiation

**Abstract.** Microstructure, mechanical properties, cyclic plastic deformation behavior and fatigue strength of ultrafine-grained (UFG) magnesium alloy AZ91 processed by equal channel angular pressing (ECAP) were investigated. ECAP of originally cast alloy results in development of bimodal structure, improved yield stress, tensile strength and ductility when compared to the as-cast state. Endurance limit based on  $10^7$  cycles is also improved, however exhibits large scatter. Initiation of fatigue cracks takes place in regions of large grains in the bimodal structure, where the content of  $Mg_{17}Al_{12}$  particles is low.

### Introduction

The AZ91 alloy is the most widely used magnesium alloy exhibiting a good combination of tensile strength at room temperature, castability, weldability under controlled atmosphere and favorable cost [1, 2]. The disadvantage of this alloy is its poor formability and low ductility, which is a consequence of its hexagonal close-packed (hcp) crystal structure and high volume of precipitates.

Grain refinement has been known since many years as a way to improve tensile strength of metals and alloys, including ductility. Since the last two decades methods of severe plastic deformation (SPD) for grain size refinement has been intensively developed, e.g. [2]. SPD methods combined with thermomechanical processing were applied also to the AZ91 alloy, e.g. [1]. The majority of studies on AZ91 alloy deal with the influence of SPD on microstructure and related basic mechanical properties, i.e. yield stress, tensile strength and ductility [5-7]. The investigation was focused on the structure changes from the dendritic to the fine-grained one and on the  $Mg_{17}Al_{12}$  particle refinement, morphology and distribution. It has been shown that the grain size and the size of intermetallic phases and their distribution are strongly dependent on the ECAP process parameters, primarily on the number of passes through the ECAP die. After low number of passes, the obtained structure is not fully homogenous. Areas with larger grains and areas with smaller grains coexist in the structure; with increasing number of passes the homogeneity increases. After low number of passes also large unchanged  $Mg_{17}Al_{12}$  particles remain in the structure.

As regards the tensile strength and ductility the investigations bring clear evidence of pronounced improvement provided that the UFG structure is homogenous. The grain boundary strengthening and the presence of fine  $Mg_{17}Al_{12}$  particles are considered to be the main strengthening mechanisms.

The knowledge on the fatigue properties of UFG Mg alloys and the mechanism of crack initiation is rather poor. While the enhancement of tensile properties of light alloys produced by SPD is appreciable, the improvement of fatigue strength is often weaker [7].

The aim of this paper is to present the results of an investigation of microstructure of cast AZ91 alloy after ECAP and its mechanical properties, as well as, the cyclic stress-strain response and fatigue strength. The attention was paid to the relation of the observed UFG microstructure and fatigue crack initiation.



## Experimental material

The cast AZ91 magnesium alloy was processed by ECAP. The SPD was performed at temperature of 300 °C. The intersecting angle of the die channels was 120°. The billets were subjected to 6 passes by the route Bc through the ECAP die. Cylindrical rods of 80 mm length and 15 mm in diameter as semiproducts for preparation of specimens were machined from the ECAPed billets. Chemical composition of material is given in Table 1.

Table 1 Chemical composition of AZ91

elements	Al	Zn	Mn	Si	Fe	Be	Ni	Cu	Mg
wt. %	8.7	0.65	0.25	0.006	0.003	0.0008	0.0006	0.0005	rest

## Experiments

Both the light microscopy (LM) and the scanning electron microscopy (SEM) were applied to reveal the AZ91 microstructure. The specimens were mechanically ground (SiC papers), polished (diamante suspension) and etched by 2% Nital etchant.

Tensile tests were performed on cylindrical specimens with the gauge length of 30 mm and the gauge length diameter of 6 mm. The tests were performed on the testing machine ZWICK Z020. Three specimens in as-cast state and three specimens in SPD state were used for the determination of tensile properties.

Vickers hardness (HV 0.5) was measured on specimens prepared either from the radial sections of as-cast and ECAPed billets and on radial sections of the gauge length of specimens tested for high-cycle fatigue.

Fatigue tests were conducted on cylindrical specimens with geometry shown in Fig. 1. The specimen gauge length was carefully ground (SiC papers no. 800, 1200 and 2500) and subsequently polished (diamond paste, 1  $\mu$ m) to get the smooth surface for the following observation on SEM with the aim to identify early fatigue cracks.

Two fatigue testing machines were used. Experiments were started at the servohydraulic testing machine Shimadzu EHF. During the first

50 cycles the test frequency was 0.1 Hz. Then it was increased to 1 Hz until 100 cycles were reached. After 500 cycles the test frequency was increased to 5 Hz. After elapsed 3000 cycles the frequency was increased to 10 Hz. At the pre-defined number of cycles the hysteresis loops were recorded; for this purpose the loading frequency was decreased during recording to 0.1 Hz. When the specimen lifetime exceeded  $1 \times 10^6$  cycles, the loading was continued on a resonant fatigue machine Amsler HFP510 with loading frequency of 60 Hz. Tests were conducted under controlled load with the stress ratio  $R = -1$  at room temperature in laboratory air.

## Results

The applied ECAP treatment resulted in a formation of macroscopically inhomogeneous microstructure. The microstructure can be characterized as composed from fine-grained areas with small particles of intermetallic phases  $Mg_{17}Al_{12}$  and intermetallic phases on AlMn basis (Fig. 2a). The small  $Mg_{17}Al_{12}$  particles are localized both within the grains and on the grain boundaries. The average grain size in fine-grained areas is of about 3.5  $\mu$ m. Except of fine-grained areas, clusters of larger grains with small  $Mg_{17}Al_{12}$  particles predominantly on grain boundaries can be observed, Fig. 2 a, b. The average density of  $Mg_{17}Al_{12}$  particles in clusters of large grains is substantially lower

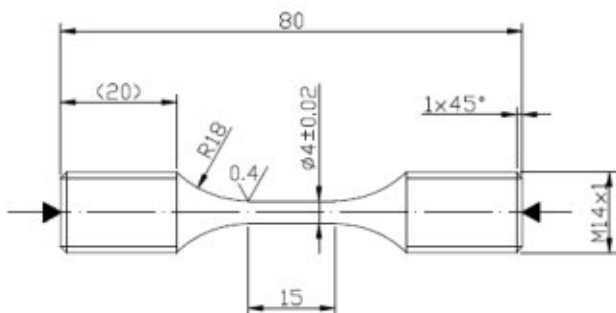
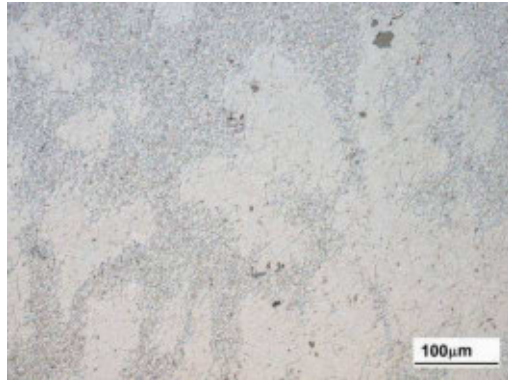
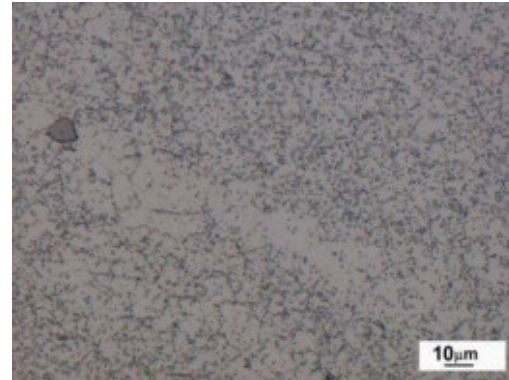


Fig. 1 Geometry of specimen for fatigue tests

than in the fine-grained regions. From the macroscopic point of view the microstructure after ECAP can be characterized as bimodal. The size of the larger grains is slightly dependent on their position in clusters. The grains located close to the cluster boundary are larger than the grains in the centre of clusters. The size of larger grains in clusters varies from 10 to 15  $\mu\text{m}$ . The bimodal microstructure as observed by means of SEM is shown in Fig. 3.

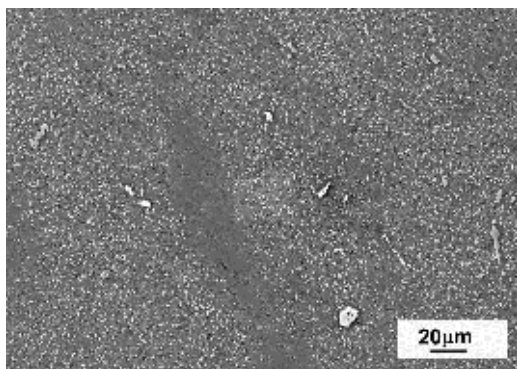


a) bimodal microstructure after ECAP

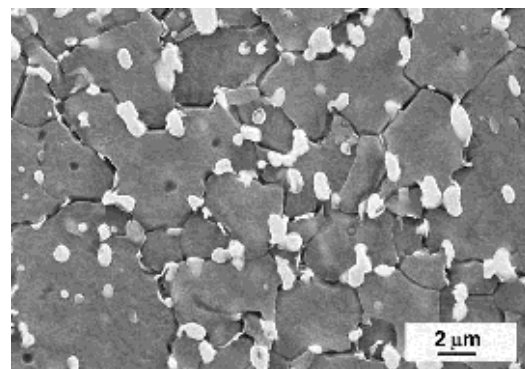


b) detail of bimodal microstructure, precipitates distribution

Fig. 2 Microstructure of AZ91, LM, etch. Nital



a) non-uniform distribution of  $\text{Mg}_{17}\text{Al}_{12}$  particles



b)  $\text{Mg}_{17}\text{Al}_{12}$  precipitates on the grain boundaries in the fine-grained areas

Fig. 3 Microstructure of AZ91 after ECAP, SEM, etch. Nital

The hardness of ECAPed alloy was determined both in the clusters of large grains and also in fine-grained areas with high density of  $\text{Mg}_{17}\text{Al}_{12}$  particles. The results show that the hardness differs only in the frame of the experimental scatter. The hardness of ECAPed material measured before fatigue testing was  $71 \pm 9 \text{ HV } 0.5$  and  $78 \pm 8 \text{ HV } 0.5$  after fatigue testing (measured on specimens broken during testing at applied stress amplitudes). Determined hardness is only slightly higher than the values found for as-cast state:  $64 \pm 7 \text{ HV } 0.5$ .

The stress-strain diagrams obtained from tensile tests of ECAPed specimens are shown in Fig. 4. The tensile strength determined on three specimens is  $R_m = 321 \pm 21 \text{ MPa}$ , the yield stress  $R_{p0.2} = 160 \pm 4 \text{ MPa}$  and the ductility  $5.4 \pm 4.7 \%$ . For comparison Fig. 4 shows also stress-strain diagrams for as-cast state, having  $R_m = 167 \pm 8 \text{ MPa}$ ,  $R_{p0.2} = 87 \pm 8 \text{ MPa}$  and ductility  $3.1 \pm 0.4 \%$ .

The UFG AZ91 softens under stress control at the beginning of the test, Fig. 5. After the maximum of the plastic strain amplitude  $\epsilon_{ap}$  is reached (nearly for  $10^3$  cycles, see Fig. 5) continuous cyclic hardening takes place. The plastic strain amplitude decreases below  $10^{-5}$ . Contrary to this the material in as-cast state cycled at the same stress amplitudes exhibits continuous hardening since the beginning of the tests and substantially larger extent of cyclic plasticity.

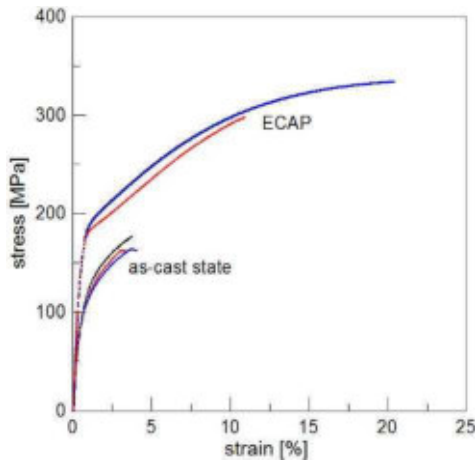


Fig. 4 Stress-strain diagrams for ECAPed and as-cast material

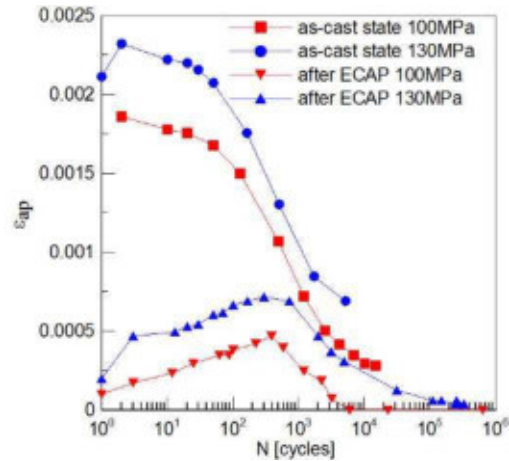


Fig. 5 Cyclic deformation curves for ECAPed and as-cast material

The S-N data of UFG AZ91 can be seen in Fig. 6. The data exhibit a significant scatter, particularly in the high-cycle region. There are run-out specimens in the interval of the stress amplitudes 90 to 130 MPa and simultaneously failed specimens with the lifetime of the order of  $10^4$  cycles can be found in this interval.

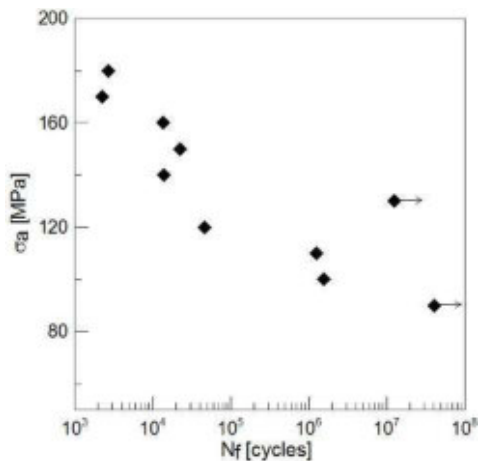


Fig. 6 S-N curve of UFG AZ91 alloy

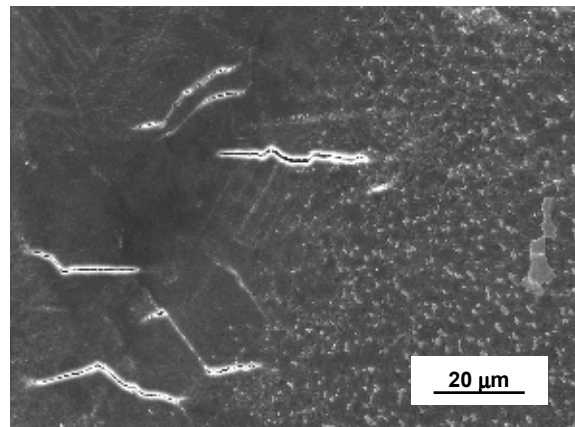


Fig. 7 Cracks initiated in clusters of large grains

Fatigue cracks were found to initiate on tested specimens surface in regions with larger grains, where the density of  $Mg_{17}Al_{12}$  particles is low and where the long slip bands forms. This behavior illustrates Fig. 7.

## Discussion

The mechanical properties of UFG materials prepared by ECAP are strongly influenced by the details of the SPD process. The microstructure of AZ91 depends on the number of ECAP passes and also on the initial size and morphology of  $Mg_{17}Al_{12}$  precipitates. Chen et al. [7] reported homogeneously refined grains after two ECAP passes of originally hot-rolled AZ91. The tensile strength was increased markedly to 417 MPa. This value is higher than that determined in the present work for originally as-cast AZ91 alloy processed by six ECAP passes. The grain size in the paper by Chen et al. [7] was  $2\ \mu m$  and the structure was homogeneous. Contrary to this the microstructure of the cast alloy subsequently processed by SPD is bimodal, consisting of fine-grained areas with the average grain size  $3.5\ \mu m$ , which resembles to the structure described in [7]. Also the distribution and size of the precipitates is very similar. In the as-cast material processed by ECAP there are except of fine-grained areas also clusters of larger grains with low density of

precipitates. It can be assumed that just in these areas the plastic deformation is easier and they can bear the substantial part of the plastic deformation. The fine-grained regions are more resistant to deformation. This explains both the lower tensile strength and higher ductility of bimodal UFG microstructure when compared to the fully homogeneous microstructure observed after ECAP of the hot-rolled alloy [7].

The Vickers hardness was found to be increased only moderately by ECAP, namely from  $64 \pm 7$  HV 0.5 for as-cast state to  $71 \pm 9$  HV 0.5 for ECAPed state. The scatterbands are overlapping. It is interesting to mention that the hardness of the UFG material was the same in the both components of bimodal structure. No difference in hardness was found between the fine-grained areas and larger grain clusters with lower content of precipitates. The observed weak increase of hardness caused by ECAP is in agreement with the finding of Chung et al. [9]. They report an inverse proportion of hardness of AZ31 and AZ61 to the grain size.

The initiation of fatigue cracks in conventionally grained Mg alloys takes place in preferably oriented grains. The mechanism is often quasicleavage, which is characteristic for hcp structures. In the AZ91D fatigue cracks initiate in Al-poor  $\alpha$  phase in slip bands, or on the boundaries between  $\alpha$  phase and  $Mg_{17}Al_{12}$  precipitates or by cracking of large  $Mg_{17}Al_{12}$  precipitates, [9]. The initiation was observed both on the surface and on the pores. In UFG AZ91 alloy investigated in this study the crack initiation took place only on the surface, which was obvious from fractography of failed specimens. Cracks originated in the large grained areas of the bimodal structure where the density of precipitates is low. It means that just these areas and their fatigue resistance govern the fatigue strength. The characteristic features of crack initiation resemble to the mechanism known for conventional AZ91 alloy. At higher stress amplitudes multiple crack initiation was observed, Fig. 7. The cracks, which initiated along the straight slip lines, later on tend to propagate by the opening mode macroscopically perpendicularly to the principal stress. Occasionally also cracks in larger precipitates which remained from the original as-cast structure unchanged by ECAP process were observed. However, these cracks did not further propagate.

The endurance limit based on  $2 \times 10^6$  cycles equal 55 MPa was determined by Wolf et al. [9] for cast AZ91D alloy. Similarly, Gu et al. [10] found value of 50 MPa for  $10^7$  cycles. Murugan et al. [11] determined by means of a high frequency shaker the endurance limit  $45 \pm 10$  MPa for  $10^7$  cycles. From the summary of these data it follows that the average value of the endurance limit of as-cast alloy is of about 50 MPa. This value is lower than the fatigue strength of AZ91 after ECAP determined in this study. It is well below the scatterband of S-N data in high-cycle region, Fig. 6. The lowest stress amplitude at which a fatigue failure was observed was 100 MPa. From the comparison it can be concluded, that the applied ECAP procedure improves both the basic mechanical properties and also the endurance limit of AZ91 alloy in the same extent.

## Conclusions

1. Cast AZ91 magnesium alloy processed by six ECAP passes at 300 °C exhibits bimodal microstructure consisting of clusters of larger grains with  $Mg_{17}Al_{12}$  particles predominantly on the grain boundaries and areas of smaller grains with  $Mg_{17}Al_{12}$  both at the grain boundaries and also within the grains. The particle density in small-grained areas is substantially higher than in the clusters of larger grains.
2. The ECAP increases the tensile strength by the factor of two from  $167 \pm 8$  MPa for as-cast state to  $321 \pm 21$  MPa for ECAPed state. The ductility increased from  $3.1 \pm 0.4$  % to  $15.4 \pm 4.7$  %. The Vickers hardness (HV 0.5) increases only moderately.
3. The as-cast alloy exhibits continuous cyclic hardening, whereas the material after ECAP exhibits quite expressive cyclic softening followed by hardening.
4. Fatigue limit based on  $10^7$  cycles is  $110 \pm 20$  MPa and is by a factor of 2 higher than the values published in literature for as-cast alloy. However the high-cycle S-N data of UFG structure exhibit significant scatter. The initiation of fatigue cracks takes place in the regions of large grains in the bimodal structure, where the content of  $Mg_{17}Al_{12}$  particles is low.

## Acknowledgement

The Czech Science Foundation under contract 108/10/2001 financially supported this work. The support is gratefully acknowledged. This work has been also supported by the specific research project no. FSI-S-11-14 (ID no. 22172) and the European Regional Development Fund in the framework of the research project NETME Centre under the Operational Program Research and Development for Innovation No. CZ.1.5/2.1.00/01.002.

## References

- [1] B.L. Mordike, T. Ebert, Magnesium. Properties - applications - potential. *Mat. Sci. Eng. A302* (2001) 37-45.
- [2] K.N. Braszczyńska-Malik, Precipitates of  $\gamma$ -Mg<sub>17</sub>Al<sub>12</sub> Phase in AZ91 Alloy, in: [http://cdn.intechopen.com/pdfs/12741/InTech-Precipitates\\_of\\_gamma\\_mg17al12\\_phase\\_in\\_mg\\_al\\_alloys.pdf](http://cdn.intechopen.com/pdfs/12741/InTech-Precipitates_of_gamma_mg17al12_phase_in_mg_al_alloys.pdf)
- [3] R.Z. Valiev, R.K. Islamgaliev, I.V. Alexandrov, Bulk nanostructured materials from severe plastic deformation, *Progress in Materials Science*. 45 (2000) 103-189.
- [4] C.W. Chung, R.G. Ding, Y.L. Chiu, W. Gao, Effect of ECAP on microstructure and mechanical properties of cast AZ 91 magnesium alloy, *J. Phys.: Conf. Ser.* 241 (2010) 1-4.
- [5] J. Gubicza, K. Máthis, Z. Hegedűs, G. Ribárik, A.L. Tóth, Inhomogeneous evolution of microstructure in AZ91 Mg-alloy during high temperature equal-channel angular pressing, *J. Alloys Comp.* 492 (2010) 166-172.
- [6] K. Máthis, J. Gubicza, N.H. Nam, Microstructure and mechanical behavior of AZ91 Mg alloy processed by equal channel angular pressing, *J. Alloy Comp.* 394 (2005) 194-199.
- [7] B. Chen, D.-L. Lin, L. Jin, X.-Q. Zeng, Ch. Lu, Equal-channel angular pressing of magnesium alloy AZ91 and its effect on microstructure and mechanical properties, *Mat. Sci. Eng. A*. 483-484 (2008) 113-116.
- [8] Y. Estrin, A. Vinogradov: Fatigue behaviour of light alloys with ultrafine grain structure produced by severe plastic deformation: An overview. *International Journal of Fatigue* 32 (2010) 898-907.
- [9] C.S. Chung, D. K. Chun, H.K. Kim: Fatigue properties of fine grained magnesium alloys after severe plastic deformation. *J of Mech. Sci. and Technol.* 19 (2005) 1441-1448.
- [10] B. Wolf, C. Fleck, D. Eifler, Characterization of the fatigue behaviour of the magnesium alloy AZ91D by means of mechanical hysteresis and temperature measurement, *Int. J. Fat.* 26 (2004) 1357-1363.
- [11] X.N. Gu, W.R. Zhou, Y.F. Zheng, Y. Cheng, S.C. Wei, S.P. Zhong, T.F. Xi, L.J. Chen: Corrosion fatigue behaviors of two biomedical Mg alloys-AZ91D and WE43-in simulated body fluid. *Acta Biomaterialia* 6 (2010) 4605-4613.
- [12] G. Murugan, K. Raghukandan, U.T.S. Pillai, B.C. Pai, K. Mahadevan: High cyclic fatigue characteristics of gravity cast AZ91 magnesium alloy subjected to transverse load. *Materials and Design* 30 (2009) 2636-2641.

## **Metallography XV**

10.4028/www.scientific.net/MSF.782

## **Microstructure and Mechanical Properties of Ultrafine-Grained Magnesium AZ91 Alloy**

10.4028/www.scientific.net/MSF.782.384

### **DOI References**

[3] R.Z. Valiev, R.K. Islamgaliev, I.V. Alexandrov, Bulk nanostructured materials from severe plastic deformation, *Progress in Materials Science*. 45 (2000) 103-189.

[http://dx.doi.org/10.1016/S0079-6425\(99\)00007-9](http://dx.doi.org/10.1016/S0079-6425(99)00007-9)

[4] C.W. Chung, R.G. Ding, Y.L. Chiu, W. Gao, Effect of ECAP on microstructure and mechanical properties of cast AZ 91 magnesium alloy, *J. Phys.: Conf. Ser.* 241 (2010) 1-4.

<http://dx.doi.org/10.1088/1742-6596/241/1/012101>

[5] J. Gubicza, K. Máthis, Z. Hegedűs, G. Ribárik, A.L. Tóth, Inhomogeneous evolution of microstructure in AZ91 Mg-alloy during high temperature equal-channel angular pressing, *J. Alloys Comp.* 492 (2010) 166-172.

<http://dx.doi.org/10.1016/j.jallcom.2009.11.150>

[6] K. Máthis, J. Gubicza, N.H. Nam, Microstructure and mechanical behavior of AZ91 Mg alloy processed by equal channel angular pressing, *J. Alloy Comp.* 394 (2005) 194-199.

<http://dx.doi.org/10.1016/j.jallcom.2004.10.050>

[7] B. Chen, D. -L. Lin, L. Jin, X. -Q. Zeng, Ch. Lu, Equal-channel angular pressing of magnesium alloy AZ91 and its effect on microstructure and mechanical properties, *Mat. Sci. Eng. A.* 483-484 (2008) 113-116.

<http://dx.doi.org/10.1016/j.msea.2006.10.199>

[10] B. Wolf, C. Fleck, D. Eifler, Characterization of the fatigue behaviour of the magnesium alloy AZ91D by means of mechanical hysteresis and temperature measurement, *Int. J. Fat.* 26 (2004) 1357-1363.

<http://dx.doi.org/10.1016/j.ijfatigue.2004.04.005>



- V. [29] L. Kunz, S. Fintova, Fatigue behaviour of AZ91 magnesium alloy in as-cast and severe plastic deformed conditions, 11th International Fatigue Congress, Pts 1 and 2, 891-892 (2014) 397-402.

## Fatigue behaviour of AZ91 magnesium alloy in as-cast and severe plastic deformed conditions

Ludvík Kunz<sup>1, a\*</sup> and Stanislava Fintová<sup>1, 2, b</sup>

<sup>1</sup>Institute of Physics of Materials, AS CR, Žižkova 22, 616 62 Brno, Czech Republic

<sup>2</sup>CEITEC – Central European Institute of Technology, Brno University of Technology, Technická 3058/10, 61600 Brno, Czech Republic

<sup>a</sup>kunz@ipm.cz, <sup>b</sup>fintova@ipm.cz; \* corresponding author

**Keywords:** AZ91, ECAP, microstructure, mechanical properties, cyclic plastic deformation, fatigue crack initiation

**Abstract.** Fatigue strength, crack initiation and microstructure were experimentally investigated in an as-cast AZ91 alloy and in ultrafine-grained (UFG) AZ91 alloy processed by equal channel angular pressing (ECAP). The microstructure after ECAP is bimodal, consisting of fine-grained regions and clusters of larger grains with lower density of intermetallic particles. It has been found that the ECAP substantially increases the tensile strength (factor of two), improves ductility (factor of five) and improves the fatigue strength in low-cycle fatigue region. The improvement of the endurance limit based on  $10^7$  cycles is weak.

The cyclic slip bands, as sites of the fatigue crack initiation on material surface, were investigated. Focussed ion beam technique (FIB) was applied to reveal the surface relief and the microstructure in the vicinity of early fatigue cracks. No grain coarsening was observed in the close vicinity of the initiated cracks. Fatigue cracks in ultrafine-grained structure develop both in the regions of larger grains and also in the fine grained areas. Two types of crack initiation were observed.

### Introduction

Fatigue behaviour of UFG materials prepared by severe plastic deformation (SPD) attracts the interest of researchers since two decades. It has been shown that the improved ultimate tensile strength and ductility of UFG materials when compared to their conventionally grained (CG) counterparts does not mean by itself that the fatigue strength is also improved. It depends on material, parameters and technical details of the SPD method and even on the type of the cyclic loading. UFG materials are in a non-equilibrium state and are prone to the dynamic grain coarsening during the cyclic loading. This influences the fatigue crack initiation and subsequently the fatigue strength.

Magnesium alloys were intensively developed and studied in the forties of the last century [1]. The marked concern of researchers about them appears again since the last twenty years. The main driving forces are automotive industry and the requirements of market to manufacture cheap light-duty components. The basic advantages of Mg alloys are low density and high specific strength. A particular role within the broad spectrum of Mg alloys plays the AZ91. It is a die-cast alloy, which covers the majority of applications [2].

The influence of SPD, particularly ECAP on the microstructure and mechanical properties of Mg alloys has been investigated with the following conclusions. Extruded or hot rolled AZ31 alloy exhibits better tensile and fatigue properties than the material sequentially processed by ECAP [3-5]. In other words, SPD seems not to be a suitable way how to improve mechanical properties of extruded Mg alloys. On the other hand, the UFG AZ61 alloy exhibits slightly longer fatigue life than its CG counterpart [3]. ECAP results in grain size refinement; however, in the case of extruded materials the yield stress may be lower after SPD. The original fibre texture of extruded AZ61 is replaced by a new texture and the result is appreciable decrease of the yield stress in spite of the

grain refinement after ECAP by the route Bc [6-7]. The texture after ECAP depends on the details of the process, particularly on the processing route. After processing by 6 passes by route A even an increase of the yield stress was observed. Jin et al. [8] observed for commercially extruded and by the route Bc at temperatures 453 and 573 K processed AZ31 alloy significant grain refinement and increase of ductility and strength. The S-N curve of AZ31B processed by ECAP strongly depends on the number of passes in low-cycle fatigue region; one and two passes result in an increase of the lifetime whereas processing by 8 passes has an opposite effect [9]. The application of back pressure has a beneficial effect. The stress-strain dependences of UFG AZ31 were found to be strongly orientation dependent (loading along or perpendicular to the pressing direction) [10].

As to the authors knowledge the data on the fatigue strength of AZ91 alloy after ECAP are not available in the open literature. There are only data documenting that ECAP effectively refines grains and the  $Mg_{17}Al_{12}$  phase and thus improves tensile strength, yield stress and ductility. Chen et al. [11] observed a remarkable increase of the yield stress to 289 MPa and the tensile strength to 417 MPa of a cast, subsequently heat treated and finally by ECAP processed AZ91 alloy. Also the elongation to rupture was higher. The microstructure after ECAP was homogeneous with a grain size of about 2  $\mu m$ . The small  $Mg_{17}Al_{12}$  precipitates were distributed mainly at the grain boundaries. The ECAP of AZ91 alloy at 543 K results in formation of small spherical precipitates. Their size in the grain interiors is smaller than in the vicinity of the grain boundaries [12].

The objectives of this study are to experimentally determine, further understand and compare the fatigue behaviour of as-cast AZ91 alloy and AZ91 alloy processed by ECAP. Particular attention is devoted to the initiation and early fatigue crack propagation.

## Material and experiments

The AZ91 alloy (chemical composition in wt. % is 8.7 Al, 0.65 Zn, 0.25 Mn, 0.006 Si, 0.003 Fe, 0.0008 Be, 0.0006 Ni, 0.2225 Cu, rest Mg) was investigated in as-cast and in UFG state after severe plastic deformation by ECAP. The ECAP was conducted at temperature 573 K. The intersecting angle of the die channels was 120°. The processing route Bc was used and six passes were applied. Cylindrical rods of 80 mm length and 15 mm in diameter were final semi-products for machining of specimens for tensile and fatigue tests.

Fatigue testing was performed under controlled load in symmetrical tension-compression. The direction of the loading of UFG material (both fatigue and tensile) coincided with the extrusion direction. The cylindrical specimens with thread heads and the gauge length of 15 mm and diameter 4 mm were used.

The surface of the specimens gauge length was carefully polished. The slip bands, fatigue crack initiation and early crack propagation were observed by means of scanning electron microscopy (SEM). Focussed ion beam (FIB) technique was applied to reveal the area and structure close to the initiation sites of fatigue cracks.

## Results

The microstructure of cast material consists of a solid solution dendrites and an eutectic consisting of solid solution and plate-like particles of intermetallic phase  $Mg_{17}Al_{12}$ . Large primary  $Mg_{17}Al_{12}$  intermetallic particles and AlMn based particles are also present in the structure, Fig. 1.

The ECAP resulted in a structure, which can be characterized as fine-grained with small spherical intermetallic particles of the  $Mg_{17}Al_{12}$  phase. However, the structure (even after six passes by ECAP) is not fully homogenous in the whole volume from the macroscopic point of view. It can be characterized as bimodal, Fig. 2. The majority of material volume consists of areas with small grains and higher density of spherical  $Mg_{17}Al_{12}$  particles. However, also areas of larger grains with lower density of the  $Mg_{17}Al_{12}$  particles can be found in the structure. An example of the transition between these two areas is shown in Fig. 3. The average grain size in the fine grained areas is  $3.3 \pm 0.5 \mu m$  whereas in the large grain areas the grain size is  $9.9 \pm 4.5 \mu m$ .

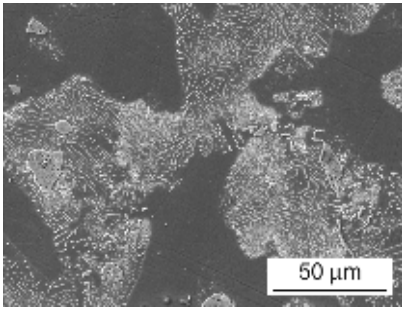


Fig. 1. Microstructure of cast AZ91 alloy.

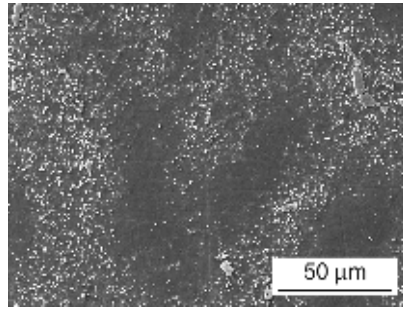


Fig. 2. Bimodal microstructure of AZ91 after ECAP.

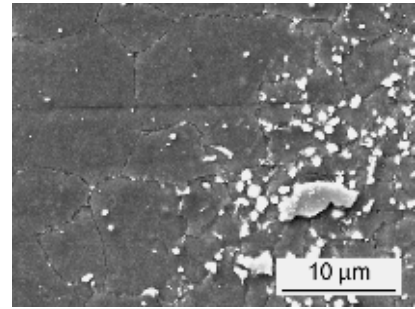


Fig. 3. Transition from fine to large grained area.

The tensile properties of the UFG material in the extrusion direction are significantly improved when compared to the original as-cast state. The tensile strength,  $\sigma_{UTS}$ , determined on three specimens increased from  $167 \pm 8$  MPa for cast alloy to  $321 \pm 21$  MPa for UFG material, the yield stress,  $\sigma_{0.2}$ , increased from  $87 \pm 8$  MPa to  $160 \pm 4$  MPa and the ductility from  $3.1 \pm 0.4$  % to  $15.4 \pm 4.7$  %.

Fig. 4 shows comparison of the fatigue life of cast and UFG alloy. The improvement of the fatigue life due to ECAP is obvious. The fatigue life of UFG specimens at stress amplitudes higher than 85 MPa is longer that of cast specimens. The shift in number of cycles to failure is nearly two orders of magnitude.

Fatigue loading of the cast material at the stress amplitudes below 80 MPa did not result in failure after  $10^7$  cycles. Arrows in Fig. 4 indicate unfailed, run-out specimens. There is a sharp knee on the S-N curve for  $10^5$  cycles. The S-N curve of UFG material decreases continuously and for  $10^7$  cycles meets the horizontal line of the S-N curve of the cast material. No fatigue failures were observed for both materials at the stress amplitudes below 80 MPa.

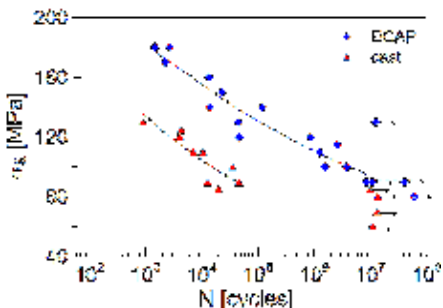


Fig. 4. Comparison of fatigue life of cast and UFG AZ91 alloy.

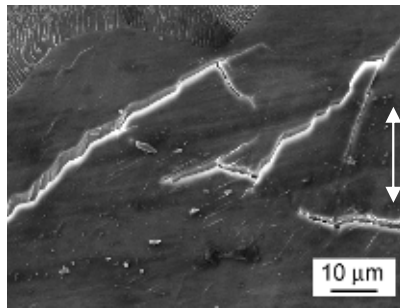


Fig. 5. Initiation of cracks in cast material.  $\sigma_a = 120$  MPa,  $N = 4 \times 10^3$  cycles.

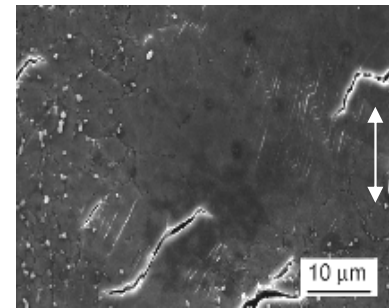


Fig. 6. Initiation of cracks in UFG material in large grained areas.  $\sigma_a = 180$  MPa,  $N = 1.5 \times 10^3$  cycles.

Fig. 5 shows a typical example of fatigue crack initiation in cast material. The arrow in the figure indicates the loading direction. Cracks initiate at long slip bands which develop in solid solution. They terminate at eutectic regions. Multiple crack initiation is characteristic for higher stress amplitudes.

Initiation of fatigue cracks in UFG material took place in both constituents of the bimodal structure. At high stress amplitudes systems of parallel cyclic slip bands develop in large grained areas. They are most often inclined at the angle of nearly 45 degree to the loading direction, Fig. 6. Fatigue cracks develop from these slip bands. The early cracks are opened and there are clear signs of material shifting along the trace of the slip band on the material surface. The cracks further tend to propagate along the plain macroscopically perpendicular to the loading axis. Similarly to the initiation in the cast alloy multiple crack initiation is a typical at high stress amplitudes. The whole

process is similar to that which takes place in the cast material, only the length of the slip bands and cracks initiated along them is substantially shorter.

Initiation of fatigue cracks was observed also in fine grained areas of the bimodal structure. The cracks initiate without apparent relation to the cyclic slip bands, Fig. 7. The cracks start often on the grain boundaries, which are in general oriented perpendicularly to the loading direction. Arrows in Fig. 8 indicate such early fatigue cracks. In the case of high stress amplitudes cracking of large primary particles was observed, however these cracks did not usually propagate into the surrounding matrix.

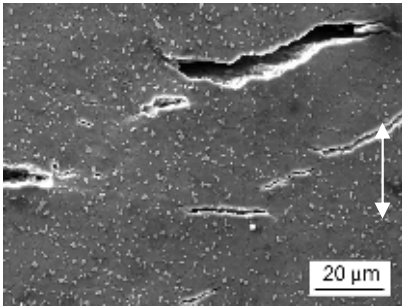


Fig. 7. Initiation of cracks in UFG material in fine grained areas.  $\sigma_a = 180$  MPa,  $N = 1.5 \times 10^3$  cycles.

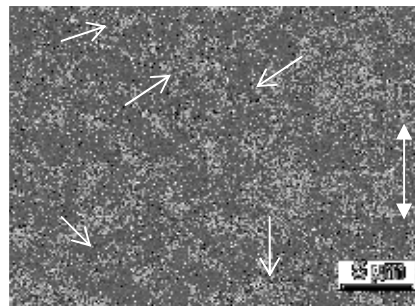


Fig. 8. Cracked grain boundaries in fine grained area.  $\sigma_a = 180$  MPa,  $N = 1.5 \times 10^3$  cycles.

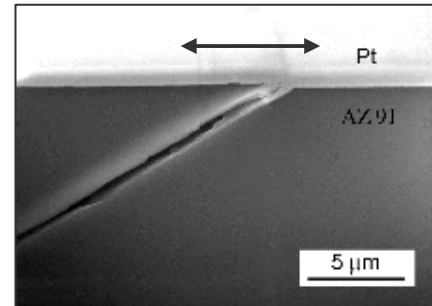


Fig. 9. FIB cut through an early crack in UFG material.

At the polished gauge length of cast specimens cycled at the stress amplitudes above the knee numerous slip bands and multiple crack initiation was observed. At the polished gauge length of the broken cast specimen cycled at the stress amplitude 85 MPa corresponding to the knee slip bands and cracks were found. On the other hand, on the unfailed specimen cycled at the same stress amplitude (for  $10^7$  cycles) no signs of the cyclic plasticity were found. In the case of UFG alloy, the number of slip bands rapidly decreases with decreasing stress amplitude. The fractographic observation confirms that at lower stress amplitudes one fatal crack was initiated at the surface and propagated through the specimen cross-section.

The section across a fatigue crack which was initiated in large grained area of the bimodal structure shows Fig. 9. The section was cut perpendicularly to the free surface by FIB. The crack is straight and inclined to the surface at an angle of nearly 30 degrees. The loading axis was parallel to the specimen surface. The surface, covered by platinum layer, is without any signs of slip activity in terms of extrusion/intrusion relief. The crack is open. A step between the both sides of the crack mouth at the specimen surface is visible. No changes of microstructure in the vicinity of the fatigue crack by means of backscatter electron image were detected.

## Discussion

Chung et al. [13] investigated the microstructure of as-cast AZ91 processed by ECAP at 593 K. Similarly to the present study they found a bimodal structure after two ECAP passes, however in their case the structure was after 6 passes homogeneous. Both the  $\sigma_{UTS}$  and the yield stress remained after the second pass nearly constant. As regards the absolute values they are of about 10% lower than values determined in this work. The reason may be the slightly higher ECAP processing temperature.

The scatter of experimental values of  $\sigma_{UTS}$ ,  $\sigma_{0.2}$  and ductility is quite low, though the microstructure was bimodal with substantially different volume ratio of both constituents in tested specimens. Consequently, the degree of bimodality seems to have no influence on the basic mechanical properties of AZ91 alloy processed by ECAP.

The fatigue strength of wrought Mg alloys AZ31 and AZ61 processed by ECAP is often slightly worse, or the improvement is only marginal. For cast AZ91 alloy processed by ECAP a considerable shift of the S-N curve of two orders of magnitude in the number of cycles to failure was found for the cyclic loading with the stress amplitudes above 90 MPa. The S-N curve of the cast AZ91 exhibits the pronounced knee at the stress amplitude 90 MPa, which corresponds to the fatigue life in the range  $10^4$  to  $10^5$  cycles. Loading at the stress amplitudes lower than 80 MPa does not result in fatigue failure before  $10^7$  cycles. This finding corresponds well to the value 80 - 90 MPa of the endurance limit of cast AZ91 alloy summarized in [1]. The S-N curve of UFG material does not exhibit the kink, decreases continuously and meets the horizontal line of the S-N curve of the cast material in the region of lives of the order of  $10^7$ .

The experimental data for UFG material exhibit substantial scatter in the high-cycle fatigue region. It follows from Fig. 4 that in the stress amplitude interval ranging from 90 to 130 MPa there are some run-out specimens and also failed specimens. For more precise determination and comparison of the endurance limits of cast and UFG AZ91 the time consuming experimental determination by the stair-case method would be necessary.

Limited deformability of hexagonal-close packed structure governs the cracking of Mg alloys. The vacuum die-cast AZ91 under tensile tests fails by brittle fracture with little deformation [14] and the fracture mode is of cleavage nature. The cleavage takes place usually along the (0001) crystallographic planes. The interface of Mg and  $Mg_{17}Al_{12}$  often acts as crack initiation source. Eisenmeier et al. [15] observed initiation of fatigue cracks in vacuum die-cast AZ91 of high purity (in low-cycle region) at cavities at or beneath the surface. Multiple crack initiation and coalescence of early cracks were identified as a damage mechanism. The observation performed in this work on cast material confirms the cleavage mechanism of cracking along the slip bands. However, contrary to the results published in [15] no influence of cavities or other defect on the crack initiation was found. The initiation along the slip bands was decisive damage mechanism.

The crack initiation in UFG AZ91 in large grained areas is similar to that observed in the cast alloy. The slip bands are the most frequent sites of the crack initiation. The early cracks are straight and their appearance indicates that the mechanism of their origin is cleavage. The only difference to the cast material consists in the length of the slip bands, which is related to the grain size. In the cast material the slip bands are substantially longer. FIB section through the crack, Fig. 9, does not reveal any surface relief. No extrusions in the neighborhood of the crack are visible. On the other hand, a clear step is on the specimen surface. This indicates that the cleavage is the most probable damage mechanism resulting in initiation of cracks in large grained areas. The initiation of cracks in the fine grained areas is not related to the development of slip bands and their cracking. Cracks develop on the grain boundaries.

The observed two different mechanisms of the crack initiation can explain the difference in the shape of S-N curves. The knee on the curve of cast material can be explained by the fact, that the endurance limit is the lowest stress amplitude which can result in development and cracking of slip bands in the areas of solid solution. The absence of the knee on the S-N curve of the UFG material can be explained by the fact that after extinction of slip band formation at the low stress amplitudes, initiation of cracks on grain boundaries starts to be responsible for the fatigue strength.

## Conclusions

ECAP of cast AZ91 alloy by 6 passes by the route Bc at 573 K results in development of bimodal microstructure. Basic mechanical properties, i.e. ultimate tensile strength, yield stress and ductility are superior to those of cast alloy. The improvement of the fatigue strength is substantial in low-cycle fatigue region. The S-N curves of cast and UFG material meet in the region of the endurance limit based on  $10^7$  cycles.

Fatigue cracks initiate in both components of the bimodal microstructure. In areas of larger grains slip bands are sites of the crack initiation. The mechanism is similar to that reported for CG



Mg alloys and is of a cleavage type. In the fine grained structure, crack initiation at the grain boundaries is decisive and determines the fatigue strength.

### Acknowledgement

The Czech Science Foundation under the contract 108/10/2001 and Ministry of Education of the Czech Republic under the project CZ.1.07/2.3.00/30.0039 supported this work.

### References

- [1] H. Altwicker et al., *Magnesium und seine Legierungen*, J. Springer Verlag, Berlin, 1939.
- [2] B.L. Mordike, T. Ebert, *Magnesium. Properties - applications - potential*, Mat. Sci. Eng. A302 (2001) 37-45.
- [3] Ch.S. Chung, D.K. Chun, H.K. Kim, *Fatigue properties of fine grained magnesium alloys after severe plastic deformation*, J. of Mech. Sci. and Technol. 7 (2005) 1441-1448.
- [4] H.K. Kim, Y.I. Lee, Ch. S. Chung, *Fatigue properties of fine-grained magnesium alloy produced by equal channel angular pressing*, Scripta Mater. 52 (2005) 473-477.
- [5] Z. Zúberová, L. Kunz, T.T. Lamark, Y. Estrin, M. Janeček, *Fatigue and tensile behavior of cast, hot-rolled, and severely plastically deformed AZ31 magnesium alloy*, Met. Mat. Trans. 38A (2007) 1934-1940.
- [6] W.J. Kim, C.V. An, Y.S. Kim, S.I. Hong, *Mechanical properties and microstructure of an AZ61 Mg alloy produced by equal channel angular pressing*, Scripta Mater. 42 (2002) 39-44.
- [7] W.J. Kim, S.I. Hong, Y.S. Kim, S.H. Min, H.T. Jeoung, J.D. Lee, *Texture development and its effect on mechanical properties of an AZ61 Mg alloy fabricated by equal channel angular pressing*, Acta Mater. 51 (2003) 3293-3307.
- [8] L. Jin, D. Lin, D. Mao, X. Zeng, W. Ding, *Mechanical properties and microstructure of AZ31 Mg alloy processed by two-step equal channel angular extrusion*, Mater. Letters 59 (2005) 2267-2270.
- [9] L. Wu, G.M. Stoica, H.H. Liao, S.R. Agnew, E.A. Payzant, G. Wang, D.E. Fielden, L. Chen, P. Liaw, *Fatigue property enhancement of magnesium alloy, AZ31B, through equal channel angular pressing*, Met. Mat. Trans. 38A (2007) 2283-2289.
- [10] S.R. Agnew, J.A. Horton, T.M. Lillo, D.W. Brown, *Enhanced ductility in strongly textured magnesium produced by equal channel angular processing*, Scripta Mater. 50 (2004) 337-381.
- [11] B. Chen, D.L. Lin, L. Jin, X.Q. Zeng, Ch. Lu, *Equal-channel angular pressing of magnesium alloy AZ91 and its effects on microstructure and mechanical properties*, Mat. Sci. Eng. A483-484 (2008) 113-116.
- [12] J. Gubicza, K. Máthis, Z. Hegedűs, G. Ribárik, A.L. Tóth, *Inhomogeneous evolution of microstructure in AZ91 Mg-alloy during high temperature equal-channel angular pressing*, J. of Alloys and Comp. 492 (2010) 166-172.
- [13] C.W. Chung, R.G. Ding, Y.L. Chiu, M.A. Hodgson, W. Gao, *Microstructure and mechanical properties of an as-cast AZ91 magnesium alloy processed by equal channel angular pressing*, IOP Conf. Series: Mat. Sci. and Eng. 4 (2009) 012012.
- [14] Y.Z. Lü, Q.D. Wang, W.J. Ding, X.Q. Zeng, Y.P. Zhu, *Fracture behaviour of AZ91 magnesium alloy*, Materials Letters 44 (2000) 265-268.
- [15] G. Eisenmeier, B. Holzwarth, H.W. Höppel, H. Mughrabi, *Cyclic deformation and fatigue behaviour of the magnesium alloy AZ91*, Mat. Sci. Eng. A319-321 (2001) 578-582.

## 11th International Fatigue Congress

10.4028/www.scientific.net/AMR.891-892

### Fatigue Behaviour of AZ91 Magnesium Alloy in as-Cast and Severe Plastic Deformed Conditions

10.4028/www.scientific.net/AMR.891-892.397

#### DOI References

- [2] B.L. Mordike, T. Ebert, Magnesium. Properties - applications - potential, *Mat. Sci. Eng. A302* (2001) 37-45.  
[http://dx.doi.org/10.1016/S0921-5093\(00\)01351-4](http://dx.doi.org/10.1016/S0921-5093(00)01351-4)
- [3] Ch.S. Chung, D.K. Chun, H.K. Kim, Fatigue properties of fine grained magnesium alloys after severe plastic deformation, *J. of Mech. Sci. and Technol.* 7 (2005) 1441-1448.  
<http://dx.doi.org/10.1007/BF03023903>
- [4] H.K. Kim, Y.I. Lee, Ch. S. Chung, Fatigue properties of fine-grained magnesium alloy produced by equal channel angular pressing, *Scripta Mater.* 52 (2005) 473-477.  
<http://dx.doi.org/10.1016/j.scriptamat.2004.11.007>
- [6] W.J. Kim, C.V. An, Y.S. Kim, S.I. Hong, Mechanical properties and microstructure of an AZ61 Mg alloy produced by equal channel angular pressing, *Scripta Mater.* 42 (2002) 39-44.  
[http://dx.doi.org/10.1016/S1359-6462\(02\)00094-5](http://dx.doi.org/10.1016/S1359-6462(02)00094-5)
- [7] W.J. Kim, S.I. Hong, Y.S. Kim, S.H. Min, H.T. Jeoung, J.D. Lee, Texture development and its effect on mechanical properties of an AZ61 Mg alloy fabricated by equal channel angular pressing, *Acta Mater.* 51 (2003) 3293-3307.  
[http://dx.doi.org/10.1016/S1359-6454\(03\)00161-7](http://dx.doi.org/10.1016/S1359-6454(03)00161-7)
- [8] L. Jin, D. Lin, D. Mao, X. Zeng, W. Ding, Mechanical properties and microstructure of AZ31 Mg alloy processed by two-step equal channel angular extrusion, *Mater. Letters* 59 (2005) 2267-2270.  
<http://dx.doi.org/10.1016/j.matlet.2004.09.061>
- [10] S.R. Agnew, J.A. Horton, T.M. Lillo, D.W. Brown, Enhanced ductility in strongly textured magnesium produced by equal channel angular processing, *Scripta Mater.* 50 (2004) 337-381.  
<http://dx.doi.org/10.1016/j.scriptamat.2003.10.006>
- [11] B. Chen, D.L. Lin, L. Jin, X.Q. Zeng, Ch. Lu, Equal-channel angular pressing of magnesium alloy AZ91 and its effects on microstructure and mechanical properties, *Mat. Sci. Eng. A483-484* (2008) 113-116.  
<http://dx.doi.org/10.1016/j.msea.2006.10.199>
- [12] J. Gubicza, K. Máthi, Z. Hegedűs, G. Ribárik, A.L. Tóth, Inhomogeneous evolution of microstructure in AZ91 Mg-alloy during high temperature equal-channel angular pressing, *J. of Alloys and Comp.* 492 (2010) 166-172.  
<http://dx.doi.org/10.1016/j.jallcom.2009.11.150>
- [14] Y.Z. Lü, Q.D. Wang, W.J. Ding, X.Q. Zeng, Y.P. Zhu, Fracture behaviour of AZ91 magnesium alloy, *Materials Letters* 44 (2000) 265-268.  
[http://dx.doi.org/10.1016/S0167-577X\(00\)00041-0](http://dx.doi.org/10.1016/S0167-577X(00)00041-0)
- [15] G. Eisenmeier, B. Holzwarth, H.W. Höppel, H. Mughrabi, Cyclic deformation and fatigue behaviour of the magnesium alloy AZ91, *Mat. Sci. Eng. A319-321* (2001) 578-582.  
[http://dx.doi.org/10.1016/S0921-5093\(01\)01105-4](http://dx.doi.org/10.1016/S0921-5093(01)01105-4)

- VI. [30] S. Fintová, L. Kunz, Initiation of fatigue cracks in AZ91 Mg alloy processed by ECAP, IOP Conference Series: Materials Science and Engineering, 63 (2014) 012159.

# Initiation of fatigue cracks in AZ91 Mg alloy processed by ECAP

S Fintová<sup>1</sup> and L Kunz<sup>2</sup>

<sup>1</sup> Brno University of Technology, CEITEC BUT – Central European Institute of Technology, Technická 3058/10, 616 00 Brno, CZ, e-mail: [stanislava.fintova@ceitec.vutbr.cz](mailto:stanislava.fintova@ceitec.vutbr.cz)

<sup>2</sup> Institute of Physics of Materials AS CR, Žitkova 22, 616 62 Brno, CZ, e-mail: [kunz@ipm.cz](mailto:kunz@ipm.cz)

**Abstract.** Mechanism of fatigue crack initiation was investigated in ultrafine-grained (UFG) magnesium alloy AZ91 processed by equal channel angular pressing (ECAP). Fatigue behaviour of UFG material was compared to the behaviour of material in an initial as-cast state. Focused ion beam technique (FIB) was applied to reveal the surface relief and early fatigue cracks. Two substantially different mechanisms of crack initiation were observed in UFG structure, which can be characterized as bimodal even after 6 ECAP passes by route Bc. The bimodality consists in a coexistence of very fine grained areas with higher content of Mg<sub>17</sub>Al<sub>12</sub> particles and areas exhibiting somewhat larger grains and lower density of particles. The fatigue cracks which initiate in areas of larger grains are related to the cyclic slip bands; this initiation mechanism is similar to that observed in cast alloy. The second initiation mechanism is related to the grain boundary cracking which takes place predominantly in the fine grained areas.

## 1. Introduction

Magnesium alloys are used especially because of their low weight but still good mechanical properties. Based on the chemical composition and resulting microstructure, different ratio among individual material properties can be reached [1 – 7].

Though there is a relatively extensive knowledge on relation of microstructure and mechanical properties of Mg alloys, methods of further improvement of the mechanical properties is still a discussed issue, permanently activated by engineering practice and industrial demands. One of the ways how to improve mechanical properties is application of severe plastic deformation (SPD). Equal channel angular pressing (ECAP) is one of the most studied and explored techniques. ECAP treatment performed at elevated temperatures can improve tensile properties of magnesium alloys, corrosion properties and also fatigue strength [8, 9]. On the other hand also lowering of tensile and fatigue strength were reported for wrought Mg alloys processed by ECAP [10, 11, 12]. Elevated temperatures under which the SPD is applied are necessary for activation of sufficient amount of slip systems in magnesium hcp crystallographic lattice. It has been shown that suitable heat treatment of the initial cast alloy before ECAP promotes formation of more homogenous structure and the ECAP refines than the structure more effectively. When a proper heat treatment is applied before ECAP, only 2 passes through ECAP die are sufficient to refine the structure and significantly improve the yield stress and tensile strength. Following passes through ECAP die homogenize the structure whereas the influence on mechanical properties of treated material is weak [5, 7, 8].

AZ91 magnesium alloy is one of the most often used magnesium alloys from AZ group. It contains relatively high volume of alloying elements; high volume of Al results in larger amount of Mg<sub>17</sub>Al<sub>12</sub> intermetallic particles, which can be exploited in material hardening due to the treatment by ECAP [5]. ECAP process rises the yield stress ( $\sigma_{0.2}$ ) and ultimate tensile strength ( $\sigma_{UTS}$ ) (almost 100 % improvement), and, particularly, improves the ductility (A) (almost 500 % improvement) due to the substantial grain refinement [5, 7, 13].

The AZ91 alloy is primarily intended and used for fabrication of cast components. The fatigue behaviour of AZ91 in cast state was examined in [4, 14]. It has been shown that the endurance limit is of about 80 MPa. Wolf et al. [4] studied the fatigue behavior and the



mechanism of fatigue crack initiation and growth. They reported that the initiation of fatigue cracks takes place due to localization of the cyclic plastic deformation in slip bands which are formed in solid solution areas. Fatigue cracks initiate at the surface micro-relief at in-/extrusions and on interfaces between brittle  $Mg_{17}Al_{12}$  intermetallic particles and ductile solid solution matrix. Also an  $Mg_{17}Al_{12}$  intermetallic particle cracking was observed. The authors draw also the attention to the role of pores present in the material which can be sites of fatigue crack initiation.

The studies dealing with fatigue behaviour, crack initiation and growth in ECAPed AZ91 magnesium alloy are very rare. That is why this study was focused on the experimental determination of the S-N curve, investigation of mechanisms of fatigue crack initiation in UFG AZ91 processed by ECAP and comparison with the behaviour of the as-cast state.

## 2. Material and experiments

AZ91 magnesium alloy with chemical composition given in Table 1 was investigated. Cast billets were used with no preliminary heat treatment for ECAP. The processing temperature  $300^{\circ}C$  was sufficient to perform the severe plastic deformation without cracking. Bc route was applied and the intersecting angle of the die channels was  $120^{\circ}$ . The billets were treated by 6 passes.

Table 1. Chemical composition of AZ91 magnesium alloy, wt. %.

elements	Al	Zn	Mn	Si	Fe	Be	Ni	Cu	Mg
wt. %	8.7	0.65	0.25	0.006	0.003	0.0008	0.0006	0.0005	rest

The semi-products used for machining of the fatigue specimens were cylindrical rods of 80 mm length and 15 mm in diameter. The specimen geometry is shown in Fig. 1. Gauge length of the specimens was carefully polished for the following inspection with the aim to reveal the development of slip bands and cracks. The procedure of gauge length preparation consisted of mechanical grinding (SiC papers, No. 800, 1200 and 2500) and mechanical polishing ( $1\ \mu m$  diamond paste). In some cases also electrolytic polishing or etching before the testing was applied. Due to the reaction of the chemical solutions with the surface the microstructure was visible and the relationship of the structural features and the crack initiation can be examined.

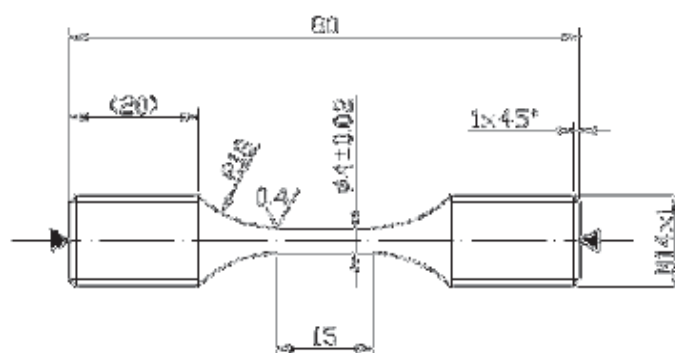


Fig. 1. Fatigue test specimen geometry.

Load controlled cycling in symmetrical tension-compression (load ratio  $R = -1$ ) was used for fatigue testing in the Shimadzu EHF-F1 servo-hydraulic system. The loading frequency was in the range 0.1 to 10 Hz in the low-cycle fatigue region. When the specimen lifetime exceeded  $1 \times 10^6$  cycles, the specimen was moved to the Amsler HFP 5100 resonant fatigue

machine and the loading was continued with a frequency of about 60 Hz. Tests were conducted at room temperature in laboratory air.

Tescan LYRA 3 XMU FEG/SEM x FIB scanning electron microscope (SEM) was used for observation and analysis of microstructure and the examination of specimen gauge length surface after fatigue tests. Focused ion beam (FIB) technique was applied to examine the characteristic features of microstructure and formation of surface relief and early cracks.

### 3. Results and discussion

#### 3.1. Structure

The structure of cast specimens consists of solid solution of alloying elements in magnesium, eutectic (solid solution of alloying elements in magnesium +  $Mg_{17}Al_{12}$  particles) and discontinuous precipitates and intermetallic particles. The solid solution consists of grains with the average grain size of  $185 \pm 70 \mu m$ . The characteristic structure of AZ91 in cast state is shown in Fig. 2a.

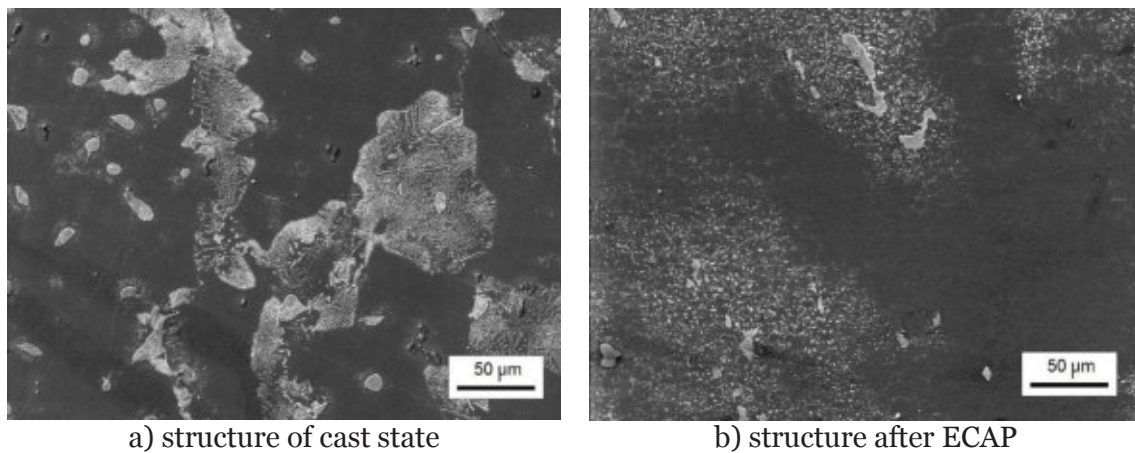


Fig. 2. Characteristic structure of AZ91 magnesium alloy, etched by Nital, SEM.

The structure of specimens treated by 6 passes of ECAP consists of grains of solid solution of alloying elements in magnesium,  $Mg_{17}Al_{12}$  intermetallic particles and AlMn based intermetallic particles. The structure can be characterized as bimodal from the macroscopic point of view. There are areas with small grains there with the average grain size of  $3.3 \pm 0.5 \mu m$  with large amount of small  $Mg_{17}Al_{12}$  particles. Besides these fine grained areas there are also areas with larger grains, with the average grain size of  $9.9 \pm 4.5 \mu m$  where the density of small  $Mg_{17}Al_{12}$  particles is markedly lower. A typical example of the bimodal structure of AZ91 after ECAP is shown in Fig. 2b. It can be seen that some amount of large primary  $Mg_{17}Al_{12}$  particles and AlMn based intermetallic particles remained in the ECAPed structure.

The observed bimodality of structure after ECAP can be explained by missing heat pretreatment of cast material before ECAP. According to the observation by Chen et al. [15] the microstructure of AZ91 magnesium alloy after ECAP looks to be strongly influenced by the structure before ECAP treatment. When the heat pretreatment is optimal, the ECAP results in creation of fine grained structure as early as after 2 passes. Following passes cause only homogenization of the structure, without any important influence on the grain size. In the case of missing heat pretreatment the structure obtained after 6 passes can remain bimodal as in the present study. Simultaneously, the tensile properties and ductility of bimodal structure are substantially improved when compared to the cast state [5, 7, 8, 13].



### 3.2. S-N curves of cast and ECAPed material

The experimentally determined S-N curves in Fig. 3 show improvement of fatigue properties of AZ91 magnesium alloy processed by ECAP treatment.

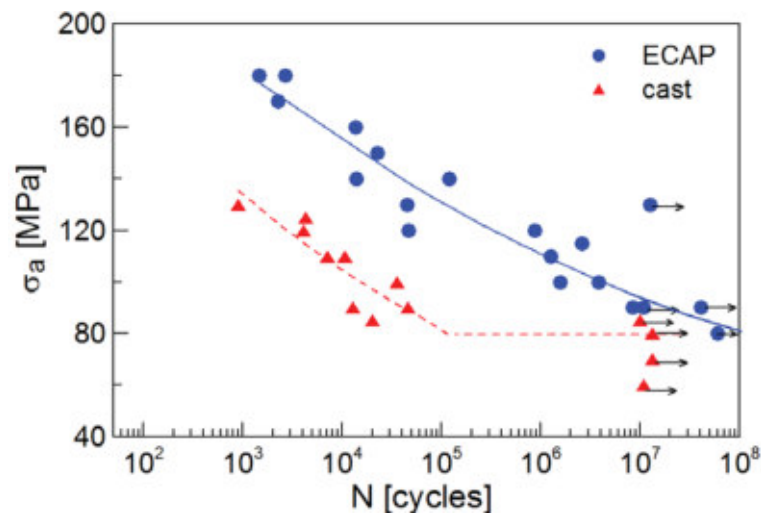


Fig. 3. Fatigue test results.

The S-N curve of cast AZ91 exhibits a typical knee. All the specimens tested at higher stress amplitudes than 80 MPa failed before they reached  $10^5$  cycles. Specimens tested at the stress amplitudes below 80 MPa exceeded  $10^7$  cycles without failure. They were considered run-outs and the corresponding points are denoted by arrows in the Fig. 3.

Specimens machined from ECAPed billets tested at same stress amplitudes as specimens manufactured from the cast material exhibit higher number of cycles to the failure. The S-N curve of ECAPed material is shifted by two orders of magnitude towards higher lifetimes in comparison with the as-cast state. The curve does not exhibit the knee in the investigated interval of the stress amplitudes and number of cycles to failure. The fatigue life continuously increases with decreasing stress amplitude and meets the horizontal part of the S-N curve of the cast material in the region of  $10^7$  to  $10^8$  cycles. The experimental results clearly indicate that the ECAP of cast AZ91 does not bring a benefit as regards the high cycle fatigue strength.

### 3.3. Crack initiation

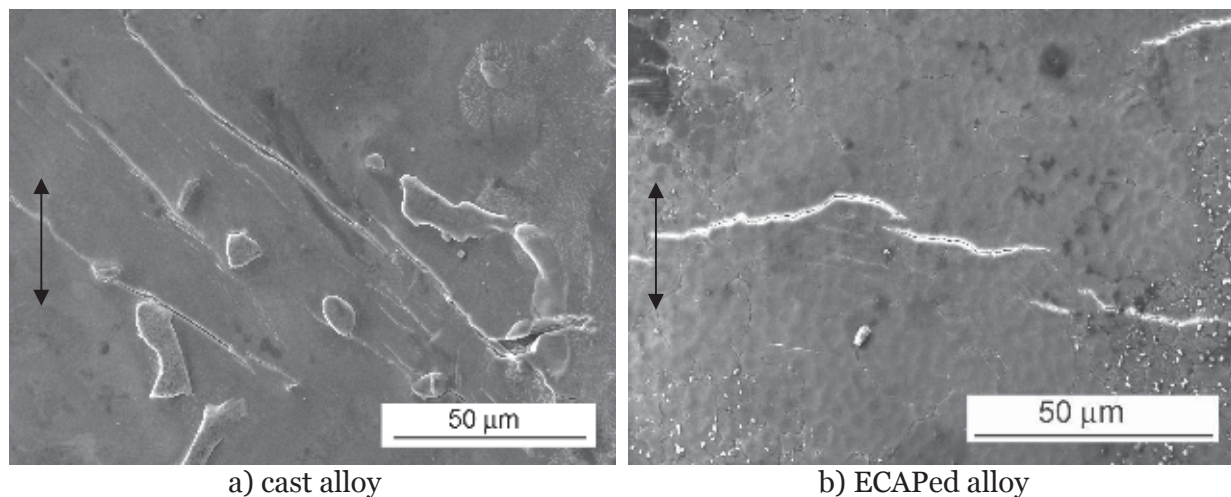
In both states of examined material the solid solution areas are the more ductile constituents where the cyclic plastic deformation takes place. The eutectic and large  $Mg_{17}Al_{12}$  and AlMn based intermetallic particles are substantially harder constituents of the structure.

In the cast material the slip band formation was observed on the specimen surface in the areas of solid solution. The length of the bands is limited by the dimension of areas of solid solution, Fig. 4a. No slip bands were observed in the eutectic. The cracks initiate on the long well developed slip bands, often inclined at the angle of  $45^\circ$  to the loading axis. The cracks develop lengthwise the slip bands and often exhibit remarkable opening. Later on the cracks tend to grow perpendicularly to the loading axis. When the brittle constituents are present in the crack trail they fail by brittle manner or the crack grows through the interface of the solid solution and the hard particle, due to concentration of stress ahead of the crack tip. These observations are in agreement with Wolf et al [14] who observed the crack initiation on slip bands formed in the solid solution areas and on structural defects which were present in their material. In the material examined in this study no internal defects related to the crack initiation were found. It was observed that with decreasing stress amplitude, the count of slip bands drops very quickly. Below 85 MPa no slip bands on the polished and etched specimen

gauge length were observed even after  $10^7$  cycles. Thus the stress amplitude 85 MPa can be considered a threshold for slip band formation in as cast structure.

In the material after ECAP the mechanism of the fatigue crack initiation in the large grain areas of the bimodal structure (grain size about  $10\ \mu\text{m}$ ) was found to be qualitatively the same as observed in the cast material. The grains formed by solid solution with low density of  $\text{Mg}_{17}\text{Al}_{12}$  particles were predominant places of slip band formation, Fig. 4b. The slip bands are, due to small grain size, much shorter than in the cast material. Also the distance between parallel slip bands in the ECAPed material is smaller. The whole process is substantially scaled down when compared to the cast state. Also the transition to the crack propagation perpendicularly to the loading axis starts much earlier, i.e. for quite short cracks developed in slip bands. This is shown in Fig. 4b, where the cracks macroscopically propagate perpendicularly to the loading axis (marked by arrows in Fig. 4b). The crack initiation in a slip band requires a definite amount of cyclic plasticity to produce the necessary material damage. This is in agreement with observations of Chung et al. [8]. It is obvious, that the crack initiation and early crack growth in a fine grained structure are more difficult than in the coarse grained case due to higher number of barriers.

Similarly to the cast state, with decreasing stress amplitude the number of slip bands rapidly decreases. The multiple crack initiation ceases quickly and single crack initiation becomes decisive. Below 120 MPa no slip bands on the polished and etched specimen gauge lengths were observed. Consequently, this stress amplitude can be considered a threshold for formation of the slip bands in the fine-grained structure. Simultaneously, the stress amplitude 130 MPa is a level, at which a run-out specimen was found, Fig. 3. Nevertheless, some specimens failed also below this stress level. This means that at least one crack had to initiate on the specimen gauge length and this crack caused the fatigue failure. Detailed inspection of the fracture surfaces of specimens which failed below 130 MPa together with observation of microstructure gave evidence that the initiation took place in the large grained area.



a) cast alloy  
b) ECAPed alloy  
Fig. 4. Slip bands and fatigue cracks on the specimen surface after fatigue loading.

Results of the examination of the surface relief and microstructure in the vicinity of early cracks by FIB are shown in Fig. 5 and 6. A set of slip bands in cast material can be seen in Fig. 5a. This set was covered by protective platinum layer for the FIB cutting and following surface relief observation. Fig. 5b documents high extrusions above the plain surface which correspond to the slip bands visible in the Fig. 5a. Intrusions are inexpressive; however material damage along the straight slip planes below them can be seen. In the case of long slip bands the well developed straight cracks along these planes are visible. The initiation of

fatigue cracks in Mg alloys is often described in literature as quasi-cleavage [16], without detailed description of the inherent mechanism. The existence of well-developed extrusions witnesses for severe concentration of the cyclic plasticity and slip activity within the slip bands. From this aspect the mechanism of crack initiation resembles that known from f.c.c. metals.

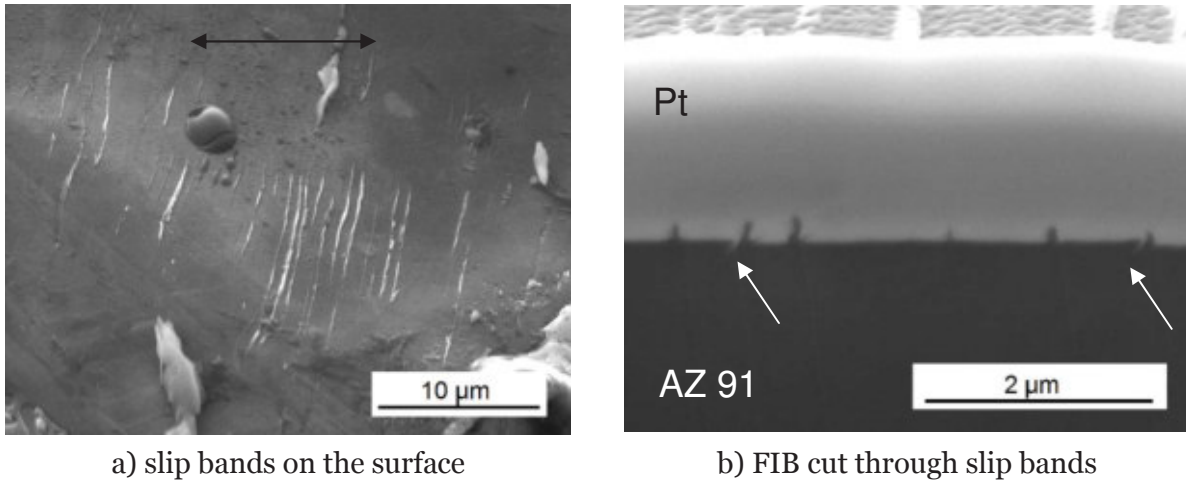


Fig. 5. Slip bands in cast alloy, specimen tested at  $\sigma_a = 120$  MPa,  $N_f = 4\ 088$  cycles.

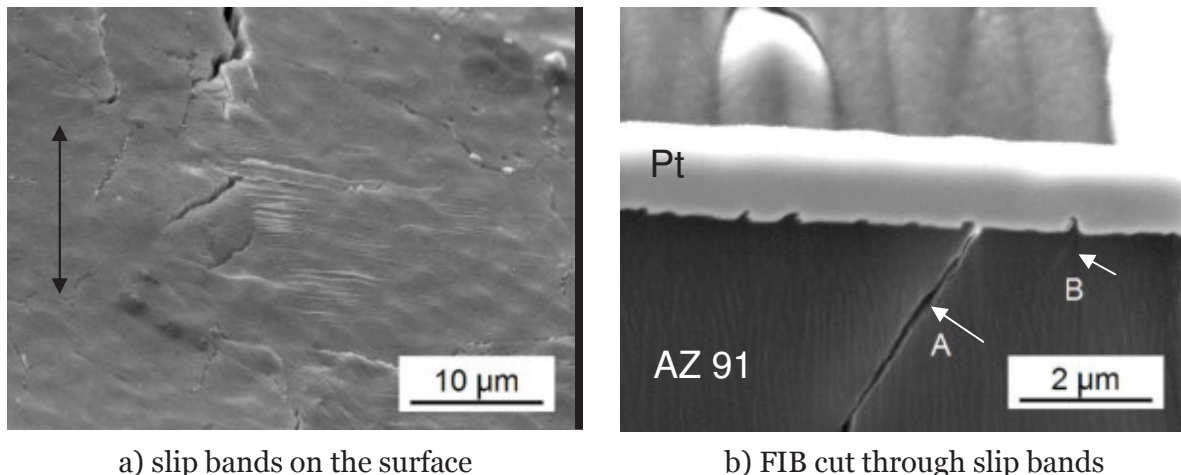


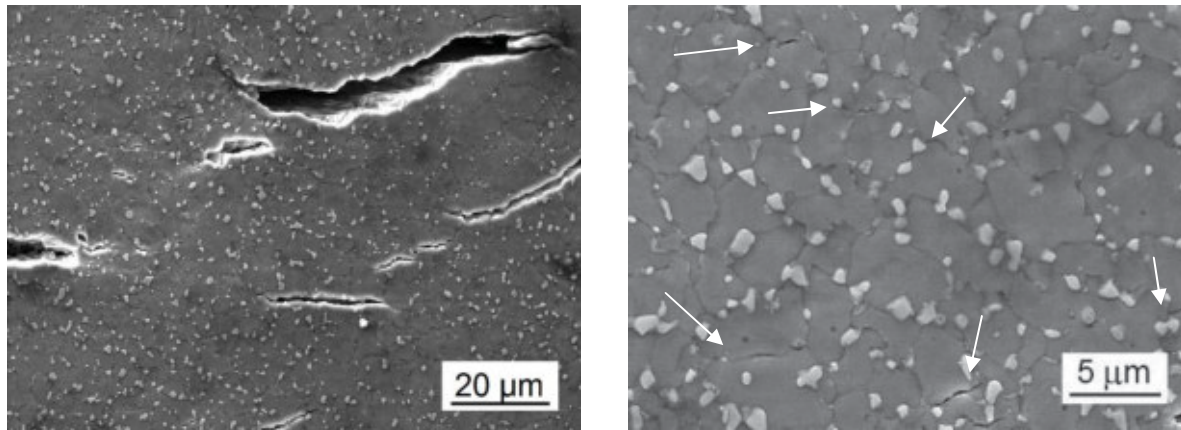
Fig. 6. Slip bands in alloy after ECAP, specimen tested at  $\sigma_a = 180$  MPa,  $N_f = 1\ 473$  cycles.

An example of the surface of large grained area of the bimodal structure after fatigue loading can be seen in Fig. 6a. The slip bands with clear extrusions appear only in suitably oriented grains, whereas neighboring grains does not exhibit any apparent slip activity in terms of slip band formation. Fig. 6b shows the FIB cut perpendicular to the surface and nearly perpendicular to the slip bands. Similarly to the cast material the extrusion profile is visible on the surface. Some of extrusions are related to cracks. The crack denoted by A is well developed, running crystallographically along the slip plane into material interior. The fracture surfaces are clearly separated and the crack runs across the whole grain. The crack denoted by B, which is also related to the extrusion on the surface is short (about 1  $\mu\text{m}$ ) and does not represent fully separated material. It is worthwhile to mention that there seems not to be any relation between the height of extrusions and the length of a related crack.

From Fig. 6a it is evident that besides the slip bands, grain boundary cracks appear in the structure. An example of this type of cracking in fine grained area is shown in Fig. 7. In the



neighbouring grains no apparent signs of cyclic plasticity in terms of slip bands can be detected. This type of crack initiation was not observed in the cast material.



a) cracks in area with small grains

b) detail of grain boundary cracks

Fig. 7. Grain boundary cracks in alloy after ECAP, specimen tested at  $\sigma_a = 180$  MPa,  $N_f = 1\,473$  cycles.

### 3.4. Fatigue life

ECAP treatment obviously improves fatigue strength in the low-cycle fatigue region. This effect is related to substantially higher  $\sigma_{UTS}$  and  $\sigma_{0.2}$  of the alloy after SPD treatment, which is connected with microstructural changes and strengthening due to the ECAP [5, 13]. However, no significant difference in the endurance limit based on  $10^7$  cycles of the cast alloy and the alloy after ECAP follows from the experimental data shown in Fig. 3. For both tested material states, similar stress amplitude can be considered as the endurance limit; 80 MPa for as-cast state and 90 MPa for ECAPed alloy. The value for cast material corresponds well with the average value of the endurance limit 80 - 90 MPa of cast AZ91 alloy based on large set of literature data [1]. Simultaneously this amplitude is the threshold amplitude for development of slip bands which are sites of initiation of fatigue cracks. In material processed by ECAP the development of slip bands which are responsible for initiation of fatigue cracks ceases when the stress amplitude decreases below 120 MPa. However, due to the existence of simultaneous crack initiation mechanism related to the grain boundary cracking the endurance limit further decreases. The number of experimental S-N points presented in Fig. 3 in the region of endurance limit is not very high. It would be worthwhile to determine experimentally the endurance limit for ECAPed material by stair case method and to evaluate statistically the scatter of data for both states of material. However, this task is beyond the range of this work.

## 4. Conclusions

- ECAP treatment improves the fatigue strength of AZ91 alloy. The S-N curve is shifted by two orders of magnitude towards higher number of cycles to failure when compared to the cast alloy. The endurance limit for  $10^7$  cycles of cast and ECAPed alloy is nearly the same.
- Two types of the fatigue crack initiation were observed. In the cast material the cracks initiate exclusively in the cyclic slip bands. They are formed in solid solution areas with low density of  $Mg_{17}Al_{12}$  particles. In the alloy processed by ECAP identical mechanism operates, however due to small grain size the lengths of slip bands in which cracks develop is substantially smaller. Besides initiation in slip bands grain boundary cracking was observed in ECAPed alloy.

## Acknowledgments

The Czech Science Foundation under the contract 108/10/2001 and Ministry of Education of the Czech Republic under the project CZ.1.07/2.3.00/30.0039 supported this work.

## References


- [1] Altwicker H et al 1939 *Magnesium und seine Legierungen* (Berlin: J. Springer Verlag)
- [2] Němcová A et al 2009 *Mat. Eng.* **16** (4) pp 5-10
- [3] Bukovina M, Škorík V, Hadzima B *Proc. TRANSCOM 2009* (University of Žilina) pp 37-42.
- [4] Eisenmeier G 2001 *Mat. Sci. and Eng. A* **319-321** pp 578-582
- [5] Chung C W et al 2010 *J. Phys.: Conf. Ser.* **241** 012101
- [6] Ebel-Wolf B, Walther F, Eifler D 2008 *Mat. Sci. and Eng. A* **486** pp 634-640
- [7] Yamashita A, Horita Z, Langdon T G 2001 *Mater. Sci. and Eng. A* **300** pp 142-147
- [8] Chung C W et al 2009 *IOP Conf. Series: Mat. Sci. and Eng.* **4** doi:10.1088/1757-899X/4/1/012012
- [9] Chen B et al 2008 *Mat. Sci. Eng. A* **483-484** pp 113-116
- [10] Chung Ch S, Chun D K, Kim H K 2005 *J. of Mech. Sci. and Technol.* **7** pp 1441-1448
- [11] Kim H K, Lee Y I, Chung Ch S 2005 *Scripta Mater.* **52** pp 473-477
- [12] Zúberová Z et al 2007 *Met. Mat. Trans.* **38A** pp 1934-1940
- [13] Chen B et al 2008 *Mat. Sci. and Eng. A* **483-484** pp 113-116
- [14] Wolf B, Fleck C, Eifler D 2004 *Int. J. Fat* **26** pp 1357-1363
- [15] Chen B et al 2008 *Mat. Sci. and Eng. A* **483-484** pp 113-116
- [16] *Fatigue and Fracture* 1996 ASTM Handbook vol.19 (ASTM Int. Materials Park, OH., U.S.A.) p.875.

- VII. [31] B. Hadzima, F. Nový, L. Trško, F. Pastorek, M. Jambor, S. Fintová, Shot peening as a pre-treatment to anodic oxidation coating process of AW 6082 aluminum for fatigue life improvement, *The International Journal of Advanced Manufacturing Technology*, 93 (2017) 3315-3323.





# Shot peening as a pre-treatment to anodic oxidation coating process of AW 6082 aluminum for fatigue life improvement

Branislav Hadzima<sup>1</sup> · František Nový<sup>2</sup> · Libor Trško<sup>1</sup>  · Filip Pastorek<sup>1</sup> · Michal Jambor<sup>2</sup> · Stanislava Fintová<sup>3</sup>

Received: 28 March 2017 / Accepted: 30 June 2017 / Published online: 15 July 2017  
© Springer-Verlag London Ltd. 2017

**Abstract** Shot peening with glass beads was used as a pre-treatment to anodic oxidation of AW 6082 aluminum alloy to eliminate the negative effect of the anodized layer on fatigue strength. Shot peening with intensity 6N and coverage of 100% was able to significantly improve the fatigue strength of the experimental material and when  $N = 3 \times 10^9$  cycles is considered the fatigue strength increased from  $\sigma_a = 80$  MPa to  $\sigma_a = 110$  MPa. Creation of the anodized surface layer with thickness of approximately 30  $\mu\text{m}$  on the pre-treated surface decreased the fatigue strength, when compared to the shot peened surface, almost in the whole measured region; however, the fatigue strength was still higher than for not treated material. The positive effect of shot peening on fatigue strength was a result of creation of compressive residual stress field with maximum of  $-200$  MPa and depth of 350  $\mu\text{m}$ . Fracture surface analysis showed that this deformed surface layer had increased resistance to fatigue crack initiation and propagation in the early stages and cracks created on the anodized surface layer were unable to propagate directly to the material and new initiation of fatigue crack was required; however, it was still accelerated by the sharp notch which the crack created.

**Keywords** Fatigue life · AW 6082 aluminum alloy · Anodizing · Shot peening · Ultrasonic fatigue testing

## 1 Introduction

Complex aluminum alloys are attractive materials for all applications which require high ratio of strength and weight combined with high corrosion resistance in various environments [1–3]. Those applications include various structural components in aeronautical and automotive industry. High corrosion resistance of aluminum and its alloys is a result of passivation process which occurs on the materials surface.

Atoms of aluminum react with oxygen from surrounding air and create a thin (only a few atomic layers thick)  $\text{Al}_2\text{O}_3$  ceramic coating. This thin coating provides protection of the alloy under it against reaction with many ambient chemical environments, thus assures high corrosion resistance. However, this passivation layer can be corrupted by reaction with chlorides in environments as sea water, polluted industrial air and salt water from winter roads. In the case when ambient environment does not allow contact of de-passivated surface with air, the base material is not protected and starts reacting with the ambient environment. This later results in the so-called pitting corrosion which escalates in significant degradation of the material properties. In the case of cyclic loading of the component, pits serve as fatigue crack initiation points, thus they accelerate the fatigue damage process.

The process of anodize coating is commonly used to improve the resistance of the passivated surface layer. This process is based on controlled growing of columnar amorphous  $\text{Al}_2\text{O}_3$  surface layer, where the thickness is much greater than of the one created naturally. Besides the improved corrosion resistance, this layer also provides a significant increase of the wear resistance due to its high hardness. Even when it seems

✉ Libor Trško  
libor.trsko@rc.uniza.sk

<sup>1</sup> Research Centre, University of Žilina, Univerzitná 8215/1, 010 26 Žilina, Slovakia

<sup>2</sup> Department of Materials Engineering, University of Žilina, Univerzitná 8215/1, 010 26 Žilina, Slovakia

<sup>3</sup> CEITEC IPM, Institute of Physics of Materials AS CR, Žitkova 22, Brno 616 62, Czech Republic

that anodized coatings are solving the major corrosion issue of aluminum alloys, they have negative effects on other, mainly mechanical properties. The amorphous coating is not completely uniform and contains many micro-cracks and micro-pores. Cracking also occurs during loading of the component due to extremely different moduli of elasticity of the coating and the substrate. In fact, cracks are extremely narrow, so corrosive environment is barely able to get inside the crack due to its surface tension (besides few liquids with extremely high penetration). However, those cracks serve as a strong stress concentration points (notches) in the process of cyclic (fatigue) loading, thus accelerate the process of fatigue crack initiation [4–8]. Since the fatigue crack initiation represents usually more than 90% of total number of cycles to fracture, accelerating this process significantly reduces fatigue life of the particular component.

The shot peening as a surface treatment has proven that it is possible to significantly improve the fatigue resistance of various structural materials by introduction of compressive residual stresses and grain refinement of the surface layer. This application includes all commonly used structural materials as steels [9–12], aluminum alloys [13–15], nickel and titanium alloys [16, 17] and even magnesium alloys [17]. Integrity and quality of the surface layer depend on the used shot peening parameters and proper care has to be taken when considering the peening process parameters such as Almen intensity and Coverage [18, 19]. Using the shot peening as a pre-treatment to anodize coating provides a chance to restore the fatigue properties of an anodized component. In this study, an analysis was performed of the influence of hybrid surface treatment by shot peening and anodizing on fatigue life of the AW 6082 aluminum alloy in high and ultra-high cycle region.

## 2 Experimental material and surface treatment

The wrought AW 6082-T651 aluminum alloy was used as experimental material, which is widely used in automotive and aeronautical applications. The chemical composition and mechanical properties of the experimental material are provided in Tables 1 and 2, respectively. Mechanical properties were obtained by the standard tensile test, with the strain rate  $1 \times 10^{-3} \text{ s}^{-1}$  and the test was performed in the longitudinal direction of extruded bar (direction of extrusion). Mechanical properties are characterized by good combination of tensile

**Table 1** Chemical composition of AW 6082 aluminum alloy in wt.%

Mg	Si	Fe	Cu	Mn	Zn	Ti	Cr	Al
0.76	0.88	0.35	0.04	0.45	0.04	0.03	0.04	Rest

**Table 2** Mechanical properties of AW 6082 aluminum alloy

Yield strength (MPa)	UTS (MPa)	Ductility (%)	Modulus of elasticity (GPa)
222	307	13.5	68.1

strength and high ductility what creates possibility of successful surface strengthening by shot peening. The high ultimate tensile strength is a result of precipitation hardening process by means of metastable  $\text{Mg}_2\text{Si}$  precipitates.

The microstructure of the experimental material (Fig. 1) is created by solid solution of alloying elements in aluminum together with large amount of intermetallic particles confirmed as  $\text{Mg}_2\text{Si}$  (dark gray) and  $\text{Al}_6\text{Mn}$ ,  $\text{Al}_6\text{Fe}$  (light gray).

Specimens for fatigue tests of the hour glass shape were machined from the extruded bars according to Fig. 2. Dimension marked “A” defines the length of treated surface by shot peening and anodizing. Specimens after fine turning and grinding with resulting surface roughness of  $R_a = 0.8 \text{ }\mu\text{m}$  were used for comparison of material properties in not-treated state.

Surface strengthening was performed by the air blast shot peening with Almen intensity 6N and coverage of 100%. Shot peening parameters were chosen according to [13] where various peening parameters were used on the AW 7075 aluminum alloy. One of the best performances was obtained by use of 8.3N intensity, with coverage of 100%. Since this alloy has much lower mechanical properties, even lower peening intensity was chosen to avoid damage of the surface integrity, what could result in overpeening effect (decrease of the fatigue life by shot peening surface damage) and also in creation of defective anodized layer.

To avoid the surface contamination by steel residues from ordinary cast steel peening media, fine glass beads with diameter of 0.4 mm and the impact angle  $90^\circ$  with respect to the specimen's axis were used. Presence of steel residua on the surface of aluminum alloys could cause problem with creation of the  $\text{Al}_2\text{O}_3$  passivation layer and a risk of steel contamination could completely ruin the purpose of the experiment.

The surface topography after shot peening (Fig. 3a) well documents the negative side effect of shot peening, which is the increase of the surface roughness. In this case, the arithmetical mean roughness parameter reached value of  $R_a = 3.5 \text{ }\mu\text{m}$ .

After the surface strengthening by shot peening, the sulfuric acid anodizing process (type II) [4–20] at a constant current density of  $40 \text{ mA cm}^{-2}$  in a bath containing  $250 \text{ g dm}^{-3}$   $\text{H}_2\text{SO}_4$  at  $20 \pm 0.5 \text{ }^\circ\text{C}$  for 20 min, was carried out. Sealing was done in deionized water at  $97 \text{ }^\circ\text{C}$  for a period of 4 min. The thickness of coating layer was measured by optical microscopy and was later confirmed by the SEM studies, as well. The average thickness of coating layer reached approximately  $30 \text{ }\mu\text{m}$  (Fig. 3b).

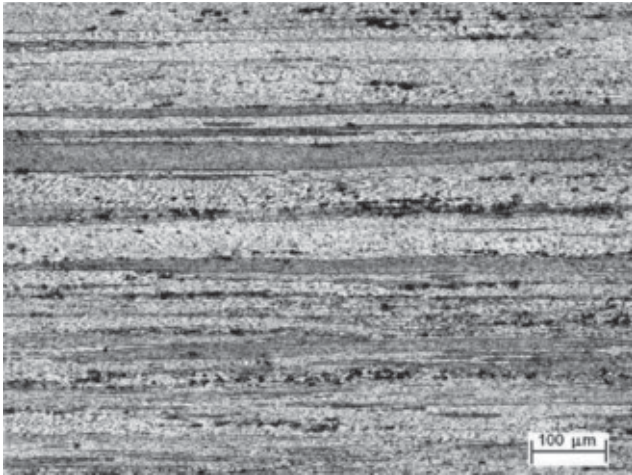


**Fig. 1** Microstructure of AW 6082-T6511 extruded aluminum alloy, longitudinal cut, etch. Tucker

### 3 Experimental results

Residual stress analysis of the as-machined and shot peened surface layer was performed with use of the X'Pert PRO diffractometer with  $\theta$ - $\theta$  goniometer and  $\text{CrK}\alpha$  radiation. The diffraction line  $\{331\}$  was analyzed with the  $\sin^2\psi$  method [21, 22] and eight different tilt angles  $\psi$  were used. The X-ray elastic constants  $\frac{1}{2}s_2 = 19.05 \text{ TPa}^{-1}$ ,  $s_1 = -4.89 \text{ TPa}^{-1}$  were used in macroscopic stress calculations. Since the X-ray diffraction stress measurement is possible only in crystalline materials, measurement of the residual stress state in the amorphous anodized coating was not possible. Another limitation of this method is caused by the material texture, which results in preferential angles of diffraction in a certain direction and the diffraction is completely lost in other  $\beta$  angles. Machining and shot peening can partially recover the properties of surface layer by redistribution of dislocations during the plastic deformation. However, during measurement of the residual stress in-depth profile by electrochemical polishing, when the boundary between influenced and not influenced material by surface treatment is reached, the diffraction is lost and no deeper measurements are possible.

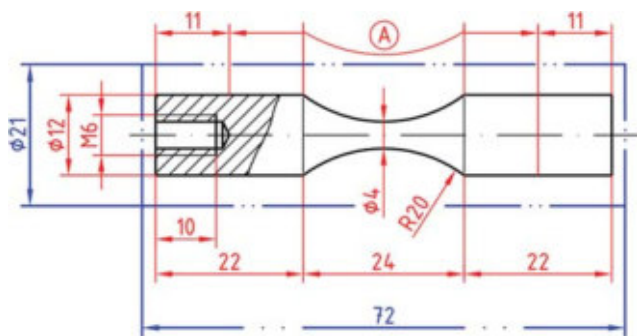


**Fig. 2** Position and dimensions of the machined fatigue test specimen with respect to dimensions of the extruded rod

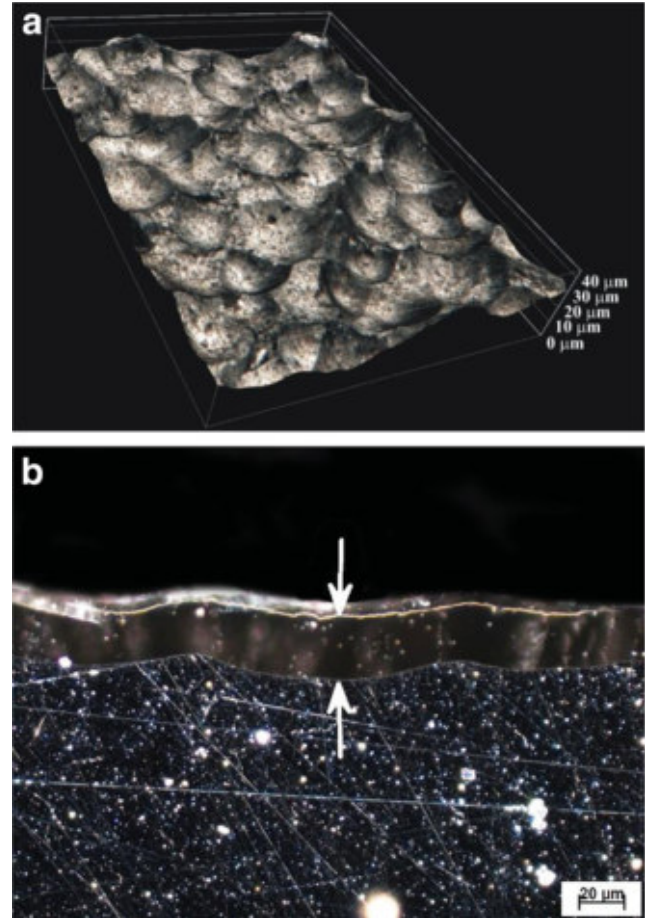


**Fig. 3** Topography of surface after shot peening (a) and thickness of the anodized coating (b)

According to the residual stress analysis results (Fig. 4), machining caused creation of a small field of tensile residual stresses. On the contrary, the shot peening created compressive residual stress field with maximal value of  $-205 \text{ MPa}$  and the depth of this field is approximately  $350 \mu\text{m}$ .

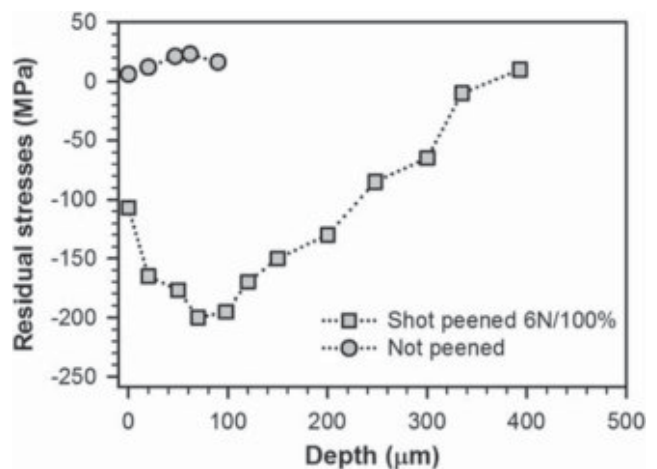


**Fig. 4** Residual stress profiles of not peened and shot peened fatigue test specimens



**Table 3** Regression parameters of fatigue life curves

Specimen type	$\sigma'_f$	$b$
NP	452	-0.082
SP	574	-0.075
SP + anodized	297	-0.042

Fatigue tests, with aim to determine the fatigue strength in the high and ultra-high cycle region, were carried out by means of the high frequency ultrasonic symmetrical tension–compression loading ( $f \approx 20$  kHz,  $R = -1$ ) at room temperature ( $T = 20 \pm 5$  °C). To obtain the mathematical dependence of the number of cycles to failure on the loading stress amplitudes, experimental results were approximated by the Basquin function, using the least square method [23]:

$$\sigma_a = \sigma'_f (N_f)^b, \tag{1}$$

where  $b$  is the exponent of fatigue life curve and  $\sigma'_f$  is the coefficient of fatigue toughness obtained by the extrapolation of stress amplitude on the first loading cycle. Regression coefficients for all three types of tested specimens are given in Table 3.

According to the fatigue test results (Fig. 5), the shot peening significantly improved the fatigue strength of the AW 6082 aluminum alloy and the improvement is more or less constant over the whole measured interval of loading cycles ( $N \approx 10^5 \div 10^{10}$ ). As expected, creation of the brittle anodized coating on the shot peened surface decreased the fatigue strength of the specimens. However, the total fatigue strength of the shot peened specimens with anodized coating is still higher than of the specimens without any surface treatment. An interesting fact is that the fatigue life curve of the shot peened and anodized specimens tends to converge at approximately  $N \approx 4 \times 10^8$  cycles with the fatigue life curve of shot peened specimens. Beyond this point, the fatigue

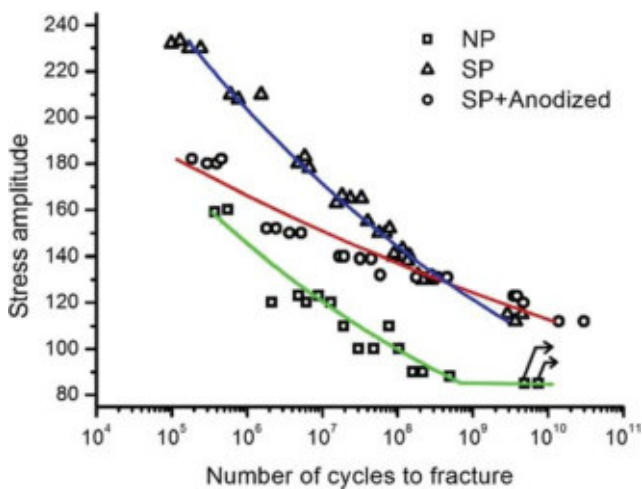


**Fig. 5** S–N curves of not peened, shot peened and shot peened + anodized specimens

strengths of specimens with shot peened and shot peened + anodized surfaces are very similar.

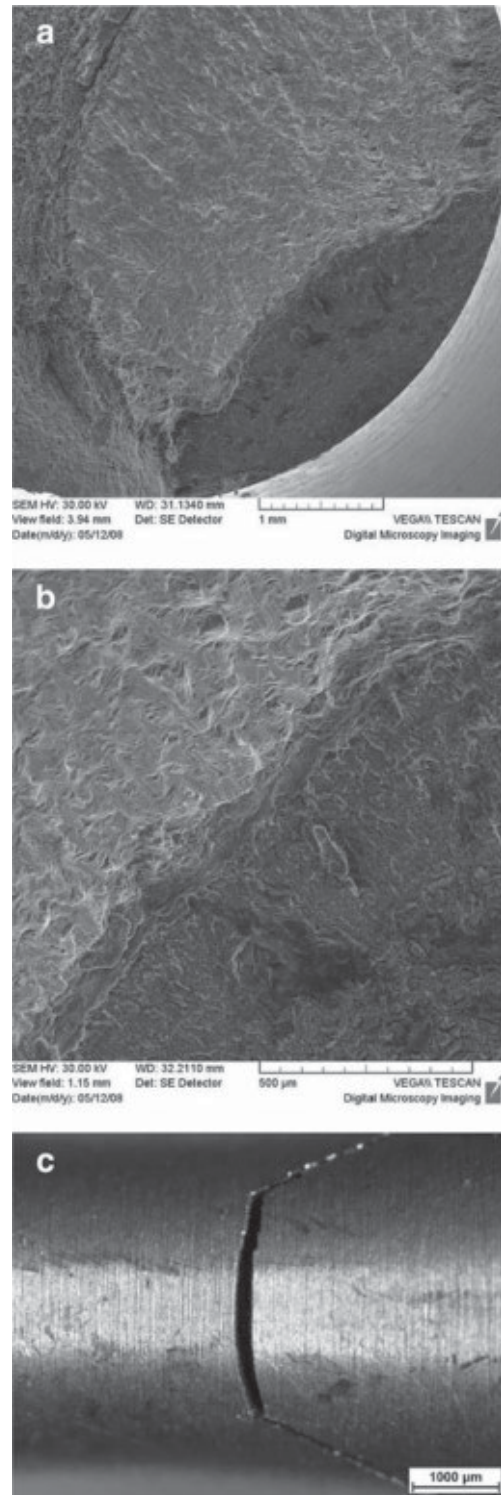


**Fig. 6** Fracture character of NP specimen: fatigue fracture initiation character (a), deviation of the fatigue crack propagation after the initialization stage (b), macro view of the fractured specimens with obvious change of the direction of the fatigue crack propagation (c)

#### 4 The fracture surface analysis

According to the fracture surface analysis of the not peened specimens, in all the cases the fatigue crack initiated on a free surface of the specimen. In the first stages, the fatigue crack initiated and propagated perpendicularly to the vector of the loading force, what assumes a non-crystallographic orientation of the fatigue crack initiation and short crack propagation (Fig. 6a). After the crack reached depth of  $0.2 \div 1$  mm under the surface, it rapidly changed the direction and mechanism of propagation (Fig. 6b). The deviation of the fatigue crack propagation was  $30 \div 35^\circ$  with respect to the vector of the loading force (Fig. 6c). In this stage, the crack propagation was significantly influenced by the deformation texture and the direction of the crack was changing with respect to different resistance to fatigue crack propagation of bands with different orientation (Fig. 7a). Even when the microstructure of the material is

full of small and brittle intermetallic phases, these were not fractured and only their separation from the matrix was observed (Fig. 7b).

Striations perpendicular to the direction of the fatigue crack propagation were often observed on the fracture surface in the area of the stable fatigue crack growth (Fig. 8a). The final fracture had a character of transcrystalline ductile fracture with dimple morphology. The size and shape of the dimples was influenced by the deformation texture and the dimples are elongated in the direction of extrusion (Fig. 8b).

Since the shot peening influences only a thin surface layer of the material, differences in fatigue damage mechanism can be observed just in the stage of fatigue crack initiation and short crack propagation. In all the shot peened specimens, the fatigue crack was initiated on the surface of the specimen (Fig. 9a). The trajectory of fatigue crack propagation in the near-surface areas

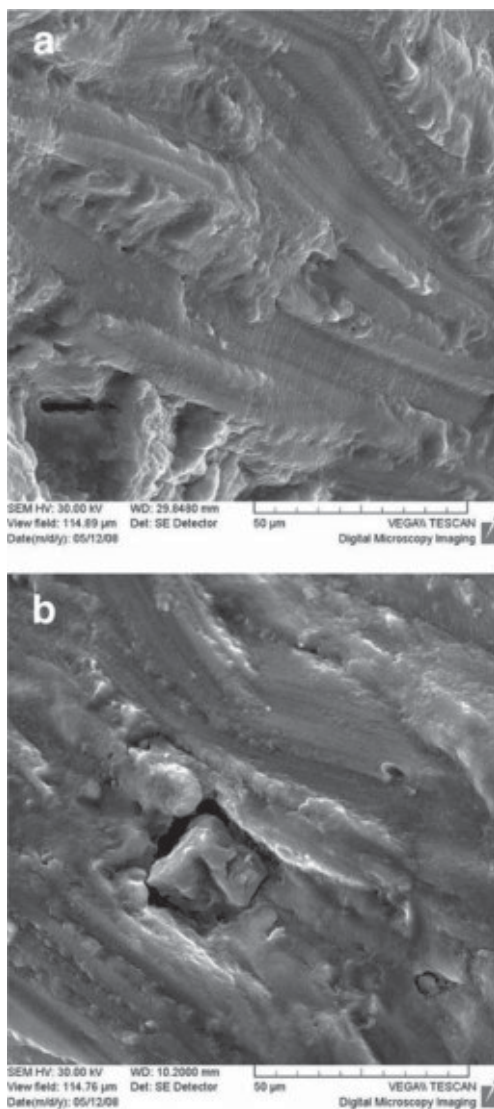


**Fig. 7** Fatigue crack propagation character: influence of the deformation texture (a) and separation of intermetallic particles from the matrix (b)

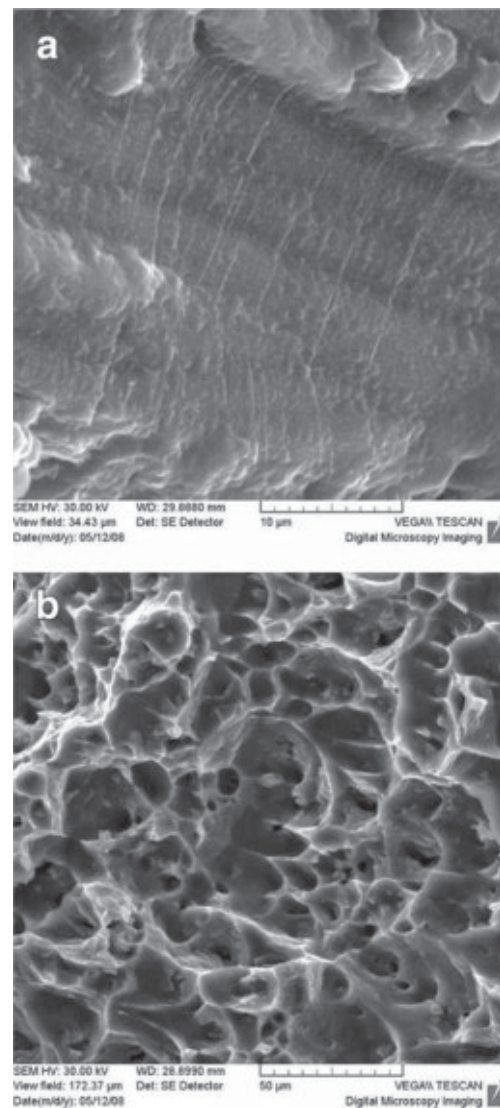


**Fig. 8** Striations present in the area of the stable fatigue crack growth (a) and the final fracture characteristic transcrystalline ductile fracture with dimple morphology (b)



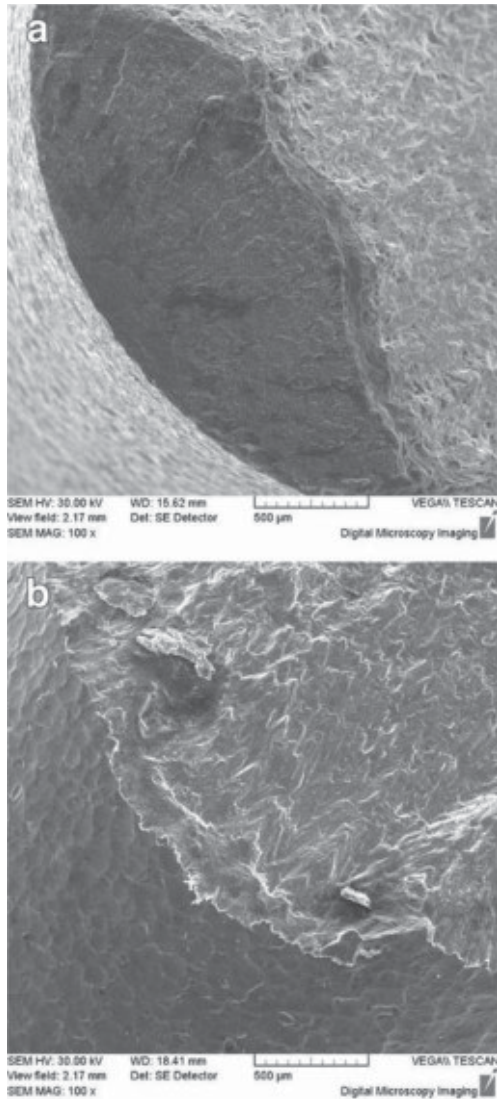


**Fig. 9** Surface fatigue crack initiation in SP specimens (a) and change of the crack path by the shot peening surface topography (b)

was also significantly influenced by the surface topography and the dimples were able to rapidly change the crack path (Fig. 9b). The closer observation of the fracture surface in the area of the stable crack propagation near to the strengthened surface layer revealed that the fatigue crack propagated in a different direction with respect to the core of the material (Fig. 10a). Different character of the fracture surface of the surface layer was also observed in the area of unstable fatigue crack propagation – final fracture (Fig. 10b).

On specimens treated with shot peening + anodizing the fatigue crack initiated also on the free surface of the specimen (Fig. 11a) with an observable ring of the brittle fractured anodized surface layer (Fig. 11b). The closer and detailed analysis of the fractured anodized layer revealed a number of defects present in the layer, which are usually points of the fatigue crack initiation (Fig. 12). Fracture also revealed the columnar character of the

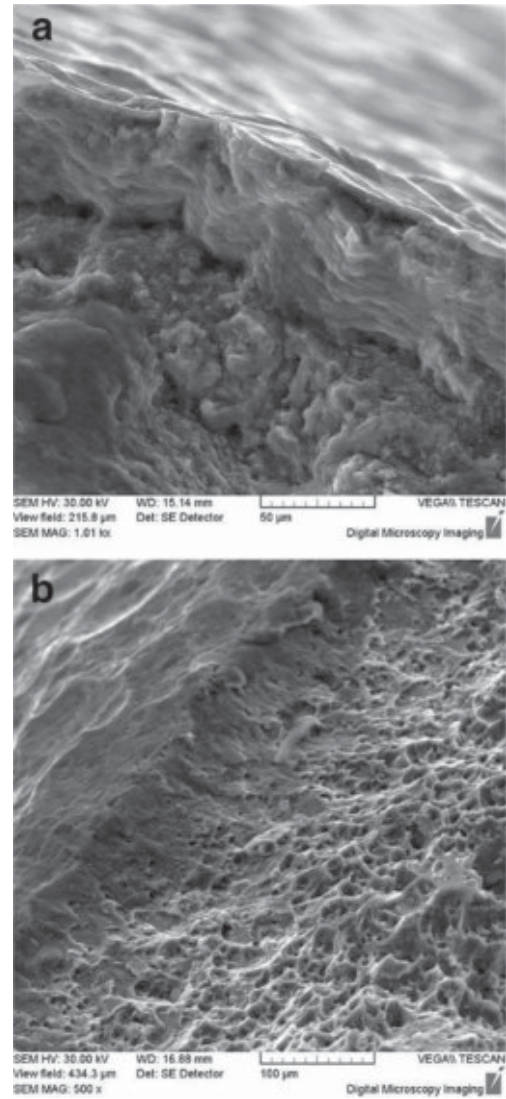


**Fig. 10** Different character of the fracture surface of the strengthened surface layer in the area of stable fatigue crack growth (a) and the final fracture (b)

anodized surface layer with columns growing perpendicularly to the specimens surface (Fig. 13).

## 5 Discussion

Due to various defects present in the artificially created  $\text{Al}_2\text{O}_3$  surface layer (Fig. 12) by anodic oxidation process, this surface treatment significantly decrease the fatigue properties of aluminum components [4–8]. Since this layer is often required to improve the corrosion resistance of aluminum alloy, together with wear resistance, the idea was to use the shot peening as a proven technology for fatigue life increase [9–17] as a pre-treatment to anodic oxidation. The shot peening with use of the glass beads with Almen intensity 6N and coverage of 100% enabled introduction of compressive residual stresses



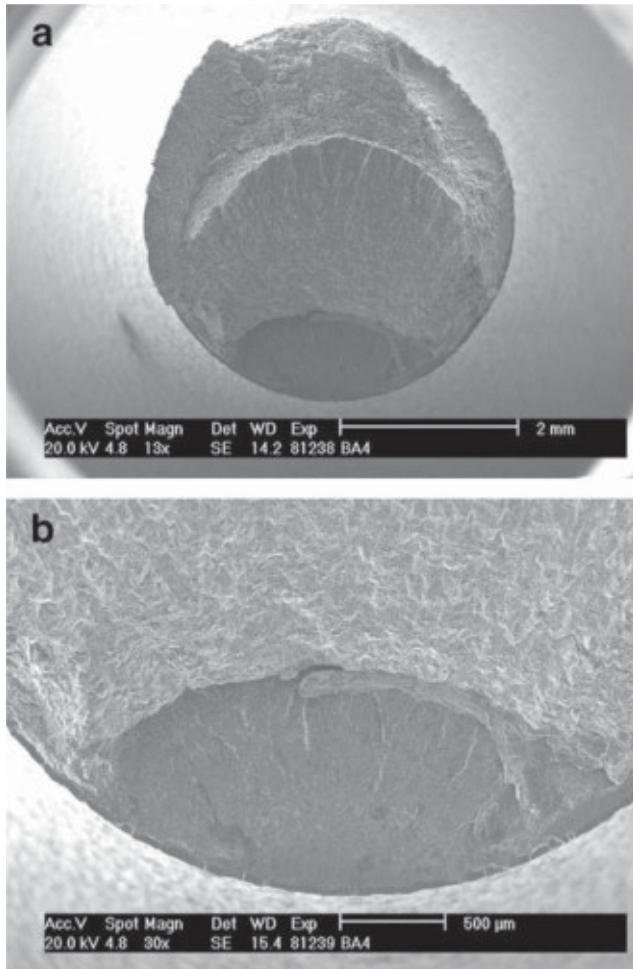


**Fig. 11** Surface fatigue crack initiation of SP + anodized specimen (a) and ring of brittle fracture on the circumference of the specimen (b)

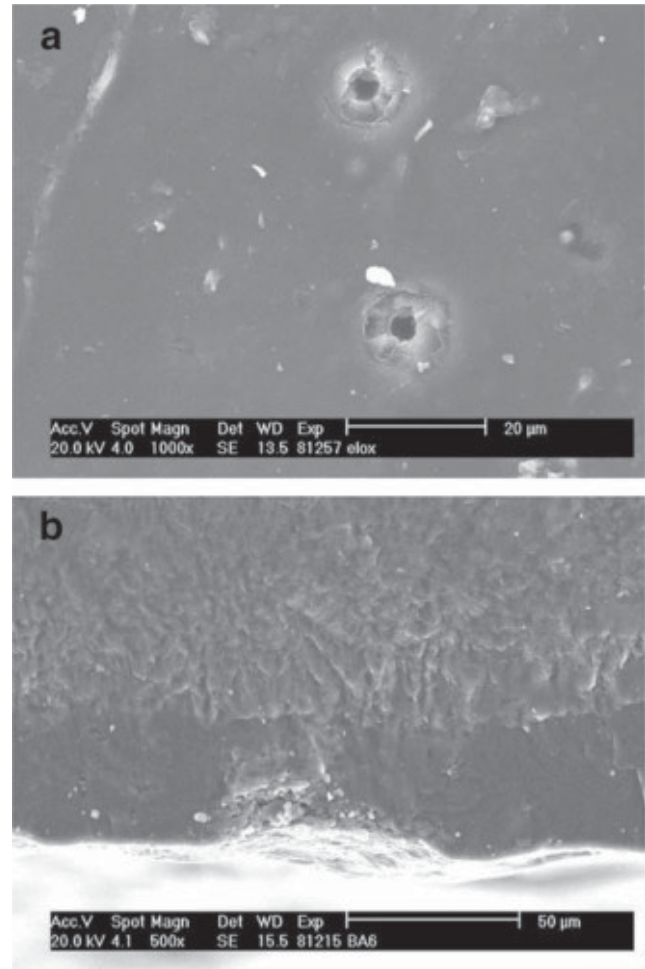


**Fig. 12** Defects present in the anodized surface layer: cavities after intermetallic particles (a), pores (b)

and grain modification to improve the fatigue life for  $N = 3 \times 10^9$  cycles from  $\sigma_a = 80$  MPa to  $\sigma_a = 110$  MPa. The maximal value of the residual stresses reaches  $-205$  MPa what is very close to the yield point (222 MPa). This is unusual for such a low peening intensity. The reason for this phenomenon is the specific geometry of the test specimen. The used gauge diameter is only 4 mm what results in high Hertzian contact stress between the surface and the shot. These high Hertzian stresses, together with the low mechanical properties of the material, result in significant plastic deformation of the surface (creation of large dimples documented in Fig. 3) and creation of high compressive residual stresses; however in just a very thin layer (about 350 μm). Similar behavior was also observed in [13] where the lowest peening intensities provided the highest values of residual stresses, but with the lowest affected depth and with increase of peening intensity the depth of the affected layer increased; however, the maximal values decreased. If larger specimens or industrial components would be considered for shot peening treatment, probably the 6N intensity would have to be reconsidered and the higher kinetic

energy of the peening stream would be required to obtain fatigue life improvement.

Following anodizing caused even further improvement of the fatigue life in the ultra-high cycle region to  $\sigma_a = 120$  MPa. However, when the lower number of cycles are considered, cycles between  $N = 10^6$  up to  $N = 2 \times 10^8$ , the shot peened surface has an advantage over the shot peened + anodized surface, but both treatments are still above the not treated material. This can be explained by significantly different moduli of elasticity of the  $Al_2O_3$  layer and the substrate AW 6082 material. When the high loading stress amplitude is applied (corresponding to the lower number of loading cycles to fracture), the brittle anodized layer starts to crack and the cracks serve as sharp notches and accelerate the fatigue crack initiation in the substrate. However, when the crack from the anodized surface layer hits the strengthened shot peened layer of the substrate, the compressive residual stresses cause necessity of re-initialization of the fatigue crack and slow down the fatigue crack growth in early stages. At low stress amplitudes, corresponding with the region above  $N = 5 \times 10^8$  cycles, the anodized layer is able to stay compact longer and together

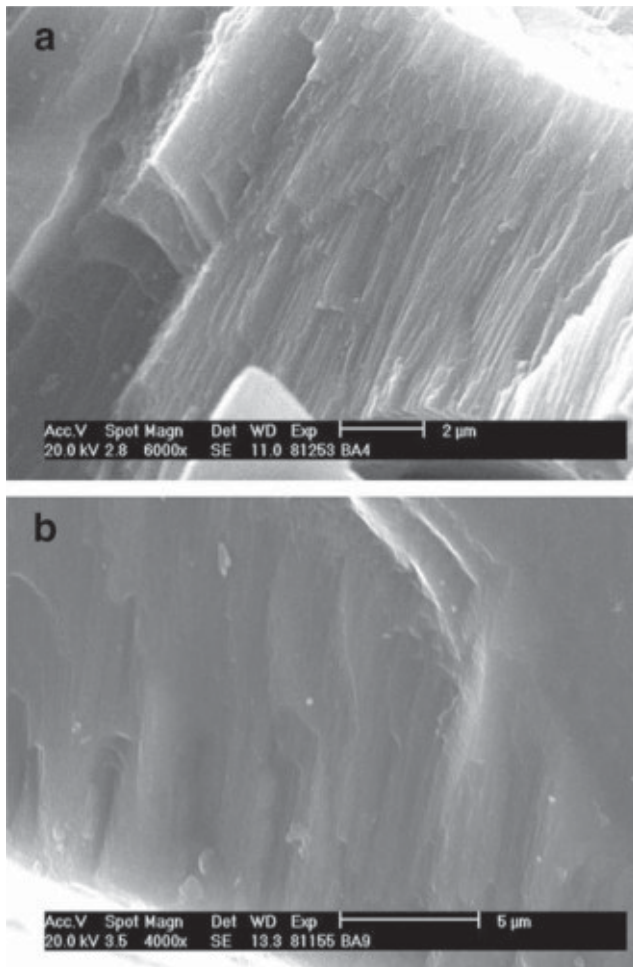


**Fig. 13** Columnar character of the anodized surface layer

with the strengthened surface layer by shot peening further improves the fatigue life.

The negative aspect of the shot peening treatment is a significant increase of the surface roughness. As it is obvious from Fig. 3b, the anodized layer copies the character of the surface, what results in a rough anodized surface. The rough surface has significantly larger surface area than, for example, the polished material, what can be problematic from the corrosion point of view [24, 25]. In addition, in the case of wear the material with higher roughness usually has a lower wear performance, however in the case of holding lubricants the surface might have an advantage to the polished one [26, 27].

## 6 Conclusions

The shot peening with glass beads was used as a pre-treatment to anodizing on AW6082 aluminum alloy with aim to reduce the negative effect of anodizing on fatigue properties of the substrate. According to results of experimental works and their discussion, the following can be concluded:

- The shot peening performed with Almen intensity 6N and coverage of 100% was able to improve the fatigue properties of the AW 6082 aluminum alloy in the whole measured region. Improvement was mainly caused by introduction of compressive residual stresses in the sub-surface layers of material.
- Anodizing had a significant influence on the fatigue life of the shot peened substrate and in the region above  $N = 6 \times 10^8$  cycles the treatment slightly improved the fatigue strength. At the higher loading stress amplitudes, corresponding to the lower number of cycles than  $N = 6 \times 10^8$ , the treatment had significantly decreased the fatigue strength when compared to the shot peened material.
- Despite the negative effect of anodizing on fatigue life, application of the shot peening as the pre-treatment caused that even with anodized surface layer, the fatigue strength was still higher than that of the not treated material in the whole investigated region of fatigue loading.

**Acknowledgements** The research was supported by European regional development fund and Slovak state budget by the project ITMS 26220220048 (50%) and Scientific Grant Agency of the Ministry of Education, Science and Sports of the Slovak Republic and Slovak Academy of Sciences, grant nos.: 1/0045/17, 1/0951/17 and 1/0123/15 and by the Ministry of Education, Youth and Sports of the Czech Republic under the project CEITEC 2020 (LQ1601).

## References

1. Hatch JE, American Society for Metals, Aluminum Association (U.S.) (1984) Aluminum : properties and physical metallurgy, American Society for Metals, Metals Park, Ohio
2. Davis JR, ASM International. Handbook Committee (1990) ASM handbook: properties and selection: nonferrous alloys and special-purpose materials. ASM International, Materials Park, Ohio
3. Polmear I (2006) Light alloys, 4th edn. Butterworth-Heinemann, Oxford
4. Fares C, Hemmouche L, Belouchrani MA, Amrouche A, Chicot D, Puchi-Cabrera ES (2015) Coupled effects of substrate microstructure and sulphuric acid anodizing on fatigue life of a 2017A aluminum alloy. *Mater Des* 86:723–734. doi:10.1016/j.matdes.2015.07.120
5. Grober D, Georgi W, Sieber M, Scharf I, Hellmig RJ, Leidich E, Lampke T, Mayr P (2015) The effect of anodising on the fatigue performance of self-tapping aluminium screws. *Int J Fatigue* 75: 108–114. doi:10.1016/j.ijfatigue.2015.02.008
6. Nie BH, Zhang Z, Zhao ZH, Zhong QP (2013) Effect of anodizing treatment on the very high cycle fatigue behavior of 2A12-T4 aluminum alloy. *Mater Des* 50:1005–1010. doi:10.1016/j.matdes.2013.03.083
7. Rajasekaran B, Raman SGS, Krishna LR, Joshi SV, Sundararajan G (2008) Influence of microarc oxidation and hard anodizing on plain fatigue and fretting fatigue behaviour of Al-Mg-Si alloy. *Surf Coat Tech* 202(8):1462–1469. doi:10.1016/j.surfcoat.2007.06.058
8. Shahzad M, Chaussimier M, Chieragatti R, Mabru C, Rezai-Aria F (2011) Surface characterization and influence of anodizing process

- on fatigue life of Al 7050 alloy. *Mater Des* 32(6):3328–3335. doi:10.1016/j.matdes.2011.02.027
9. Trsko L, Bokuvka O, Novy F, Guagliano M (2014) Effect of severe shot peening on ultra-high-cycle fatigue of a low-alloy steel. *Mater Des* 57:103–113. doi:10.1016/j.matdes.2013.12.035
  10. Moridi A, Hassani-Gangaraj SM, Vezzu S, Trsko L, Guagliano M (2015) Fatigue behavior of cold spray coatings: the effect of conventional and severe shot peening as pre-/post-treatment. *Surf Coat Tech* 283:247–254. doi:10.1016/j.surfcoat.2015.10.063
  11. Lv Y, Lei LQ, Sun LN (2015) Effect of shot peening on the fatigue resistance of laser surface melted 20CrMnTi steel gear. *Materials Science and Engineering a-Structural Materials Properties Microstructure and Processing* 629:8–15. doi:10.1016/j.msea.2015.01.074
  12. Hassani-Gangaraj SM, Moridi A, Guagliano M, Ghidini A, Boniardi M (2014) The effect of nitriding, severe shot peening and their combination on the fatigue behavior and micro-structure of a low-alloy steel. *Int J Fatigue* 62:67–76. doi:10.1016/j.ijfatigue.2013.04.017
  13. Trško L, Guagliano M, Bokůvka O, Nový F, Jambor M, Florková Z (2017) Influence of severe shot peening on the surface state and ultra-high-cycle fatigue behavior of an AW 7075 aluminum alloy. *J Mater Eng Perform* 26(6):2784–2797. doi:10.1007/s11665-017-2692-9
  14. Kikuchi S, Nakamura Y, Nambu K, Ando M (2016) Effect of shot peening using ultra-fine particles on fatigue properties of 5056 aluminum alloy under rotating bending. *Mater Sci Eng A* 652:279–286. doi:10.1016/j.msea.2015.11.076
  15. Oguri K (2011) Fatigue life enhancement of aluminum alloy for aircraft by fine particle shot peening (FPSP). *J Mater Process Technol* 211(8):1395–1399. doi:10.1016/j.jmatprotec.2011.03.011
  16. Yao CF, Wu DX, Ma LF, Tan L, Zhou Z, Zhang JY (2016) Surface integrity evolution and fatigue evaluation after milling mode, shot-peening and polishing mode for TB6 titanium alloy. *Appl Surf Sci* 387:1257–1264. doi:10.1016/j.apsusc.2016.06.162
  17. Abadie F-X, Beckmerhagen P, Belassel M, Brauss M, Clauer A, Evert T, Fricke S, Gray H, Giovanni G, Guagliano M, Halder M, Henning W, Hendry E, Huyton P, Klijsen M, Lahrman D, Muller E, Pineault J, Talukdar A (2012) Shot peening: a dynamic application and its future, 3rd edn. *Metal Finishing News*, Wetzikon
  18. Unal O (2016) Optimization of shot peening parameters by response surface methodology. *Surf Coat Technol* 305:99–109. doi:10.1016/j.surfcoat.2016.08.004
  19. Liu WC, Dong J, Zhang P, Zhai CQ, Ding WJ (2009) Effect of shot peening on surface characteristics and fatigue properties of T5-treated ZK60 alloy. *Mater Trans* 50(4):791–798. doi:10.2320/matertrans.MRA2008415
  20. Bensalah W, Elleuch K, Feki M, Depetris-Wery M, Ayedi HF (2012) Optimization of tartaric/sulphuric acid anodizing process using Doehlert design. *Surf Coat Tech* 207:123–129. doi:10.1016/j.surfcoat.2012.06.059
  21. Cullity BD (1978) *Elements of X-ray diffraction*. Addison-Wesley Publishing Company
  22. Fitzpatrick ME, Laboratory NP (2005) Determination of residual stresses by X-ray diffraction. vol č. 2. National Physical Laboratory
  23. Kohout J, Vechet S (2001) A new function for fatigue curves characterization and its multiple merits. *Int J Fatigue* 23(2):175–183. doi:10.1016/S0142-1123(00)00082-7
  24. Sivakumar B, Pathak LC, Singh R (2017) Role of surface roughness on corrosion and fretting corrosion behaviour of commercially pure titanium in Ringer's solution for bio-implant application. *Appl Surf Sci* 401:385–398. doi:10.1016/j.apsusc.2017.01.033
  25. Mhaede M, Pastorek F, Hadzima B (2014) Influence of shot peening on corrosion properties of biocompatible magnesium alloy AZ31 coated by dicalcium phosphate dihydrate (DCPD). *Mat Sci Eng C-Mater* 39:330–335. doi:10.1016/j.msec.2014.03.023
  26. Vrbka M, Krupka I, Svoboda P, Sperka P, Navrat T, Hartl M, Nohava J (2011) Effect of shot peening on rolling contact fatigue and lubricant film thickness within mixed lubricated non-conformal rolling/sliding contacts. *Tribol Int* 44(12):1726–1735. doi:10.1016/j.triboint.2011.06.019
  27. Matsui M, Kakishima H (2006) Improvement of tribological performance of steel by solid lubricant shot-peening in dry rolling/sliding contact wear tests. *Wear* 260(6):669–673. doi:10.1016/j.wear.2005.03.030

- VIII. [32] L. Trško, S. Fintová, F. Nový, O. Bokůvka, M. Jambor, F. Pastorek, Z. Florková, M. Oravcová, Study of Relation between Shot Peening Parameters and Fatigue Fracture Surface Character of an AW 7075 Aluminium Alloy, *Metals*, 8 (2018) 111.



Article

# Study of Relation between Shot Peening Parameters and Fatigue Fracture Surface Character of an AW 7075 Aluminium Alloy

Libor Trško <sup>1,\*</sup> , Stanislava Fintová <sup>2</sup>, František Nový <sup>3</sup>, Otakar Bokůvka <sup>3</sup>, Michal Jambor <sup>3</sup>, Filip Pastorek <sup>1</sup>, Zuzana Florková <sup>1</sup> and Monika Oravcová <sup>1</sup>

<sup>1</sup> Research Centre of the University of Žilina, University of Žilina, Univerzitná 8215/1, 010 26 Žilina, Slovakia; filip.pastorek@rc.uniza.sk (F.P.); zuzana.florkova@rc.uniza.sk (Z.F.); monika.oravcova@rc.uniza.sk (M.O.)

<sup>2</sup> Institute of Physics of Materials, Academy of Sciences of the Czech Republic, Žižkova 22, 616 62 Brno, Czech Republic; fintova@ipm.cz

<sup>3</sup> Department of Materials Engineering, Faculty of Mechanical Engineering, University of Žilina, Univerzitná 8215/1, 010 26 Žilina, Slovakia; frantisek.novy@fstroj.uniza.sk (F.N.); otakar.bokuvka@fstroj.uniza.sk (O.B.); michal.jambor@fstroj.uniza.sk (M.J.)

\* Correspondence: libor.trsko@rc.uniza.sk; Tel.: +421-41-513-7629

Received: 11 January 2018; Accepted: 26 January 2018; Published: 6 February 2018

**Abstract:** Shot peening is a well-known surface treatment method used for fatigue life improvement of cyclically loaded structural components. Since three main variables are considered in the peening process (peening intensity, coverage and peening media type), there is no direct way to choose the best combination of treatment parameters for the best performance, thus it has to be based on experience and laboratory tests. When shot peening is performed with inadequate parameters, or the peening process is not stable in time (decrease of the peening pressure, deterioration of the peening media and so on), it can result in significant degradation of the treated component fatigue properties, what is commonly called as the “overpeening” effect. When a premature fatigue fracture occurs in operation, the fracture surface analysis is usually the most important method of revealing the damage mechanism. This work is aimed at the study of the relation between the shot peening parameters and the fatigue fracture surface character on an AW 7075 aluminium alloy with an objective of identifying marks of overpeening and investigating the fatigue crack initiation mechanism. After performing the tests, it was observed that shot peening with optimized parameters creates a surface layer that is able to change the mechanism of the fatigue crack propagation and improve fatigue strength. On the other hand, using extensive peening parameters decrease the fatigue strength due to the creation of surface cracks and surface layer delamination.

**Keywords:** shot peening; AW 7075; fatigue; fracture surface; ultrasonic fatigue testing

## 1. Introduction

Shot peening is currently well recognized and the most widely applied surface strengthening technique for fatigue life improvement [1]. In many studies, the positive effect on fatigue life of all sorts of engineering materials, such as steels [2–4], aluminium [5,6], magnesium [7,8], titanium [9] and nickel [10] alloys, was proven. The fatigue life improvement is a result of a complex modification of the surface layer’s structural state by increasing the dislocation density (deformation strengthening), grain refinement, and by accumulation of the compressive residual stresses, which slow down the fatigue crack initiation process and increase the resistance to fatigue crack propagation in the early stages of fatigue damage [11,12].

Since it was found out that a significant part of the residual stresses relax during the cyclic loading [13] and the residual stress loss does not correspond to fatigue life improvement, another

mechanism of surface modification had to be considered to explain this uncertainty and it has been proven in many studies that this mechanism is grain refinement [2,5,13,14]. The new generation of shot peening was developed putting emphasis on the grain refinement process and that treatment is commonly called severe shot peening (SSP). It is characterized by the use of unconventionally severe parameters which are able to introduce significant grain refinement and create a nanostructural surface layer with superior mechanical properties when compared to the coarse grained equivalent [2,5,14–17]. This treatment is often able to provide superior fatigue life improvement than conventional shot peening [5,18].

The fatigue life improvement results by conventional shot peening and the severe shot peening treatment are very sensitive to the process parameters used, usually quantified by Almen intensity and coverage. However, using inappropriately severe parameters can lead to an effect called “overpeening”, which causes significant degradation of the surface layer and consequently of fatigue properties [5,19,20]. Even when there is a basic knowledge of the surface defects after extensive shot peening, described as burrs, folds and micro cracks [21], only limited information is available on degradation mechanisms that cause the decrease in fatigue life. One of the possibilities for studying them is to analyze the fracture surfaces after the fatigue test, looking for various marks and characteristics of fatigue crack initiation. Knowledge about the relation between the shot peening parameters and the fracture surface character, mainly in the stage of fatigue crack initiation, provides essential information for quality control and failure analysis when it is necessary to evaluate a posteriori the quality of the shot-peening technological process.

The aim of this research was to analyze the dependence of the fatigue life of AW 7075 aluminium alloy on the shot peening parameters and, consequently, on the fracture surface character. The main focus was given to the surface-layer integrity and fatigue crack initiation and propagation in the shot peened surface layer.

## 2. Materials and Methods

As experimental material, the AW 7075 T6511 aluminium alloy was used, in the form of extruded bars 15 mm in diameter. The T6 heat treatment for this alloy, according to [22], consists of solution heat treatment at 482 °C for 2 h, quenching in water, and aging at 130 °C for 24 h (T6 temper). The Tx511 refers specifically to plates, rolled or cold-finished rods and bars, to die or ring forgings and to rolled-ring products that are stretched to relieve residual stresses and that may receive minor straightening after stretching to comply with standard tolerances [23]. Mechanical properties (Table 1 [5]) fulfilled the required conditions according to the materials datasheet.

**Table 1.** Mechanical properties of AW 7075 aluminium alloy. Reproduced with permission from Trško, L.; Guagliano, M.; Bokůvka, O.; Nový, F.; Jambor, M.; Florková, Z. *J. Mater. Eng. Perform.* Published by Springer Nature, 2017 [5].

Ultimate Tensile Strength UTS (MPa)	Ductility A (%)	Reduction of Area Z (%)	Hardness HV10
631	4.9	15.7	175

The microstructure of extruded bars (Figure 1) was revealed by etching with Fuss solution (7.5 mL HF + 25 mL HCl + 8 mL HNO<sub>3</sub> + 1000 mL H<sub>2</sub>O) and has a strong deformation (laminar-kind) texture caused by the extrusion process. It is formed by solid solution of zinc in aluminium and a great number of large or very fine intermetallic phases. Typically, AW 7075 has a chemical composition including up-to 10 alloying elements. These elements include primarily Zn, Mg and Cu; however, appreciable and specific amounts of Fe, Si, Cr, Ti, Zr and Mn are often present (both as deliberate additions and as impurities). Over the past three decades, the microstructure of AW 7075 has been well characterized, along with the corresponding physical metallurgy. The literature gives evidence supporting the presence of the following intermetallic phases in 7xxx series alloys (not all are simultaneously present, and temper and precise composition will regulate their types and shape): MgZn<sub>2</sub>, Mg<sub>2</sub>Si, Al<sub>20</sub>Cu<sub>2</sub>Mn<sub>3</sub>,



$\text{Al}_{12}\text{Mn}_3\text{Si}$ ,  $\text{Al}_7\text{Cu}_2\text{Fe}$ ,  $\text{Al}_2\text{Cu}$ ,  $\text{Al}_2\text{CuMg}$ ,  $\text{Al}_3\text{Fe}$ ,  $\text{Al}_{12}\text{Mg}_2\text{Cr}$ ,  $\text{Al}_{20}\text{Cu}_2\text{Mn}_3$ ,  $\text{Al}_6\text{Mn}$ ,  $\text{Al}_3\text{Ti}$ ,  $\text{Al}_6\text{Zr}$ ,  $\text{Mg}_2\text{Al}_3$ ,  $\text{Al}_{32}\text{Zn}_{49}$ , and  $\text{Mg}(\text{AlCu})$  [22,24,25]. Due to deformation texture created during the extrusion process, the particles of intermetallic phases are mainly aligned in lines, when referred to the longitudinal cut (Figure 1a). On the cross cut, the cut lines of intermetallic phases appear as clusters distributed in the volume of material (Figure 1b).

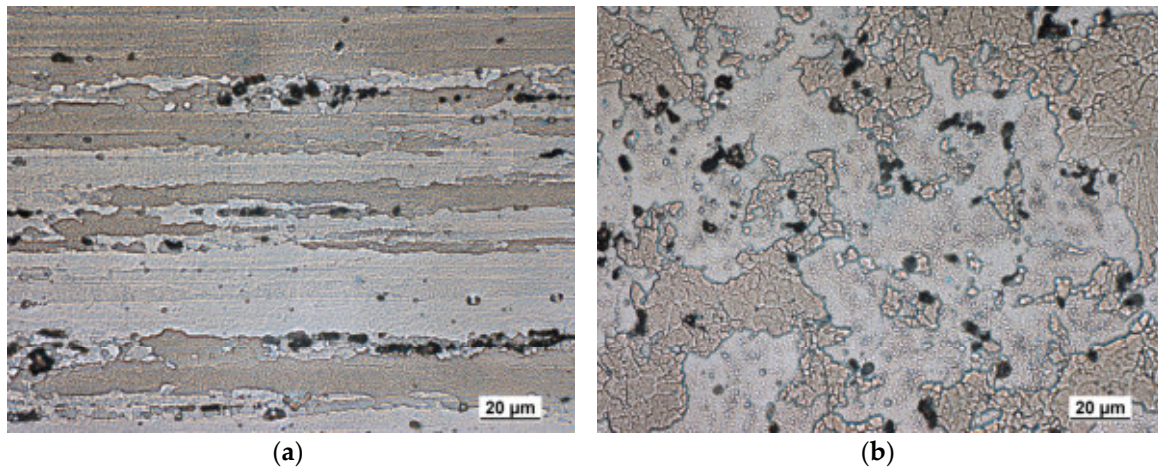


**Figure 1.** Microstructure of AW 7075 aluminium alloy—(a) longitudinal cut; and (b) cross cut.

One of the basic conditions for assuring the repeatability of the shot peening process is to evaluate the velocity of the shot stream (peening intensity) and the ratio between the surface of the material covered by dimples after the hitting of the peening media and the original surface (peening coverage). Shot peening intensity is measured by the standardized Almen test, which is referred to intensity at saturation, measured as the height of the arc created on a shot peened metal strip. Shot peening coverage is analyzed by optical methods. Coverage of 98% is a degree of coverage that can still be assessed visually. The corresponding duration of the shot peening process after which the 98% coverage degree is obtained is frequently called the shot peening time  $t_{98\%}$ . The required duration of the treatment is the product of the shot peening time  $t_{98\%}$  and a security factor  $S$ , usually 2 times  $t_{98\%}$ , which ensures that the surface of the component has a coverage of at least 100%. This means that every point of the surface is covered by a shot peening impact dimple. Higher coverage degrees are created analogically by multiplication of the time for 100% coverage. For more information about the shot peening intensity and coverage measurement refer to [1].

To provide a systematic analysis of the shot peening influence on the fatigue life of the AW 7075 aluminium alloy, air blast shot peening with five increasing peening intensities and coverages was performed (Table 2). Full fatigue life results were published in [5], while this work is focused only on the fatigue fracture surface character of the peened material. Treatment with each intensity was done on two ultrasonic fatigue test specimens used for fatigue tests at 20 kHz frequency (Lasur, Asnières, France) [26] (Figure 2). Dimension marked “A” defines the length of the shot peened surface area and dimension marked “B” was adjusted to harmonize the resonance frequency of the specimen with the resonance frequency of the ultrasonic horn used [2,26]. Fatigue tests were carried out at two loading stress levels:  $\sigma_a = 185$  MPa and  $\sigma_a = 176$  MPa. The parameters of the shot peening treatments are given in Table 2 together with the resulting surface roughness (also the roughness of the not-peened (NP) specimen is included). The gauge length surfaces of the not-peened specimens were ground with the SiC paper and polished with diamond metallography emulsion with diamond particle size of 0.7  $\mu\text{m}$ .

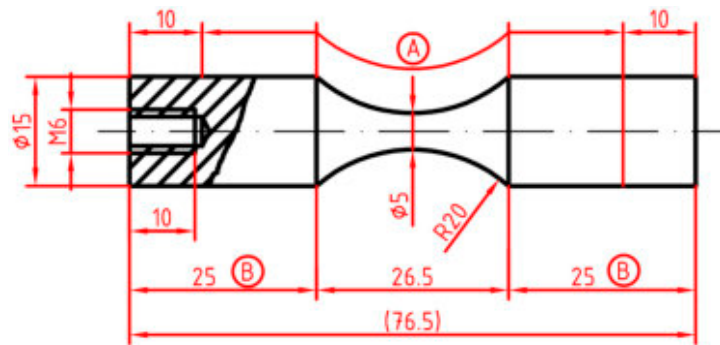


**Figure 2.** Geometry and dimensions of AW 7075 aluminium alloy specimens for fatigue tests. Dimensions are given in mm.

**Table 2.** Parameters of performed shot peening treatments and resulting surface roughness.

Label	Shot Type	Almen Intensity (0.001 inch)	Coverage (%)	Roughness Ra ( $\mu\text{m}$ )	Roughness Rz ( $\mu\text{m}$ )
NP	-	-	-	0.125	0.913
SP1	CEZ 100	8.3 N	100	2.614	14.304
SP2	CEZ 100	9.6 N	650	3.493	20.767
SP3	S110	6.9 A	100	3.849	20.712
SP4	S170	14.4 A	100	7.553	34.217
SP5	S170	14.9 A	650	7.971	35.793

### 3. Results

#### 3.1. Fatigue Life Analysis

According to the results of the fatigue tests (Figure 3) the lightest peening intensity (8.3 N/100%) increased the fatigue life of AW 7075 aluminium alloy with respect to the mechanically polished specimens. Based on the promising increase of the fatigue life of the previous treatment, the parameters for severe shot peening were chosen by a slight increase of the intensity to 9.6 N and significant increase of the coverage to 650%. This treatment provided even higher fatigue life increase, as can be seen in Figure 3. The higher peening intensity, 6.9 A/100%, had an opposite effect and caused a decrease of the fatigue life slightly under the level of the NP specimens. The higher peening intensity, 14.4 A/100%, again decreased the fatigue life and caused specimens to fracture after a number of cycles much lower than after treatment with 8.3 N/100% and even below the polished specimens. To answer the question whether shot peening with even higher parameters than 14.4 A/100% will not create a much deeper residual stress field that could again increase the fatigue life, the severe shot peening parameters of 14.9 A/650% were chosen. However, from the results in Figure 3, it is obvious that it had about the same degradation effect as the previous treatment (14.4 A/100%) and the degradation effect was saturated [2].

It is necessary to note that to provide full information about the influence of the shot peening treatment with particular parameters on the fatigue life using only two specimens is not sufficient. However, in an extruded material with no significant surface defects (as was observed in Figure 1) acting as nuclei for the fatigue crack initiation, it was enough for basic evaluation about the process parameters influence and later on these results were confirmed by the surface characteristics and the fracture surface analysis. This was confirmed by [27] where fatigue tests in the low-cycle, high-cycle and ultra-high cycle regions were carried out and the whole S-N curve is characteristic with low-scatter data. Also, results of the fatigue tests of the NP material in the high- and ultra-high cycle regions, provided in [5], confirmed the low scatter of the fatigue tests results in conditions of ultrasonic fatigue testing.

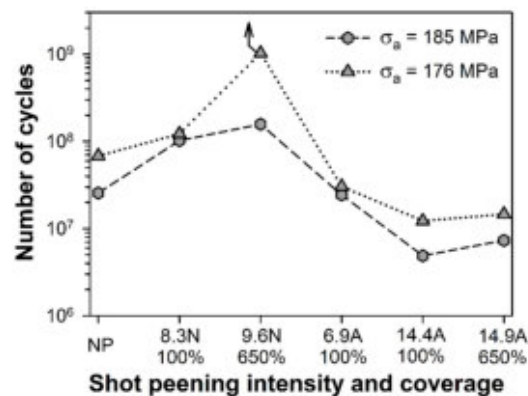


**Figure 3.** Dependence of fatigue life on the shot peening intensity and coverage of AW7075 aluminium alloy.

### 3.2. Surface Layer Characterization

To analyze the character of the surface layer and see the level of the plastic deformation, a longitudinal cut was made of one fractured specimen for each surface treatment (including polished specimen—NP), etched with the Fuss solution and analyzed by means of a scanning electron microscope (SEM). Note that the voids visible in the microstructure of Figures 4–9 are etched intermetallic particles. The surface layer of the NP specimen (Figure 4) shows a very shallow deformed surface layer, which is a result of plastic deformation introduced during the machining of the specimen's gauge length. Shot peening by 8.3 N intensity, with coverage of 100%, created a shallow but continuous and uniformly deformed surface layer with a thickness of approximately 30  $\mu\text{m}$  (Figure 5). The surface layer after treatment with the 9.6 N intensity with coverage of 650% (Figure 6) again created a shallow and uniformly deformed surface layer which was very similar to the surface layer obtained after the previous shot peening treatment (Figure 5). Again, the visible depth of the affected surface layer was approximately 30  $\mu\text{m}$ . The surface after the first two treatments was without the presence of any defects; however, an increased surface roughness was notable compared to the ground and polished specimen. Increasing the peening intensity to 6.9 A with coverage of 100% (Figure 7) and 14.4 A with coverage of 100% (Figure 8) respectively, increased the affected surface layer depth to approximately 100  $\mu\text{m}$ ; however, the severe plastic deformation caused creation of folds and micro cracks. Treatment with the 14.9 A intensity and coverage of 650% (Figure 9) caused a creation of a deformed surface layer almost twice as thick as the previous treatment and reaches almost 200  $\mu\text{m}$ . It also caused a total devastation of the surface and layers of the material started to separate. Summarization of the depth of the affected surface layers by all types of surface finishing is provided in Table 3.

**Table 3.** Depth of strengthened surface layer after various surface finishing.

Surface Finishing	Approximate Depth of Affected Layer ( $\mu\text{m}$ )
NP	15
8.3 N/100%	30
9.6 N/650%	30
6.9 A/100%	100
14.4 A/100%	100
14.9 A/650%	200



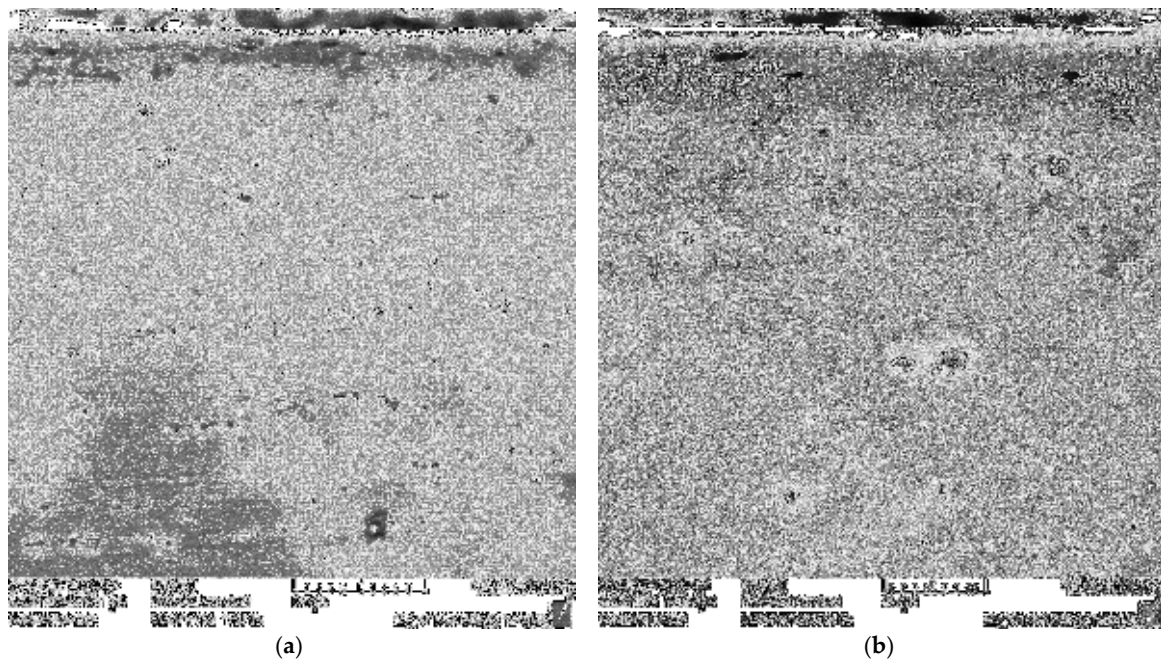


**Figure 4.** Surface layer of the not-peened (NP) specimen with shallow deformed layer after machining (a); in detail (b). Scanning electron microscope (SEM).

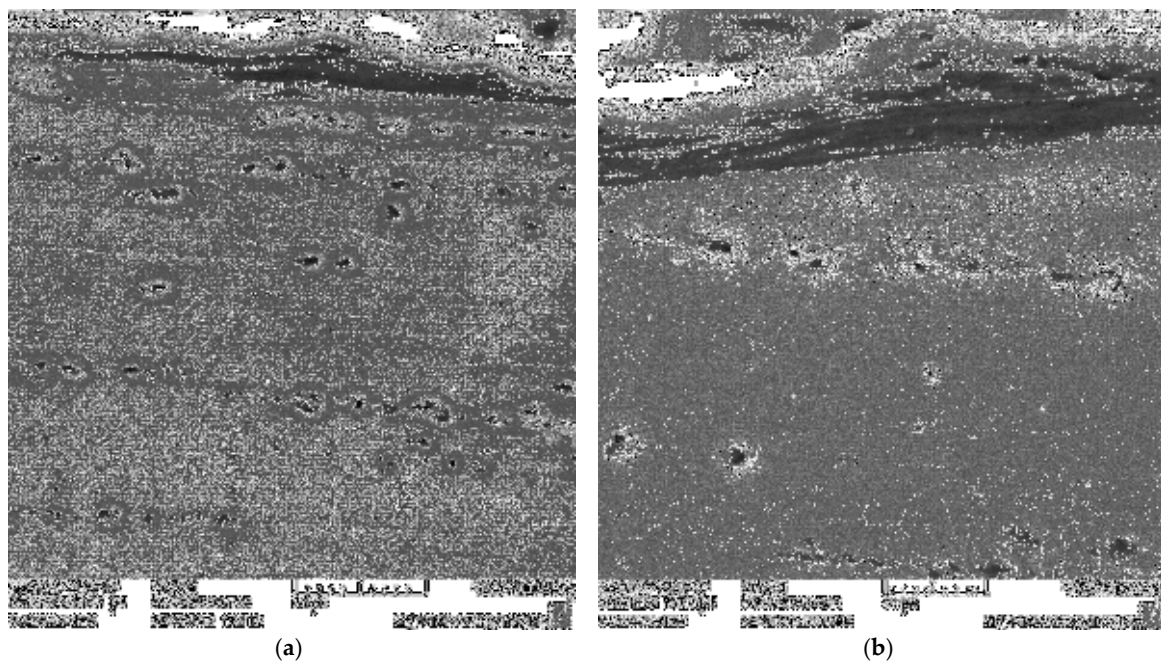


**Figure 5.** Surface layer of the 8.3 N/100% specimen with uniform strengthened layer after shot peening (a); in detail (b). SEM. Reproduced with permission from Trško, L.; Guagliano, M.; Bokůvka, O.; Nový, F.; Jambor, M.; Florková, Z. *J. Mater. Eng. Perform.* Published by Springer Nature, 2017 [5].

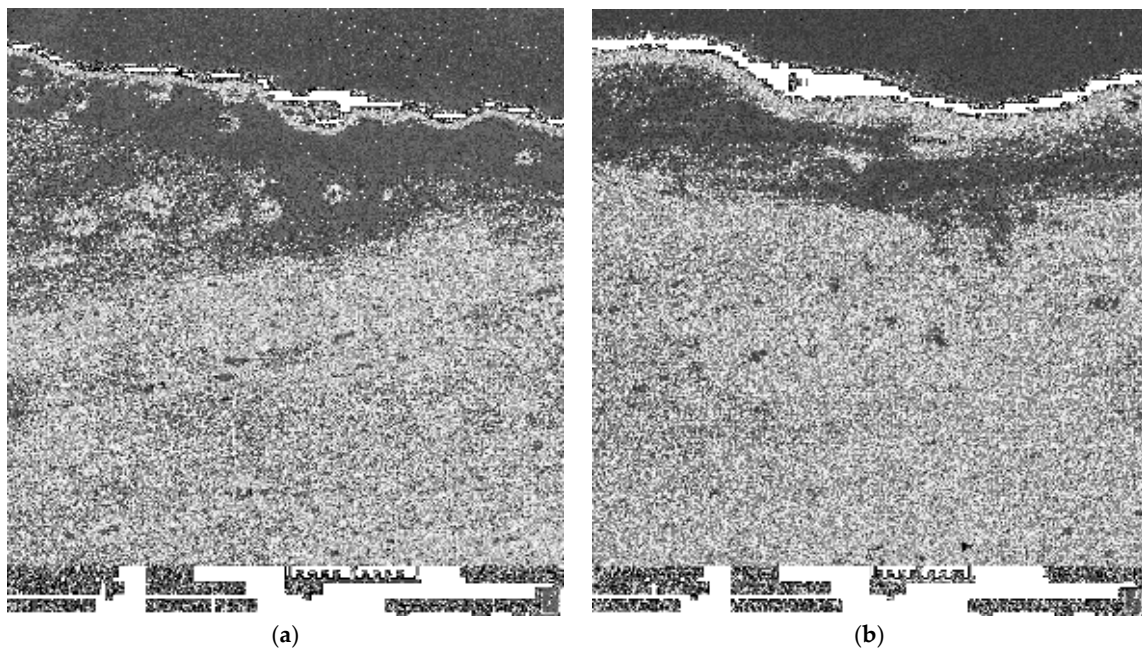


**Figure 6.** Surface layer of the 9.6 N/650% specimen with uniform strengthened layer after shot peening (a); in detail (b); SEM.

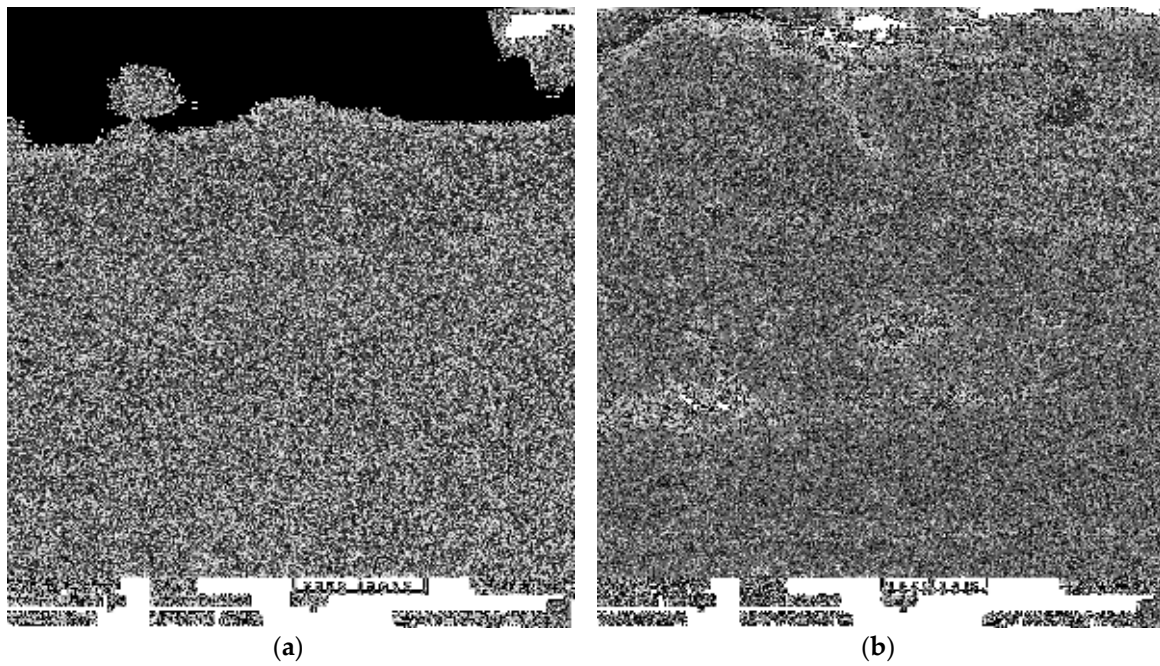


**Figure 7.** Surface layer of the 6.9 A/100% specimen with deep strengthened layer after shot peening with surface micro cracks (a); in detail (b); SEM.



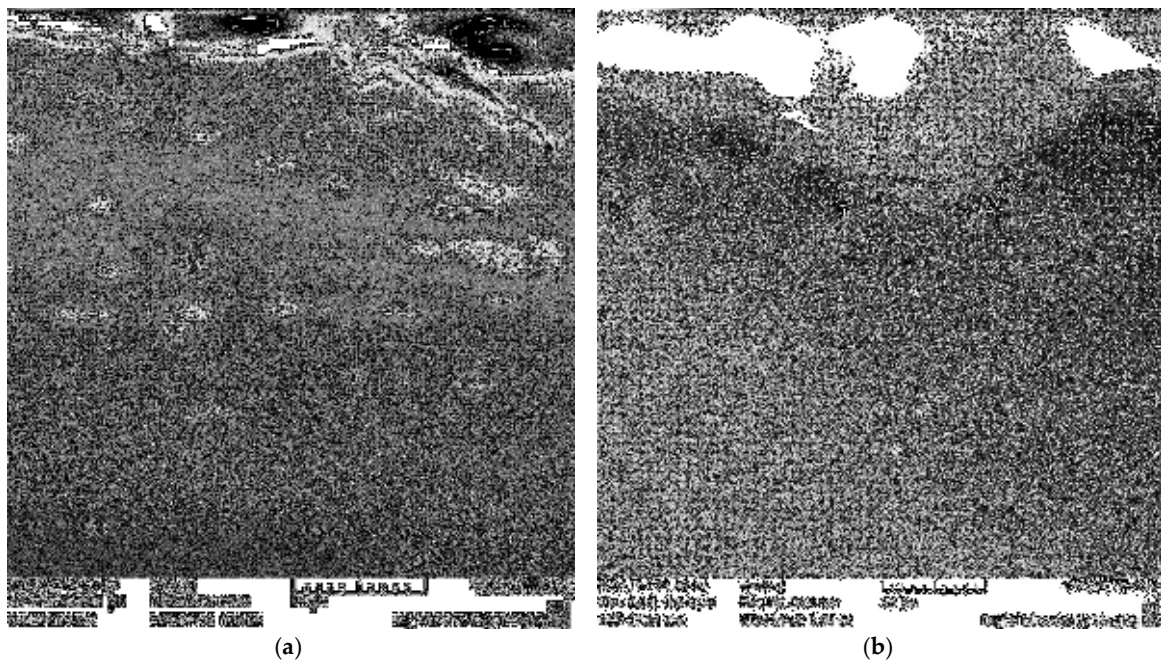


**Figure 8.** Surface layer of the 14.4 A/100% specimen with deep strengthened layer after shot peening with surface micro cracks (a); in detail (b); SEM.

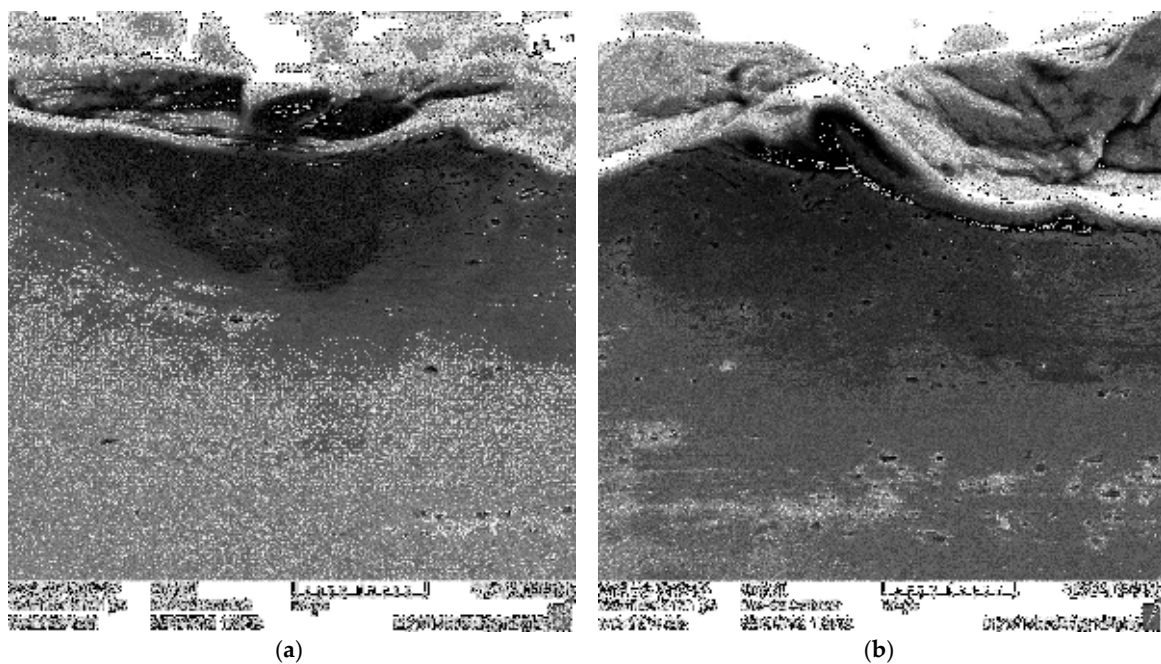


**Figure 9.** Surface layer of the 14.9 A/650% specimen with deep strengthened layer after shot peening with surface micro cracks and small layers peeling off (a); in detail (b); SEM.

### 3.3. Fracture Surface Analysis

In all the AW 7075 aluminium alloy specimens, fatigue cracks were initiated on the free surface and, initially, the crack propagated almost perpendicular to the direction of the loading force. After reaching several tenths of micrometers, the orientation of the crack propagation started to change to an angle of  $45^\circ$  up to  $60^\circ$  with respect to the vector of the loading force. This behavior was the best documented



on a longitudinal cut of the NP fatigue specimen with an initiated fatigue crack, propagated to approximately half of the cross section (Figure 10).

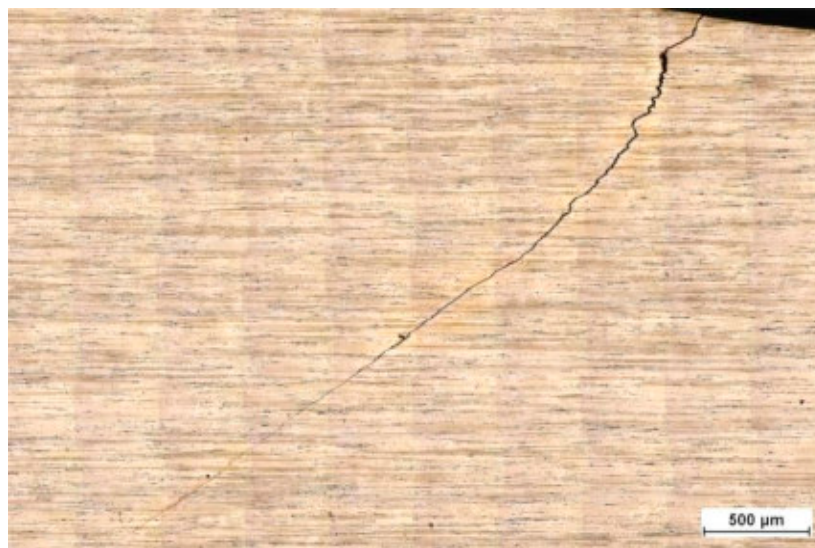


**Figure 10.** Character of the fatigue crack initiation and propagation in NP fatigue test specimen ( $\sigma_a = 176$  MPa,  $N_f = 6.8 \times 10^7$  cycles), longitudinal cut. Reproduced with permission from Trško, L.; Guagliano, M.; Bokůvka, O.; Nový, F.; Jambor, M.; Florková, Z. *J. Mater. Eng. Perform.* Published by Springer Nature, 2017 [5].

After the comparison of the close-up views of all types of the fatigue specimens, which were all tested at the stress amplitude level of  $\sigma_a = 185$  MPa (Figure 11), it is obvious that the fatigue crack propagation character is common to all of those specimens and the angle of propagation is approximately the same. The difference in the ratio between the surface fractured by the fatigue damage and the final rupture is caused by different times after which the length of the crack shifted the ultrasonic system out of resonance frequency.

When comparing the crack initiation sites on the NP and 8.3 N/100% shot peened specimens, despite the change of the surface character these have the same appearance and no difference in crack propagation in the strengthened surface layer can be observed as well (Figure 12).

On the fracture surface of a specimen treated with 9.6 N intensity and coverage of 650%, the fracture of the surface layer had a different appearance than the rest of the fracture surface. In addition, the orientation of the crack propagation in that surface layer was different, and it seems to be perpendicular to the original surface of the specimen (Figure 13).

After careful observation of the area close to the fatigue crack initiation site, two more, very narrow fatigue cracks initiated below the dominant one were found. Those cracks copy exactly the shape of the dominant crack, which means that the horizontally initiated crack is perpendicular to a vector of the applied force and then the crack propagation deviates towards the specimens' longitudinal axis (Figure 14a, marked with white arrows). After taking a closer look at the detail of the initiated crack (Figure 14b), it can be seen that the crack has no preferential orientation in relation to the surface dimples (shot peened surface morphology) and the crack propagates through the bottom of the dimples and also through the raised edges of the dimples.

Fatigue fracture of a specimen treated with the 6.9 A intensity with the coverage of 100% reveals more details of the fatigue crack initiation (Figure 15). In Figure 15a, the fatigue fracture character of the area close to the fatigue crack initiation can be seen; the strong influence of the deformation texture on the short cracks' propagation is obvious. Short fatigue cracks during their propagation had extremely small increments (approximately  $0.1 \mu\text{m}$ ), which is best documented in Figure 15b. Around the fatigue crack initiation site of this specimen, a net of secondary cracks surrounding the

area of the main crack initiation site can be observed (Figure 16). Those cracks were present only under the initiation site and, according to Figure 17, all of them were created by forking of the main crack. The fracture appearance of the treated surface layer was also slightly different than the inner part of the fatigue fracture surface, as can be seen in Figure 17.

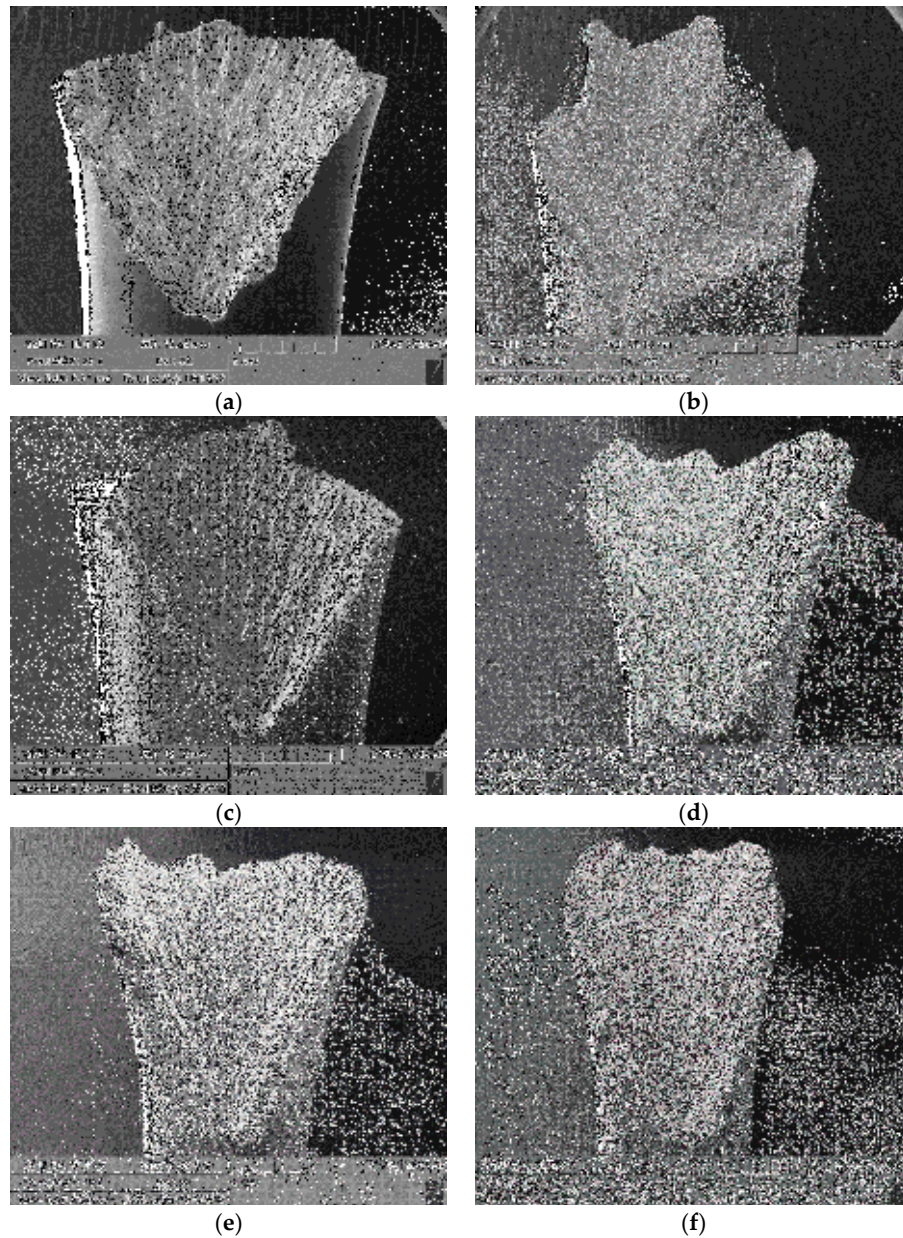


**Figure 11.** Macro views of fatigue fractures of specimens loaded at stress level  $\sigma_a = 185$  MPa, SEM. (a) NP,  $\sigma_a = 185$  MPa,  $N_f = 2.6 \times 10^7$  cycles; (b) 8.3 N/100%,  $\sigma_a = 185$  MPa,  $N_f = 1.0 \times 10^8$  cycles; (c) 9.6 N/650%,  $\sigma_a = 185$  MPa,  $N_f = 1.6 \times 10^8$  cycles; (d) 6.9 A/100%,  $\sigma_a = 185$  MPa,  $N_f = 2.4 \times 10^7$  cycles; (e) 14.4 A/100%,  $\sigma_a = 185$  MPa,  $N_f = 4.9 \times 10^6$  cycles; (f) 14.9 A/650%,  $\sigma_a = 185$  MPa,  $N_f = 7.3 \times 10^6$  cycles.



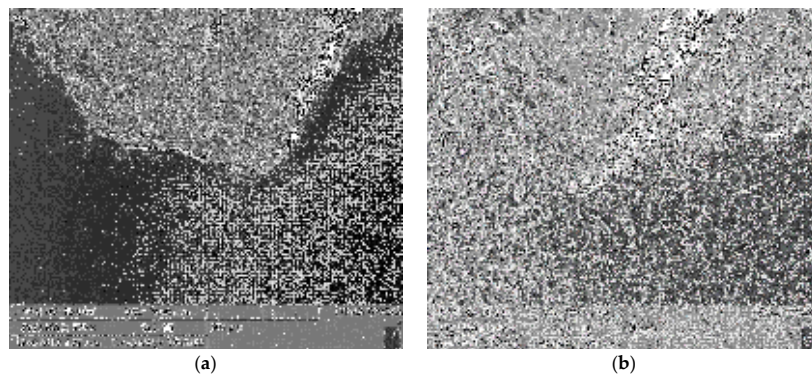


**Figure 12.** Fatigue crack initiation sites of fatigue test specimens: (a) NP,  $\sigma_a = 185$  MPa,  $N_f = 2.6 \times 10^7$  cycles; (b) 8.3N/100%,  $\sigma_a = 185$  MPa,  $N_f = 1.0 \times 10^8$  cycles, SEM.

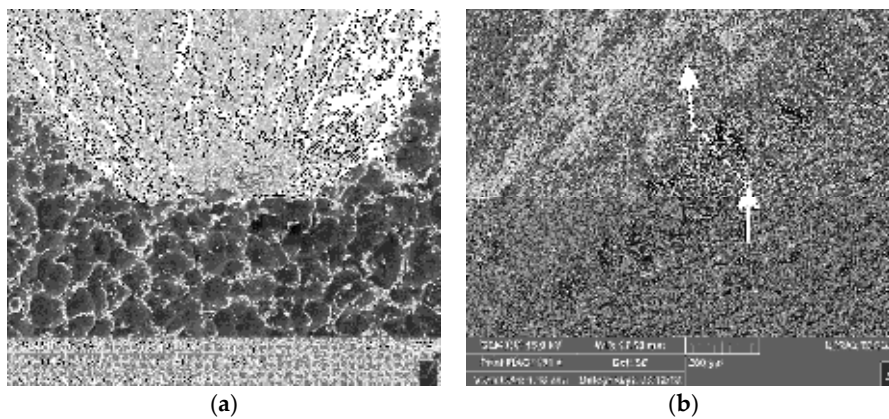


**Figure 13.** Fatigue crack initiation site of 9.6 N/650% shot peened specimen (a); and different character of fatigue crack propagation in the strengthened surface layer—the crack path with respect to the specimen's surface is marked with arrows (b);  $\sigma_a = 185$  MPa,  $N_f = 1.6 \times 10^8$  cycles, SEM. Reproduced with permission from Trško, L.; Guagliano, M.; Bokůvka, O.; Nový, F.; Jambor, M.; Florková, Z. *J. Mater. Eng. Perform.* Published by Springer Nature, 2017 [5].

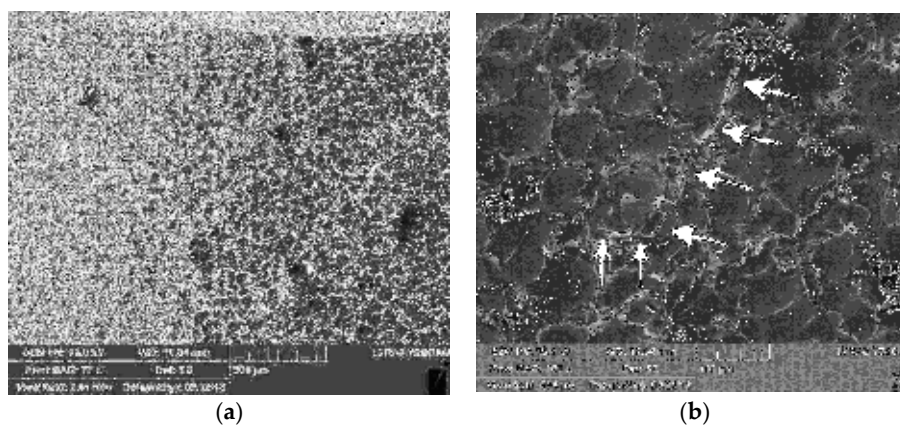


**Figure 14.** Multiple initiated fatigue cracks (a); and in detail (b); specimen treated with 9.6 N/650% parameters,  $\sigma_a = 185$  MPa,  $N_f = 2.5 \times 10^7$  cycles, SEM. Reproduced with permission from Trško, L.; Guagliano, M.; Bokůvka, O.; Nový, F.; Jambor, M.; Florková, Z. *J. Mater. Eng. Perform.* Published by Springer Nature, 2017 [5].

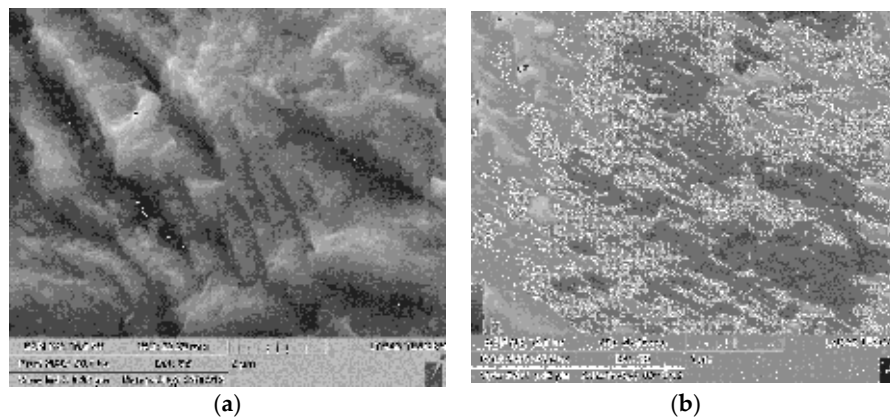


**Figure 15.** Fatigue crack propagation character near the fatigue crack initiation site (a); and extremely small propagation increments of fatigue crack (b); specimen treated with 6.9 A/100% parameters,  $\sigma_a = 185$  MPa,  $N_f = 2.4 \times 10^7$  cycles, SEM.

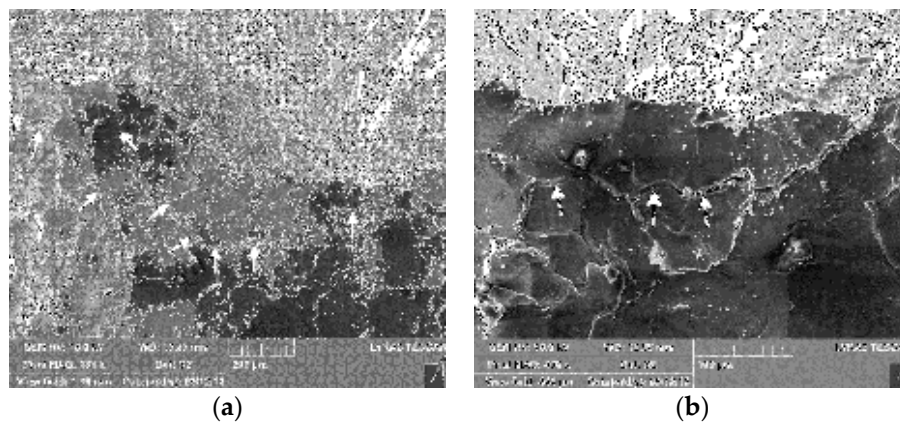


**Figure 16.** Net of secondary cracks surrounding the area under the fatigue crack initiation site (a); in detail (b); specimen treated with 6.9 A/100% parameters,  $\sigma_a = 185$  MPa,  $N_f = 2.4 \times 10^7$  cycles, SEM.

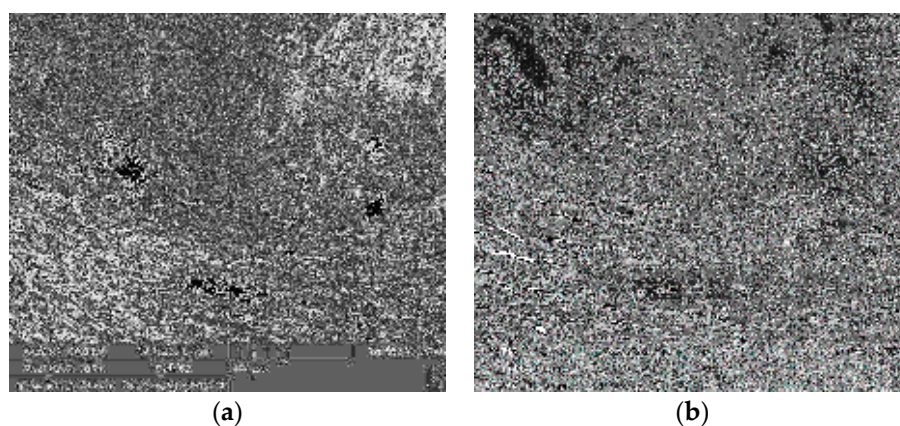


**Figure 17.** Different appearance of the strengthened surface layer on the fracture surface (a); and forking of the main crack in the area of fatigue crack initiation (b); specimen treated with 6.9 A/100% parameters,  $\sigma_a = 185$  MPa,  $N_f = 2.4 \times 10^7$  cycles, SEM.

Observation of the fracture surface of the specimen peened with the 14.4 A intensity with coverage of 100% reveals that the net of the secondary cracks under the initiation site is even more prominent (Figure 18). The fracture of the surface layer has also a different character and it is much deeper than in



previous treatments (Figure 19a). In addition, in a small number of places it was observed that whole material layers on the surface started to peel off from the specimen due to the applied cyclic loading (Figure 19b).

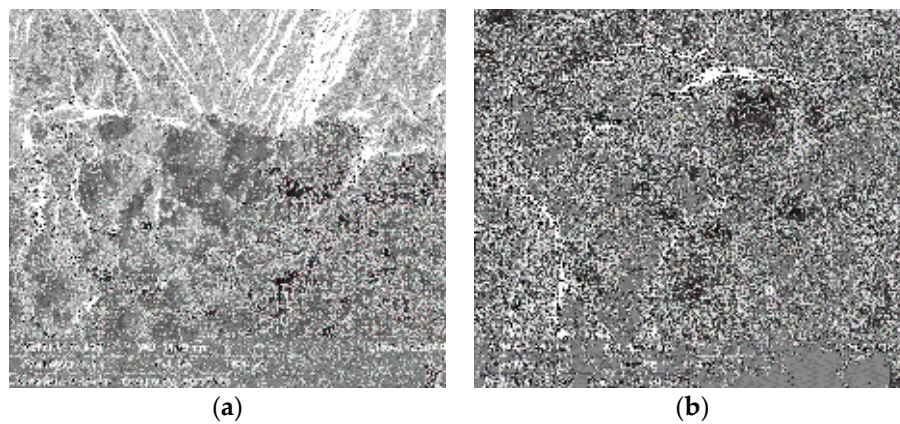


**Figure 18.** Net of secondary cracks under the fatigue crack initiation site (a); in detail (b); specimen treated with 14.4 A/100% parameters,  $\sigma_a = 185$  MPa,  $N_f = 4.9 \times 10^6$  cycles, SEM.

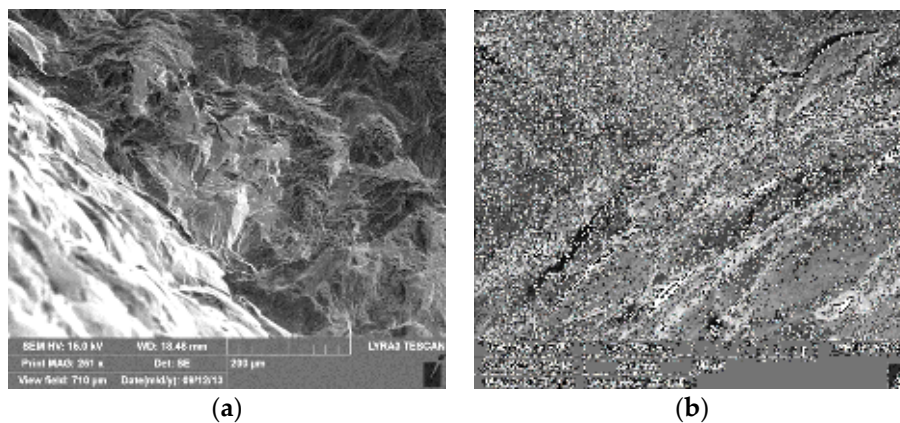


**Figure 19.** Different character of crack propagation in the strengthened surface layer (a); and peeling-off surface layer (b); specimen treated with 14.4 A/100% parameters,  $\sigma_a = 185$  MPa,  $N_f = 4.9 \times 10^6$  cycles, SEM.

The fracture surface of a specimen after the most severe shot peening treatment with the intensity of 14.9 A and coverage of 650% also shows a net of secondary cracks under the area of initiation (Figure 20). Again, a deep surface layer had a different fracture character than the rest of the fracture surface (Figure 21a), but the thickness of this layer, of a different appearance, seems not to be as uniform as in previous cases. Whole layers of material peeled off from the surface of the specimen, as can be seen in Figure 21b.



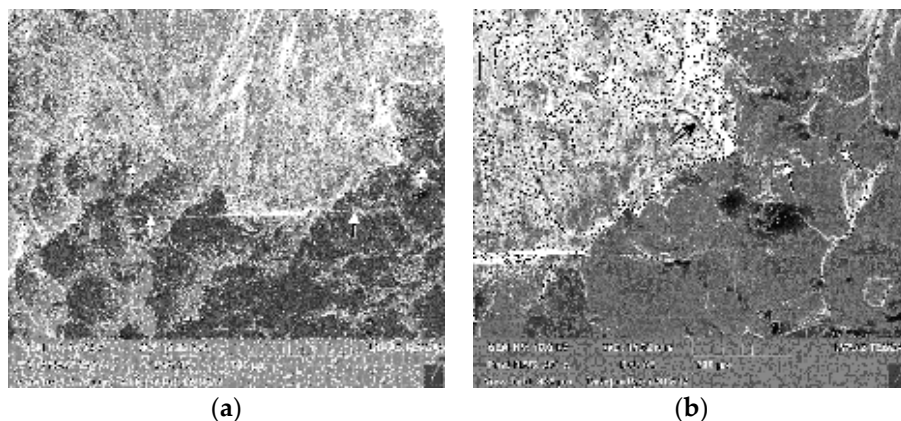


**Figure 20.** Net of secondary cracks under the fatigue crack initiation site (a); in detail (b); specimen treated with 14.9 A/650% parameters,  $\sigma_a = 185$  MPa,  $N_f = 7.3 \times 10^6$  cycles, SEM.

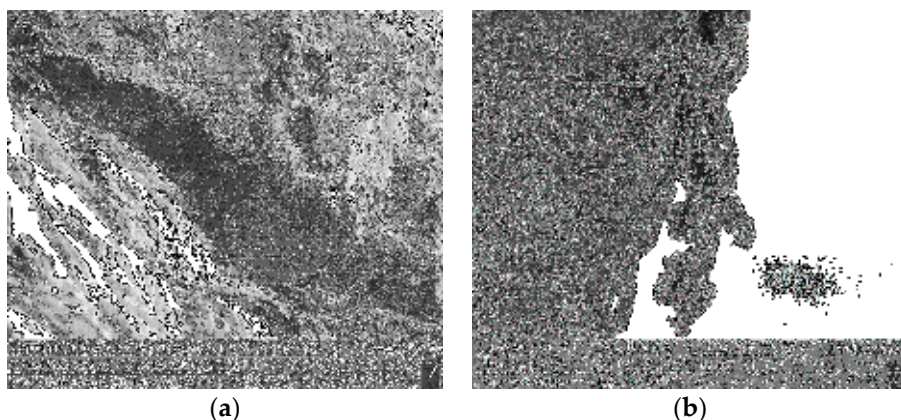


**Figure 21.** Different character of crack propagation in the strengthened surface layer (a); and peeling-off surface layer (b); specimen treated with 14.9 A/650% parameters,  $\sigma_a = 185$  MPa,  $N_f = 7.3 \times 10^6$  cycles, SEM. Reproduced with permission from Trško, L.; Guagliano, M.; Bokůvka, O.; Nový, F.; Jambor, M.; Florková, Z. *J. Mater. Eng. Perform.* Published by Springer Nature, 2017 [5].

The secondary initiated fatigue crack (Figure 22a) was extremely narrow and had a width of barely 1  $\mu\text{m}$  (Figure 22b). Again, the net of secondary cracks, copying the boundary between the affected surface layer and the core of the material, evolved and resulted in the separation of the treated surface layer from the specimen due to the cyclic loading (Figure 23).

Surface treatment by shot peening affects only the surface layers of material, so fatigue crack propagation in the core of the specimen had completely the same character in all the studied specimens, and the most characteristic figures from all of them were chosen for the best description of the fatigue crack propagation mechanism. During the fatigue crack propagation, the friction between the two fracture surfaces at high frequencies caused the creation of fretting damage on the surfaces (Figure 24a). Those damaged parts of the surface oxidized very quickly (Figure 24b) which resulted in a strong degradation of the fracture surface. Due to this oxidation, it was possible to study the fatigue propagation mechanism mainly on the boundary with the final rupture, where the material was not exposed to such a high number of cycles to create fretting damage. Fatigue cracks propagated by the transcrystalline fracture mechanism of a “band” character, which is caused by the laminar character of the microstructure after extrusion (Figure 25a). Striations, perpendicular to the direction of the fatigue crack growth direction, were present very rarely and their clear observation was possible only on one of the specimens in the crack initiation area (Figure 25b). After a closer investigation of the stable fatigue crack propagation area, it was noticed that the surface was covered with very

fine “wrinkles” created by the fracture along precipitates (Figure 26a), and many intermetallic phases present in the material were separated from the matrix (Figure 26b). The surface of the final rupture was characterized by the transcrystalline ductile fracture with coarse and fine dimple morphology. The coarse dimples (Figure 27a) were created by fractures around intermetallic phases and fine dimples around precipitates (Figure 27b).

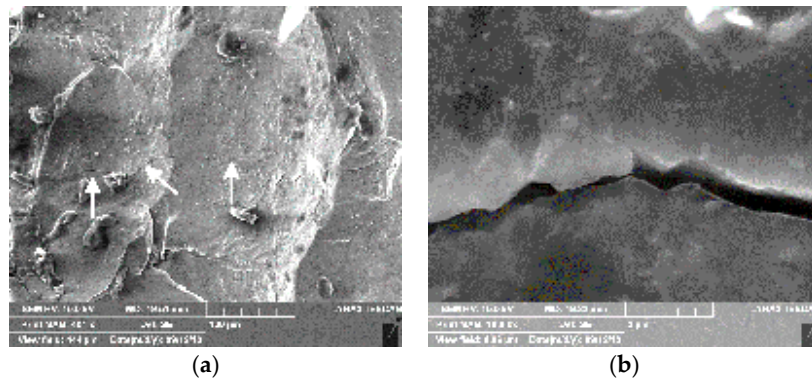


**Figure 22.** Multiple initiated fatigue cracks (a); and in detail (b); specimen treated with 14.9 A/650% parameters,  $\sigma_a = 185$  MPa,  $N_f = 7.3 \times 10^6$  cycles, SEM.

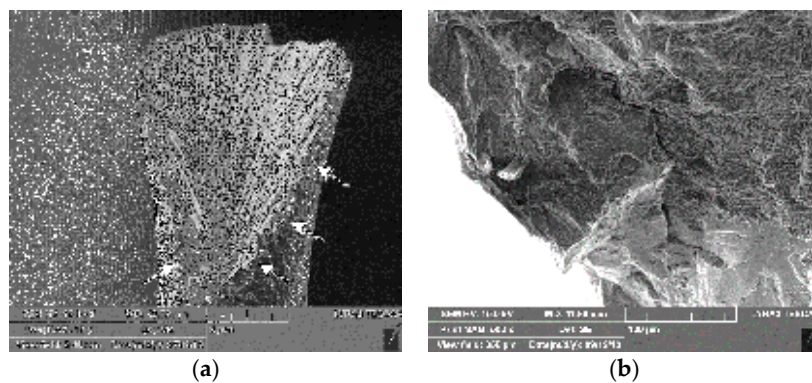


**Figure 23.** Peeling-off surface layer on the macro view (a); and in detail (b); specimen treated with 14.9 A/650% parameters,  $\sigma_a = 185$  MPa,  $N_f = 7.3 \times 10^6$  cycles, SEM.

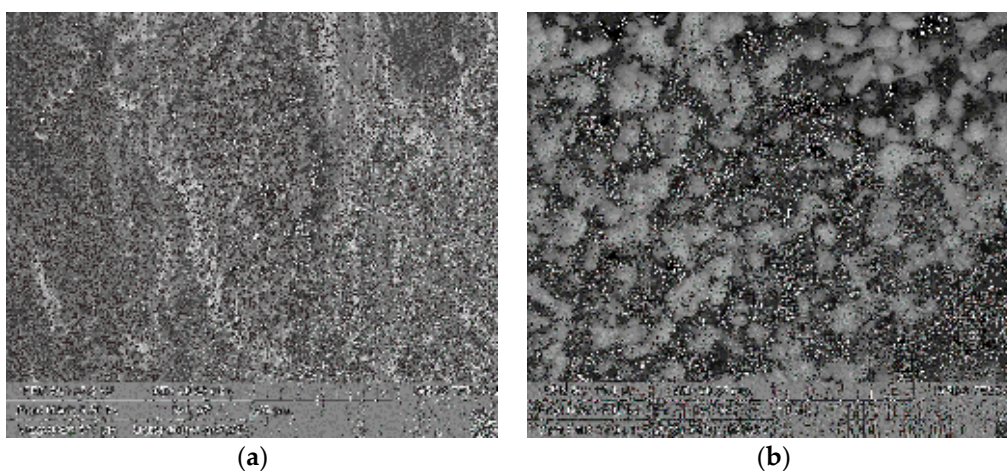


**Figure 24.** Surface layer damaged by fretting (a); and detail of the oxide created on the damaged surface (b); specimen treated with 6.9 A/100% parameters,  $\sigma_a = 185$  MPa,  $N_f = 2.4 \times 10^7$  cycles, SEM.



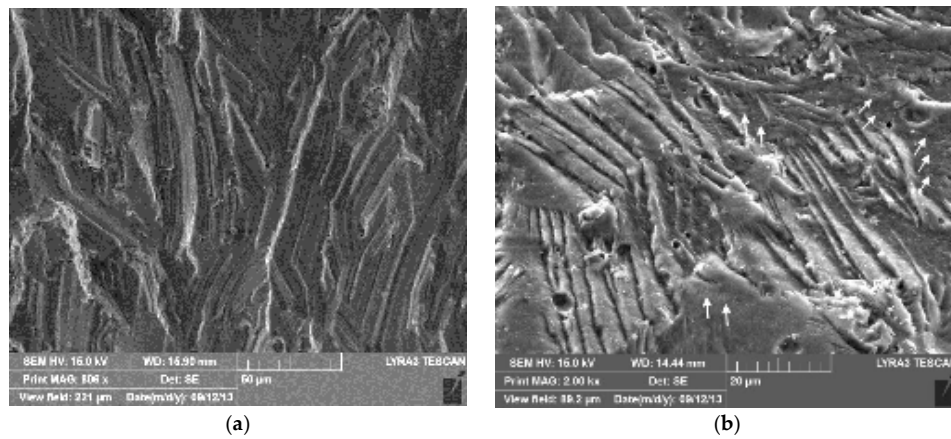


**Figure 25.** Character of the fatigue-fracture surface (a) 6.9 A/100%,  $\sigma_a = 185$  MPa,  $N_f = 2.4 \times 10^7$  cycles; and detail of the striations rarely found on the fracture surface; (b) 9.6 N/650% parameters,  $\sigma_a = 185$  MPa,  $N_f = 1.6 \times 10^8$  cycles; SEM.

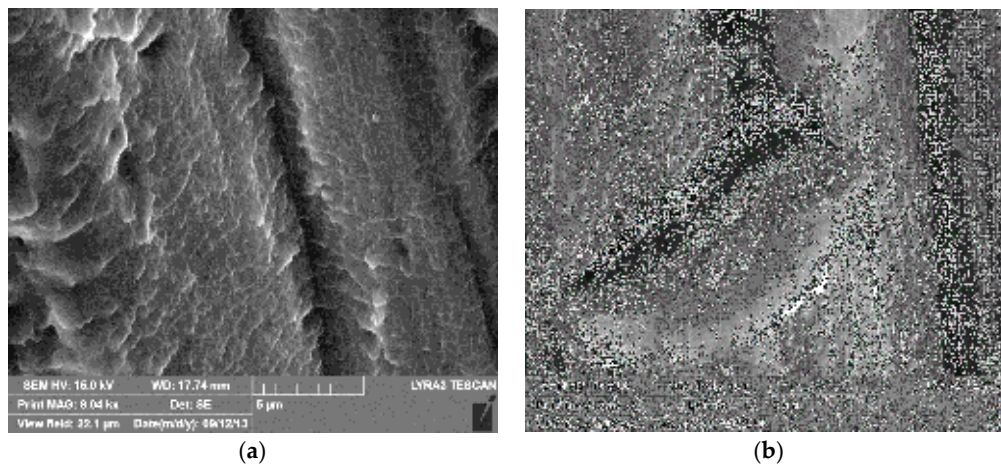


**Figure 26.** “Wrinkly” character of the fracture surface created by fracture propagation along precipitates (a) 8.3 N/100%,  $\sigma_a = 185$  MPa,  $N_f = 1.0 \times 10^8$  cycles; and separation of the intermetallic phases from the matrix; (b) NP,  $\sigma_a = 185$  MPa,  $N_f = 2.6 \times 10^7$  cycles; SEM.

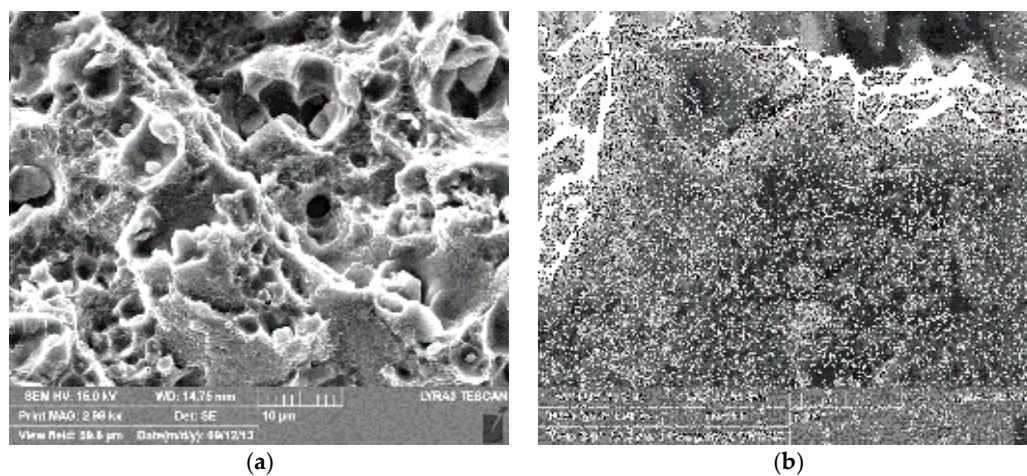


**Figure 27.** The final fracture, a transcrystalline ductile fracture with coarse dimple morphology (a) NP,  $\sigma_a = 185$  MPa,  $N_f = 2.6 \times 10^7$  cycles; and fine dimple morphology; (b) 8.3 N/100%,  $\sigma_a = 185$  MPa,  $N_f = 1.0 \times 10^8$  cycles.

#### 4. Discussion

Surface treatment by shot peening can significantly improve the fatigue properties of structural materials by the creation of a plastically deformed and grain-refined surface layer. The process of the creation of this layer with superior mechanical properties is characterized by three main mechanisms: work-hardening (increase in the dislocation density); introduction of compressive residual stresses; and grain refinement [1,2,4,5,8,14–18,28].

Fatigue test results of AW 7075 aluminium alloy justify a deeper analysis of the influence of the shot peening intensity and coverage on the fatigue lifetime and fracture surface character. Figure 3 shows the trend of the fatigue life of AW 7075 with respect to the peening parameters. The highest increase of the fatigue strength was achieved with 9.6 N/650% parameters, and further increase of the peening intensity and coverage caused a rapid drop of the fatigue strength even below that of the not-peened material.

The fatigue fracture surface analysis of specimens from AW 7075 aluminium alloy showed that in the process of fatigue crack initiation, the short crack propagation and the direction of the crack propagation are strongly affected by the material's microstructure. The multiple changes of the crack orientation at the beginning of the fatigue damage process were caused by the deformation texture created during the extrusion process. When a crack hits a deformed row with different crystallographic orientation and slightly different mechanical properties, the crack path changes to the direction with the less resistance to crack propagation. The deviation of the fatigue crack orientation of about 45° up to 60° with respect to the vector of the loading force is probably also related to the deformation texture and the vector of maximal shear stress in the cross section. This behavior was also observed in other work dealing with the fatigue of wrought aluminium alloys, but the reason is still not fully understood [29–32].

The shot peening treatment of the AW 7075 aluminium alloy with intensity of 8.3 N and coverage of 100% did not result in significant changes in the fatigue crack initiation and propagation processes. The fatigue crack propagation in the surface layer (Figure 12b) had similar character as the NP specimen (Figure 12a) so the increase of the fatigue life was mainly related to the compressive residual stress introduced during the treatment which delayed the fatigue crack initiation. Increasing the peening intensity to 9.6 N and the coverage to 650% created a work hardened surface layer (visible in Figure 6) with a different fatigue crack propagation character (Figure 13b) than for the core of the material, which corresponds to a surface layer with a higher resistance to fatigue crack propagation. This treatment also resulted in increasing the number of initiated fatigue cracks; however, this was not caused by the reduced surface integrity and creation of micro cracks after the peening process, because no such damage was observed before fatigue loading (Figure 6). The impact dimples, created on the peened surface (an increase of the surface roughness visible in Table 1) were, in fact, small surface notches with very similar geometry. Since the fatigue crack initiation in the smooth specimens represents more than 90% of all the loading cycles necessary for its fracture, multiple fatigue-crack initiation means that those cracks had to be initiated after a similar number of loading cycles. The reason is that dimples after the shot peening treatment served as fatigue crack initiation points with very similar stress conditions (defined by the similar dimple geometry, which depends on the peening media shape and size) for fatigue crack initiation, so multiple fatigue cracks were initiated at a very similar number of cycles. Due to the continuous cyclic loading, one of the cracks starts to become dominant and predetermine the specimen's fatigue lifetime. The initiated secondary fatigue cracks were very narrow (Figure 24) due to the compressive residual stress under the surface, which was closing those cracks in the early stages. The fact that even after a significant increase of the surface roughness, the fatigue life increased, means that the compressive residual stress field and grain refinement were still able to delay crack initiation and partially slow down crack propagation in the first stage of fatigue damage.

All the higher peening intensities and coverages had a strong negative effect on the fatigue life (Figure 3), which can be explained by the creation of micro cracks in the surface layer and peeling-off material from the specimen's surface (Figures 7–9). Further impact of the peening media, after

exhaustion of the material's plastic deformation ability, caused crack creation and delamination of the surface layer, because the material was not able to accumulate more energy and this energy was used for the creation of free surfaces. Again, the difference in the fatigue fracture character in the surface layers was observed, what is a result of intensive surface hardening, with an almost complete loss of the material's ductility (Figures 19a and 21a). The treatments with higher peening parameters also increased the number of initiated fatigue cracks and the non-uniform appearance of the surface layer with different fracture characteristics was observed due to the layers of material completely peeled off from the surface of the loaded specimen.

In previous work [2], the creation of micro cracks in the surface layer after severe shot peening of a low-alloyed steel was also observed; however, a positive influence of the treatment on the fatigue lifetime was still recorded. This means that even when some cracks on the surfaces are created, the strengthened layer under their tip can restrain their propagation. Thus, it does not necessarily mean that every time the peening treatment results in creation of micro cracks on the surface, the parameters used have to be considered as too extensive and the surface as overpeened. However, the peeling off of large parts of the strengthened surface layer as in Figures 8 and 9 results in non-uniformity of the layer and the process parameters could be considered as too severe. On the other hand, the ductility of the core material plays a role in the fatigue crack propagation process, when the more ductile material can still retard crack growth or stop the crack due to the absorption of the energy necessary for crack growth introduced by the cyclic loading.

## 5. Conclusions

The premature fatigue fracture of a shot peened component can be caused by using unnecessarily severe treatment parameters. This cannot just be a result of using the unoptimized surface parameters, but could also be caused by process inhomogeneity, or when the shot peening is performed on a component with a complicated shape where some parts of the surface are exposed to the peening process for a longer time or at different angles.

Increased surface roughness and multiple fatigue crack initiation on the peened surface certainly do not mean that the peening process was performed wrongly, and uniformity and consistency of the strengthened surface layer in critical places have to be evaluated as criteria for proper surface quality. The presence of a crack on the AW 7075 aluminium alloy surface after shot peening means that unnecessarily extensive shot peening parameters were used, and this treatment will not have a beneficial effect on the fatigue life of the peened component.

**Acknowledgments:** This research was supported by project of SK/RU International Technical and Scientific Cooperation no. 0393-2016, by project APVV 14-0284, projects VEGA Nos.: 1/0045/17 and 1/0029/18, project CEITEC 2020 (LQ1601) and IPMinfra (LM2015069).

**Author Contributions:** Libor Trško and Otakar Bokůvka conceived and designed the experiments and wrote the paper. Stanislava Fintová performed the fracture-surface analysis, František Nový analyzed the fracture-surface data and evaluated the fracture mechanisms. Michal Jambor with Zuzana Florková and Monika Oravcová manufactured the fatigue-test specimens and performed the ultrasonic fatigue tests. Zuzana Florková and Filip Pastorek performed the surface roughness analysis and surface-layer documentation and evaluation.

**Conflicts of Interest:** The authors declare no conflict of interest.

## References

1. Baiker, S. *Shot Peening: A Dynamic Application and Its Future*, 3rd ed.; Metal Finishing News: Wetzikon, Switzerland, 2012.
2. Trško, L.; Bokůvka, O.; Novy, F.; Guagliano, M. Effect of severe shot peening on ultra-high-cycle fatigue of a low-alloy steel. *Mater. Des.* **2014**, *57*, 103–113. [[CrossRef](#)]
3. Walker, J.; Thomas, D.; Gao, Y. Effects of shot peening and pre-strain on the fatigue life of dual phase martensitic and Bainitic steels. *J. Manuf. Process.* **2017**, *26*, 419–424. [[CrossRef](#)]



4. Zhang, J.; Li, W.; Wang, H.; Song, Q.; Lu, L.; Wang, W.; Liu, Z. A comparison of the effects of traditional shot peening and micro-shot peening on the scuffing resistance of carburized and quenched gear steel. *Wear* **2016**, *368*, 253–257. [[CrossRef](#)]
5. Trško, L.; Guagliano, M.; Bokůvka, O.; Nový, F.; Jambor, M.; Florková, Z. Influence of severe shot peening on the surface state and ultra-high-cycle fatigue behavior of an aw 7075 aluminum alloy. *J. Mater. Eng. Perform.* **2017**, *26*, 2784–2797. [[CrossRef](#)]
6. González, J.; Bagherifard, S.; Guagliano, M.; Fernández Pariente, I. Influence of different shot peening treatments on surface state and fatigue behaviour of al 6063 alloy. *Eng. Fract. Mech.* **2017**, *185*, 72–81. [[CrossRef](#)]
7. Barry, N.; Hainsworth, S.; Fitzpatrick, M. Effect of shot peening on the fatigue behaviour of cast magnesium A8. *Mater. Sci. Eng. A* **2009**, *507*, 50–57. [[CrossRef](#)]
8. Liu, W.; Wu, G.; Zhai, C.; Ding, W.; Korsunsky, A.M. Grain refinement and fatigue strengthening mechanisms in as-extruded Mg-6Zn-0.5Zr and Mg-10Gd-3Y-0.5Zr magnesium alloys by shot peening. *Int. J. Plast.* **2013**, *49*, 16–35. [[CrossRef](#)]
9. Yao, C.; Wu, D.; Ma, L.; Tan, L.; Zhou, Z.; Zhang, J. Surface integrity evolution and fatigue evaluation after milling mode, shot-peening and polishing mode for TB6 titanium alloy. *Appl. Surf. Sci.* **2016**, *387*, 1257–1264. [[CrossRef](#)]
10. Shaw, L.; Tian, J.; Ortiz, A.; Dai, K.; Villegas, J.; Liaw, P.; Ren, R.; Klarstrom, D. A direct comparison in the fatigue resistance enhanced by surface severe plastic deformation and shot peening in a C-2000 superalloy. *Mater. Sci. Eng. A* **2010**, *527*, 986–994. [[CrossRef](#)]
11. He, B.; Soady, K.; Mellor, B.; Harrison, G.; Reed, P. Fatigue crack growth behaviour in the LCF regime in a shot peened steam turbine blade material. *Int. J. Fatigue* **2016**, *82*, 280–291. [[CrossRef](#)]
12. Ferreira, N.; Ferreira, J.A.M.; Antunes, P.V.; Costa, J.D.; Capela, C. Fatigue crack propagation in shot peened al 7475-t7351 alloy specimens. *Procedia Eng.* **2016**, *160*, 254–261. [[CrossRef](#)]
13. Trsko, L.; Guagliano, M.; Lukac, P.; Bokuvka, O.; Novy, F. Effects of severe shot peening on the surface state of AW 7075 Al alloy. *Kovove Mater. Met. Mater.* **2015**, *53*, 239–243. [[CrossRef](#)]
14. Bagherifard, S.; Slawik, S.; Fernandez-Pariente, I.; Pauly, C.; Mucklich, F.; Guagliano, M. Nanoscale surface modification of AISI 316L stainless steel by severe shot peening. *Mater. Des.* **2016**, *102*, 68–77. [[CrossRef](#)]
15. Unal, O.; Varol, R. Surface severe plastic deformation of AISI 304 via conventional shot peening, severe shot peening and re-peening. *Appl. Surf. Sci.* **2015**, *351*, 289–295. [[CrossRef](#)]
16. Hassani-Gangaraj, S.; Cho, K.; Voigt, H.; Guagliano, M.; Schuh, C. Experimental assessment and simulation of surface nanocrystallization by severe shot peening. *Acta Mater.* **2015**, *97*, 105–115. [[CrossRef](#)]
17. Maleki, E. Modeling of severe shot peening effects to obtain nanocrystalline surface on cast iron using artificial neural network. *Mater. Today Proc.* **2016**, *3*, 2197–2206. [[CrossRef](#)]
18. Mikova, K.; Bagherifard, S.; Bokuvka, O.; Guagliano, M.; Trsko, L. Fatigue behavior of X70 microalloyed steel after severe shot peening. *Int. J. Fatigue* **2013**, *55*, 33–42. [[CrossRef](#)]
19. Liu, W.; Dong, J.; Zhang, P.; Zhai, C.; Ding, W. Effect of shot peening on surface characteristics and fatigue properties of T5-treated ZK60 alloy. *Mater. Trans.* **2009**, *50*, 791–798. [[CrossRef](#)]
20. Cammett, J. Are you peening too much? *Shot Peener Mag.* **2014**, *28*, 10–14.
21. Higounenc, O. Correlation of shot peening parameters to surface characteristic. In Proceedings of the 9th International Conference for Shot Peening, Paris, France, 6–9 September 2005; Niku-Lari, A., Schulze, V., Eds.; IITT-International: Paris, France, 2005; pp. 28–35.
22. Polmear, I. *Light Alloys*, 4th ed.; Butterworth-Heinemann: Oxford, UK, 2006; ISBN 978-0-75-066371-7.
23. Davis, J.R.; Committee, A.I.H. *ASM Handbook Volume 2: Properties and Selection: Nonferrous Alloys and Special-Purpose Materials*; ASM International: Almere, The Netherlands, 1998; ISBN 978-0-87170-378-1.
24. Ringer, S.P.; Raviprasad, K. Developments in age-hardenable aluminium alloys and rational design of microstructure. *Mater. Sci. Forum* **2000**, *24*, 59–94.
25. Maloney, S.K.; Hono, K.; Polmear, I.J.; Ringer, S.P. The chemistry of precipitates in an aged Al-2.1Zn-1.7Mg at % alloy. *Scr. Mater.* **1999**, *41*, 1031–1038. [[CrossRef](#)]
26. Bokuvka, O.; Nicoletto, G.; Guagliano, M.; Kunz, L.; Palcek, P.; Novy, F.; Chalupova, M. *Fatigue of Materials at Low and High Frequency Loading*, 2nd ed.; University of Zilina: Zilina, Slovakia, 2015; ISBN 978-80-554-0857-6.
27. Zapletal, J.; Věchet, S.; Kohout, J.; Liskutin, P. Fatigue lifetime of 7075 aluminium alloy from ultimate tensile strength to permanent fatigue limit. *Commun. Sci. Lett. Univ. Žilina* **2009**, *11*, 17–21.

28. Mahmoudi, A.; Ghasemi, A.; Farrahi, G.; Sherafatnia, K. A comprehensive experimental and numerical study on redistribution of residual stresses by shot peening. *Mater. Des.* **2016**, *90*, 478–487. [[CrossRef](#)]
29. Srivatsan, T.; Anand, S.; Sriram, S.; Vasudevan, V. The high-cycle fatigue and fracture behavior of aluminum alloy 7055. *Mater. Sci. Eng. A* **2000**, *281*, 292–304. [[CrossRef](#)]
30. Srivatsan, T. An investigation of the cyclic fatigue and fracture behavior of aluminum alloy 7055. *Mater. Des.* **2002**, *23*, 141–151. [[CrossRef](#)]
31. Jogi, B.; Brahmkara, P.; Nanda, V.; Prasad, R. Some studies on fatigue crack growth rate of aluminum alloy 6061. *J. Mater. Process. Technol.* **2008**, *201*, 380–384. [[CrossRef](#)]
32. Xue, Y.; McDowell, D.L.; Horstemeyer, M.F.; Dale, M.H.; Jordon, J.B. Microstructure-based multistage fatigue modeling of aluminum alloy 7075-T651. *Eng. Fract. Mech.* **2007**, *74*, 2810–2823. [[CrossRef](#)]



© 2018 by the authors. Licensee MDPI, Basel, Switzerland. This article is an open access article distributed under the terms and conditions of the Creative Commons Attribution (CC BY) license (<http://creativecommons.org/licenses/by/4.0/>).

- IX. [33] M. Arzaghi, S. Fintová, C. Sarrazin-Baudoux, L. Kunz, J. Petit, Near threshold fatigue crack growth in ultrafinegrained copper, IOP Conference Series: Materials Science and Engineering, 63 (2014) 012158.

# Near threshold fatigue crack growth in ultrafine-grained copper

M Arzaghi<sup>1</sup>, S Fintová<sup>2</sup>, C Sarrazin-Baudoux<sup>1</sup>, L Kunz<sup>3</sup>, and J Petit<sup>1</sup>

<sup>1</sup> PPRIME Institute UPR 3346 CNRS, ISAE-ENSMA, Université de Poitiers, France

<sup>2</sup> Brno University of Technology, CEITEC BUT – Central European Institute of Technology, Technická 3058/10, 616 00 Brno, Czech Republic

<sup>3</sup> Institute of Physics of Materials, AS CR, Žižkova 22, 61662 Brno, Czech Republic

E-mail: [mandana.arzaghi@isae-ensma.fr](mailto:mandana.arzaghi@isae-ensma.fr)

**Abstract.** The near threshold fatigue crack growth in ultrafine-grained (UFG) copper at room temperature was studied in comparison to conventional coarse-grained (CG) copper. The fatigue crack growth rates  $da/dN$  in UFG copper were enhanced at  $\Delta K \leq 7 \text{ MPa}\sqrt{\text{m}}$  compared to the CG material. The crack closure shielding, as evaluated using the compliance variation technique, was shown to explain these differences. The effective stress intensity factor amplitude  $\Delta K_{\text{eff}}$  appears to be the same driving force in both materials. Tests performed in high vacuum on UFG copper demonstrate the existence of a huge effect of environment with growth rates higher of about two orders of magnitude in air compared to high vacuum. This environmental effect on the crack path and the related microstructure is discussed on the basis of fractography observations performed using scanning electron microscope and completed with field emission scanning electron microscope combined with the focused ion beam technique.

## 1. Introduction

Severe plastic deformation (SPD) techniques, such as equal channel angular pressing (ECAP), have been widely used to obtain ultrafine grain (UFG) metals with high tensile strength and fairly large plasticity at low temperatures. Even though a certain number of studies have been carried out for investigating static and fatigue properties of UFG metals, very few data on fatigue crack growth resistance are available [1, 2]. Particularly, the fatigue crack propagation mechanisms for these materials should be clarified in the near threshold regime since the crack growth plays a major role in the design of safe engineering components and structures.

Reduction in the crack growth resistance with decreasing grain size was reported in Cu, Ni, Ti and Al-alloys [3-7]. This detrimental effect is attributed to the greater availability of grain boundaries in orientation favorable for crack propagation in a material with an UFG microstructure. Much less attempt has been made to identify the intrinsic propagation mechanism by eliminating closure and environmental factors, the only exception being the work by Pao et al. [8] in the case of a UFG Al-Mg alloy.

The current study aims to investigate whether or not the intrinsic propagation mechanism is altered by UFG microstructure. For this purpose, propagation of long fatigue cracks was studied in the mid stress intensity factor amplitudes and in the near threshold range in UFG copper obtained by ECAP. Crack propagation tests were conducted in air and under vacuum at  $R=0.1$  on small CT specimens. The crack growth mechanisms are discussed according to the testing environment based on local fracture surface observations and focused ion beam (FIB) cuts.

## 2. Materials and methods

### 2.1. Materials and environments



Commercially pure polycrystalline copper used in this study was annealed at 450 °C for 30 min prior to ECAP processing. The billets were processed in a 90° ECAP die up to 5- and 6-passes upon route C to obtain an UFG microstructure. Compact tension (CT) specimens with a width (W) of 16 mm and a thickness (B) of 5 mm were prepared from the central part of the billets. On these CT specimens the loading direction and notch direction, respectively, were parallel to normal direction (ND) and extrusion direction (ED). Also, CT specimens with the same dimensions as mentioned above as well as standard CT specimen (W=40 mm) were prepared from CG copper (grain size  $\bar{d} \sim 50 \mu\text{m}$ ). The specimens were pre-cracked under fatigue loading in air at room temperature, at a frequency of 20 Hz and R=0.1 in such a way that the stress intensity factor range  $\Delta K_{\text{init}} \sim 8 \text{ MPa}\sqrt{\text{m}}$  was reached at an initial crack length of  $\sim 1 \text{ mm}$ . The used environments were ambient air and high vacuum ( $\sim 10^{-6} \text{ mbar}$ ). The overall appearance of grains (size and structure) examined on a FIB cut was rather homogenous after 5-passes and 6-passes and was within the range of ultrafine grain (less than 1  $\mu\text{m}$ ).

### *2.2. Fatigue crack growth testing*

Fatigue crack growth tests were conducted on a servo-hydraulic testing machine in load control mode using a sinusoidal waveform signal for loading ( $f = 20\text{Hz}$ ,  $R = 0.1$ ). The crack length was measured on both sides of the specimens using an optical travelling microscope. The stress intensity factor range was calculated using the ASTM E647 recommendations [9]. Crack closure was measured systematically at each point by lowering the testing frequency to 0.2 Hz and recording the variation of the fatigue cycle load with respect to the displacement measured on the back face of the specimen using numerical data acquisition. Details of the closure determination technique were described in [10].

### *2.3. Fractography*

Observation of fracture surfaces was conducted on a field emission gun scanning electron microscope (FEG-SEM) using secondary electrons with an accelerating voltage of 20 kV. During fractographic analysis, attention was paid to special features on the fracture surface along the crack propagation direction. Also, detailed observations were done beneath the fracture surface on specific positions by performing cuts using FIB technique.

## **3. Results and discussion**

Fatigue crack growth curves in Fig. 1 show relationships between the Fatigue Crack Growth Rates (FCGR) and the stress intensity factor range in the UFG specimen together with the reference data for conventional coarse-grained (CG) copper. It can be seen that material subjected to 5 passes exhibits a considerable increase in the crack growth rates in the range of stress intensity factor below 7  $\text{MPa}\sqrt{\text{m}}$ ; however, the curves merge together at higher  $\Delta K$  values, namely above 7  $\text{MPa}\sqrt{\text{m}}$  (Fig. 1a).

Also, in UFG specimens, a constant deviation of crack growth direction of 22°-24° with respect to the plane perpendicular to the loading direction was observed. It is worth mentioning that according to the ASTM standard [11] for such deviations the same value of stress intensity factor as calculated in mode I loading can be used with an error of about 1%. It is already well-established that the crack closure plays a major role in promoting marked differences between the effective (near-tip)  $\Delta K_{\text{eff}}$  and the nominal (far-field)  $\Delta K$  of long cracks. The contribution of crack closure has been shown to depend on various factors [12, 13] such as length, size and geometry of the plastic wake along the crack flanks. Crack closure measurements done during the propagation test were used to calculate the effective stress intensity factor ranges as shown in Fig. 1b. It comes out from this figure that the differences observed in the nominal curves between UFG and CG copper are rationalized in terms of the



effective stress intensity factor range  $\Delta K_{\text{eff}}$  after crack closure correction. These results are in accordance with those obtained by Pao et al. [8] in the case of a UFG Al-Mg alloy.

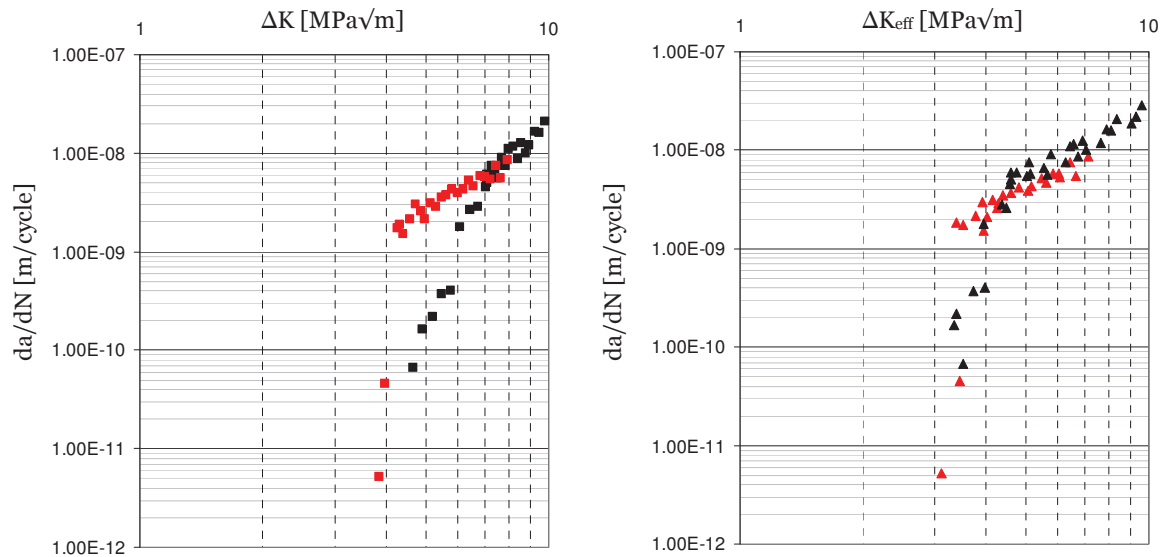


**Figure 1.** Crack growth rate of CG-Cu (black) and UFG-Cu (red) in air at room temperature and  $R=0.1$ . a)  $da/dN$  vs.  $\Delta K$  curve, b)  $da/dN$  vs.  $\Delta K_{\text{eff}}$  curve.

### 3.1. Fractography

The fracture surface morphology of CG copper tested in air (Fig. 2) is substantially different from that on the UFG copper, particularly regarding the surface roughness. Asperities of several micrometers amplitude filled with matted edges observed in CG copper (Fig. 2a) could induce higher crack closure levels than in the case of the UFG copper which exhibits a very smooth fracture surface (Fig. 2b) under comparable loading conditions.

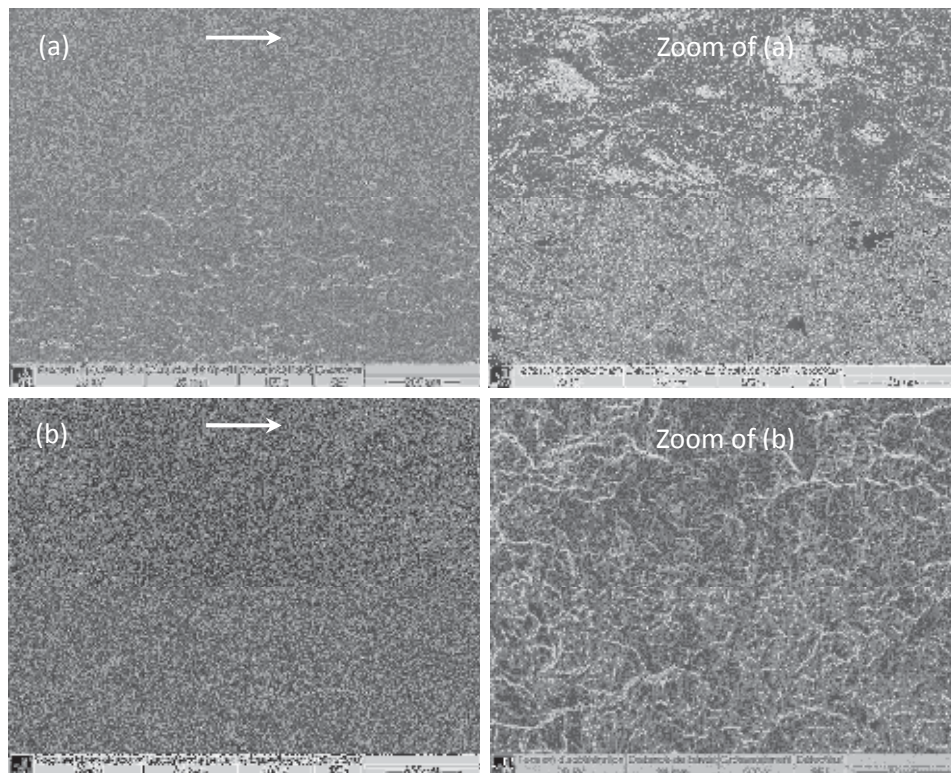


**Figure 2.** Fracture surfaces on CT specimens tested in air a) CG at  $\Delta K \sim 5 \text{ MPa}\sqrt{\text{m}}$ ,  $da/dN = 1\text{E-}9 \text{ m/cycle}$ , and b) UFG-Cu at  $\Delta K \sim 5.5 \text{ MPa}\sqrt{\text{m}}$ ,  $da/dN = 4\text{E-}9 \text{ m/cycle}$  (arrows show propagation direction).

In Fig. 3 the crack growth curve of 5C specimen tested in air is compared to the propagation of 5C and 6C specimens tested under vacuum. The two curves in vacuum are superposed. The experimental results clearly indicate a huge change in the crack propagation mechanism under vacuum as compared to the one in air, with growth rates in air more than two orders of magnitudes higher than under vacuum. Another important feature is the change in crack paths due to the change of environment as shown on the right-hand side of Fig. 3. Deviation of crack growth direction with respect to the plane perpendicular to the loading direction became greater when the crack grew under vacuum, as can be detected on the lateral surfaces of both specimens on Fig. 3. Meanwhile, whether the crack propagation plane remains constant throughout the thickness of specimen or changes within the distance from the free surface of the specimen is not yet known.

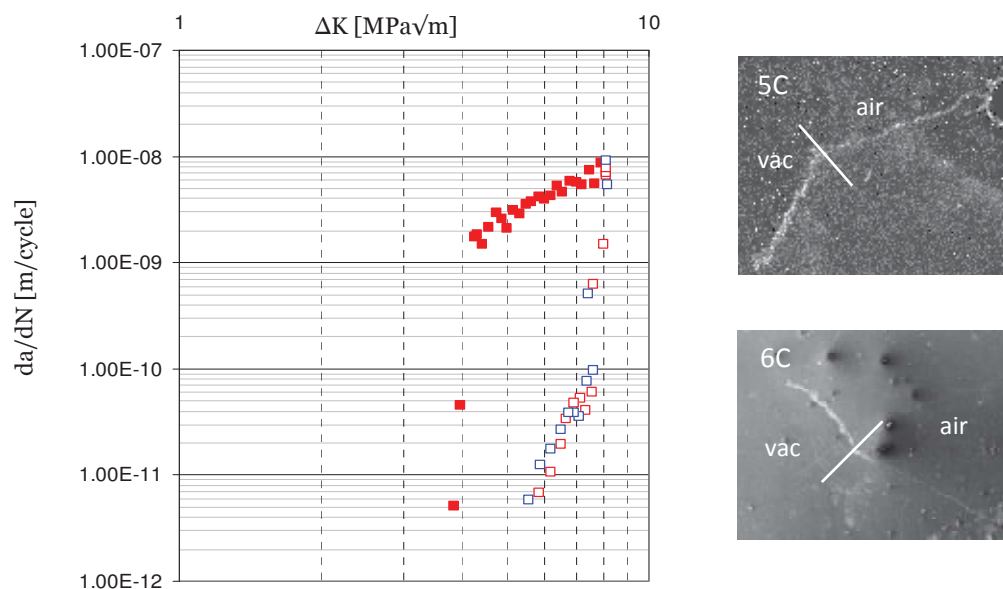


**Figure 3.**  $da/dN$  vs.  $\Delta K$  curve of 5C (red full colored) specimens tested in air superposed on curves of 5C (red) and 6C (blue) specimens tested under vacuum at room temperature and  $R=0.1$ .

### 3.2. Microfractography of fracture surfaces obtained under different environments

A comparison of the fracture surfaces of specimens tested in air and under vacuum is given in Fig. 4. The propagation in air, Fig. 4a, seems to be predominantly transgranular, very similar to a conventional stage II crack propagation mechanism. On the contrary, the spongy aspect of the fracture surface under vacuum, over the whole area, cannot be easily referred to some known crack path morphology. However, such a featureless aspect could be in accordance with an intergranular crack path, as can be seen in Fig. 4b. This hypothesis will be explored further (see section 3.3).

A quantitative explanation of the effect of environment together with the grain refinement on the fatigue threshold is not straightforward. Actually the FCGRs in this domain are, in addition to environment and crack closure, strongly influenced by several factors including slip mechanisms in accordance with deformation localization, grain (cell) dimensions, crack branching and deflection.



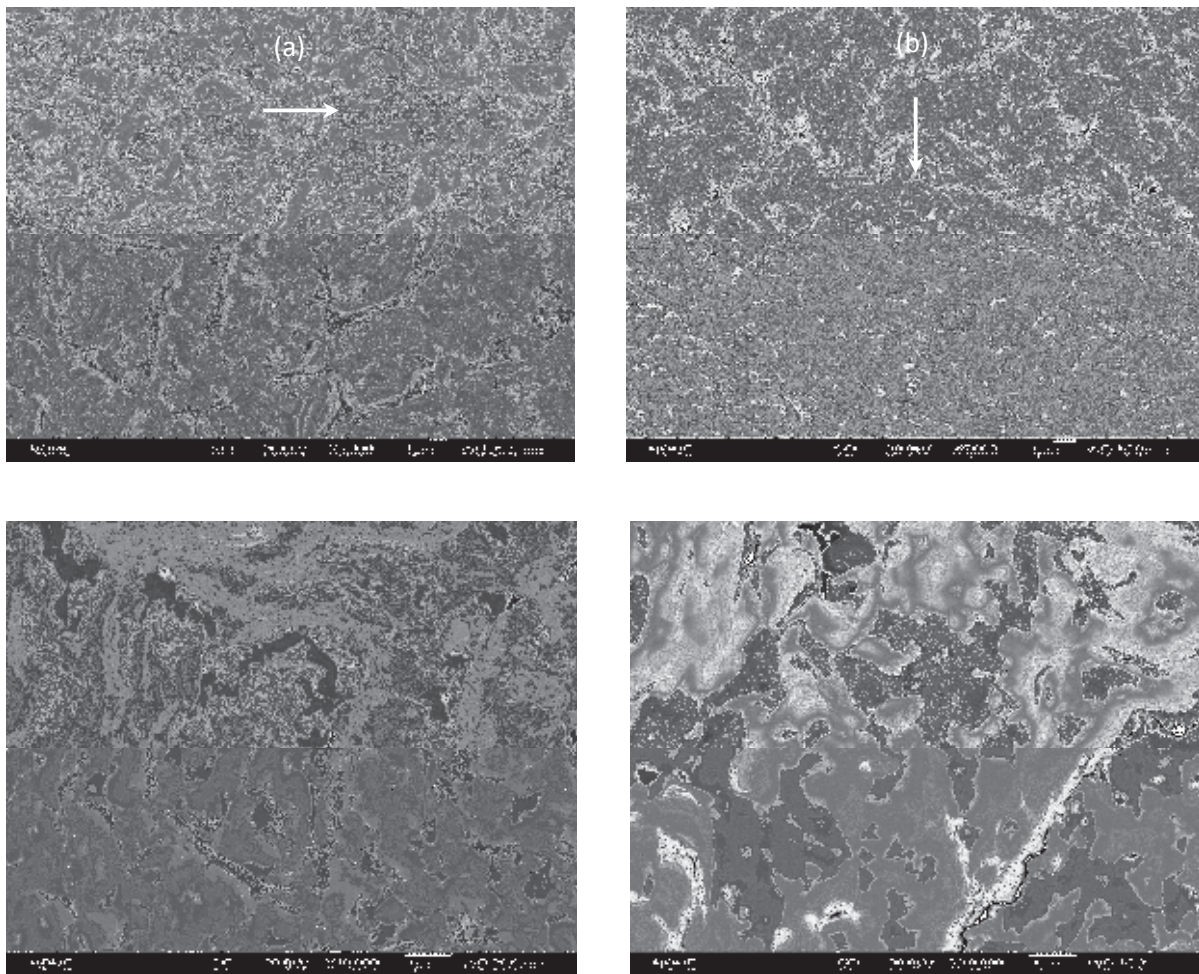


**Figure 4.** Fracture surfaces of UFG-Cu specimen tested in, a) air  $\Delta K_{\text{eff}} \sim 5.5 \text{ MPa}\sqrt{\text{m}}$ ,  $da/dN = 4\text{E-}9 \text{ m/cycle}$ , and in b) vacuum  $\Delta K_{\text{eff}} \sim 5.5 \text{ MPa}\sqrt{\text{m}}$ ,  $da/dN = 4\text{E-}11 \text{ m/cycle}$ ] (arrows show propagation direction).

Taking into account the fracture mechanisms approach and the real material microstructure, there exists a transition between near threshold regime and the intermediate fatigue stage when the size of the cyclic plastic zone (CPZ) at the crack tip becomes comparable with the grain size [12]. In the case of UFG microstructure the estimated size of the CPZ is much greater than the grain size. Hence, a large number of neighboring grains are involved in the crack tip plasticity even near the threshold. This is illustrated in Fig.5 on the lateral surface of the UFG specimen. There is an obvious difference between the area in the vicinity of the crack, crack flanks, in air and vacuum (compare two images on the top of the Fig. 5).

The extensive cyclic plasticity and slip activity in vacuum even at the threshold value ( $\Delta K \sim 5.5 \text{ MPa}\sqrt{\text{m}}$ ) is remarkable. The existence of well-developed slip bands around the crack witnesses for severe concentration of the deformation under vacuum.

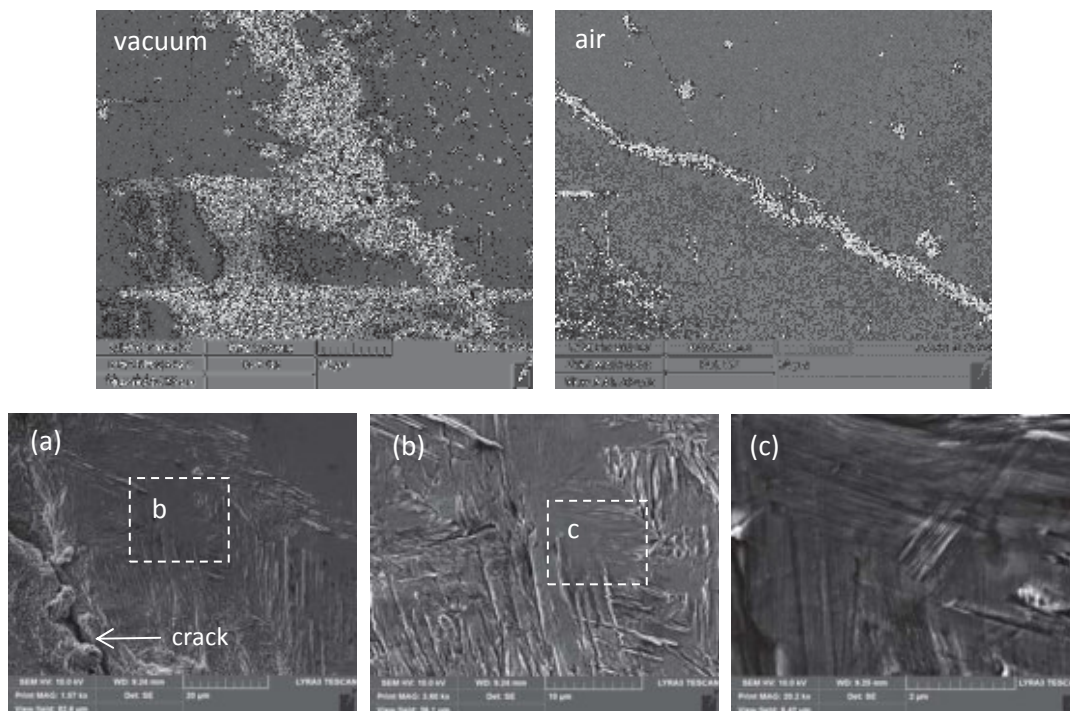


**Figure 5.** Lateral surface of 6C specimen tested in air (on the right) and in vacuum (on the left), a-c) plastic deformation activity at the crack tip (vacuum).

### 3.3. FIB cuts

In order to investigate the extent of the cyclic plastic deformation at the crack tip, Tescan LYRA 3 XMU FEG/SEM scanning electron microscope equipped with a FIB technique was used for examining the microstructure beneath the fracture surface as well as in the vicinity of the crack tip. For this purpose, the area under study was first covered by a platinum layer to protect the surface morphology from any damage that can be caused during FIB cutting as documented in Fig.6.

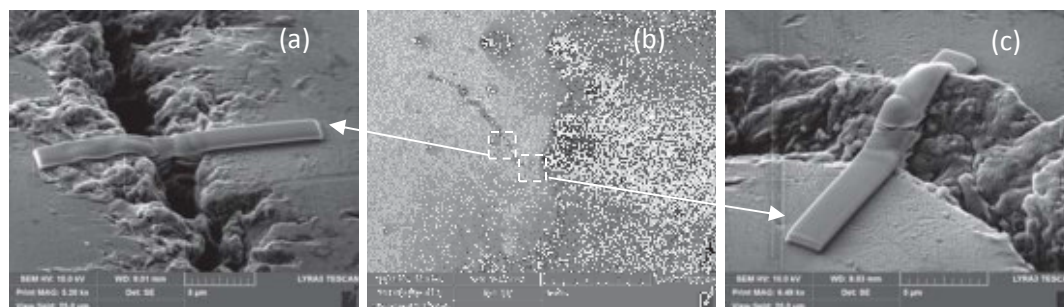


**Figure 6.** Positions of FIB observations on the 6C specimen, a) crack flanks in vacuum, b) picture of the crack on the lateral surface of specimen and c) crack flanks in air.

Fig. 7 shows two FIB cuts performed through a crack with nearly the same  $\Delta K$  value perpendicular to the plane of crack propagation and to the lateral surface. The microstructures beneath the fracture surface created under vacuum and air are shown in Fig. 7a and 7b, respectively. The UFG structure remains without any changes in the regions far



from the fracture surface; however, the grains adjacent to the fracture surface are visibly coarsened.

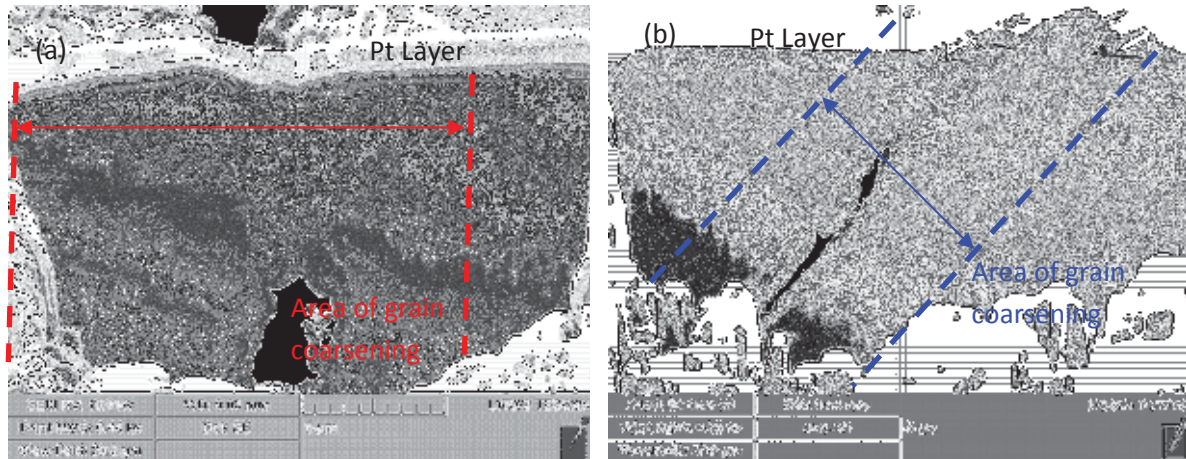


**Figure 7.** FIB section of a crack grown in, a) air  $\Delta K$  8.14~ MPa $\sqrt{m}$ ,  $da/dN = 5.3E-10$  m/cycle, and in b) vacuum  $\Delta K \sim 7.6$  MPa $\sqrt{m}$ ,  $da/dN = 9.5E-11$  m/cycle.

The border line between the grain-coarsened area and the UFG microstructure can be easily distinguished. The size of the cyclic plastic zone ( $R_{cp} \sim 16 \mu m$ ) approximately corresponds to two times the width of the region where grain coarsening occurs. These observations are in agreement with the findings of Vinogradov et al. [14]. The effect can be attributed to the dynamic grain coarsening and development of characteristic dislocations structures observed in low cycle fatigue testing at relatively large strain amplitudes [15, 16].

#### 4. Conclusions

From this preliminary study on the influence of the testing environment on the fatigue crack propagation in UFG copper, the following conclusions can be made:

- 1) In the region of low  $\Delta K$  values, the faster fatigue crack propagation in UFG copper in air is explained by a reduced shielding effect of crack closure when compared to the conventional CG copper.
- 2) At the very low crack growth rates, the fracture surface of the CG material exhibits a higher roughness associated to the intergranular facets which contribute to the shielding effect of crack closure in contrast with the very even and smooth fracture surface in the UFG material.
- 3) The similitude of the effective crack propagation behavior after closure correction suggests that the same crack growth mechanism (transgranular stage II propagation related to mode I crack opening) operates in both materials regardless of the difference in the grain size.
- 4) For  $\Delta K$  values higher than 7 MPa $\sqrt{m}$ , the crack growth rates are similar in UFG and conventional copper.
- 5) A huge effect of air environment in comparison to the high vacuum is put forward in the UFG copper. This effect is accompanied by a strong crack path deviation which is probably related to a shear controlled slip localization and seems to result from an intergranular propagation mechanism.

6) Observations using a FIB technique revealed a substantial grain coarsening in the vicinity of the crack tip, and crack wakes in the UFG microstructure. Very tortuous and branched crack path under vacuum was very different from a transgranular stage II crack path in air.

### Acknowledgments

Authors gratefully thank Pr. J.-J. Fundenberger for providing ECAPed specimens elaborated at LEM3 laboratory, Metz, France. Ministry of Education of the Czech Republic under the project CZ.1.07/2.3.00/30.0039 and the project of Czech Science Foundation 108/10/2001 supported this work.

### References

- [1] Estrin Y, Vinogradov A 2010 *Int. J. Fatigue* **32** 898.
- [2] Mughrabi H, Höppel H 2010 *Int. J. Fatigue* **32** 1413.
- [3] Chung CS, Kim JK, Kim HK, Kim WJ 2002 *Mater Sci Eng A* **321** 39.
- [4] Hanlon T, Tabachnikova ED, Suresh S 2005 *Int. J. Fatigue* **27** 1147.
- [5] Vinogradov A 2007 *J. Mater. Sci.* **42** 1797.
- [6] Collini L 2010 *Eng. Frac. Mech.* **77** 1001.
- [7] Vinogradov A, Kawaguchi T, Kanek Y, Hashimoto S 2011 *Mater. Trans. Special issue on Adv. Mater. Sci. in Bulk Nanostructured Metals* The Japan Institute of Metals.
- [8] Pao PS, Holtz RL, Jones HN, Feng CR 2009 *Int. J. Fatigue* **31** 1678.
- [9] ASTM E647-05 Standard Test Method for Measurement of Fatigue Crack Growth Rates, ASTM International, 2008.
- [10] Arzaghi M, Sarrazin-Baudoux C, Petit J 2014 *Advanced Materials Research* **891-892** 1099.
- [11] Forth SC, Herman DJ, James MA, Johnston WM ASTM Special Technical Publication 2005.
- [12] Newman Jr JC, Elber W Mechanical of fatigue crack closure. Philadelphia, (USA): American Society for Testing and Material Pub; 1988 ASTM.
- [13] RC McClung, JC Jr Newman Advances in fatigue crack closure measurement and analysis, vol. 2. Philadelphia (USA): American Society for Testing and Materials Pub; 1999 ASTM.
- [14] Vinogradov A, Stolyarov VV, Hashimoto S, Valiev RZ 2001 *Mater Sci Eng A* **318** 163.
- [15] Agnew SR, Weertman JR 1998 *Mater Sci Eng A* **244** 145
- [16] Hoppel HW, Mughrabi H, Vinogradov A 2009 *Bulk Nanostructured Materials*, ed. By M. Zehetbauer and R. Z. Valiev, Wiley-VCH Verlag GmbH, Germany 481.

- X. [34] S. Fintová, M. Arzaghi, I. Kuběna, L. Kunz, C. Sarrazin-Baudoux, Fatigue crack propagation in UFG Ti grade 4 processed by severe plastic deformation, *International Journal of Fatigue*, 98 (2017) 187-194.



# Fatigue crack propagation in UFG Ti grade 4 processed by severe plastic deformation



S. Fintová<sup>a,b,\*</sup>, M. Arzaghi<sup>c</sup>, I. Kuběna<sup>a</sup>, L. Kunz<sup>a</sup>, Ch. Sarrazin-Baudoux<sup>c</sup>

<sup>a</sup> Institute of Physics of Materials, Academy of Sciences of the Czech Republic, v. v. i., Žitkova 22, 616 62 Brno, Czech Republic

<sup>b</sup> CEITEC IPM, Institute of Physics of Materials, Academy of Sciences of the Czech Republic, v. v. i., Žitkova 22, 616 62 Brno, Czech Republic

<sup>c</sup> Pprime Institute UPR3346, Université de Poitiers, ISAE-ENSMA, Téléport 2, 1. avenue Clément Ader, BP40109, F86961 Futuroscope-Chasseneuil Cedex, France

## ARTICLE INFO

### Article history:

Received 18 November 2016

Received in revised form 16 January 2017

Accepted 18 January 2017

Available online 20 January 2017

### Keywords:

Titanium

Fatigue

Crack growth

Crack closure

Equal channel angular processing

## ABSTRACT

Fatigue crack growth was investigated in commercially pure Ti grade 4 processed by severe plastic deformation. The ultrafine-grained structure was prepared by means of equal channel angular pressing technique followed by cold drawing. The growth of fatigue cracks was investigated also in the as-received coarse-grained state of material for comparison.

The fatigue crack growth rate in the ultrafine-grained material was found to be higher and the threshold stress intensity range  $\Delta K_{th}$  for crack growth lower than in the coarse-grained Ti, 2.5 and 4.7 MPa m<sup>1/2</sup>, respectively. A combination of transcrystalline and intercrystalline crack growth was typical for all crack growth rates in the coarse-grained material. Contrary to the combined fracture mechanism in coarse-grained Ti only transcrystalline crack growth was a characteristic feature of crack propagation in the ultrafine-grained material.

It has been found that the experimentally and theoretically determined values of closure are in reasonable agreement. Crack closure calculated according to the Newman model taking into account only plasticity induced closure was in the range from 67% to 69% of  $K_{max}$  for as-received and 70% for UFG state of material. Crack closure determined experimentally was 67% of  $K_{max}$  for as-received and 67% for UFG CP Ti grade 4.

Investigation of fracture surfaces did not bring any evident signs of the effects of fracture surface morphology resulting in roughness induced closure or oxide induced closure under testing conditions used. This indicates that plasticity induced closure seems to be a dominant closure mechanism in both states of the investigated Ti grade 4.

© 2017 Elsevier Ltd. All rights reserved.

## 1. Introduction

Four basic grades of commercially pure (CP) titanium alloys differing with respect to their oxygen content from 0.18% (grade 1) to 0.40% (grade 4) resulting in an increase of yield stress are available for engineering applications [1,2]. Grade 4 is characterized by maximum content of oxygen and 0.5% of Fe [2] and has the highest tensile strength among the four CP titanium grades [3]. It has sufficient ductility and moderate formability. The benefit of high strength is retained up to moderate temperatures [3].

CP titanium and other Ti -  $\alpha$  alloys are used mainly in the chemical and petrochemical industries [2]. In particular, grade 4 is suitable for a wide range of chemical and marine applications

due to its excellent corrosion resistance. Moreover, it can be used in continuous service at elevated temperatures up to 425 °C and intermittent service up to 540 °C [3]. CP titanium alloys have better biocompatibility than other titanium alloys which make them preferential for medical applications [4].

Typical crystal structure of CP titanium grades at room temperature is  $\alpha$  h.c.p. type. Small amount of spheroidal  $\beta$  phase occurs usually at the grain boundaries with increasing impurity level (especially Fe) [3].

Decreasing of the grain size is one of the ways to improve strength of metallic materials. It has been shown that intensive grain refinement due to severe plastic deformation (SPD) can significantly improve strength of CP titanium [4–10]. For instance, combination of equal channel angular pressing (ECAP) with additional mechanical treatment (mostly rolling) improves the ultimate tensile strength of ultrafine-grained (UFG) Ti to more than 1000 MPa [11,12]. Grain refinement using SPD treatment was also reported to have a slightly positive influence on corrosion proper-

\* Corresponding author at: Institute of Physics of Materials, Academy of Sciences of the Czech Republic, v. v. i., Žitkova 22, 616 62 Brno, Czech Republic.

E-mail addresses: [fintova@ipm.cz](mailto:fintova@ipm.cz) (S. Fintová), [mandana.arzaghi@isae-ensma.fr](mailto:mandana.arzaghi@isae-ensma.fr) (M. Arzaghi), [kubena@ipm.cz](mailto:kubena@ipm.cz) (I. Kuběna), [kunz@ipm.cz](mailto:kunz@ipm.cz) (L. Kunz), [christine.baudoux@ensma.fr](mailto:christine.baudoux@ensma.fr) (Ch. Sarrazin-Baudoux).

ties of the CP titanium grade 2 [13]. However, the treatment did not affect material corrosion resistance in a notable way, so the influence cannot be considered neither positive nor negative.

Fatigue properties of CP Ti grades were also observed to be improved due to the grain refinement. Cavaliere [14,15] who studied the fatigue crack behavior of CP Ti grade 2 reported significant influence of intensive grain refinement via SPD processing on propagation of long fatigue cracks. A decrease of  $\Delta K_{th}$  and an increase of crack propagation rate were observed. The fatigue limit of CP Ti grade 2 is enhanced by ECAP (of 67%) when compared to the coarse-grained material [10]. A comparison of fatigue behavior of CP Ti grade 4 with other light alloys showed a significant improvement of fatigue properties due to the grain refinement [6,16].

The data on crack growth behavior, crack growth mechanism and material response to the fatigue loading are available only in limited extent in the literature as to the authors' knowledge for CP titanium grade 4 with conventional grain size and in UFG state. However, differences in the fatigue behavior among individual CP Ti grades due to the different level of alloying elements are assumed. The aim of this paper is to experimentally determine and compare the fatigue crack propagation behavior of long cracks and material response to the fatigue loading for both states. Moreover, a particular attention was paid to the mechanism of the crack growth and the role of crack closure.

## 2. Experimental material and procedure

Fatigue crack growth tests were performed on CP Ti grade 4 in as-received state (coarse-grained material) and in a state after processing consisting from ECAP followed by cold drawing.

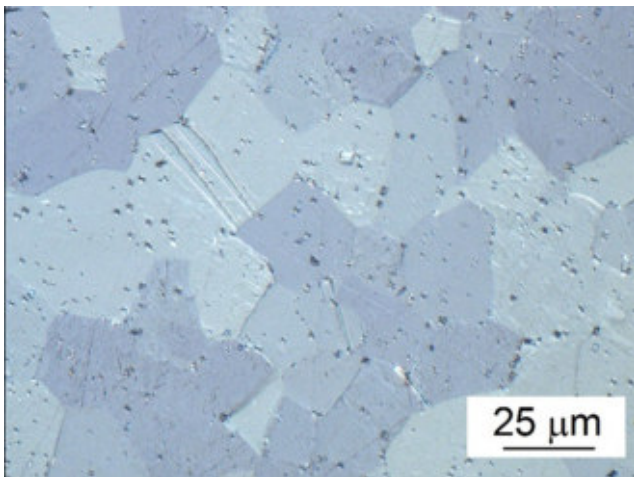


Fig. 1. Microstructure of Ti grade 4 in as-received state, SEM, etch. 100 ml H<sub>2</sub>O + 100 ml HNO<sub>3</sub> + 100 ml HF, LM.

The microstructure of commercially pure Ti grade 4 in the as-received state consisted of polyhedral recrystallized  $\alpha$  phase grains with the average grain size of  $16.3 \pm 1.0 \mu\text{m}$  (determined by intercept method involving an actual count of the number of grains intercepted by a test line calculated from 15 measurements), see Fig. 1. Due to the content of Fe also a small amount of dispersed  $\beta$  phase was observed in the material. Small amount of deformation twins was present in the coarse-grained microstructure due to the material fabrication procedure.

Ultrafine-grained Ti was prepared by ECAP at the temperature of 250 °C upon route B<sub>C</sub>. Four passes were applied to reach a final billet with cross-section dimensions of  $11 \times 11 \text{ mm}$ . ECAP was followed by cold drawing at 200 °C. The resulting dimensions of the final round bars for specimen manufacturing were 6 mm in diameter and nearly 1 m in length.

Tensile tests were performed on a hydraulic ZWICK Roell 1871 testing machine. Specimens with a gauge length of 12 mm and the gauge diameter of 3 mm were machined from round bar semi-products. Tests were performed with the cross-head speed of 1 mm/min.

Fatigue crack growth tests were conducted on a servo-hydraulic testing machine equipped by Digital Electronics by INSTRON under load control at room temperature. The loading signal was sinusoidal with frequency of 20 Hz. Based on the specimen geometry given by the material semiproduct dimensions after processing the load ratio  $R$  was set to 0.1. Due to the dimensions of the semi-products, non-standard specimens for crack growth determination has to be manufactured, Fig. 2. The specimen length was 70 mm, width 5.5 mm and thickness 2 mm. The starter notch with the length of 0.8 mm and width of 0.3 mm was machined by spark sputtering technique in the middle of the specimen length. The lateral surfaces of the specimen were mechanically ground by SiC papers (grits 800–1200–4000) and polished by 1  $\mu\text{m}$  diamond paste and OP-S colloidal silica suspension for final polishing (0.04  $\mu\text{m}$ ). The reason for the very careful preparation of the surface was optical crack length measurement and the observation of surface relief evolution in the plastic zone at the fatigue crack tip and in the crack wake. The crack length (defined as a projection of the crack to the direction perpendicular to the loading axis), was measured using an optical travelling microscope. The load shedding procedure was used for initiation of the crack from the notch. The actual measurement was performed on cracks having the minimum length of 1 mm and the procedure fulfilled the E 647-05 standard [17].

The crack closure was experimentally determined by means of specimen stiffness changes during the loading and unloading at low frequency (0.2 Hz) by clip extensometer. Extensometer was fixed on the specimen having the notch for the crack initiation in the center between the blades.

The stress intensity factor  $K_I$  was calculated by Eq. (1) based on finite element computation:

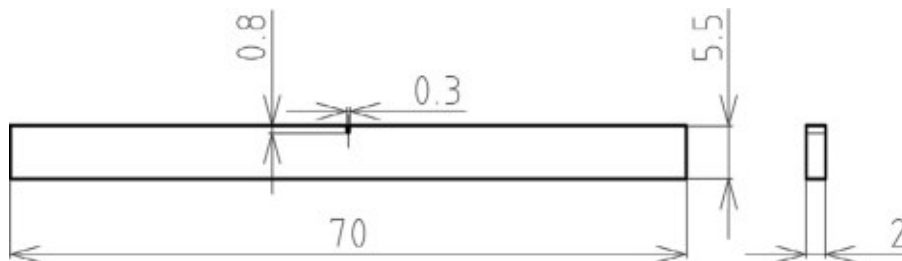


Fig. 2. Geometry of specimen for crack growth tests.



$$K_I = \sigma \sqrt{\pi a} \cdot \left( 9447.99 \left( \frac{a}{W} \right)^7 - 28802.02 \left( \frac{a}{W} \right)^6 + 36092.14 \left( \frac{a}{W} \right)^5 - 23846.4 \left( \frac{a}{W} \right)^4 + 8887.76 \left( \frac{a}{W} \right)^3 - 1840.37 \left( \frac{a}{W} \right)^2 + 194.79 \left( \frac{a}{W} \right) - 6.75 \right) \quad (1)$$

where  $\sigma$  is applied stress,  $W$  specimen thickness and  $a$  is a crack length.

The observation of microstructure and the macro-observation of the crack paths were performed by light optical microscopy (LM) by means of Neophot 32. Tescan LYRA 3 XMU FEG/SEM scanning electron microscope (SEM) was used for study of the specimen lateral surfaces in the vicinity of the crack paths and fracture surfaces. Electron backscatter diffraction (EBSD) analysis was applied to reveal the microstructure in the wake of the crack and in front of the crack tip. The details of UFG microstructure were analyzed using transmission electron microscope JEOL JEM 2100F.

### 3. Results

#### 3.1. Microstructure

Severe plastic deformation by ECAP and drawing resulted in substantial grain refinement. The equiaxed coarse-grained structure changed to a structure with elongated grains parallel to the direction of processing. Fig. 3. The average  $\alpha$  phase grain size was around 250 nm in the section perpendicular to the processing direction and up to 1.5  $\mu\text{m}$  in the section parallel to the processing direction.

#### 3.2. Tensile properties

Ultimate tensile strength ( $\sigma_{UTS}$ ) of the UFG Ti determined on three specimens was  $951 \pm 4$  MPa, the proof stress ( $\sigma_{0.2}$ ) was  $854 \pm 7$  MPa and the elongation  $16.1 \pm 1.5\%$ . The  $\sigma_{UTS}$  for as-received material was  $758 \pm 6$  MPa, the  $\sigma_{0.2}$   $503 \pm 10$  MPa and elongation  $30.6 \pm 5\%$ .

#### 3.3. Fatigue crack growth

The experimentally determined points of the fatigue crack growth curves for the as-received and UFG Ti grade 4 are shown in Fig. 4. Two specimens from each state of material were tested.

A clear difference can be seen between crack growth rates in both materials. The data for UFG material are shifted to higher crack growth rate values. The threshold for the growth of long cracks,  $\Delta K_{th}$ , of UFG titanium is lower by a factor of nearly two when compared to the coarse-grained as-received state. From the

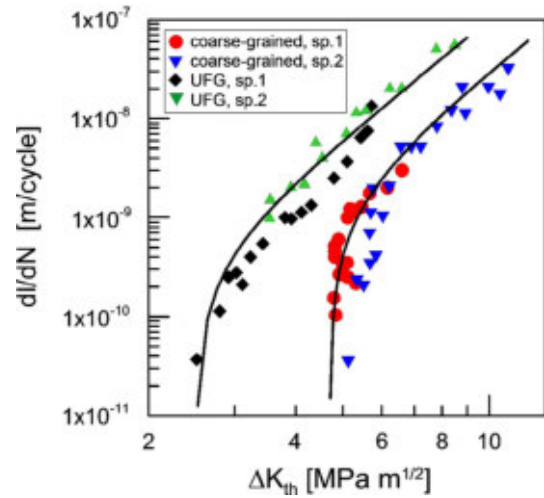


Fig. 4. Fatigue crack growth curves.

trend of the data in Fig. 4 it can be estimated that the threshold values of the UFG and coarse-grained Ti are 2.5 and 4.7  $\text{MPa m}^{1/2}$ , respectively.

The full lines in Fig. 4 represent the Eq. (2) [18]:

$$\frac{dl}{dN} = A \cdot (\Delta K^n - \Delta K_{th}^n) \quad (2)$$

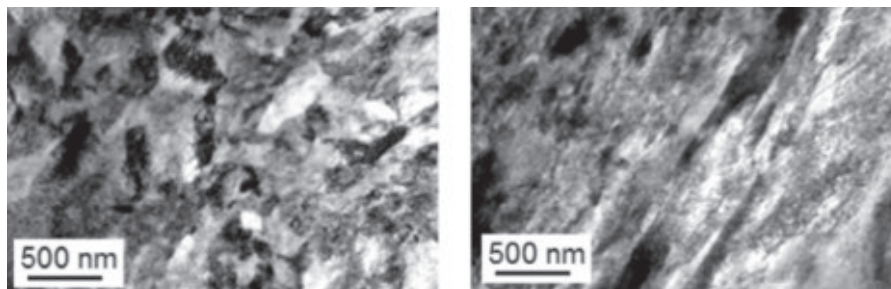
where for coarse grained material  $A = 3 \times 10^{-12} (\text{MPa m}^{1/2})^{-n} \text{mc}^{-1}$ ,  $n = 4$  and  $\Delta K_{th} = 4.7 \text{ MPa m}^{1/2}$  and for UFG material  $A = 1 \times 10^{-11}$ ,  $n = 4$  and  $\Delta K_{th} = 2.5 \text{ MPa m}^{1/2}$ .

#### 3.4. Crack closure

The opening stress intensity factor  $K_{op}$ , estimated experimentally in the Paris region of the crack growth curves for the coarse-grained as-received Ti was  $33.5 \pm 4.5\%$  of  $K_{max}$  which is the maximum stress intensity factor in a load cycle, and  $32.75 \pm 10\%$  of  $K_{max}$  for the UFG material. Paris region is defined as a region of the crack growth curve showing linear dependence of the fatigue crack growth rate on the stress intensity factor range. Taking into account the statistical deviation of measurements, it can be concluded that the closure in both materials are very similar.

Closure effect was calculated applying crack opening function,  $f$ , which has been defined by Newman [19] considering only plasticity induced crack closure, Eqs. (3)–(7):

$$f = \frac{K_{op}}{K_{max}} = \max(R, A_0 + A_1 R + A_2 R^2 + A_3 R^3) \quad R \geq 0 \quad (3)$$



(a) Ti grade 4 microstructure after ECAP and drawing, perpendicular cut to the processing direction

(b) Ti grade 4 after ECAP and drawing, parallel cut to the processing direction

Fig. 3. Microstructure of UFG Ti grade 4, TEM.

where the coefficients  $A_i$  are calculated by following equations:

$$A_0 = (0.825 - 0.34\alpha + 0.05\alpha^2) \left[ \cos \left( \frac{\pi}{2} \frac{\sigma_{max}}{\sigma_0} \right) \right]^{1/\alpha} \quad (4)$$

$$A_1 = (0.415 - 0.071\alpha) \sigma_{max} / \sigma_0 \quad (5)$$

$$A_2 = 1 - A_0 - A_1 - A_3 \quad (6)$$

$$A_3 = 2A_0 + A_1 - 1 \quad (7)$$

where  $\alpha$  is a plane stress/strain constraint factor, and  $\sigma_{max}/\sigma_0$  is the ratio of the maximum applied stress ( $\sigma_{max}$ ) to the flow stress ( $\sigma_0 = \sigma_{UTS}/\sigma_{0.2}$ ). Eq. (8) was used for calculation of the constraint factor of one-dimensional crack  $\alpha$  [19]:

$$\alpha = 1.15 + 1.4e^{-0.95 \left( \frac{K_{max}}{\sigma_{0.2} \sqrt{W}} \right)^{1.5}} \quad (8)$$

where  $W$  is a specimen thickness and  $\sigma_{0.2}$  is a tensile proof stress.

The results of numerical analysis show that  $\Delta K_{eff} = (K_{max} - K_{op})$  [19] varies from 67% to 69% of  $K_{max}$  for as-received and makes 70% for UFG state of material. This is in good agreement with the experimentally determined values of the opening stress intensity factor.

### 3.5. Crack path

The macro-views of fatigue cracks in both materials are shown in Fig. 5a and b. It is obvious from the comparison that the crack path in the as-received coarse-grained material has higher tortuosity than in the UFG material.

The differences in the crack paths tortuosity are documented at higher magnification by means of SEM in Fig. 6. The trajectory of

the crack propagating in the as-received Ti, Fig. 6a, is substantially more serrated than the trajectory in the UFG state, Fig. 6b.

Micrographs of the cracks propagating with the rate of  $1 \times 10^{-8}$  m/cycle and crack tips in both materials are shown in Fig. 7. It can be seen, that the crack paths in the coarse-grained material is more serrated and the crack branching often appears. The lateral specimen surfaces were carefully polished with the aim to find signs of cyclic plasticity in the form of slip bands in the plastic zone or in the crack wake. Though the surface was well polished before testing, no such signs in the crack vicinity were found. Similarly, no apparent manifestation of cyclic plasticity at the crack tip was observed.

The matching fracture surfaces are in some places (Fig. 7, indicated by the arrow) shifted in the direction of the crack growth. In the areas of the crack branching a shift in the direction perpendicular to the specimen surface sometimes appears (Fig. 7a, marked by the arrow).

An attempt to reveal some signs of plastic deformation at the crack vicinity (in terms of the changes of microstructure) was made by EBSD in both studied materials, Fig. 8 (grain boundaries angle  $>10^\circ$ ). Intergranular in combination with transgranular fatigue fracture surface in as-received Ti is obvious on EBSD map, Fig. 8a. Crack propagation along the grain boundaries is marked by “I” in Fig. 8a. The transcrystalline propagation is indicated by “T”. However, no apparent changes of the grain size were revealed by EBSD.

### 3.6. Fracture surface

Fracture surfaces of specimens after fatigue crack propagation tests were examined by SEM. Differences in the appearance of

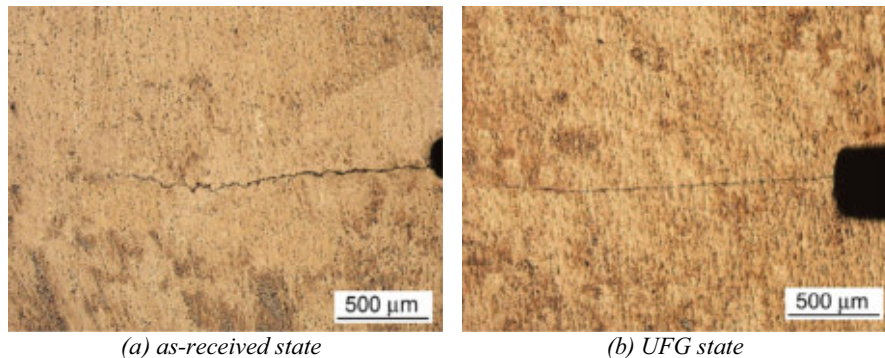


Fig. 5. Crack path macro-view; more tortuous for as-received Ti and smoother for UFG Ti state, LM.

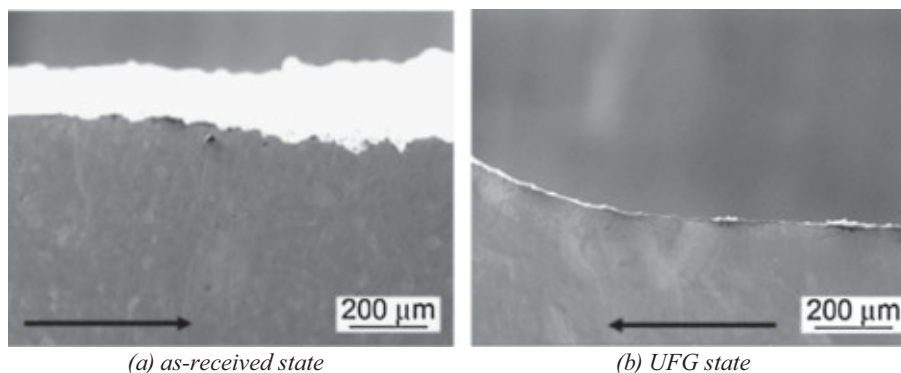


Fig. 6. Crack paths, SEM. Arrows indicate the crack growth direction.

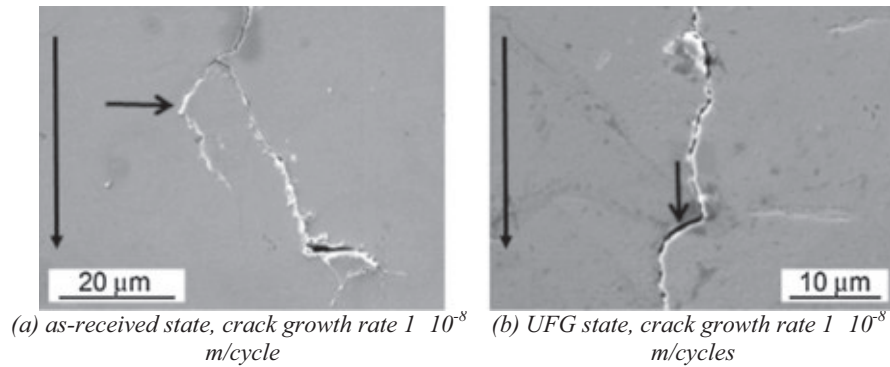


Fig. 7. Crack path, SEM. Vertical arrows on the left side indicate the crack growth direction.

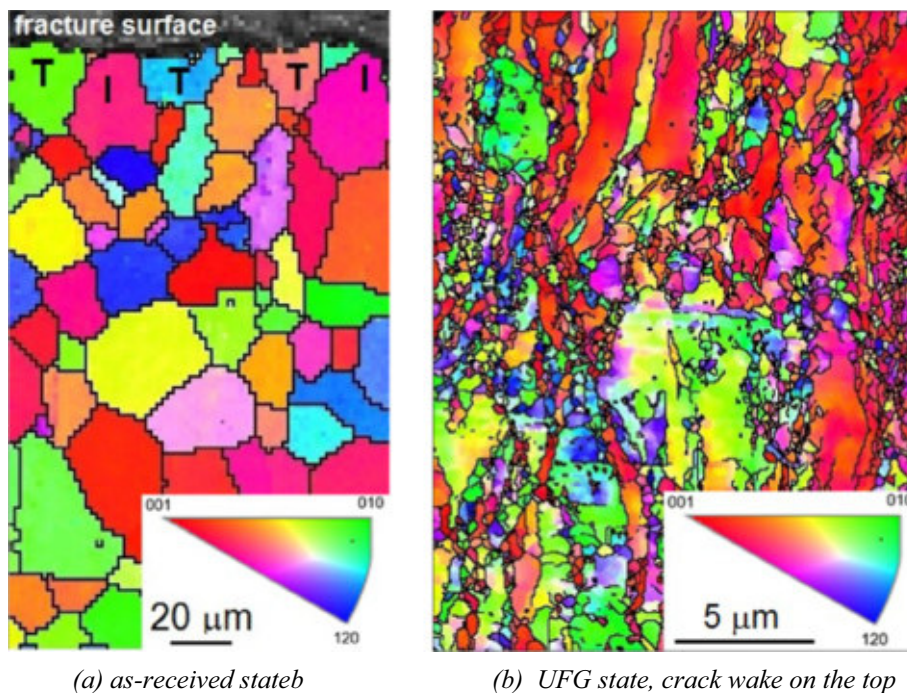


Fig. 8. Grain orientation observation, EBSD.

the fracture surfaces of coarse-grained as-received state and UFG Ti correspond to the observation by LM and EBSD.

Fracture surface of titanium in as-received state, Fig. 9, is characteristic by combination of intergranular and transgranular quasi-cleavage areas. Crack branching and secondary cracks can be often found (examples shown in Fig. 9 by arrows; black – transcrystalline, white – intercrystalline fracture surface).

From the comparison of Fig. Fig. 9a–c it is obvious that there is no difference in the fracture surface appearance for crack rates ranging from the  $10^{-8}$  m/cycle to the threshold region. No apparent influence of the applied load ( $\Delta K$ ) on fracture surface features was observed.

The fracture surface appearance of UFG Ti is substantially different from the appearance of coarse-grained material. Fracture surface of UFG Ti seems to have transcrystalline character, Fig. 10. No signs of the intercrystalline fracture were observed even at high magnification, Fig. 10d. Similarly to the case of coarse-grained material no difference in the fracture surface and thus the crack

growth mechanism for crack rates ranging from  $10^{-8}$  m/cycle to the threshold was observed, Fig. 10a–c.

#### 4. Discussion

ECAP treatment followed by cold drawing resulted in significant grain refinement of CP Ti grade 4. The tensile properties were improved; the ultimate tensile strength  $\sigma_{UTS}$  increased by 25% and the proof stress  $\sigma_{0.2}$  even by 70%. On the other hand, the elongation decreased by 53%. This finding is consistent with results on Ti published in [4–10,14,15]. Grain refinement resulted in improvement of strength connected with decrease of material plasticity.

Grain refinement leads to deterioration of the resistance to the growth of long cracks in UFG Ti, Fig. 4. Higher crack growth rates and lower  $\Delta K_{th}$  value were experimentally determined for UFG material. This observation is qualitatively in agreement with the observation on UFG Ti grade 2 [14,15]. Sensitivity of material to



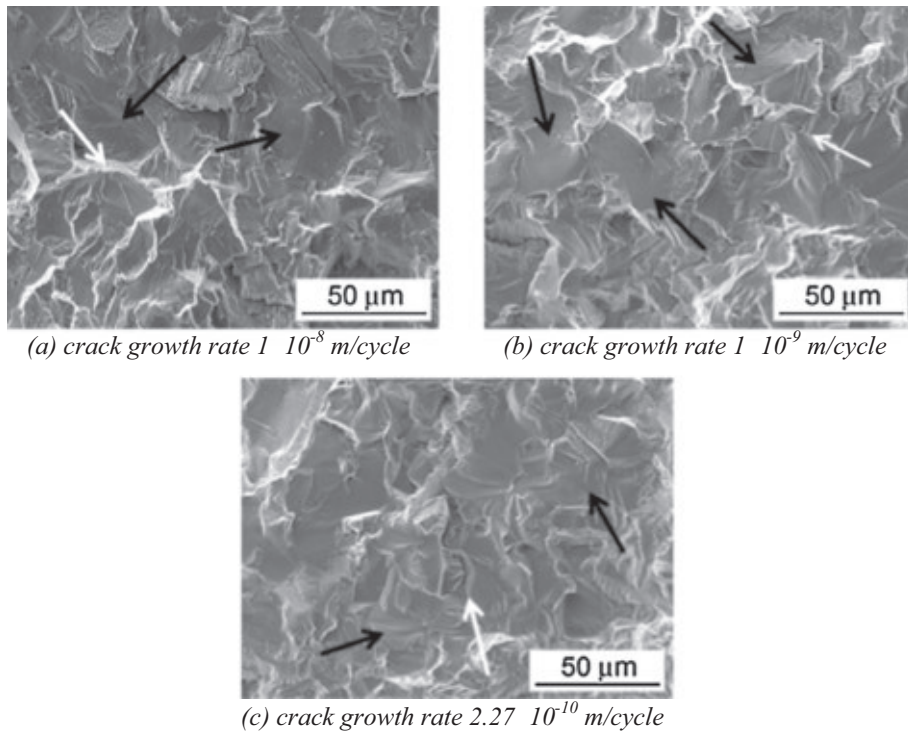


**Fig. 9.** Fracture surface, as-received state, SEM.

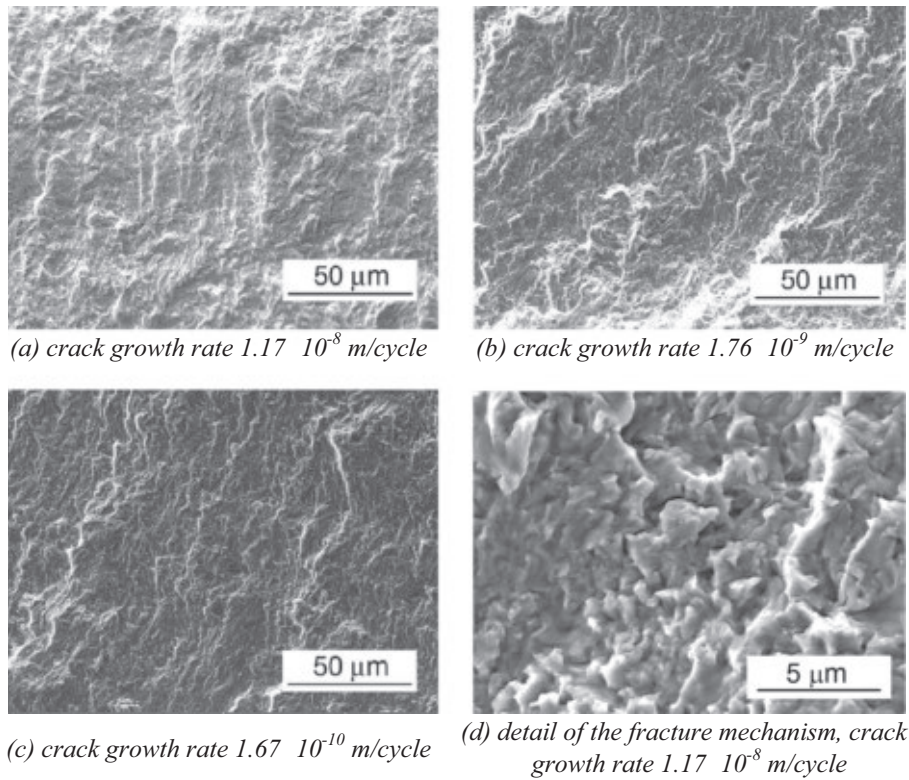


**Fig. 10.** Fracture surface, UFG state, SEM.

the crack initiation decreases with decreasing grain size, however, also the resistance to the crack growth decreases with decreasing grain size

Crack growth characteristics are in correlation with tensile properties of the experimental material. Higher plasticity of the coarse-grained material when compared to the UFG material state

resulted in higher resistance of the Ti to the crack initiation and retards the crack growth rate. H.c.p. structure of Ti in combination with significant plastic deformation due to the UFG structure processing resulted in material strengthening. However, improvement of strength characteristics (due to the increase of dislocation density and grain boundaries amount, [4,5,20]) was connected with decrease of plasticity of the material. As a result lower resistance of the material to the crack initiation and propagation was observed when compared to the coarse grained Ti.

The effect of crack closure on the crack propagation and threshold values has been investigated and discussed since many decades. Three main effects influencing the crack closure are (i) plasticity induced closure, (ii) oxide induced closure and (iii) roughness induced closure [18,21]. The plasticity induced closure plays a role under plane stress conditions, i.e. for thin specimen. It is caused by premature contact between the crack facets due to permanent residual displacements arising from prior plastic zone left in the wake of a growing fatigue crack. The oxide induced closure is caused by presence of corrosion products on fresh created fatigue fracture surfaces of growing cracks resulting in the wedging effect. The roughness induced closure results from the rough nature of the fracture surface causing premature contact of the crack facets. The closure occurs when the crack tip opening displacements become comparable to the size of the fracture surface asperities/features. Several numerical models for calculation of contribution of individual effects were proposed in literature [22–24]. Newman model, [19], considering only plasticity induced crack closure used in the present study showed quite good agreement with the experimentally determined data for both materials. The measured closure (in the Paris region of crack growth curves) was similar for both material states. This means that the grain size did not influence the closure level.

The good correspondence between measured values of crack opening and values determined by Newman model taking into account only plasticity induced closure indicates that the plasticity induced closure is the main part of closure both in the coarse-grained and UFG Ti cycled under given conditions. With the aim to identify experimentally the reasons for crack closure SEM observations of the crack vicinity, EBSD analysis of crack wakes and observations of fracture surfaces were performed.

Though the lateral surfaces of specimens were carefully polished, no signs of the cyclic plastic deformation in terms of cyclic slip bands were observed in the crack vicinity, Fig. 7. On the other hand, higher crack tortuosity and crack branching is a characteristic feature of the crack growth in coarse-grained material, Figs. 5 and 6. Similar observation was published by Cavaliere [14,15], who observed a decrease of  $\Delta K_{th}$  and an increase of crack propagation rate at  $R = 0.25$  for UFG Ti grade 2, pure Al, Ni and Cu produced via ECAP. Less pronounced fracture surface morphology and crack path smoothing was observed for the UFG state, which is again in agreement with [14,15]. However, authors did not provide information about the specimen surface and response of the material to the loading in terms of signs of plastic deformation or closure effect. Inspection of the crack path on the specimen surface of both materials revealed areas, in which the fracture surfaces are shifted in the direction of the crack growth, see arrows Fig. 7a and b and the matching of the opposite fracture surfaces is not perfect. In the case of as-received material also material shift in the direction perpendicular to the specimen surface sometimes appears, Fig. 7a, particularly in the regions of crack branching. This clear roughness induced closure effect, however, may be related only to the surface grains, where the constraint is low. The correspondence of the measured and theoretically determined values supports this idea.

The  $\alpha$  phase which forms the Ti grade 4 microstructure is hardly deformable at room temperature. The cyclic plasticity is thus limited. In combination with high loading rates, especially in Ti grades

3 and 4 with higher content of oxygen, fracture can be caused by cleavage of  $\alpha$  titanium along basal crystallographic planes [2]. This specific fracture mode typically occurs when the local normal stress exceeds critical stress along basal crystallographic plane (0001) [2]. The result is combination of intergranular and transgranular quasi-cleavage fracture with the presence of crack branching and secondary cracks in as-received coarse-grained Ti. The propensity to cleavage fracture is reduced when the grain size decreases. This is related to the increasing difficulty of nucleating of cleavage cracks in small grains [2], and explains the transgranular fatigue fracture surface observed in UFG material.

Good corrosion resistance of CP Ti and no apparent macroscopic signs of oxidation of the fracture surfaces (which are often observed e.g. in steels loaded at ambient laboratory conditions when the crack growth approaches the threshold) are further supporting facts for the idea that the effect of closure in both studied materials can be considered as plasticity induced. Further, detailed study of the fracture surfaces did not reveal any signs of damage (crushing). All these facts point out that there is no or only very limited contribution of oxide and roughness induced closure.

## 5. Conclusions

Experimental investigation of the fatigue crack growth in coarse-grained and UFG commercially pure Ti grade 4 processed by ECAP and followed by cold drawing enables following conclusions:

- UFG CP Ti grade 4 exhibits higher crack growth rates when compared to the coarse-grained material in the Paris range and near threshold  $\Delta K$  regime.
- The threshold value  $\Delta K_{th}$  of UFG material is lower than the value for coarse-grained Ti. The estimated value for UFG Ti is 2.5 MPa m<sup>1/2</sup>. And for coarse-grained material 4.7 Pa m<sup>1/2</sup>.
- Transcrystalline fatigue crack growth is characteristic for UFG Ti, whereas combination of transcrystalline and intercrystalline fracture is typical for the coarse-grained Ti. No difference in the fracture surface appearance was observed for crack growth rates ranging from 10<sup>−8</sup> m/cycle to the threshold on the fracture surface for both the material states.
- Crack closure determined experimentally was in good agreement with results calculated according to the Newman model, taking into account only plasticity induced closure. However, no clear signs of cyclic plasticity in terms of cyclic slip bands in the crack wake or changes of material microstructure adjacent to the propagating crack were revealed by SEM observations and EBSD.
- The performed experimental study and analysis of results indicate no or only very limited contribution of oxide and roughness induced closure.

## Acknowledgement

This research was carried out under the project CEITEC 2020 (LQ1601) with financial support from the Ministry of Education, Youth and Sports of the Czech Republic under the National Sustainability Programme II. The research was conducted in the frame of IPMinfra supported through project No. LM2015069 of MEYS.

## References

- [1] Leyens C, Peters M. Titanium and titanium alloys: fundamentals and applications. Wiley; 2006.
- [2] Lütjering G, Williams JC. Titanium. Berlin Heidelberg: Springer; 2007. p. 175–97.



- [3] Welsch G, Boyer R, Collings EW. *Materials properties handbook: titanium alloys*. ASM International; 1993.
- [4] Li Y, Pang Ng H, Jung H-D, Kim H-E, Estrin Y. Enhancement of mechanical properties of grade 4 titanium by equal channel angular pressing with billet encapsulation. *Mater Lett* 2014;114:144–7.
- [5] Purcek G, Yapici GG, Karaman I, Maier HJ. Effect of commercial purity levels on the mechanical properties of ultrafine-grained titanium. *Mater Sci Eng, A* 2011;528:2303–8.
- [6] Estrin Y, Vinogradov A. Fatigue behaviour of light alloys with ultrafine grain structure produced by severe plastic deformation: an overview. *Int J Fatigue* 2010;32:898–907.
- [7] Michel' J, Buršák M, Lacková P. Influence of deformation technology on fatigue properties of titanium. *Mater Eng – Materialove inžinierstvo* 2014;21:88–93.
- [8] Vinogradov AY, Stolyarov VV, Hashimoto S, Valiev RZ. Cyclic behavior of ultrafine-grain titanium produced by severe plastic deformation. *Mater Sci Eng, A* 2001;318:163–73.
- [9] Stolyarov VV, Zhu YT, Lowe TC, Islamgaliev RK, Valiev RZ. A two step SPD processing of ultrafine-grained titanium. *Nanostruct Mater* 1999;11:947–54.
- [10] Kim W-J, Hyun C-Y, Kim H-K. Fatigue strength of ultrafine-grained pure Ti after severe plastic deformation. *Scripta Mater* 2006;54:1745–50.
- [11] Stolyarov VV, Zhu YT, Alexandrov IV, Lowe TC, Valiev RZ. Grain refinement and properties of pure Ti processed by warm ECAP and cold rolling. *Mater Sci Eng, A* 2003;343:43–50.
- [12] Stolyarov VV, Zeipper L, Mingler B, Zehetbauer M. Influence of post-deformation on CP-Ti processed by equal channel angular pressing. *Mater Sci Eng, A* 2008;476:98–105.
- [13] Balyanov A, Kutnyakova J, Amirhanova NA, Stolyarov VV, Valiev RZ, Liao XZ, et al. Corrosion resistance of ultra fine-grained Ti. *Scripta Mater* 2004;51:225–9.
- [14] Cavaliere P. Fatigue properties and crack behavior of ultra-fine and nanocrystalline pure metals. *Int J Fatigue* 2009;31:1476–89.
- [15] Cavaliere P, Panella FW, Suresh S. Fatigue crack behavior of ultra fine grain pure metals produced via severe plastic deformation, in: *Atti del Congresso IGF19, Milano, Italy; 2007*. p. 9–16.
- [16] Semenova IP, Salimgareeva GK, Latysh VV, Lowe T, Valiev RZ. Enhanced fatigue strength of commercially pure Ti processed by severe plastic deformation. *Mater Sci Eng, A* 2009;503:92–5.
- [17] A. E647-05. Standard test method for measurement of fatigue crack growth rates. West Conshohocken, PA: ASTM International; 2005.
- [18] Klesnil M, Lukáš P. *Fatigue of metallic materials*. Academia; 1992.
- [19] Newman Jr JC. A crack opening stress equation for fatigue crack growth. *Int J Fract* 1984;24:5.
- [20] Greger M, Kander L, Snášel V, Černý M. Microstructure evolution of pure titanium during ECAP. *Mater. Eng. – Materiálové inžinierstvo* 2011;18:97–104.
- [21] Zerbst U, Vormwald M, Pippan R, Gänser H-P, Sarrazin-Baudoux C, Madia M. About the fatigue crack propagation threshold of metals as a design criterion – a review. *Eng Fract Mech* 2016;153:190–243.
- [22] Walker K, Wang CH, Newman JC. Junior fatigue crack closure due to surface roughness and plastic deformation. *Adv Mater Res* 2014;891–892:6.
- [23] Crapps J, Daniewicz SR. A macrostructural model for simulating the combined effects of roughness and plasticity induced fatigue crack closure. *Int J Fatigue* 2012;45:15–30.
- [24] Correia José AFO, De Jesus Abílio MP, Moreira Pedro MGP, Tavares Paulo JS. Crack closure effects on fatigue crack propagation rates: application of a proposed theoretical model. *Adv Mater Sci Eng* 2016;2016:11. , <https://www.hindawi.com/journals/amse/2016/3026745/>.

- XI. [35] R. Konecna, S. Fintova, G. Nicoletto, P. Sandera, Shrinkage pores and fatigue behavior of cast Al-Si alloys, *Materials Structure & Micromechanics of Fracture*, 465 (2011) 354-357.

## Shrinkage pores and fatigue behavior of cast Al-Si alloys

R. Konečná<sup>1, a</sup>, S. Fintová<sup>1</sup> and G. Nicoletto<sup>2, b</sup>

<sup>1</sup> Dept. of Materials Engineering, University of Žilina, Žilina, Slovakia

<sup>2</sup> Dept. of Industrial Engineering, University of Parma, Parma, Italy

<sup>a</sup>radomila.konecna@fstroj.uniza.sk, <sup>b</sup>gianni.nicoletto@unipr.it

**Keywords:** cast Al-Si alloys, fatigue, casting defects, shrinkage pores, metallography

**Abstract.** The fatigue strength of cast Al-Si alloys is strongly sensitive to the presence of casting defects. Extensive rotating bending fatigue testing of cast AlSi7Mg alloy at room temperature and 50 Hz is reported showing that shrinkage pores are the critical casting defect. The porosity of selected fatigue specimens extracted from castings is characterized with metallography using different pore sizing criteria. Data are fitted to EVS distributions and used for critical size prediction. Fatigue fracture surfaces are inspected in the SEM and the critical pores originating the fatigue cracks identified and measured according to criteria used in the metallographic inspection.

### Introduction

Aluminum-alloy castings offer a good strength-to-weight ratio at a reasonable cost, resulting in widespread use for components in automotive applications. However, for components exposed to cyclic loading, the fatigue behavior of the casting can be limited by the heterogeneous solidification microstructure, especially the presence of microporosity. It is well documented that the fatigue strength of cast Al-Si alloys depends primarily on casting defects as they favor fatigue crack initiation and that the size of the pores rather than just the percentage porosity dominates component performance, [1]. Metallographic methods are readily used to study porosity in Al-Si castings and measurements of largest pore sizes found in many micrographs can be fitted to Extreme Value Statistics (EVS). Such distribution can be subsequently used for extrapolating pore size expected in realistic material cross-sections, [2].

In this contribution, the pore size distribution of fatigue specimens extracted from AlSi7Mg alloy castings are metallographically characterized according to different equivalent size criteria and used for EVS characterization. The specimens are then tested in fatigue under rotating bending at room temperature and 50 Hz. The fracture surfaces of each specimen are then inspected in the SEM and the pores originating the fatigue fracture are identified and measured according to criteria used in the metallographic inspection. Conclusions are drawn on the equivalent pore size definition.

### Material and experimental procedures

The material studied here is a cast alloy AlSi7Mg. Many fatigue specimens were extracted from actual industrial castings and a selected number of them were preliminarily examined using metallographic methods. The micrograph of Fig. 1 shows the typical dendritic structure outlined by the dispersion of fine reinforcing eutectic silicon particles. The spacing of the secondary dendritic arms (SDAS) is known to correlate with the local freezing rate.

The Extreme Value Statistics approach has been proposed to estimate the upper bound pore size of standard 2-D measurements of pore populations using metallographic observations, [2]. The approach is based on i) measurements of largest pore equivalent sizes found in a significant number of metallographic fields of view and ii) verification that data fit the Gumbel's distribution. In the affirmative case, the distribution is used for extrapolating pore sizes expected in large, realistic material cross-sections. A detailed description of the theoretical framework of the LEVD method is given elsewhere, [3,4]. Pore size and morphology were evaluated by light microscopy at 50 x magnification (i.e. control area  $S_0 = 1.62 \text{ mm}^2$ ) with the image analysis program NIS Elements 3.0.

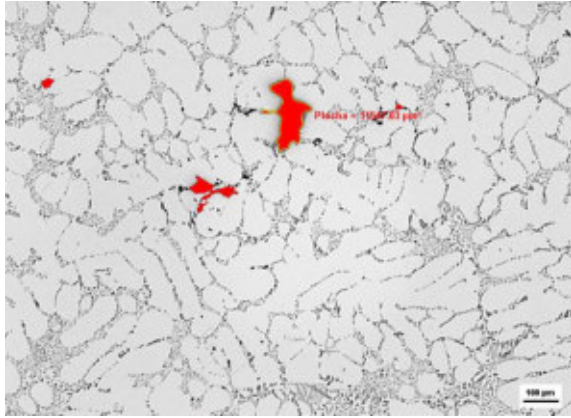


Fig. 1 - Typical micrograph used for pore size characterization

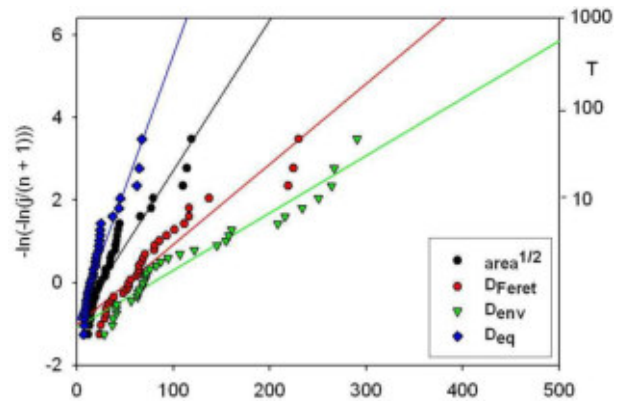


Fig. 2 - EVS plots using different definitions of equivalent pore size  $(Area)^{1/2}$ ,  $D_{eq}$ ,  $D_{Ferret}$ ,  $D_{env}$

Pore morphology poses a challenge to the metallographic characterization of largest pore sizes, namely when a definition of equivalent pore size is assumed to define the severity in fatigue of a 2-D view of the pore, such as Fig. 1. Pore morphology depends on the formation process. Gas pores have a compact spherical shape due to the effect of the pressurized gas during freezing. On the other hand, microshrinkage pores have an elongated morphology because they develop interdendritically, Fig. 1. Typical equivalent size definitions found in the literature are:  $(Area)^{1/2}$ ,  $D_{eq} = (4Area/\pi)^{1/2}$ , Feret diameter  $D_{Ferret}$ . [2,5,6]. Depending on this assumption, different prediction trends are found and shown in the plot of Fig. 2 for a single specimen. Other fatigue specimens were characterized likewise to quantify the variability.

While the linearity requirement is satisfied in Fig. 2, the predicted pore size for a given return period T can be very different depending on the assumed equivalent size. Models based on fracture mechanics usually estimate fatigue lives by integration of kinetic crack laws between an initial size and a critical size, [7]. In the case of casting pores the expected largest pore is considered an estimate of the initial crack size and has a strong influence on estimated lives.



Fig. 3 - 3D reconstruction of a shrinkage pore using X-ray computed tomography.

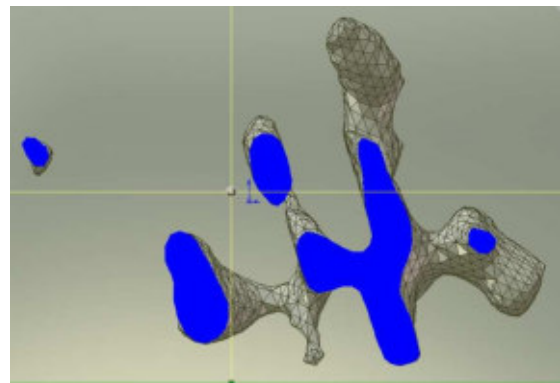


Fig. 4 - Random section through a shrinkage pore and resulting 2D porosity.

The branched nature of shrinkage pores due to its interdendritic development poses an additional challenge to metallography. Fig. 3 shows the 3D reconstruction of an actual shrinkage pore in AlSi7Mg obtained by x-ray microtomography, [8]. To simulate metallographic inspection, the 3-D pore is randomly sectioned to show the resulting pore geometry in 2D and the result is given in Fig. 4. It is likely that a shrinkage pore appears as multiple neighboring isolated pores and the determination of the equivalent size of the largest of the multiple neighboring pores results in a severe underestimate of the actual pore size. Previous studies demonstrated that pores observed on the fracture surfaces were 2 to 5 times larger than those observed on metallographic planes regardless of the alloy and casting process, [6]. Therefore, criteria should be established to correctly

estimate the actual shrinkage pore size by metallographic methods including morphology and coalescence of neighboring pores. In the light of Fig. 4, Fig. 1 can be re-examined and the neighboring pores in red considered as belonging to a single shrinkage pore whose size can be estimated from the multiple pore envelop size  $D_{env}$ . Using this approach, an additional trend line is determined and shown in Fig. 2. The critical role of the equivalent pore size definition for shrinkage pores is demonstrated by the observation that, for a given  $T$  value, the estimated critical pore size is in the 1-to-5 ratio.

**Fatigue behavior and crack initiating pores**

Rotating bending fatigue experiments were performed on the AlSi7Mg alloy specimens at room temperature and 50 Hz. Fig. 5 shows the large (i.e. up to two orders of magnitude) scatter in fatigue life due to the influence of casting pores. In all fatigue experiments the fracture initiated at casting pores located near or at the free specimen surface, i.e. where the stress amplitude is highest. S-N curves predicted with a fatigue crack propagation model from an initial surface defect are also included in Fig. 5, [7].

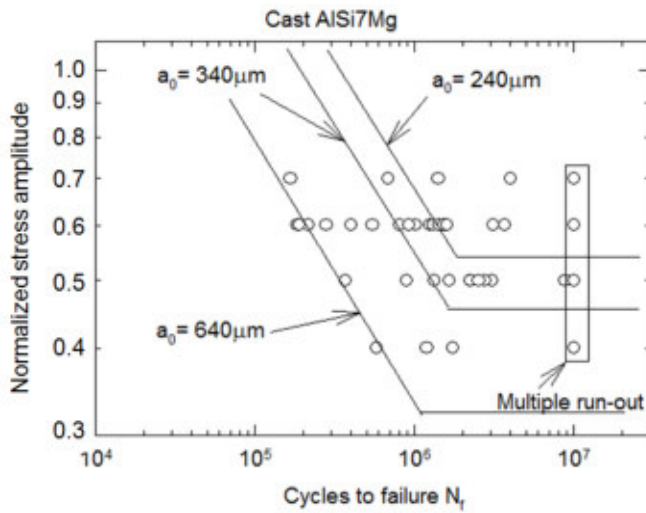


Fig. 5 Fatigue response of rotating bending specimens made of cast AlSi7Mg.

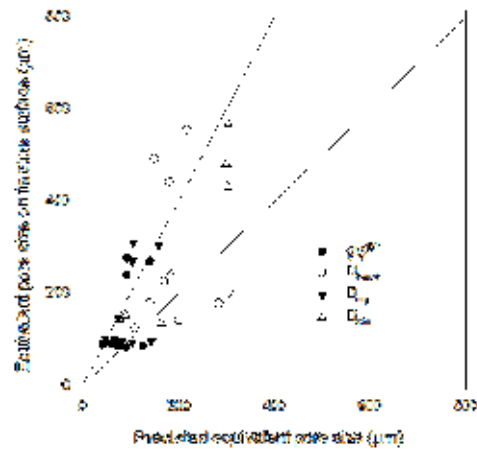


Fig. 6 Predicted vs. observed equivalent pore sizes.

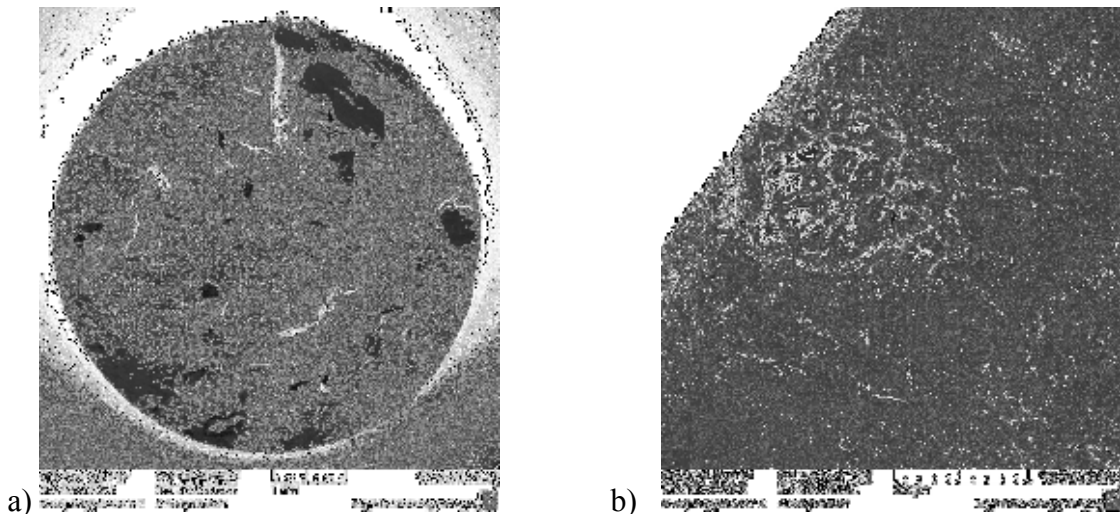


Fig. 7 a) Fatigue fracture surface with multiple crack initiations; b) critical casting pore.

Selected fatigue fracture surfaces were inspected in the SEM. Fig. 7a shows a global view of the broken specimen with evidence of multiple initiation sites at different pores and Fig. 7b shows the



critical pore where fatigue initiated. Fig. 7 demonstrates that cracks at pores develop to a surface semielliptical shape.

Equivalent sizes of the critical pores found in the broken fatigue specimens were determined using the different definitions used to determine the EVS plots, such as in Fig. 2, and are correlated to the estimated pore sizes for the appropriate return period  $T$  (i.e. given by the ratio between the area of the highly specimen stressed cross-section and the area of the metallographic magnified field of view) in Fig. 6. The pore sizing criterion used in the metallographic characterization influences the estimated critical pore size. Generally, actual critical pores are larger than estimated critical pores. However, the correlation is better when the  $D_{env}$  and  $D_{Feret}$  criteria are used. If the different critical pore size estimates are used in the fracture mechanics model applied in Fig. 5, only  $D_{Feret}$  and  $D_{env}$  would give pore sizes that are compatible with the initial crack sizes of the fatigue model. A thorough validation of this conclusion is currently under way.

## Conclusions

The main conclusions drawn from this study of the role of shrinkage pores on the fatigue behavior of cast AlSi7Mg are the following:

- EVS is applicable to the pore size population characterization by metallographic methods;
- the fatigue response of specimen extracted from Al-Si casting shows a large scatter in life;
- fatigue crack initiation always occurred at shrinkage pores near the free surface;
- for the irregular 3-D shape of shrinkage pores, specific sizing criteria were proposed;
- fatigue life estimates can be obtained by a fracture mechanics model with the initial crack size estimated from EVS.

## Acknowledgments

This work was done as a part of the KEGA grant No.3/6110/08. It is also consistent with the objectives of MATMEC, one of Emilia-Romagna newly established regional net-laboratories (<http://www.matmec.it/>).

## References

- [1] Wang, Q.G., Apelian, D., Lados, D. A.: Fatigue behavior of A356-T6 aluminum cast alloys. Part I. Effect of casting defects, *Journal of Light Metals* 1, 2001, pp. 73-84.
- [2] Murakami, Y. *Metal Fatigue: Effects of Small Defects and Nonmetallic Inclusions*, Elsevier, Oxford, 2002.
- [3] Nicoletto, G., Konečná, R., Baicchi, P., Majerová, V.: Casting Porosity and Long-life Fatigue Strength of a Cast Al-alloy, In: *Materials Science Forum*. - ISSN 0255-5476. - Vol. 567-568, 2007, pp. 393-396.
- [4] Konečná, R., Fintová, S., Nicoletto, G.: Influence of the casting pores' origin on the fatigue properties of cast Al-Si alloy, *Procs Metallography*, Stará Lesná, 2010.
- [5] Gao, Y.X. et al.: A micro-cell model of the effect of microstructure and defects on fatigue resistance in cast aluminum alloy, *Acta Mat.* 52 (19), 5435-5449, 2004.
- [6] Wang, Q.G., Jones P.E.. Prediction of Fatigue Performance in Aluminum Shape Castings Containing Defects, *Metallurgical and Materials Trans B*, 38B, 615-621, 2007.
- [7] Nicoletto, G., Baicchi, P., Konečná, R.: Fatigue life prediction of Al-Si alloys with casting defects, In: *2nd Fatigue symposium Leoben, Austria*. 2008. - ISBN 978-80-01-04162-8. pp. 2-11.
- [8] Anzelotti, G., Fintová, S., Konečná, R., Nicoletto, G.: Casting pore characterization by x-ray computed tomography and metallography. In: *26th Danubia-Adria Symposium Montanuniversität Leoben, Austria*. 2009. - ISBN 978-3-902544-02-5. pp. 3-4.

## **Materials Structure & Micromechanics of Fracture VI**

10.4028/www.scientific.net/KEM.465

### **Shrinkage Pores and Fatigue Behavior of Cast Al-Si Alloys**

10.4028/www.scientific.net/KEM.465.354

#### **DOI References**

[1] Wang, Q.G., Apelian, D., Lados, D. A.: Fatigue behavior of A356-T6 aluminum cast alloys. Part I. Effect of casting defects, *Journal of Light Metals* 1, 2001, pp. 73-84.

10.1016/S1471-5317(00)00008-0

[5] Gao, Y.X. et al.: A micro-cell model of the effect of microstructure and defects on fatigue resistance in cast aluminum alloy, *Acta Mat.* 52 (19), 5435-5449, 2004.

10.1016/j.actamat.2004.07.035

[6] Wang, Q.G., Jones P.E.. Prediction of Fatigue Performance in Aluminum Shape Castings Containing Defects, *Metallurgical and Materials Trans B*, 38B, 615-621, 2007.

10.1007/s11663-007-9051-4

- XII. [36] R. Konecna, G. Nicoletto, S. Fintova, Statistical description of largest pore sizes in cast Al-Si alloys, 25th Danubia-Adria Symposium on Advances in Experimental Mechanics, (2008) 123-124.



## 25th Danubia-Adria Symposium on Advances in Experimental Mechanics

České Budějovice (Budweis) and Český Krumlov  
September 24, 2008 - September 27, 2008  
Czech Republic



### STATISTICAL DESCRIPTION OF LARGEST PORE SIZES IN CAST AL-SI ALLOYS

R. Konečná<sup>^</sup>, G. Nicoletto<sup>\*</sup>, S. Fintová<sup>^</sup>

<sup>^</sup> Dept. of Materials Engineering – University of Žilina – Slovakia  
radomila.konecna@fstroj.uniza.sk;

<sup>\*</sup> Dept. of Industrial Engineering – University of Parma – Parma – Italy  
gianni.nicoletto@unipr.it;

Cast aluminum alloys are increasing used in the automotive industry due to their excellent castability, corrosion resistance, and especially their high strength-to-weight ratio. Their application for cast components subjected to dynamic loading has motivated considerable interest on the fatigue behavior of cast Al-Si alloys. Besides the microstructural characteristics, fatigue strength of cast aluminum components heavily depends on the casting pores formed during solidification because they favor fatigue crack initiation due to high local stress concentration, [1]. Pores are the most common defects and are almost inevitable with the casting technologies used in industry. The severity of pores in fatigue intuitively depends on size, morphology and density. However there is no definite consensus of the most appropriate severity indicator because shrinkage pores are branched discontinuities while gas pore are roundish cavities. A common measure is the equivalent size obtained from area cross-sectional measurements obtained by metallography, [2].

The present work is aimed to identify a method to predict the influence of shrinkage pores (pore size population and shape) on the fatigue response of cast Al-Si alloys starting from a metallographic characterization of the pore population. Fatigue experiments on specimens of Al-Si alloys are presented along with the microstructure and porosity characterization using light microscopy. A SEM investigation of fracture surfaces of broken specimens for fatigue crack initiation is also presented and used in the discussion.

Smooth specimens were tested at different stress amplitude levels under rotating bending load at 50 Hz frequency. Since the objective was the correlation of stress amplitude, number of

cycles and the pore influence on a specimen-to-specimen basis, four fatigue specimens were examined in detail by metallography and fractography. A preliminary characterization of microstructure uniformity as described by SDAS showed that all specimens had quite similar basic structure.

The size of casting porosity was studied on metallographic specimens using a light optical microscope and the statistical sampling method proposed by Murakami, [3]. The image analysis program LUCIA Metallo 5.0 was applied for detailed evaluation of porosity. The equivalent size  $(A)^{1/2}$ , with A the area of the pore was used to describe the influence of a pore in fatigue. To characterize the size population of the largest pores, the equivalent sizes  $(A)^{1/2}$  with A the area of the largest pore found in a statistical significant number of metallographic fields of view were determined and used in conjunction with the largest extreme value distribution (LEVD), [3].

As a drawback of the method, the random 2-D sections through pores are expected to underestimate the largest sizes of the critical pores that actually originate fatigue fractures. Therefore, the fracture surfaces of the failed specimens were analyzed in the SEM of IPM-Brno to identify places of crack initiations and estimate size and number of initiating pores.

The fatigue test results are presented in columns 2 and 3 of Tab.1. In all cases the fatigue fracture started from pores, on or near the surface because of the rotating bending load condition. Multiple fracture initiation places were also typical of all fracture surfaces. Fig. 1 shows a specimen with multiple crack initiation and Fig. 2 an example of the determination of the initiating pore size by digital image analysis.

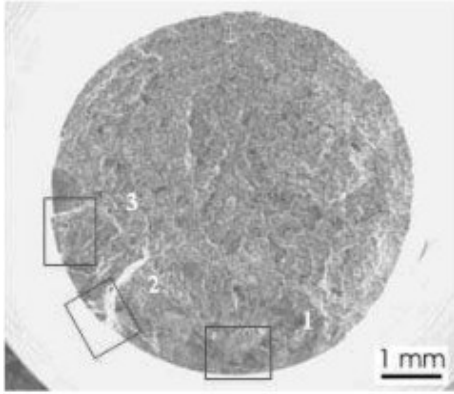


Fig. 1 Fatigue fracture surface.

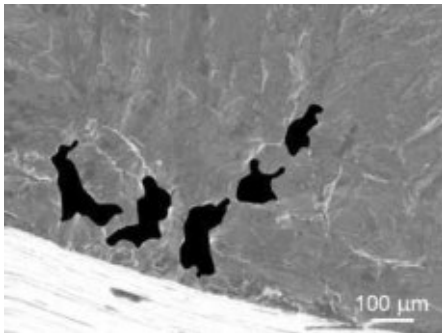


Fig. 2 Pore initiating a fatigue crack.

The results of the fractographic investigation in the SEM are also summarized in columns 3 and 4 of Tab. 1 and show that the large scatter in the fatigue data with the unpredictability of the combine role of stress amplitude and pore size on the actual fatigue life. Interestingly, a correlation between number of initiating defects and fatigue life rather than largest critical pore size and fatigue life is observed. Also, no correlation between stress amplitude and number of initiating pores is determined.

Application of the LEVD approach for characterizing largest defect sizes in materials requires the setup of the measurement procedure in the light microscope (i.e. magnification). In the case of casting pores in Al-Si alloys there is also the influence of different types of pores and their density. Fig. 3 shows a plot where all pore sizes are arranged in a Gumbel's probability plot. No data set conforms to a unique statistical description. However, if a transition pore size, [1], in the range of 25-50 μm, is used to separate large, potentially fatigue-critical casting pores from small, non

detrimental pores, then the data fit reasonably individual lines as shown in Fig. 4.

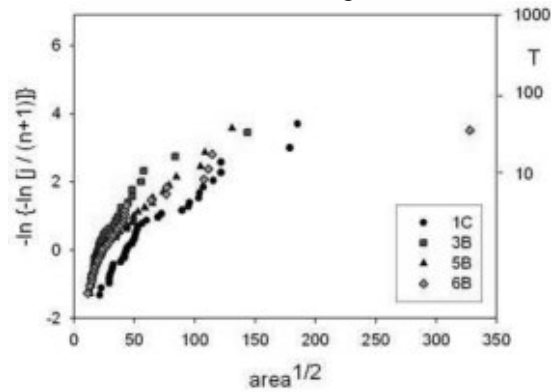


Fig. 3 LEVD plots for casting pores.

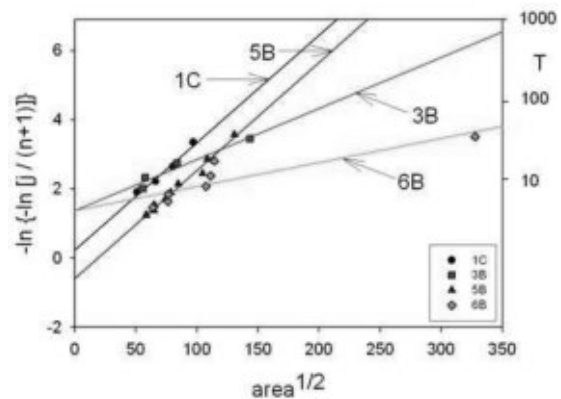


Fig. 4 LEVD plots for the largest pores only.

An estimate of the critical pore size using these trend lines requires a suitable return period  $T=S/S_0$ . In this case considering the rotating bending condition where a small volume of material is under maximum stress and  $S_0 = 1.86 \text{ mm}^2$ , a value of  $T=10$  is used to obtain the estimates given in column 6 of Tab. 1.

Acknowledgments

This work was done as a part of VEGA grant No.1/3194/06 and KEGA grant No.3/6110/08.

**References**

1. Wang Q. G., Apelian D., Ladoss D. A., *Journal of Light Metals 1*, 2001, 73-84
2. Nicoletto G., Baicchi P., Konečná R., *Procs. 2<sup>nd</sup> Leoben Fatigue Symposium*, W. Eichseder ed. , 2008
3. Murakami Y., *Metal Fatigue: Effects of Small Defects and Nonmetallic Inclusions*, Elsevier, Oxford, 2002, 320.

Specimen	S [MPa]	N <sub>f</sub>	No. of initiations n <sub>i</sub>	Largest critical pore size [μm]	(A <sub>cr</sub> ) <sup>1/2</sup> for T = 10
3B	80	2 074 770	2	66	52
5B	70	669 562	3	373	85
6B	60	870 745	3	69	105
1C	50	3 611 605	2	482	130



- XIII. [37] S. Fintova, R. Konecna, G. Nicoletto, Influence of shrinkage porosity on the fatigue behaviour of cast AlSi7Mg, Metal 2010: 19th International Metallurgical and Materials Conference, (2010) 690-695.

## INFLUENCE OF SHRINKAGE POROSITY ON THE FATIGUE BEHAVIOR OF CAST AISi7Mg

Stanislava FINTOVÁ<sup>a</sup>, Radomila KONEČNÁ<sup>a</sup>, Gianni NICOLETTO<sup>b</sup>

<sup>a</sup> *Department of Materials Engineering, University of Žilina, Univerzitná 1, 01026 Žilina Slovakia, stanislava.fintova@fstroj.uniza.sk*

<sup>b</sup> *Department of Industrial Engineering, University of Parma, Viale G.P. Usberti, 181/A, 43100 Parma, Italy, gianni.nicoletto@unipr.it,*

### Abstract

Cast defects are always present in aluminum castings due to the production process. Because of the negative influence of porosity on the fatigue properties, the porosity knowledge is the key-step in the fatigue life prediction of Al-Si castings. This contribution presents rotating bending fatigue tests that were planned and performed on specimens of modified AISi7Mg cast alloy based on the largest defect size characterization by metallography. For the production of the fatigue test specimens, separately cast bars were produced with different treatments of the liquid metal before casting. The objective was to determine the role of modifiers on fatigue response using a limited number of test specimens. The largest defect size on individual specimens was predicted using a statistical pore size distribution obtained with metallography and used in fatigue test planning. Predicted and actual sizes of critical pores observed on the fatigue fracture surface of broken specimens were compared.

### 1. INTRODUCTION

Aluminum alloys are increasingly used in structural applications controlled by low weight requirements, (i.e. aircraft and automotive industry) for their excellent specific strength (i.e. strength-to-density ratio). The Al-Si alloys are the most used Al-alloys when the casting process is considered [1].

The presence of pores in cast Al-Si alloys reduces fatigue life of an order-of magnitude or more compared to a defect-free material because practically eliminates the crack initiation phase. It was also found that there is a threshold defect size (i.e. in the range 25-50  $\mu\text{m}$ , [1]) for fatigue crack initiation from a pore. Below this threshold size, fatigue crack initiation occurs at eutectic particles or by slip band formation. Typically, fatigue endurance is reduced when the size of porosity increases. Therefore, the quality of the castings is strictly related to the porosity control [2].

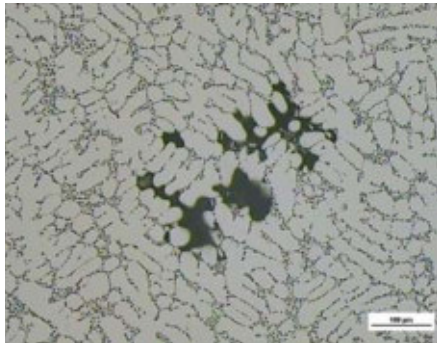
In this contribution rotating bending fatigue tests were planned based on the largest defect size prediction according to the Largest Extreme Value Distribution theory [3]. For the defect size characterization, the pore area<sup>1/2</sup> definition was used according to [4]. The defects observed on the fatigue fracture surfaces after the fatigue test were compared with the predicted largest defect sizes.

### 2. EXPERIMENTAL MATERIAL AND PROCEDURE

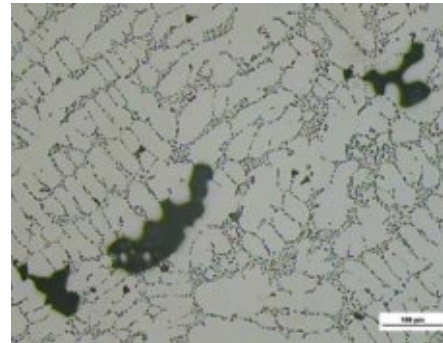
The experimental material was the cast aluminum alloy AISi7Mg heat treated to T6. The material of the set 4 was modified by LVE tablets based on sodium salts and degassed by nitrogen for 10 minutes. The bars of the set 5 were treated with using the same way as for the set 4 and cast after the subsiding of the modification effect of LVE tablets. The bars were separately cast to the steel moulds. The metallographic specimens were extracted from the cast bars before the production of the fatigue tests specimens. Rotating bending fatigue tests were performed at the University of Parma in Italy. The structural analysis was carried

out applying metallographic techniques and digital image analysis software on metallographic polished cross sections and was performed at the University of Žilina.

Typical examples of the microstructure with defects of the AlSi7Mg aluminum alloy specimens are shown in Fig. 1. The microstructure consists from primary dendrites of  $\alpha$ -phase (solid solution of Si in Al) and eutectics ( $\alpha$ -phase + Si particles) located in interdendritic spaces. The Si particles had a rounded shape on the metallographic section due to the optimal alloy modification. Porosity was present in all materials due to the casting process. The typical examples of the defects observed on metallographic specimens are also shown in Fig. 1.



a) set 4



b) set 5

**Fig. 1** Typical examples of microshrinkages observed on metallographic cross-sections

The metallographic evaluation, the measurements of defect size and the pore morphology evaluation were performed with a light microscope and the image analysis program NIS Elements 3.0. The aim was the statistical characterization of pore sizes to be used for the prediction of the largest defect size according to the Largest Extreme Value Distribution (LEVD) theory [3]. The porosity was evaluated at 50x magnification and the controlled area  $S_0$  was 1.62 mm<sup>2</sup>.

The rotating bending fatigue tests for the two material sets were planned based on the results of the previous pore size characterization by metallographic methods and porosity prediction using LEVD theory. Smooth 6 mm diameter fatigue specimens were tested at different stress amplitude levels (from 80 to 30 MPa) at 50 Hz frequency.

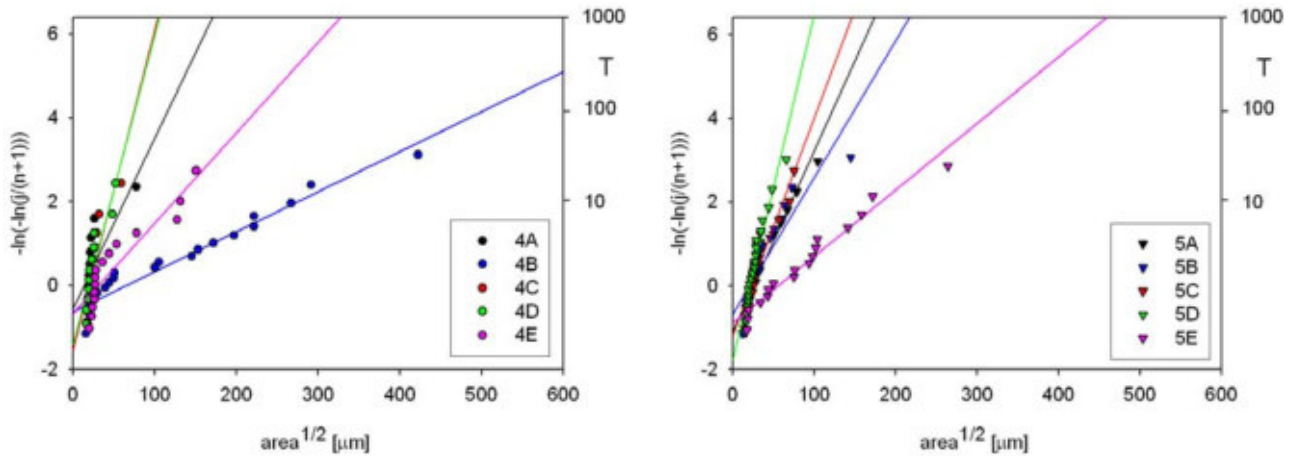
### 3. EXPERIMENTAL RESULTS

#### 3.1 Porosity evaluation, characterization and prediction

The metallographic specimens of set 4 were characterized by quite small casting defects with morphology of microshrinkage pores as it is shown in Fig. 1a. Except in one case (i.e. specimen 4B with large defects in the central part) the defects in the specimens of set 4 were uniformly distributed on the metallographic sections. The porosity of the specimens of set 5 was in the shape of the microshrinkage pores, Fig. 1b. Except the specimen 5E the amount of porosity was small and the sizes of observed defects were smaller compared to the defects of set 4. Specimen 5E had the largest defects in the set.

The value of the  $(\text{area})^{1/2}$  was used as characterizing pore size and as severity indicator in fatigue. The results of the porosity evaluation according to the LEVD theory, [3], are summarized in the Fig. 2. The pore size observed on the metallographic specimens of set 4 had a large scatter. The smallest pore sizes were measured on the specimens 4D and 4C, then 4A, 4E and the largest defects were present in the specimen

4B. On the specimen 4B the largest defect sizes were measured and also the scatter of the measured values was the largest one in the case of this specimen. Similar differences in the measured largest defects sizes for the specimens from the set 5 cast after the subsiding of the LVE tablets modification effect were observed. In this case the smallest porosity was measured on the specimens 5D, 5C, 5A and 5B and the largest one on the specimen 5E.



a) set 4

b) set 5

**Fig. 2** LEVD plots

The plots of Fig. 2 can be used for the comparison of individual specimens and planning of fatigue experiments. For a given stress amplitude, the longest fatigue life was expected for the specimens with smallest pores because of the influence of pore size on fatigue properties. For a given stress amplitude, the number of cycles to the fatigue fracture is assumed to increase with decreasing pore size. The predicted largest defect size for the area  $S = 10 \text{ mm}^2$ , the representative area of the most loaded area of the rotating bending fatigue specimens, were calculated using the appropriate return period  $T$  in the plot of Fig. 2 and are given in the Tab. 1.

**Tab. 1** Predicted defect sizes and rotating bending fatigue tests results

	SDAS [μm]	predicted largest defect size	$S_a$ [MPa]	$N_f$ [cycles]		SDAS [μm]	predicted largest defect size	$S_a$ [MPa]	$N_f$ [cycles]
<b>4C</b>	22	43	80	41	<b>5D</b>	20	43	80	670 789
<b>4D</b>	21	43	50	104 655	<b>5C</b>	21	56	70	99
<b>4A</b>	21	56	35	12 463 211	<b>5A</b>	21	65	50	439 338
<b>4E</b>	21	111	40	97	<b>5B</b>	21	74	45	962 505
<b>4B</b>	20	246	30	2 360 844	<b>5E</b>	21	165	35	36

For all metallographic specimens, the predicted largest defect sizes were larger than the threshold defect size for the fatigue crack initiation (i.e. in the range 25-50 μm, [1]). And so in the comparison of both sets, the smaller porosity was observed on the specimens from the set 5 cast after the subsiding of the modification effect compared to the set 4 modified by LVE tablets and degassed. Therefore superior fatigue properties for the set 5 were assumed compared to set 4.

For completeness, the values of Secondary Dendrite Arm Spacing (SDAS), obtained according to the straight line method (i.e. line length=12 cm) [5], are summarized in the Tab. 1 because SDAS characterize the material structure. It is observed that the values of SDAS are similar for all specimens of both sets.

### 3.2 Fatigue tests results

The fatigue test results are shown in the Fig. 3, where the number of cycles to the fracture ( $N_f$ ) is plotted versus the nominal stress amplitude  $S_a$  (i.e. S–N curve). The fatigue specimens were tested considering the porosity evaluation and the largest defect size prediction for the area  $S = 10 \text{ mm}^2$  given in Tab. 1.

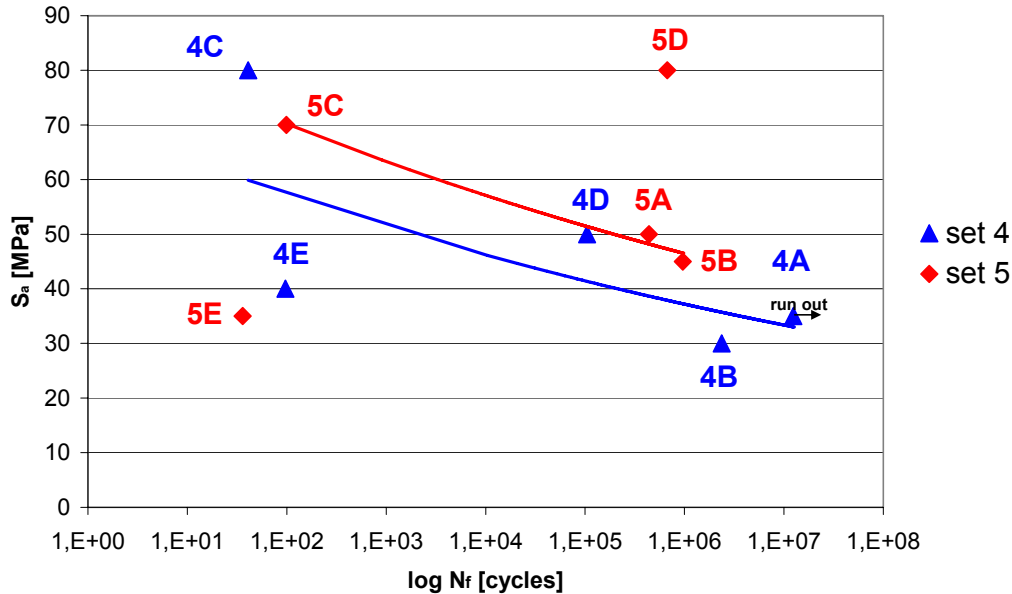


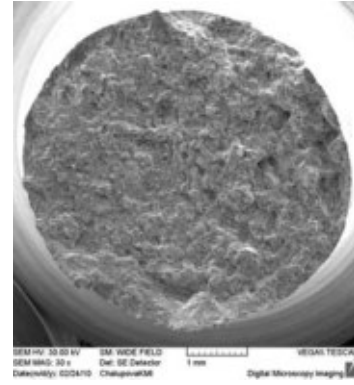
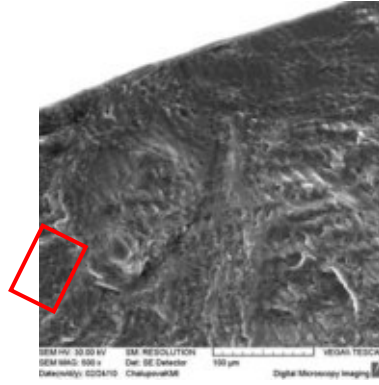
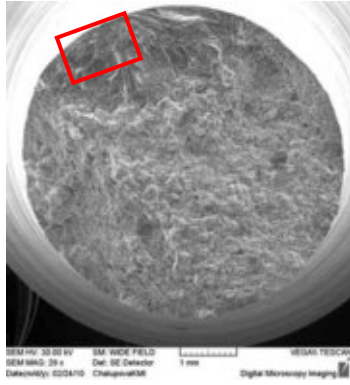
**Fig.3** S-N curve

The specimens from each set with the smallest predicted largest defect size were tested at the largest stress level amplitude. With increasing of the predicted largest defect size, the applied stress level amplitude decreased. The prediction according to the porosity characterization that the set 4 is worse in terms of fatigue behavior than set 5 was verified. The plot shows a very large scatter between the two material sets and among specimens of the same material. It demonstrates that the largest pore sizes in the tested material volume affect dramatically the fatigue response. Specimens failed within 100 load cycles. While 4C and 5C were subjected to relatively high stress amplitude, specimens 4E and 5E apparently contained large initial defects with essentially propagated by brittle fracture mechanisms.

### 3.3 Fractographic analysis

Some chosen specimens broken during the fatigue tests were examined in SEM. The fracture surfaces and the crack initiation places (IP) are shown in Fig. 4. The fracture surfaces of the specimens, except the specimen 4D, were characterized by the fatigue region and the final static fracture. The results show, that for all the examined specimens the fatigue fracture occurred because of the presence of a casting defect on or near the free surface of the specimen. This is due to the rotating bending load condition that develops the highest stress on the surface of the tested specimen.

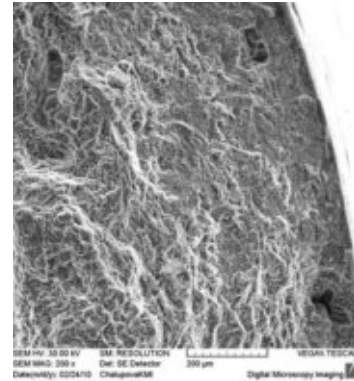
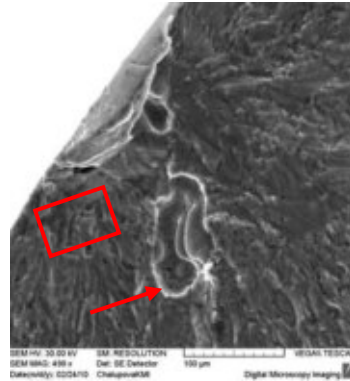
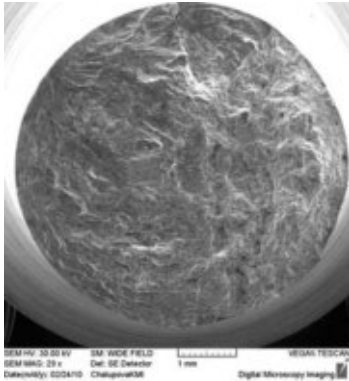




a) specimen 4B,  $S_a = 30$  MPa,  $N_f = 2\,360\,844$  cycles

b) specimen 4B, IP

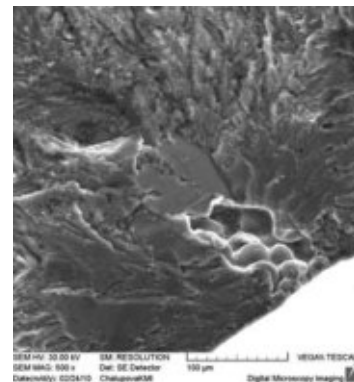
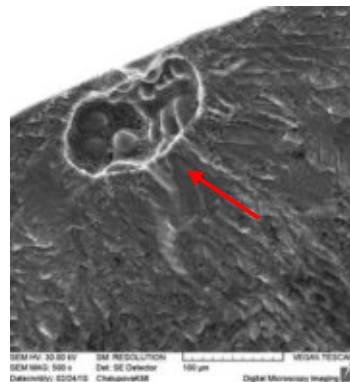
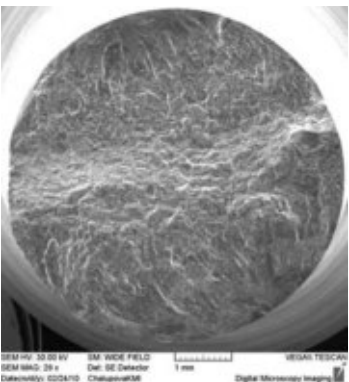
c) specimen 4D,  $S_a = 50$  MPa,  $N_f = 104\,655$  cycles



d) specimen 5B,  $S_a = 45$  MPa,  $N_f = 962\,505$  cycles

e) specimen 5B, IP

f) specimen 5B, defects below the specimens free surface



g) specimen 5D,  $S_a = 80$  MPa,  $N_f = 670\,789$  cycles

h) specimen 5D, IP 1

i) specimen 5D, IP 2

**Fig. 4** Fatigue fracture surfaces

Only in the case of the specimen 5D the multiple fatigue crack initiation occur, Fig. 4g. In the other cases only one IP on the fatigue fracture surfaces were found, Fig. 4a and Fig. 4d. In the case of the specimen 4D to identify the fatigue crack initiation place was not possible. Also it was not possible to distinguish fatigue region on the fracture surface.

In the cases of the specimens 5B and 5D it was possible to estimate the size of the defects observed on IP on the fatigue fracture surfaces. The critical defect at the IP of the specimen 5B, Fig. 4e, had the size  $\text{area}^{1/2} = 75 \text{ }\mu\text{m}$ , which is almost the same of the predicted largest defect size for this specimen for the area  $S = 10 \text{ mm}^2$ , see Tab.1. In the case of the specimen 5D the predicted largest defect was smaller than the measured critical size of  $107 \text{ }\mu\text{m}$ .

#### 4. CONCLUSIONS

The rotating bending fatigue tests on two sets (i.e. 4 and 5) of limited number of specimens from cast AlSi7Mg alloy were planned and performed after the metallographic evaluation of the respective pore size population. The following conclusions can be proposed:

- the fatigue behavior of AlSi7Mg cast after subsiding of the modification effect of LVE tablets is slightly better than AlSi7Mg modified with LVE tablets of sodium salts and degassed by nitrogen for 10 minutes,
- similar largest defects sizes for the area  $S = 10 \text{ mm}^2$  were predicted for both sets,
- the number of cycles to the fracture reasonably correlate with the predicted largest defect sizes,
- the different scatter in defect sizes between two material sets obtained by LEVD analysis and metallography correlate with fatigue data scatter,
- the porosity evaluation can be used for the fatigue test planning and comparison of different materials using a limited number of specimens.

#### ACKNOWLEDGEMENTS

*This work was done as a part of KEGA grant No.3/6110/08.*

#### LITERATURE

- [1] WANG, Q. G. – APELIAN, D. – LADOS, D. A. Fatigue behavior of A356-T6 aluminum cast alloys. Part I. Effect of casting defects. Journal of Light Metals 1, 2001, p. 73-84.
- [2] KONEČNÁ, R. – NICOLETTO, G. – MAJEROVÁ, V.: Largest extreme value determination of defect size with application to cast Al-Si alloys porosity, METAL 2007, Ostrava: TANGER 2007, CD ROM
- [3] MURAKAMI, Y. Metal Fatigue: Effects of Small Defects and Nonmetallic Inclusions, Elsevier, Oxford, 2002.
- [4] KONEČNÁ, R. – FINTOVÁ, S. – NICOLETTO, G.: Influence of the casting pores' origin on the fatigue properties of Al-Si cast alloys, Metallography 2010, In press.
- [5] Atlas métalographique des alliages d'aluminium. CTIF, Paris, 1980.

- XIV. [38] S. Fintova, R. Konecna, G. Nicoletto, Largest defect sizes distribution application to the Al-Si alloys, Metal 2009, Conference Proceedings, (2009) 428-434.

## LARGEST DEFECT SIZES DISTRIBUTION APPLICATION TO THE Al-Si ALLOYS

Stanislava Fintová<sup>a</sup>  
Radomila Konečná<sup>a</sup>  
Gianni Nicoletto<sup>b</sup>

<sup>a</sup> Department of Materials Engineering, University of Žilina, Univerzitná 1, 01026 Žilina Slovakia, [stanislava.fintova@fstroj.uniza.sk](mailto:stanislava.fintova@fstroj.uniza.sk)

<sup>b</sup> Department of Industrial Engineering, University of Parma, Viale G.P. Usberti, 181/A, 43100 Parma, Italy, [gianni.nicoletto@unipr.it](mailto:gianni.nicoletto@unipr.it)

### Abstract

Casting defects such as gas pores and shrinkages typically occur in castings. Since defects favor early fatigue crack initiation, the total fatigue life is controlled by porosity. Usually the fatigue life decreases when the volumetric fraction of porosity increases and also depends on defect size, morphology and location with respect to the free surface of casting. Experiments show that shrinkage pores are especially detrimental because of considerable size and irregular morphology. Eutectic Si particles and intermetallic phases have a minor role compared to casting pores on the fatigue properties.

In this contribution unmodified and Sr-modified specimens of a cast Al-Si alloy were used. Metallographic specimens were extracted from broken fatigue specimens and pore population investigated using image analysis software. Murakami's statistical method based on the "Largest extreme value distribution" (LEVD) theory for predicting the largest defect size in real castings from a metallographic investigation was used. In this paper, alternative extrapolation criteria for critical pore size prediction are examined. Two different approaches of statistical evaluation of the largest defect sizes measured by metallographic method were compared here with results from fatigue tests. A threshold size of casting defects for fatigue crack initiation was also taken to the consideration.

### 1. INTRODUCTION

Aluminum alloys are increasingly used in structural applications controlled by low weight requirements, (i.e. aircraft and automotive industry) for their excellent specific strength (i.e. strength-to-density ratio). The Al-Si alloys are the most used Al-alloys when the casting process is considered [1].

Formation of porosity and microshrinkage cavities are almost inevitable in the sand casting process [2]. They often result in limited mechanical properties including low strength, ductility and fracture toughness, erratic crack initiation and crack propagation characteristics, potentially accompanied by a lack of pressure tightness [3]. The presence of pores reduces fatigue life of an order-of magnitude or more compared to a defect-free material because the crack initiation phase is practically eliminated. There is, however, a threshold defect size (i.e. in the range 25-50  $\mu\text{m}$ ) for fatigue crack initiation from a pore, [5]. Below this threshold size, fatigue crack initiation will occur at oxides or by slip band formation [5].

Casting defects have a detrimental effect on fatigue life by shortening not only fatigue crack propagation, but also the initiation period. The decrease in fatigue life is directly correlated to the increase of defect size [4, 5]. Therefore, the quality of the castings is strictly related to porosity control [2].

Metallographic measurements of the pore size population are one of the earliest characterizations available for new components. Unfortunately, random 2-D sections through pores do not provide good estimates of the defect size without further data analysis. Pores observed on fracture surfaces are 2 to 5 times larger than those observed on the metallographic planes regardless of alloy and casting process [6]. Pores responsible for fatigue failures are normally the largest in the stressed volume,

and can be 10 times larger than the “maximum pore size” measured in random metallographic sections. In this case, the maximum pore size in a cast component can be estimated from the metallographic data using EVS (extreme value statistics) [6].

The present work adopts the Murakami’s statistical method, [7], for the prediction of the largest defect sizes in real castings based on the application of LEVD to polished cross-sections of metallographic specimens. The digital image analysis software (NIS Elements 3.0) was used for the evaluation of size and morphology of porosity. The aim is the comparison of the predicted defect sizes from the LEVD plots for all measured data and from LEVD plots for values larger than a threshold size as determined from data bi-linearity.

## 2. MATERIAL AND EXPERIMENTAL PROCEDURE

The unmodified and Sr-modified cast hypoeutectic AlSi7Mg alloy heat treated to the T6 regime was used as experimental material.

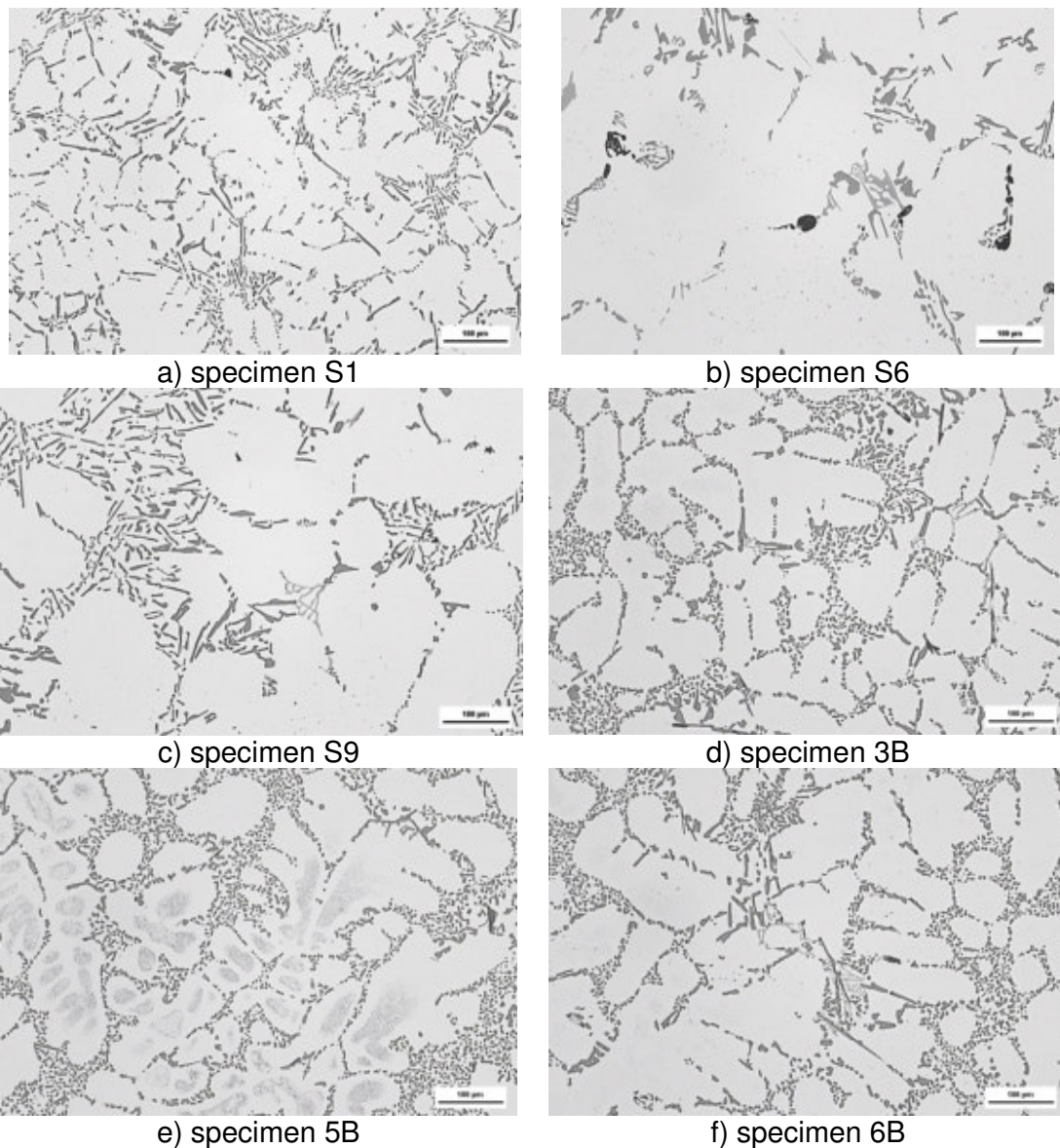


Fig. 1 Typical microstructure of tested specimens, etched by 0,5% HF



The specimens for microstructure analysis and porosity evaluation were delivered after fatigue tests from the University of Parma (Italy) where the fatigue tests were performed. Three batches of unmodified specimens (S1, S6 and S9), three specimens in each batch, were delivered. Three modified specimens extracted from real casting (3B, 5B and 6B) were used for the porosity characterization and metallographic evaluations. All the modified specimens were modified by the optimal amount of Sr. Specimens from the batch S1 were cast separately and the specimens from the batches S6 and S9 were extracted from real castings. Experimental materials were sand cast.

After the fatigue tests, metallographic specimens from the tested bars were extracted. The structural analysis was carried out applying metallographic techniques and digital image analysis software on polished cross-sections. Typical microstructures are shown in Fig. 1. The microstructure is characterized by primary dendrites of  $\alpha$ -phase (solid solution of Si in Al with maximum solubility limit 1.59 % at eutectic temperature 577 °C) and by a eutectic structural component ( $\alpha + \text{Si}$ ) located between the secondary dendrite arms. The eutectic silicon particles in the case of specimens S1, S6 and S9 have a needle shape because of the unmodified liquid metal, Fig. 1 a-c. In the case of the specimens 3B, 5B and 6B the eutectic phase grew as thin, interconnected rods between  $\alpha$ -dendrites because the liquid metal was modified by an optimal amount of Sr. The modified silicon rods appear as round particles on the metallographic section, Fig. 1 d-f. Intermetallic phases are also located in the interdendritic areas. Evaluation of the secondary dendrite arm spacing (SDAS) was performed according to the linear method (i.e. line with the length = 12 cm) [7].

The porosity was evaluated on metallographic specimens using a light optical microscope at the University of Zilina. Typical pores are shown in Fig. 2. For the porosity evaluation the digital image analysis software (NIS Elements 3.0) was used. The Largest Extreme Value Distribution (LEVD) and Murakami's approach, [7], were used for the statistical description of the largest observed pore size in metallographic specimens and for the prediction of the largest defect sizes in real castings.

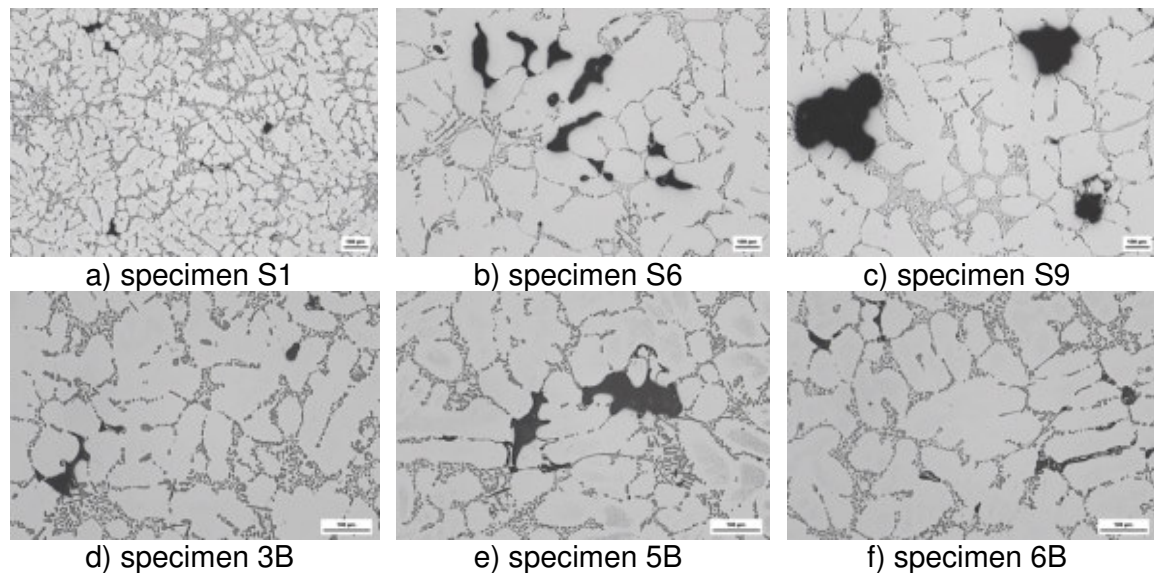


Fig. 2 Typical pores

### 3. EXPERIMENTAL RESULTS AND DISCUSSION

#### 3.1 Fatigue tests results

The fatigue test results are presented in Tab.1. Several smooth specimens, except the specimens from the batch S9, were tested at different stress amplitude

levels (from 80 to 60 MPa) according to the rotating bending configuration at 50 Hz frequency. The specimens from the batch S9 were tested on pull-push loading and the specimens from the batches S1 and S6 were tested under rotating bending loading. The specimens 3B, 5B and 6B modified by the optimal amount of Sr were tested under rotating bending loading.

Since the objective was the correlation of stress amplitude, number of cycles and largest pore size on a specimen to specimen basis, a preliminary characterization of microstructure uniformity as described by SDAS was carried out. The SDAS results are also shown in Tab. 1. The values were similar in the cases of the modified specimens 3B, 5B and 6B (from 53  $\mu\text{m}$  to 58  $\mu\text{m}$ ), but there were a quite large scatter in the SDAS results for the unmodified specimens S1, S6 and S9 (from 40  $\mu\text{m}$  to 100  $\mu\text{m}$ ).

In the case of the stress amplitude  $S_a = 80$  MPa the fatigue lives of the tested specimens are different. The fatigue life of the specimen 3B was the longest one compare to all other specimens. The specimen S9 and 3B were tested at the same stress level but under different loading conditions so it is not possible to compare the number of cycles to the fracture. At the stress amplitude  $S_a = 70$  MPa the specimens S6 and 5B were tested and their fatigue lives were similar. Quite small differences in the number of cycles to the fracture were observed in cases of the specimens S1 and 6B which were tested at the stress amplitude  $S_a = 60$  MPa. The number of cycles to fracture was smaller for the unmodified specimens compare to the modified ones. The differences and similarities in fatigue lives can be explained by the inhomogeneity of cast materials and by the presence of the porosity with the large scatter in size.

Table 1 Fatigue tests results, SDAS results and the largest pores sizes predictions

Specimen	$S_a$ [MPa]	$N_f$ [cycles]	SDAS [ $\mu\text{m}$ ]	Estimated largest pore size $(A)^{1/2}$ in [ $\mu\text{m}$ ] from LEVD plots for $S = 10 \text{ mm}^2$	
				All data	Only data larger than threshold
S1	60	403 170	40	106	no threshold
S6	70	619 149	86	58	no threshold
S9	80	588 151	100	310	353
3B	80	2 074 770	53	60	14
5B	70	669 562	56	71	70
6B	60	870 745	58	113	30

### 3.2 LEVD plots

The size of casting porosity was studied on metallographic specimens in a light optical microscope. The Largest Extreme Value Distribution (LEVD) and Murakami's approach, [7], were used for the statistical description of the largest observed pore sizes in metallographic specimens and for the prediction of the largest defect sizes in real castings as shown in the plots of Fig. 3. As a representative measure of a casting pore size, the  $(A)^{1/2}$  parameter was used with  $A$  the largest pore area found under 50 x magnification in a statistical significant number of control windows. The statistical distribution obtained by fitting largest pore size data for a specific control area  $S_0$  (i.e. here  $S_0 = 1.86 \text{ mm}^2$ ) was then used to estimate the size of the largest defect size in a given area  $S$  larger than  $S_0$  using the return period  $T = S/S_0$  also shown in the plots of Fig.3 [7]. In the present study the largest defect sizes expected on an area  $S = 10 \text{ mm}^2$ , representative of the highly stressed area of the rotating bending fatigue specimen, were determined by extrapolation of the regression line in the LEVD plot.

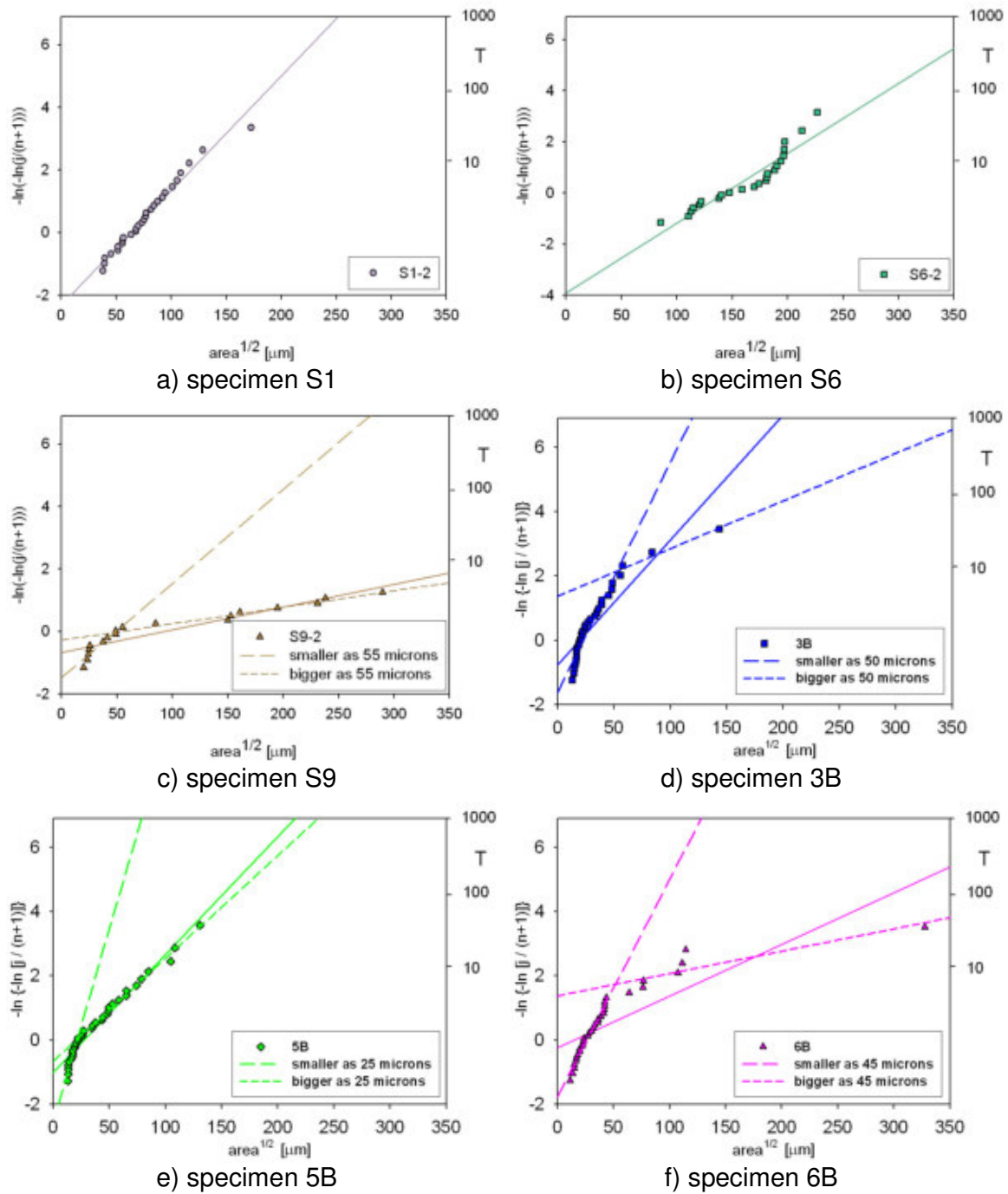


Fig. 3 LEVD plots

In the case of Fig. 3 a-b the data in the LEVD plot are appreciably linear. In the other cases, the data in LEVD plots do not show a unique linear behavior, Fig. 3 c-f. The experimental nonlinearity identifies a defect size where a transition occurs. Two different lines, one for defects smaller and one for defects larger than the transition value, respectively, can be fitted to the data. The transition data can be interpreted as a threshold value below which pore sizes are not critical for fatigue. In all cases the threshold defect sizes are in the range 30-50  $\mu\text{m}$ , in accordance with [5].

The sizes of the largest defects which can occur in real casting predicted from the LEVD plots of all measured values will be different than the sizes predicted from LEVD plots for defects larger than the threshold. The predicted largest defect sizes are shown in Tab. 1. In all cases the largest defect sizes predicted from the LEVD plots for all measured values were larger than the critical defect size for the fatigue crack initiation.

In the cases of the specimens 3B and S9 tested at the highest stress level (see Tab. 1) the differences between the two predictions of a largest defect size predicted are large. The fatigue lives of those specimens corresponded with the predictions from the LEVD plots for all values. The explanation can be in the presence of a large number of defects smaller than the threshold for the change of distribution which was also similar as the critical defect size for the fatigue crack initiation. The sizes of defects observed on the polished cross-sections of the metallographic specimen 3B were predominantly smaller than the critical defect size for the fatigue crack initiation and just few defects bigger than this critical size were measured there. This porosity population can be the explanation for the largest number of cycles to the fracture measured during the fatigue tests. The largest defect size predicted for the area  $S = 10 \text{ mm}^2$  for this specimen ( $60 \text{ }\mu\text{m}$ ) from the LEVD plot for all measured values was bigger than the critical defect size for the fatigue crack. But the predicted largest defect size ( $14 \text{ }\mu\text{m}$ ) from the LEVD plot for values bigger than the threshold for the distribution change ( $50 \text{ }\mu\text{m}$  in this case) was smaller than the critical defect size. The predicted largest defect size for the specimen S9 tested at the same stress level were quite big, (Tab. 1) and as we assumed the fatigue life of this specimen was shorter than the fatigue life of the specimen 3B even loading was different.

The predicted largest defect sizes for the area  $S = 10 \text{ mm}^2$  for the specimens S6 and 5B tested for fatigue on the stress level 70 MPa were quite similar, (Tab. 1), with the difference  $12 \text{ }\mu\text{m}$  between the largest defects predicted for those specimens. The values for the specimen S6 fitted the criterion of linearity and so they were described just by one line. The distribution of the largest defects sizes measured on the specimen 5B changed and it prompts for the description of values by two lines for the defects smaller and bigger than the threshold for the distribution change ( $25 \text{ }\mu\text{m}$ ). But the sizes of the largest defects from LEVD for all measured values and from LEVD for values bigger than the threshold are in this case almost the same.

The specimens S1 and 6B tested at the stress level 60 MPa reached similar fatigue lives as the specimens tested on the stress level 70 MPa. This corresponds with the largest defect sizes for the area  $S = 10 \text{ mm}^2$  predicted from the LEVD plot for all measured values, which were quite large (Tab. 1) and so they have a big influence to the fatigue life. The largest defect size predicted for the specimen 6B from the LEVD plot from the defects bigger than the threshold is small compare to the one predicted from LEVD for all values (Tab. 1) and it is smaller than the critical defect size for the fatigue crack initiation.

Comparison of the size of defects observed on the unmodified specimens (S1, S6 and S9) it is not assumed that the Si particles had just the minor influence to the fatigue live of tested specimens.

The predicted largest defects sizes do not correlated with the SDAS measurements results in the case of unmodified and modified specimens. The size of SDAS is dependent on casting process and cooling rate which is done by thickness of walls. Specimens were taken from real castings (except specimen S1) where the thickness is different and because of this reason it is complicated to compare SDAS results.

#### 4. CONCLUSIONS

Casting pores occur typically in Al-Si casting. Because of their negative influence, the fatigue behavior should be estimated on the basis of the largest pore size expected in the part. Therefore the prediction of the largest defect size in the Al-Si casting is a key-step in the prediction of its fatigue properties. The following conclusions are reached from this study:

- Casting pore sizes do not quite correlate with SDAS measurement.
- In all cases the largest defects sizes predicted from LEVD plots for all measured values were bigger than the critical defect size for fatigue crack initiation 25-50  $\mu\text{m}$ .
- Two trend lines for small and large pores are in some cases more suitable for statistical description of measured data. The sizes of largest defects, which can occur in real castings, predicted using LEVD plots from data larger than the threshold would be larger as the sizes predicted from all measured data.

#### Acknowledgement

This work was done as a part of the KEGA grant No.3/6110/08. It is also consistent with the objectives of MATMEC, Emilia-Romagna regional net-lab (<http://www.matmec.it/>).

#### REFERENCES

- [1] BRYANT, J.D., WHITE, D.R.: *Aluminium and magnesium for automotive applications*. The Minerals Metals and Materials Society; 1996.
- [2] KONEČNÁ, Radomila, NICOLETTO, Gianni, MAJEROVÁ, Viera. Largest extreme value determination of defect size with application to cast Al-Si alloys porosity. In: METAL 2007: 16. mezinárodní konference metalurgie a materiálů : 22.-24.5.2007 Červený zámek, Hradec nad Moravicí, Česká Republika [CD-ROM] Ostrava: TANGÉR ve spolupráci s MARQ, May, 2007, p 94, ISBN 978-80-86840-33-8.
- [3] AMMAR, H. R., SAMUEL, A. M., SAMUEL, F. H. Porosity and the fatigue behavior of hypoeutectic and hypereutectic aluminium-silicon casting alloys. In *International journal of Fatigue*, 2007.
- [4] WANG, Q. G., APELIAN, D., LADOS, D. A. Fatigue behavior of A356-T6 aluminum cast alloys. Part I. Effect of casting defects. In *Journal of Light Metals* 1, 2001, p. 73-84.
- [5] SKALLERUD, B. Fatigue life assessment of aluminium alloys with casting defects. In *Engineering Fracture Mechanics*; 44:857-74, 1993.
- [6] WANG Q. G., JONES P. E. Prediction of Fatigue Performance in Aluminum Shape Castings Containing Defects. The Minerals, Metals & Materials Society and ASM International 2007, doi: 10.1007/s11663-007-9051-4.
- [7] *Atlas métalographique des alliages d'aluminium*. CTIF, Paris, 1980.



- XV. [39] G. Nicoletto, R. Konecna, S. Fintova, Characterization of microshrinkage casting defects of Al-Si alloys by X-ray computed tomography and metallography, *International Journal of Fatigue*, 41 (2012) 39-46.



## Characterization of microshrinkage casting defects of Al–Si alloys by X-ray computed tomography and metallography

Gianni Nicoletto<sup>a,\*</sup>, Radomila Konečná<sup>b</sup>, Stanislava Fintova<sup>b</sup>

<sup>a</sup> Department of Industrial Engineering, University of Parma, Italy

<sup>b</sup> Department of Materials Engineering, University of Žilina, Slovakia

### ARTICLE INFO

#### Article history:

Received 27 April 2011

Received in revised form 30 December 2011

Accepted 6 January 2012

Available online 17 January 2012

#### Keywords:

Al–Si alloys

Casting defect

Fatigue behavior

X-ray computed tomography

Metallography

### ABSTRACT

The statistical pore size characterization by metallography in the framework of Extreme Value Statistics (EVS) is presented and applied to different sets of cast AlSi7Mg specimens. Specimen production by separate casting or by extraction from automotive cast parts is found to result in different SDAS and porosity (i.e. pore morphology and size) but did not influence the fatigue strength. The application of two equivalent pore size definitions (i.e. maximum Feret diameter and  $(Area)^{1/2}$ ) combined with the EVS approach is discussed in terms of predicted critical pore sizes and observed fatigue strengths. The role of casting pore morphology on stress concentration is investigated using the X-ray computed tomography and the finite element method.

© 2012 Elsevier Ltd. All rights reserved.

### 1. Introduction

Cast Al–Si alloys are widely used in fatigue critical structural applications, such as engine blocks, cylinder heads, and chassis and suspension components, for their excellent combination of mechanical and technological properties and to improve automotive fuel economy [1].

Fatigue properties of aluminum castings are strongly dependent on the casting defects and little affected by chemical composition, heat treatment, or solidification time, as reflected by dendrite arm spacing and the shape and size of eutectic silicon and intermetallic phases [2–10]. Typical defects of casting are macro pores and micro pores and bifilms [5]. While macropores (i.e. larger than a few mm) can be identified by X-ray inspection during quality check, micropores and bifilms are invisible to this kind of inspection. Since the presence of casting defects and discontinuities is almost inevitable in cast aluminum alloys and aluminum alloys have no apparent fatigue endurance limit, a defect-tolerant approach to fatigue design should be used, as proposed in [7–11]. Such an approach is based on the crack propagation life estimated from the crack growth rate law of the material and the initial crack size estimate. Typically, empirical models based on traditional linear elastic fracture mechanics (i.e. long crack behavior) are used although the short crack behavior has been also considered in [11].

The accuracy of the life prediction strongly depends on the prior knowledge of the defect population for a given material. The size of the largest defect has been recognized as the most important parameter in determining the fatigue properties of aluminum castings. The larger the maximum defect size, the lower the fatigue strength. Therefore, any defect tolerant design approach for materials containing defects should be based on a method to estimate the largest defect size distribution. In this context the approach and procedure developed by Murakami and coworkers [11,12], represents a fundamental starting point. In short, metallographic inspection of a selected material cross-section and determination of the largest pore size in many fields of view allows constructing a statistical description of the largest pore size using Gumbel's extreme value distribution. Such a distribution is then used to estimate the largest pore size in realistic part cross-sections by extrapolation [12,13]. The procedure has been applied by many researchers to a wide range of materials with appreciable success [11–14]. The Extreme Value Statistics (EVS) approach is based on two key assumptions: (i) the distribution of defects is uniform in the material, (ii) the pore size is well described by the parameter  $(Area)^{1/2}$  where Area is the area of the largest pore measured on a metallographic section.

However, the combination of complex part geometry and solidification process typical of Al–Si alloys is known to give different pore types and sizes in different sections of the casting [11]. The morphology of casting pores in Al–Si alloys is typically classified either as gas pore or microshrinkage pore [1]. While the former is

\* Corresponding author.

E-mail addresses: [gianni.nicoletto@unipr.it](mailto:gianni.nicoletto@unipr.it) (G. Nicoletto), [radomila.konecna@fstroj.uniza.sk](mailto:radomila.konecna@fstroj.uniza.sk) (R. Konečná).

typically rounded and spheroidal, the latter is branched and elongated. In practice, the distinction is not always straightforward.

The application of metallography (i.e. essentially a 2-D analysis) to pore sizing is expected to give a biased response. In recent years, Buffière and coworkers pioneered the application of high resolution synchrotron X-ray computed tomography (x-CT) to pore characterization in cast Al–Si alloys and graphite cast irons [6,15,16]. The application of x-CT allows the accurate non-destructive 3-D reconstruction of pores within a volume of aluminum alloy (i.e. distribution, size and morphology). In [15] x-CT was used to study the early stages of fatigue crack nucleation and growth from pores. While most of the studied cracks stopped after their length reached the initiating defect size, microcracks initiated on the largest defects or defect clusters continued to grow with short crack behavior. In this last case, crack shape became semielliptical. A substantial part of the lifetime (25% of the total estimated fatigue life) was necessary for the crack to surround the pore and assume a semielliptical shape. The usefulness of x-CT when applied to cast aluminum parts was also discussed in [17].

In this paper the statistical pore size characterization by metallography is initially examined adopting the EVS. The prediction methodology of maximum defect size based on two-dimensional (2-D) metallographic data is applied to individual fatigue specimens produced by direct casting of AlSi7Mg (equivalent to A356) alloy while other specimens were extracted from a complex automotive cast part. Questions emerging from this first approach motivate the investigation of an alternative pore characterization technique. Therefore, x-CT is used to reconstruct the 3-D distribution of casting pores in AlSi7Mg. Shrinkage pores, which are highly irregular in shape, are constructed and assessed in terms of stress concentration using finite element modeling.

## 2. Fatigue testing of cast AlSi7Mg

Defect sizing methods are applied here to casting pores of AlSi7Mg alloy produced by sand casting and used in automotive applications. The chemical composition and static strength properties of the material under study are within the standard values for the alloys AlSi7Mg following the heat treatment called T6

**Table 1**  
Tensile properties of AlSi7Mg.

	Mean value	Std dev.
Ultimate strength $R$ (MPa)	293	9
Yield stress $R_s$ (MPa)	219	17
Elongation to rupture $A$ (%)	8.1	1.3
Young's modulus $E$ (GPa)	75.12	2.7

[9]. The Mg addition to the alloy leads to the formation of the  $Mg_2Si$  intermetallic phase by precipitation hardening, which is a part of the mentioned heat treatment. The reference mechanical properties of the present AlSi7Mg alloy are summarized in Table 1.

The fatigue testing was conducted on four sets of smooth specimens subjected to rotating bending (reference section diameter of 6 mm) at a frequency of 50 Hz following a stair-case procedure applied to at least 15 samples per set to characterize fatigue strength at 10 million cycles. Two sets, denominated A and B, were machined out of separately cast bars of fatigue specimens and two sets, C and D, were extracted from industrial castings of complex shape, (i.e. engine heads).

SDAS (secondary dendrite arm spacing) measurements of  $\alpha$ -phase dendrites (alpha is solid solution of Si in Al) and characterization of eutectic Si particles were performed on polished and etched specimen sections (Nital 3%) after fatigue testing. Typical micrographs of AlSi7Mg microstructure with microshrinkages are shown in Fig. 1. SDAS measurements demonstrate that samples cast separately (sets A and B) solidified and cooled considerably faster than the material of the industrial casting (sets C and D) because their SDAS ratio is about 0.5, as shown in Table 2.

In all cases the fatigue fracture initiated at one or multiple casting pores located near or at the free surface of the specimen minimum cross section, see Fig. 2, confirming the key role played by pores in the fatigue behavior of cast Al–Si alloys. The fatigue data of the four different specimen sets are also shown in Table 2 and reveal that the fatigue strength in this case does not significantly change with specimen production method. The scatter in fatigue strength is high because all failures were observed to initiate at casting pores. The present fatigue strength data however agree with literature data [7,18]. A conclusion of this experimental portion of the work is that SDAS depends on the casting process but does not closely correlate with high-cycle fatigue strength.

## 3. Metallography and statistical evaluation of defects

### 3.1. EVS approach for defect sizing

Metallography is routinely used to study microstructure and porosity in Al–Si castings. This technique typically investigates optically and under high magnification small section of a part. Defects of different kinds can be identified and accurately measured. However, to transform metallography from a material quality assessment technique to a predictive tool for estimating part performance requires the support of a statistical framework so that its localized measurements can be extrapolated to larger sections or entire engineering parts.

Murakami and coworkers [12], developed such a framework and defined an experimental procedure aimed at estimating the

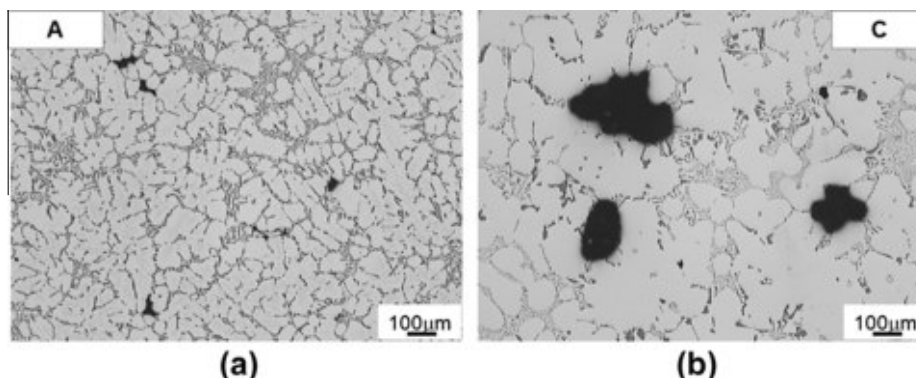


**Fig. 1.** Typical metallographic micrographs of AlSi7Mg obtained by (a) casting in metal mold (set A) and (b) extracted from industrial cast part (Set C) (etching Nital 3%). The dendritic structure (light gray) and eutectic Si particles (dark gray) are shown along with casting pores (black).

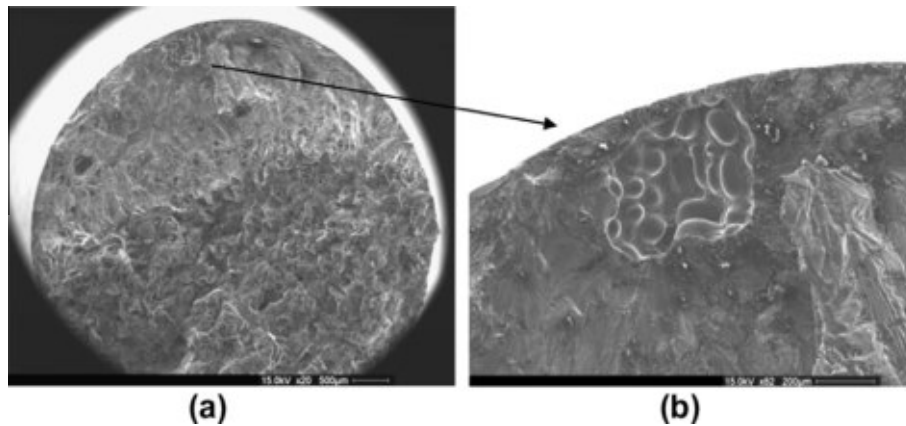


**Fig. 2.** (a) SEM macroview of the typical fatigue fracture of AlSi7Mg specimens and (b) magnification of the casting pore where fatigue failure initiated (pore size approx 500  $\mu\text{m}$ ).

largest defect expected in a volume of material and, consequently, the fatigue performance based on the fatigue crack propagation from such a critical defect [9–11]. Extensive application [12], to a variety of materials (bearing steel, tool steel, cast iron, Al-alloys and Ti-alloys etc.) and material defects (inclusions, oxides, pores etc.) have proved that EVS applies to the description of the largest defect sizes. The procedure is now briefly reviewed and then applied to cast AlSi7Mg produced in different ways.

In the EVS approach a statistically significant number of metallographic fields of view (i.e. 30 or more,) are analyzed and the largest pore or inclusion in each image identified and measured. Murakami proposed that the square root of the area of the largest pore in the 2-D view,  $(\text{Area})^{1/2}$ , is considered as the equivalent defect size for fatigue assessment. The advantages of using the largest pores instead of using conventional ratings makes this procedure focused on the upper tail of the defect distribution [12].

The cumulative distribution function  $F$  of EVS [12], is given by:

$$F(x) = \exp[-\exp[-(x - \lambda)/\delta]] \quad (1)$$

where  $x$  is the equivalent size of the largest pore. In Eq. (1),  $\lambda$  and  $\delta$  are referred to as the location and the scale parameter, respectively.  $\lambda$  is the  $x$  value which has a cumulative probability of 0.367 ( $\lambda$  is the 36.7% quantile), while  $\delta$  is proportional to the scatter of the  $x$  variable. Eq. (1) can be rearranged to a linear equation by taking the natural logarithm of Eq. (1) twice as follows:

$$-\ln(-\ln F(x)) = x\delta - \lambda\delta \quad (2)$$

When data appreciably fulfills the linearity condition, the EVS parameters  $\lambda$  and  $\delta$  can be calculated by the least squares method.

The EVS description of the maximum defect size can be used to predict by extrapolation the largest pore size expected in a real part volumes. Let  $x$  be the equivalent size of the largest pores and  $S_0$  be the inspection area used for the sampling, then the characteristic largest defect in an area  $S$  (the maximum pore size, which is expected to be exceeded once in the area  $S$ ) is the pore size corresponding to a return period  $T$  defined as

$$T = S/S_0 \quad (3)$$

Since  $T = 1/(1-P)$ , from Eq. (2) the dimension of the defect with return period  $T$  can be calculated as:

$$x(T) = \lambda - \delta \ln[-\ln(1 - 1/T)] \quad (4)$$

### 3.2. Application of EVS analysis to casting pores in AlSi7Mg

The specimens of the four sets of AlSi7Mg used in the fatigue testing phase were employed for the statistical pore size character-

ization according to the EVS methodology outlined in the previous section. All pore size data were measured with NIS-Elements 3.0 image analysis software (Nikon Instruments Europe B.V.) on magnified metallographic images.

EVS was originally developed to quantify the role of inclusions, which are typically compact in shape [12], and the  $(\text{Area})^{1/2}$  was demonstrated to satisfactorily describe defect severity on fatigue. Casting pores can have different origins and may have quite complex and variable morphology. A comparison of the largest pore morphology found in specimens obtained by direct casting in metal mold (set B) and by extraction from industrial cast part (Set D) is shown in Fig. 3. Pores of set B are small, branched and sharp edged while pores of set D are large and rounded.

Recently, the maximum Feret diameter was proposed in [11] as an equivalent pore size definition in terms of its severity in fatigue and as an alternative to  $(\text{Area})^{1/2}$ . The maximum Feret diameter of a pore is the maximum of multiple diameter measurements, where the “diameter” is the largest distance between any two points belonging to the pore boundary in a 2-D view.

Here, the  $(\text{Area})^{1/2}$  parameter was initially used to characterize largest pore sizes and the data of the four specimen sets were inserted in the EVS probability plot of Fig. 4a. The largest pore sizes of all four sets are well represented by straight lines with high regression coefficients. The largest pore size distribution of the sets A and B (i.e. specimens obtained by direct casting in bars) are mutually similar and very different from the sets C and D (i.e. specimens taken from industrial castings).

The results of an application of the return period  $T$  concept to the largest equivalent size  $(\text{Area})^{1/2}$  distributions of Fig. 4a is presented in Table 3 and predicts largest pore sizes of sets C and D that are approx. 2.15 larger than the largest pore size estimates of sets A and B. This conclusion apparently contradicts the assumed correlation between defect size and fatigue strength widely accepted in literature [12], because the present four sets of specimens, shown in Table 2, have comparable fatigue strengths at  $10^7$  cycles. On the other hand, Murakami reported a satisfactory correlation of the largest pore sizes described uniquely by the  $(\text{Area})^{1/2}$  parameter and fatigue strength in cast Al–Si alloys [23].

Therefore, the max Feret diameter parameter was adopted next to characterize the same pores in the four material sets and the data are shown in the EVS plot of Fig. 4b. It is observed that all four sets are well represented by straight lines and that the Feret diameter definition typically yields considerably larger equivalent sizes than the  $(\text{Area})^{1/2}$  definition. On the other hand, for a given return period  $T$ , Table 3 demonstrates that the predicted max Feret diameters of sets C and D are only approx. 1.3 times larger than the max pore diameters of sets A and B. Although the largest pore size rank-

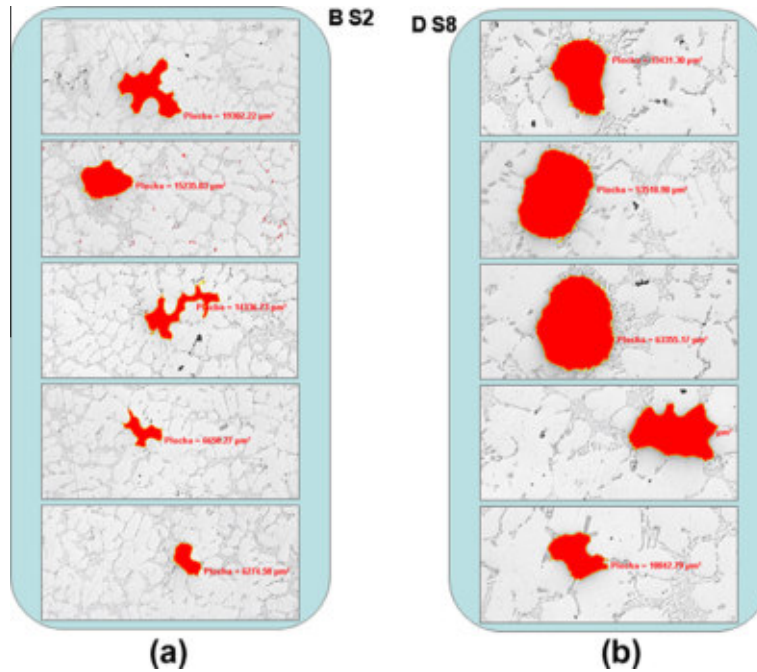


Fig. 3. Examples of largest pores used for EVS application to AlSi7Mg obtained by (a) casting in metal mold (set B) and (b) extracted from industrial cast part (set D).

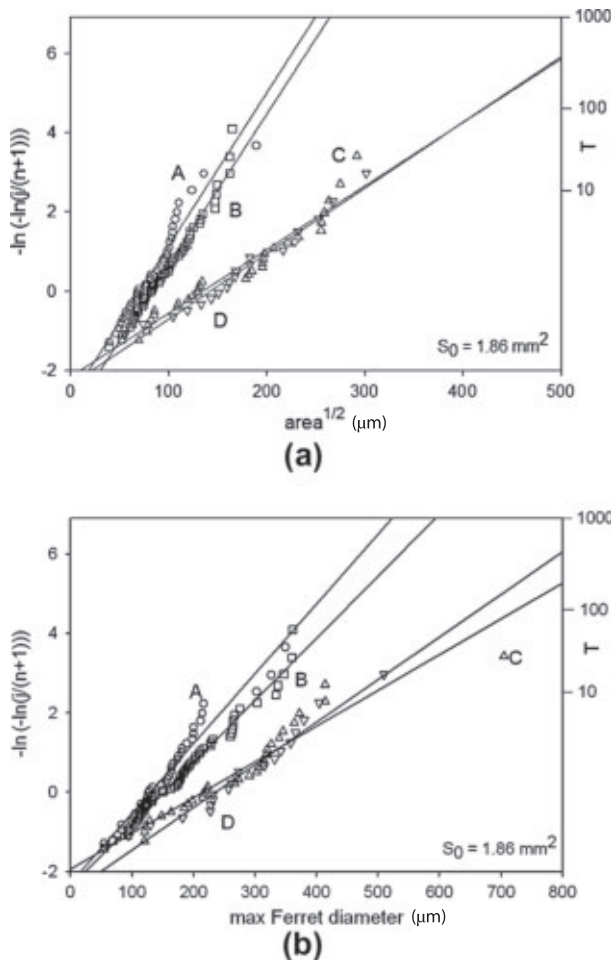


Fig. 4. EVS analysis for four different sets of cast AlSi7Mg using (a) Murakami's  $(Area)^{1/2}$  pore sizing parameter and (b) max Feret diameter parameter.

ing of the present four material sets according to the max Feret diameter does not strictly correlate the fatigue data of Table 2, nonetheless the largest pore size ratio is now considerably reduced (1.3 vs. 2.15) compared to the  $(Area)^{1/2}$  parameter. If it were 1, the estimated pore sizes for the four material sets would be the same and fatigue strength should be similar. These results confirm the key role of equivalent size parameter selection on fatigue strength prediction and fatigue fracture model development.

### 3.3. Morphology of casting pores

In the previous section it was concluded that fatigue strength ranking of the four specimen sets based on the max Feret diameter definition of critical pores is closer to the experimentally observed one. Now the morphology of casting pores is also assumed to play a significant role.

Gas pores are quite common in Al–Si castings and are compact in shape (i.e. near spherical) so a unique sizing parameter (i.e. related to spherical radius) obtained by metallographic section can describe and compare fatigue severity of pores. On the other hand, micro shrinkage pores, typical of the Al–Si casting materials, and here especially of sets A and B, see Fig. 3, are branched and fully 3D. Metallographic sectioning of this kind of pore may reveal a variety of pore configurations, from multiple small neighboring pores to elongated single pores, that make the application of EVS methodology quite challenging.

To test the hypothesis that a single parameter (i.e.  $(Area)^{1/2}$  or maximum Feret diameter) may not be fully able to describe the effect of a casting pore on the fatigue strength of the present Al–Si alloys, an investigation of pore morphology was carried out in this work. The degree of elongation or, conversely, the circularity  $S$  (or sphericity in 3D) of a pore was measured on metallographic images according to the following definition:

$$S = 4\pi A/P^2 \quad (5)$$

where  $A$  is the pore area and  $P$  the perimeter of the same pore. The parameter  $S$  ranges between 0 (i.e. the pore collapses to a line) and 1 (i.e. the pore is a circle).



A classification of the largest pores using circularity  $S$  vs. equivalent size  $(Area)^{1/2}$  in the present AlSi7Mg produced in the two different ways is shown in Fig. 5. All the pores considered here are larger than an equivalent size of  $50\ \mu\text{m}$  because the multitude of very small pores (less  $50\ \mu\text{m}$  in size) found in the materials are considered irrelevant on the fatigue behavior. Those pores are probably related to micro-shrinkages that appear at the end of the solidification.

To interpret the results of Fig. 5 it has to be reminded that only the largest pores in a casting control the fatigue strength. The largest pores in separately cast material cluster at a representative equivalent size of  $150\ \mu\text{m}$  and a circularity of 0.2 while largest pores in castings cluster at representative equivalent size of  $240\ \mu\text{m}$  and circularity of 0.4. Therefore, Fig. 5 shows that the material extracted from industrial castings is characterized by pores of larger size and higher circularity compared to those of the separately cast bars. On the other hand, the pores of individually cast bars are smaller and more elongated. The large pores show in both cases a strong correlation between size and circularity although the slope of the regression line is quite different.

The plot of Fig. 5 demonstrates also that the pore morphology trend of the material from industrial castings of this study is similar to that found in a computed tomography study of an AlSi7Mg alloy [6], where a sphericity parameter rather than the present circularity parameter was used.

Based on this characterization of the porosity and the results of the fatigue tests, it is concluded that the use of only an equivalent size, either  $(Area)^{1/2}$  or max Feret diameter, may not be able to rationalize the influence of porosity on the response to a high number of fatigue cycles. To shed light on this issue, in the next section an accurate 3D shape reconstruction of casting pores in AlSi7Mg was sought by applying the powerful and innovative micro-computed tomography [19], and the actual 3D stress concentration of the different pore types determined using the finite element method.

#### 4. Influence of casting pore morphology on 3D stress concentration

Initially the basics of the X-ray computed tomography technique is outlined, then the application to the present cast AlSi7Mg is described, finally the combined use of representative 3D pore geometries and the finite element method is proposed to investigate the actual 3D stress concentration of casting pores.

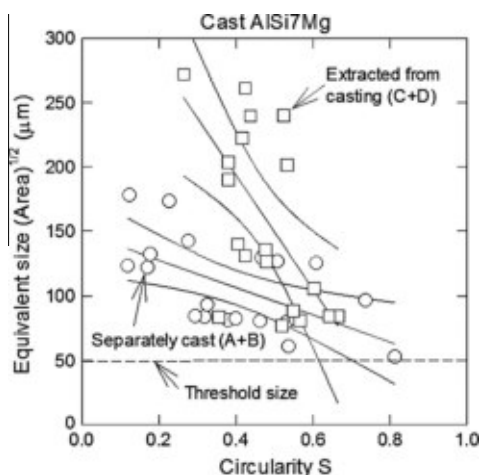


Fig. 5. Morphology of largest casting pores in experimental sets of AlSi7Mg described by the equivalent size  $(Area)^{1/2}$  vs. circularity  $S$ .

#### 4.1. X-ray Computed tomography

X-ray computed tomography (x-CT) is an imaging method where individual projections (radiographs) recorded from different viewing directions are used to reconstruct the internal structure of the object of interest. It offers the additional advantage of being noninvasive and nondestructive. The spatial and contrast resolution involved in the present problem of interest requires the use of high-resolution X-ray CT, also termed micro-Computed Tomography ( $\mu\text{CT}$ ). According to [19], the division between conventional x-CT and  $\mu\text{CT}$  is assumed to include results obtained with at least  $50\text{--}100\ \mu\text{m}$  spatial resolution. The penetrating power of a high-density focused X-ray beam can be exploited to reconstruct sub millimeter internal defects in cast metals [17,19].

The internal reconstruction presented here is based on 2D frontal scanning of the sample followed by the cross sectional reconstruction (i.e. slice) by a back projection algorithm. Internal pores are easily identified in the slice as dark spots in a light background. x-CT provides a stack of slices; see Fig. 6a; whose number depends on the slice-to-slice distance and on the volume investigated. The 3D reconstruction of the internal pores starts from the automatic identification of the pores of the various stacked cross-sections, Fig. 6b. Since the gray level of each pixel is proportional to the density of the material, it is possible to distinguish if the pixel belongs to a cavity or to the metal. Pores within a solid body appear darker compared to the surrounding matrix. Fig. 6b shows the identification of a pore cross-section and the consequent result after applying suitable threshold levels. After applying the same threshold to all slices, a 3D reconstruction of the internal pores was obtained with an ad hoc software developed in [20] using the public domain, Java-based image processing ImageJ software functions, (i.e. <http://rsb.info.nih.gov/ij/>). The stacking of pore cross-sections results in the 3-D shape of the pore as shown in Fig. 6c. The assembly of voxels can be transformed into a smoothed outer surface using the open-source 3D computer graphics software, (i.e. [www.blender.org](http://www.blender.org)). The pore surface geometry is then stored using the STL standard, used primarily in rapid prototyping.

#### 4.2. 3D reconstruction of casting pores by $\mu\text{CT}$

The  $\mu\text{CT}$  scanning of small specimens of AlSi7Mg was performed at the TOMOLAB Laboratory of Elettra Synchrotron in Trieste [21]. TOMOLAB uses a cone beam micro CT, equipped with an X-ray generator with a power generated from 40 kV to 130 kV, with a maximum current of  $300\ \mu\text{A}$ . It is also equipped with a CCD acquisition system cabinet, in order to vary the spatial resolution of the system [21]. Beam power and absorption by the material are factors which determine the maximum thickness investigated. The major limitations on this technique are associated with the limited volume which can be analyzed as the X-ray beam must cross the entire section of the material. In this case the volume is limited by the shape of cylinder, 4 mm in diameter and 1 mm in length. The micro-tomography-imaging set-up consists of a precision mechanical stage that allows for accurate rotation and positioning of the sample and an electronic high-resolution detector system. The 3D numerical image, obtained after reconstruction of 1800 projections taken over  $360^\circ$  consists in a 3-D map of X-ray attenuation coefficients. The voxel size is  $5\ \mu\text{m}^3$ .

A general view of the porosity in the investigated volume of AlSi7Mg is shown on Fig. 7. The volume is populated by many pores of different geometry and size. A global evaluation of porosity and statistics regarding pores is readily obtained via the software used.

Fig. 8 shows two typical reconstructed casting pores of different morphology. They are selected because the compact and rounded pore of Fig. 8a is similar to pores of sets C and D, see Fig. 3b. It will

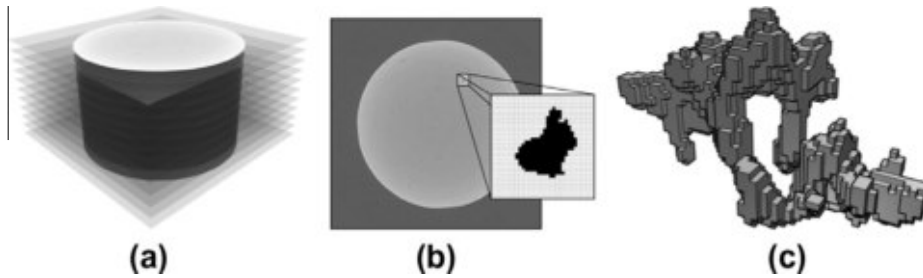


Fig. 6. Scheme for 3D pore reconstruction; (a) stack of slices; (b) pore identification in each slice and (c) pore reconstructed by voxel assembly.

be defined quasi-gas pore because the lower part is rounded while the top is similar to a shrinkage pore. The high spatial resolution of micro x-CT allowed also the reconstruction of the intricate geometry of the shrinkage pore of Fig. 8b, which is representative to pores of sets A and B, see Fig. 3a. The structural influence of these realistic pores is now investigated using the finite element method.

#### 4.3. Stress concentration at casting pores

The fatigue damage and failure mechanisms of cast Al–Si alloys are affected by the presence of pores of critical size because they promote rapid fatigue crack initiation, see Fig. 2. Local stress/strain concentration at such pores is influenced by the pore geometry and its distance from neighboring pores and from free surfaces. When the nominal stress increases, plastic deformation develops locally at the pore with an accelerated damage accumulation. The variety

of factors affecting local stress concentration can be readily investigated by finite element analysis (FEA).

The main value of this portion of the study is the use of actual 3D shrinkage pore geometry rather than either a 2D metallographic view of a pore [7], or an idealized 3D model of a pore [7]. Previously in [22], the three-dimensional porosity to be imported into the FEA software for the elastic stress was obtained using X-ray tomography with a resolution of approximately 100  $\mu\text{m}$ , which is therefore considerably lower than in the present case. More recently in [23], the  $\mu\text{CT}$  technique was applied to finely reconstruct the entire porosity in fatigued cast aluminum specimens and used to quantify the pore influence zone associated to the volume of matrix stressed above the yield stress on the basis of elastic finite element analysis. In the present work, which is an evolution of [24], the attention is focused only on two archetypical pores identified in the reconstructed material volume by  $\mu\text{CT}$ . They were selected and incorporated into a finite element model with the aim of assessing the role of pore morphology on local stress concentration.

The commercial FEA software ABAQUS was used. The elastic–plastic constitutive material model was introduced, although only the elastic results are discussed here. The present is a simplified description of the expected local damage process because homogeneous mechanical properties of the matrix material are assumed while in reality stress and strain distributions at the pore tip are influenced by the mechanical properties and local distribution of the microstructural phases. However, while that local pore geometry was accurately reconstructed by  $\mu\text{CT}$ , the real inhomogeneous material structure and mechanical properties of the different phases were not.

Therefore the pore first is inserted as a cavity in a finite element model of a cylindrical volume to simulate the push–pull test. The region surrounding the pores is modeled with a refined mesh so as to correctly estimate the local stress concentration as a function of geometry and type of loading. The element type used for meshing the material volume (and the pore surface) was the four-node linear tetrahedral elements (C3D4) of the ABAQUS code. A preliminary convergence study was performed to achieve accurate surface description and peak surface stress stability. A typical pore surface mesh shown in Fig. 9a demonstrates the micron-size of the smallest element. To control the computational burden, mesh size grading was applied to exploit the notion that removed from the notch the stress is uniform. The total number of finite elements for the FE models was typically about  $2 \times 10^5$ . The stress distribution is then mapped on the internal surface of the pore where the peak value is expected. Application of the far-field load aligned with the  $y$ -axis results in the stress distribution for the quasi-gas pore shown in Fig. 9b and a stress concentration factor  $K_t$ , defined as the ratio of the peak von Mises stress and the nominal far-field stress, for that specific initial pore orientation.

A coordinate system centered in the pore center of gravity and two rotation angles  $\phi$  and  $\theta$  about the  $x$ - and  $z$ -axis, respectively,

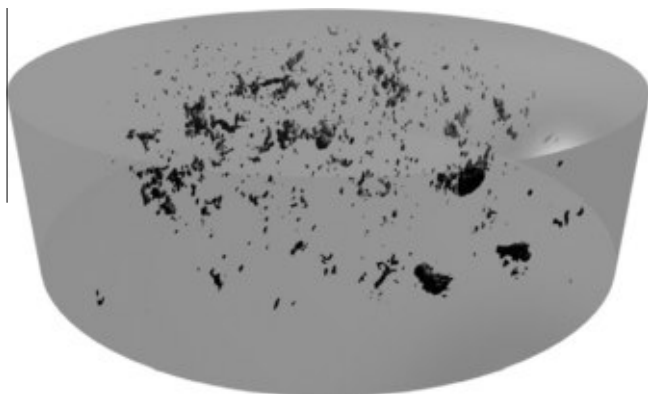


Fig. 7. 3-D pore distribution and morphology in a volume of AlSi7Mg obtained by X-ray CT (volume size: 4 mm dia  $\times$  1 mm height).

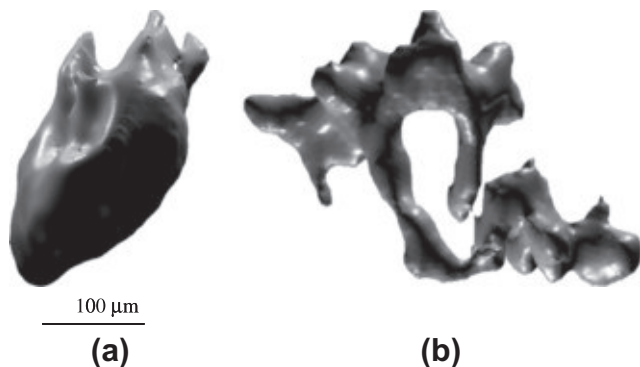


Fig. 8. Types of pores revealed by X-ray CT – (a) quasi-gas pore – (b) shrinkage pore.

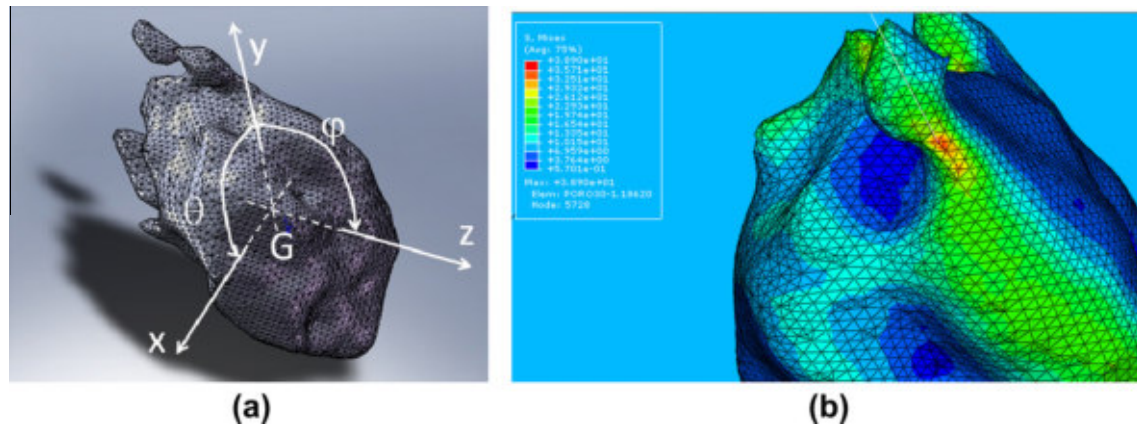


Fig. 9. (a) Coordinate system location and rotational angles for a pore ( $y$ -axis is parallel to loading direction) and (b) typical stress distribution on pore surface.

are defined in Fig. 9a to investigate the combined role of pore morphology and loading direction on  $K_t$ . In this computational part of the study, each pore of Fig. 8 was discretely rotated with respect to, separately, the two angles  $\phi$  and  $\theta$  in the range  $0$ – $90^\circ$  and a new FE model generated each time to be then solved for a  $K_t$  estimate. Although these repeated analyses do not cover all possible pore orientation with respect to the load direction, they provide a relevant indication of the  $K_t$  variability due to a change in load direction. Fig. 10 shows the distribution of  $K_t$  as a function of the angles  $\theta$  and  $\phi$  defined in Fig. 9a for the two pores of Fig. 8 and Table 2 summarizes the main results.

The average  $K_t$  depends on the type of pore with  $K_t = 3.28$  for the shrinkage pore and  $K_t = 2.98$  for the quasi-gas pore. The difference between them is limited to about 10%. On the other hand they are considerably larger than  $K_t = 2$ , the theoretical value for a spherical cavity in tension [7]. Interestingly the standard deviation of  $K_t$  is larger for the quasi-gas pore than for the shrinkage pore: the min–max  $K_t$  range is 2.2–3.4 for the former and 3.0–3.5 for the latter. A reason is in the morphological variation (i.e. rounded vs. elongated) of the quasi-gas pore compared to the shrinkage pore.

The present data are compared to a previous study by Gao and coworkers [7]. The 3D nature of a pore was idealized as a spherical cavity, which could be located at specific distances from the free specimen surface. In that case the stress concentration factor  $K_t$  was found to range from about 2 for the case of an isolated pore

in the material to very high values (i.e.  $K_t = 4$  or 5) when the pore is very near to the free surface.

While it is true that near-surface pores are typically critical in both push–pull and rotating bending fatigue tests because specimens are machined out of castings, the as-cast surface of Al–Si cast parts of industrial applications has a pore-free surface layer [1], so critical pores in actual parts are expected to be located at some depth from the surface [17]. The present  $K_t$  results ( $K_t = 3$ – $3.3$ ) are possibly more representative of pore severity than both the high values due to free surface effect ( $K_t = 4$ – $6$ ) and the spherical simplification ( $K_t = 2$ ) used in fatigue model development [7].

### 5. Combined role of casting pore size and morphology on fatigue strength

The high cycle fatigue strength results of cast AlSi7Mg reported initially in this paper have shown: (i) an insensitivity to the production route and (ii) a fatigue crack initiation at large casting pores. Since a microstructural parameter like SDAS did not correlate with experimental high cycle fatigue strength of cast AlSi7Mg the focus of the study was placed on large pore characterization. As far as pore sizing, the application of the maximum Feret diameter as the equivalent pore size definition combined with the EVS approach yielded always larger pore size estimates than the  $(Area)^{1/2}$  definition, see Table 3. The estimated critical pore sizes of four cast AlSi7Mg according to the largest Feret diameter parameter show also a better correlation with the experimental long life fatigue strengths than the  $(Area)^{1/2}$  parameter, see Tables 2 and 3. As far as pore morphology, sharp microshrinkage pores typical of two specimen sets (i.e. A and B) are characterized by a higher stress concentration than the more rounded pores typical of the other two sets (i.e. C and D), see Fig. 3 and Table 4.

From the foregoing the qualitative conclusion is that the combined effect of larger and rounded pores on the fatigue strength of industrial casting is equivalent to the effect of smaller and elongated pores on the fatigue strength of separately cast specimens. Although no specific guideline can be defined yet for dealing with

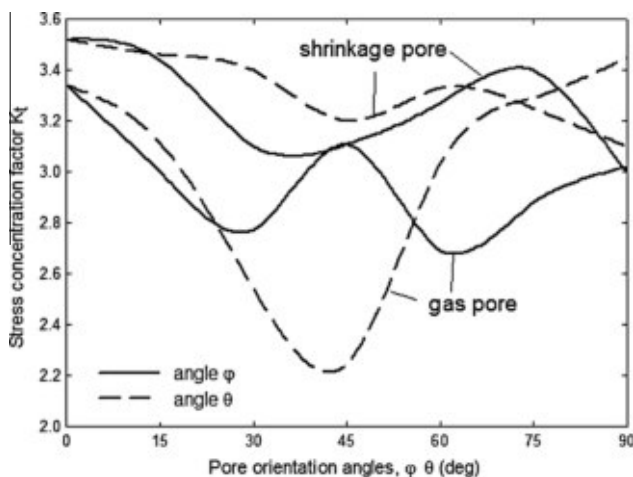


Fig. 10. Stress concentration factor of the pores of Fig. 8 in tension for different pore orientations.

Table 2  
Microstructure and fatigue strength of four specimen sets of cast AlSi7Mg.

Set	Specimen production	SDAS ( $\mu\text{m}$ )	Fatigue strength at $10^7$ cycles $S_w$ (MPa)
A	Separately cast	39.8	62.8
B	Separately cast	38.0	60.3
C	Extracted from casting	93.0	50.0
D	Extracted from casting	88.7	61.2



**Table 3**

Predicted largest pore sizes for a return period  $T = 100$  using different equivalent pore size definitions.

Set	$(Area)^{1/2}$ ( $\mu\text{m}$ )	Max Feret diameter( $\mu\text{m}$ )
A	190	395
B	203	440
C	422	725
D	422	665

**Table 4**

Stress concentration factor  $K_t$  for the pores of Fig. 8.

	Quasi-gas pore		Shrinkage pore	
	$K_t(\theta)$	$K_t(\varphi)$	$K_t(\theta)$	$K_t(\varphi)$
Average $K_t$	2.97	3.00	3.26	3.32
Std dev	0.22	0.45	0.20	0.15

the fatigue dependence of cast AlSi materials on shrinkage pores, a pore-size-correction factor depending on pore morphology (i.e. increasing contribution with pore elongation) should be introduced and is under investigation.

## 6. Conclusions

Fatigue testing of specimens of cast AlSi7Mg obtained by separate casting or by extraction from automotive cast parts demonstrated an insensitivity of long life fatigue strength from the production process and the critical role of casting pores as fatigue initiators. A statistical pore size characterization by metallography and EVS was carried out and discussed along with an FEM investigation of pore morphology considering realistic pores obtained by  $\mu\text{CT}$ . The following conclusions were reached:

- The application of the maximum Feret diameter as the equivalent pore size definition combined with the EVS approach provides larger pore size estimates.
- The estimated critical pore sizes of four cast AlSi7Mg according to the largest Feret diameter parameter show a better correlation with the experimental long life fatigue strengths than the  $(Area)^{1/2}$  parameter.
- A morphological contribution of microshrinkage pores in cast AlSi7Mg was demonstrated using the combination of  $\mu\text{CT}$  technique and finite element analysis.
- The average stress concentration factors  $K_t$  of realistic pores are higher than for an idealized spherical pore geometry and lower for a metallographic 2D pore cross-section. This result highlights the uniqueness of the information provided by  $\mu\text{CT}$  and the need for a morphology-dependent pore size correction factor.
- It is confirmed that metallography and the EVS approach combine into a reliable quality inspection technique suitable for the industrial environment.

## Acknowledgements

The authors thank Dr. Dreossi and Dr. Sodini at Elettra Sincrotrone Trieste for their contribution to image acquisition and analysis and the support of experimental research by national Slovak project VEGA 1/0242/10.

## References

- [1] Bryant JD, White DR. Aluminium and magnesium for automotive applications. The Minerals Metals and Materials Society; 1996.
- [2] Sonsino CM, Ziese J. Fatigue strength and applications of cast aluminium alloys with different degree of porosity. *Int J Fatigue* 1993;15:75–84.
- [3] Couper MJ, Neeson AE, Griffiths JR. Casting defects and the fatigue behaviour of an aluminium casting alloy. *Fatigue Fract Eng Mater Struct* 1990;13(3):213–27.
- [4] Debayeh AA, Xu RX, Du BP, Topper TH. Fatigue of cast aluminium alloys under constant and variable-amplitude loading. *Int J Fatigue* 1996;18:95–104.
- [5] Wang QG, Apelian D, Lados DA. Fatigue behavior of A356-T6 aluminum cast alloys. Part I. Effect of casting defects. *J Light Metals* 2001;1:73–84.
- [6] Buffiere JY, Savelli S, Jouneau PH, Maire E, Fougères R. Experimental study of the porosity and its relation to fatigue mechanisms of model Al–Si7–MgO cast Al alloy. *Mater Sci Eng A* 2001;316:115–26.
- [7] Gao YX, Yi JZ, Lee PD, Flower HM, Lindley TC. The effect of porosity on the fatigue life of cast aluminium–silicon alloys. *Fatigue Fract Eng Mater Struct* 2004;27:559–70.
- [8] Linder J, Arvidsson A, Kron J. The influence of porosity on the fatigue strength of high-pressure die cast aluminium. *Fatigue Fract Engng Mater Struct* 2006;29:357–63.
- [9] Nicoletto G, Konečná R, Baicchi P, Majerova V. Casting porosity and long-life fatigue strength of a cast Al-alloy. In: *Procs. Int. Conf. MSMF 5, Brno, Czech Republic*; 2007.
- [10] Lados DA, Apelian D. Fatigue crack growth characteristics in cast Al–Si–Mg alloys: Part II Life predictions using fatigue crack growth data. *Mater Sci Eng A* 2004;385:187–99.
- [11] Wang QG, Jones PE. Prediction of fatigue performance in aluminum shape castings containing defects. *Metall Mater Trans B* 2007;38B:615–21.
- [12] Murakami Y. *Metal fatigue: effects of small defects and nonmetallic inclusions*. Elsevier; 2002.
- [13] Beretta S, Blarasin A, Endo M, Giunti T, Murakami Y. Defect tolerant design of automotive components. *Int J Fatigue* 1997;19:319–33.
- [14] Beretta S, Anderson C, Murakami Y. Extreme value models for the assessment of steels containing multiple types of inclusion. *Acta Mater* 2006;54:2277–89.
- [15] Ferrie E, Buffiere JY, Ludwig W. 3D characterization of the nucleation of a short fatigue crack at a pore in a cast Al alloy using high resolution synchrotron microtomography. *Int J Fatigue* 2005;27:1215–20.
- [16] Verdu C, Adrien J, Buffiere JY. Three-dimensional shape of the early stages of fatigue cracks nucleated in nodular cast iron. *Mater Sci Eng A* 2008;483–484:402–5.
- [17] Powazka P et al. Computed tomography – an alternative and complement to traditional metallographic investigations of porosity in cast aluminum. In: *Procs 2nd fatigue symp. Leoben*; 2008. p. 51–66
- [18] Atzori B, Meneghetti G, Susmel L. Fatigue behaviour of AA356-T6 cast aluminium alloy weakened by cracks and notches. *Eng Fract Mech* 2004;71:759–68.
- [19] Stock SR. *Microcomputed tomography – methodology and applications*. Boca Raton, USA: CRC Press; 2009.
- [20] Anzelotti G. PhD thesis in Industrial Engineering, University of Parma, Italy; 2010.
- [21] Anon. <<http://www.elettra.trieste.it/Labs/TOMOLAB/>>.
- [22] Hardin R, Beckermann C. Prediction of the fatigue life of cast steel containing shrinkage porosity. *Metal Trans* 2009;40A:581–97.
- [23] Vanderesse N, Maire É, Chabod A, Buffiere J-Y. Microtomographic study and finite element analysis of the porosity harmfulness in a cast aluminium alloy. *Int J Fatigue* 2011;33:1514–25.
- [24] Nicoletto G, Anzelotti G, Konecna R. X-ray computed tomography vs. metallography for pore sizing and fatigue of cast Al-alloys. In: *Procs. Fatigue 2010, Prague, Czech Republic*; 2010.

- XVI. [40] S. Fintová, R. Konečná, G. Nicoletto, Microstructure, defects and fatigue behavior of cast AlSi7Mg alloy, in, 2013, pp. 223-231.



## MICROSTRUCTURE, DEFECTS AND FATIGUE BEHAVIOR OF CAST AISi7Mg ALLOY

Stanislava Fintová<sup>1)</sup>, Radomila Konečná<sup>1)\*</sup>, Gianni Nicoletto<sup>2)</sup>

<sup>1)</sup> University of Žilina, Faculty of Mechanical Engineering, Žilina, Slovakia

<sup>2)</sup> University of Parma, Faculty of Engineering, Parma, Italy

Received: 07.10.2012

Accepted: 20.05.2013

\*Corresponding author: e-mail: radomila.konecna@fstroj.uniza.sk, Tel.: +421 415132604, Department of Materials Engineering, Faculty of Mechanical Engineering, University of Žilina, Univerzitná 1, 010 26 Žilina, Slovakia,

### Abstract

The cast AISi7Mg alloy prepared using different modifier was studied. The main factor influencing fatigue properties were the casting defects. Using metallography and statistical approach, Larger Extreme Value Distribution (LEVD) theory, the structure and the porosity were evaluated. According to the largest defects sizes prediction fatigue tests were performed. Fatigue cracks were initiated on the casting defects present on the specimen free surface or just below the surface identified using SEM. Specimens fatigue life was influenced by the size of the defect in the initiation place and the number of initiation places. The specimens fatigue behaviour corresponded with the assumptions according to the LEVD.

**Keywords:** aluminium alloy, casting, defects, fatigue

### 1 Introduction

Cast aluminum alloys are increasingly used in the automotive industry due to their excellent castability, corrosion resistance, and especially their high strength-to-weight ratio. Their application for cast components subjected to dynamic loading has motivated considerable interest on the fatigue behavior of cast Al-Si alloys. Besides the microstructural characteristics, fatigue strength of cast aluminum components heavily depends on the casting defects formed during solidification because they favor fatigue crack initiation due to high local stress concentration [1].

The fatigue properties of Al-Si alloys are influenced besides the porosity also by the structural features like the dendrites fineness, intermetallic phases and the materials heat treatment [2]. In the case of the presence of the casting defects the influence of the structural features play just a minor role [3, 4, 5].

The defects often result in poor mechanical properties including limited strength and ductility, variable fracture toughness, irregular crack initiation and crack propagation characteristics, potentially accompanied by a lack of pressure tightness [6]. The effect of porosity on fatigue life has been summarized as follows: pores reduce the time for crack initiation by creating a high stress concentration in the material adjacent to the pores; because of this, most of the fatigue life is spent in crack growth [7].

There exists a critical defect size, [3], (in Sr modified cast A356 alloy, the critical defect size is in the range of 25-50  $\mu\text{m}$ ) for fatigue crack initiation, below which the fatigue crack initiates from other intrinsic initiators such as eutectic particles and slip bands.

In this contribution the influence of the porosity on the fatigue behavior of cast AlSi7Mg alloys is studied. The used specimens were prepared using different modifiers and casting process. From the obtained bars the specimens for the metallographic evaluation, and also the porosity evaluation using the metallographic methods, and the specimens for the fatigue tests were prepared. After the porosity evaluation according to the Largest Extreme Value Distribution (LEVD) theory [8] the fatigue tests were planed and performed. The fatigue fracture surfaces of the specimens broken during the fatigue tests were examined using SEM and the fatigue crack initiation places were identified. At the end all the obtained results were confronted and the relations between them were found.

## 2 Experimental material(s) and methods

As the experiment material the cast AlSi7Mg alloy in this study was used. The studied specimens were mould casted in the shape of bars. From each bar, the metallographic specimens and the smooth 6 diameter specimens for the rotating bending fatigue test were prepared. The casted specimens were divided into 6 batches, according to the casting process and used modifier, see **Table 1**. For each batch five bars were cast.

**Table 1** Specification of individual specimen batches

Batch	Casting process specification
2	cast after the modification by pure Na
3	cast after the subsiding of the modification effect of Na
4	cast after the modification by sodium salts and degassing by N during 10 min
5	cast after the subsiding of the modification effect of Na salts and degassing
6	cast after the modification by Sr
7	cast after the modification by Sr and gassing by the Begaser tablets

After the casting, the bars were treated by heat treatment T6 consisting in solution annealing and artificial aging.

Each specimen was examined by metallographic methods. The microstructure of the specimen was defined by the SDAS (Secondary Dendrite Arm Spacing) factor and also the casting defects using the image analysis program NIS Elements 3.0 were evaluated. The casting defect sizes present in the microstructure were evaluated using Murakami's approach based on statistical method Largest Extreme Value Distribution (LEVD) theory.

For the estimation of the actual defect size different approaches for the defects size characterization were used. Typical equivalent size definitions found in the literature are:  $\text{area}^{1/2}$ ,  $4(\text{area})^{1/2}/\pi$ , Feret diameter [1, 8, 9, 10]. In this contribution, the most used [8, 11] the  $\text{area}^{1/2}$  and the maximum Ferret diameter as the defects size describing values were used.

The Murakami's approach is based on the evaluation of the largest defect size on the field of view. In this method a number,  $n$ , of separated regions (control areas), each with the same area  $S_0$  of the selected image magnification, are chosen on the polished surface of metallographic sections, and the equivalent size,  $\text{area}^{1/2}$ , of the largest pore within each region is recorded. The result is a set of  $n$  observations of maximum sizes  $\text{area}^{1/2}$  and the Gumbel distribution [8] is fitted to these data. Under the Gumbel distribution the points are expected to lie close to the line. The fitted distribution is then used to estimate the size of the largest defect size in a given region  $S$  larger than the control area  $S_0$ , through the return period  $T = S/S_0$ , or to compare largest defects from control areas of different sizes.

Because of the influence of the casting defects on the fatigue crack initiation and growth, this prediction can be used in planning the fatigue test conditions of the specimens. The rotating bending fatigue tests, with the 50 Hz frequency and  $R = -1$ , were performed. The stress amplitudes of the tests were in the range from 80 to 20 MPa.

After the specimens failure the fatigue surfaces were examined using the Scanning Electron Microscope (SEM) to identify and count the fatigue crack initiation places. All the obtained results were at the end compared and their dependence and mutual influences were discussed.

### 3 Results and discussion

#### 3.1 Microstructure and defects

The microstructure of the cast AlSi7Mg alloy consists of the  $\alpha$ -phase dendrites – light grey (solid solution of Si in Al) and eutectic ( $\alpha$ -phase and dark grey Si particles) situated in interdendritic spaces, **Fig. 1a**. The SDAS factor values which describe the secondary dendrite arm spacing are in the range 20-25  $\mu\text{m}$  and similar for each batch.

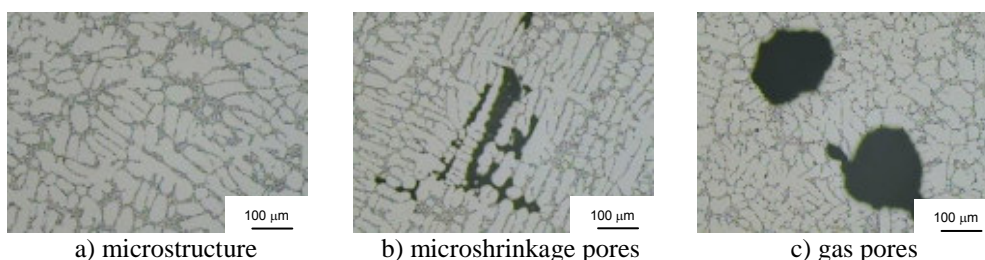


**Fig. 1** Typical microstructure and casting defects present in AlSi7Mg castings, etched by 0.5% HF

In the specimens microstructure almost in all the cases the large amount of casting defects was observed. In all the cases, except the batch 7, only the microshrinkage pores were present. In the specimens from the batch 7, because of the gassing of the liquid metal before the casting, the large gas pores and just a small amount of microshrinkage pores with the size smaller compare to the gas pores were present. The microshrinkage pores created during the solidification process are complicated in the shape and are located in the interdendritic location near the dendrites, **Fig. 1b**. The microshrinkage pores are observed on the metallographic cross section in clusters consisting from larger and smaller microshrinkage pores which can be just cut branches of one bigger shrinkage pore. The gas pores are present in the castings because of the gas saturation of the melted metal during the casting process. The gas pores are rounded in the shape and they are almost always present in the casting individually, **Fig. 1c**. In general, the gas pores should be less dangerous, in term of the fatigue crack initiation, compare to the microshrinkages [12, 13]. The arrangement of the casting defects was evaluated on the specimen's macrographs shown on **Fig. 2**. In the case of the specimens from the batches 2 and 6 the microshrinkage pores were present in the entire specimen surface, also on the specimens' free surfaces and close to them, **Fig. 2a**. In the case of the specimens from the batches 3, 4 and 5 only the small amount of defects was observed, **Fig. 2b**. The gas pores present in the specimens from the batch 7 were like in the case of the defects in the specimens from the batches 2 and 6 arranged in all the specimens' cross section and also in the fatigue crack critical localities – on the specimens' free surfaces and close to the specimens' free surfaces, **Fig. 2c**.

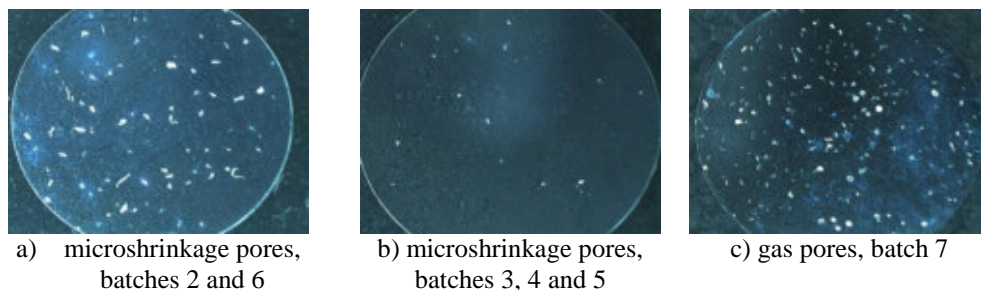


**Fig. 2** Macrographs of metallographic specimens, stereomicroscope, mag. 6.3 x

In almost all of the evaluated specimens the presence of the intermetallic phases, which are in general considered as undesirable, were observed, **Fig. 3**.

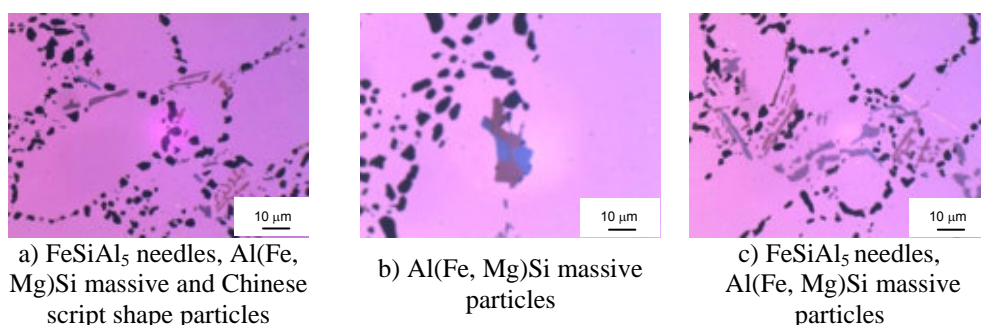


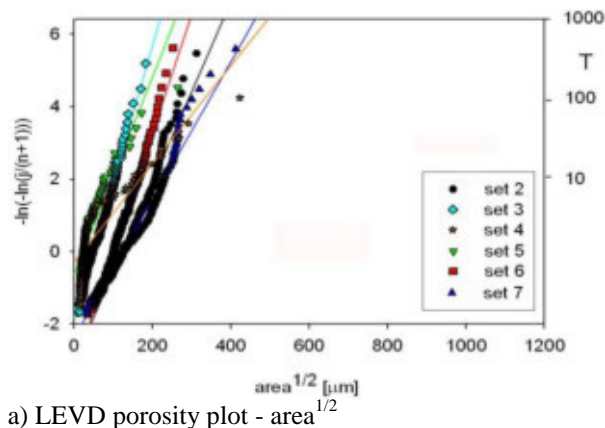
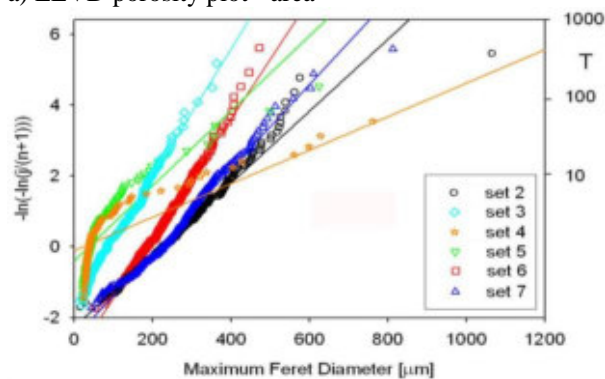
**Fig. 3** Intermetallic phases, etched by Ammonium Molybdate, polarized light

Even though the intermetallic phases can have a negative influence on the material properties and can be the initiating places for the fatigue cracks. In this case, the size and the amount of the present intermetallic phases was not sufficient to act as the fatigue crack initiators and so as the main factor for the fatigue properties decreasing the casting defects were identified. The size and the amount of the present defects were much larger compare to the present intermetallic phases.

### 3.2 The largest defect size prediction

The porosity of the specimens was evaluated on the light optical microscope Neophot 32 using the image analysis program NIS Elements 3.0. The used magnification was 50 x and the inspected area size was  $S_0 = 1.62 \text{ mm}^2$ . The largest defects were described by two different sizes the area<sup>1/2</sup> and the max. Ferret diameter sizes. The measured values are plotted to the LEVD graphs of **Fig. 4**.

Scatter of the fatigue data is typical of cast Al-Si alloys. When the number of specimens is limited, the plot describing the largest pore sizes for the individual batches of **Fig. 4** can be used to in planning the fatigue experiments. When the slope value is high the fatigue behavior of the material should be less scattered, when the slope value is low the fatigue scatter is large. For predicting the expected largest pore sizes in specimens, the data of **Fig. 4** were extrapolated to the area  $S = 10 \text{ mm}^2$  (the most stressed area of the specimens for the rotating bending fatigue tests) which is typical for small castings and the results are given in **Table 2**. In all the cases the predicted largest defect sizes are larger than the critical defect size for the preferential initiation of the fatigue crack (20 - 50 µm, [3]).

a) LEVD porosity plot -  $\text{area}^{1/2}$ 

b) LEVD porosity plot – max. Ferret diameter

**Fig. 4** LEVD porosity plots

In this case, the fatigue cracks will be initiated on the casting defects and the structural features will have just minor effect on the fatigue crack initiation.

Smaller defects sizes (i.e.  $\text{area}^{1/2}$ ) for the area  $S = 10 \text{ mm}^2$  were predicted for the specimens from the batches 4 (cast after the modification sodium salts and degassing by N during 10 min.) and 5 (cast after the subsiding of the modification effect of Na salts and degassing). Larger defects sizes were predicted for the specimens from the batches 3 (cast after the subsiding of the modification effect of Na) and 6 (cast after the modification by Sr). The largest defects sizes  $\text{area}^{1/2}$  for the area  $S = 10 \text{ mm}^2$  were predicted for the specimens from the batches 2 (cast after the modification by pure Na) and 7 (cast after the modification by Sr and gassing by the Begaser tablets). In the case of the defects description by the max. Ferret diameter values the trend predicted results is the same as in the case of the  $\text{area}^{1/2}$  predictions (**Table 2**).

### 3.3 Fatigue tests

The fatigue behavior was expected to correlate with the defect size of the predictions of **Table 2**. Therefore, the fatigue behavior of the specimens from the batches 4 and 5 was expected to be the best, followed by the batches 3 and 6 and the worst being the batches 2 and 7. Stress amplitudes applied to the specimens were relatively high (60 - 80 MPa) for batches with the small predicted defects sizes and low (40 - 20 MPa) for batches with expected large defects. From the fatigue



tests results shown in the **Table 3** it is possible to compare the influence of the used modifier (**Table 1**) on the fatigue behavior of tested batches. In the case of the specimens tested on the same stress level, it is possible to compare also the influence of the predicted largest defect size (**Table 2**) on the reached number of cycles to failure ( $N_f$ ).

**Table 2** Predicted largest defect size for the area  $S = 10 \text{ mm}^2$

Predicted largest defect size for the area $S = 10 \text{ mm}^2$			Predicted largest defect size for the area $S = 10 \text{ mm}^2$		
Specimen	area <sup>1/2</sup> [μm]	max. Ferret diameter [μm]	Specimen	area <sup>1/2</sup> [μm]	max. Ferret diameter [μm]
2E	153	315	3B	88	171
2C	184	335	3E	95	186
2A	196	414	3D	102	199
2B	210	498	3C	106	201
2D	225	419	3A	100	202
4C	43	77	5D	43	91
4D	43	102	5C	56	113
4A	56	98	5A	65	133
4E	111	263	5B	74	159
4B	246	657	5E	165	403
6E	123	247	7E	163	292
6D	132	256	7B	187	433
6B	145	272	7C	242	343
6C	160	315	7D	230	352
6A	193	347	7A	248	357

The fatigue tests results show that the best fatigue properties are reached with the specimens of batch 3 (i.e. cast after the subsiding effect of modification by pure Na, **Table 1**). At comparable stress amplitudes, the fatigue lives for batch 5 (cast after the subsiding of the modification effect of sodium salts and degassing) are longer than for batch 4 (cast after the modification by sodium salts and degassing by N during 10 min.). Both batches were prepared using Na as modifier and after degassing and the fatigue behavior follows the expectation based on the largest pore sizes, **Table 2**.

The influence of the type of modifier did not influence significantly the fatigue behavior: batch 2 (cast after the modification by pure Na) and batch 7 (and cast after the modification by Sr and gassing by the Begaser tablets) have comparable results. This observation agrees with the comparable predicted largest defects sizes according to the LEVD theory, **Table 2**. Even the shape of defect, i.e. ramified (microshrinkage) or round (pore), apparently does not influence markedly the fatigue crack initiation.

Finally, the fatigue behavior of the specimens cast after the modification by Sr (batch 6) is highly scattered and the pore size predictions were not successful in guiding the fatigue test planning. There is probably some additional factor besides porosity that affects the fatigue behavior.

**Table 3** Fatigue test results

Specimen	$S_a$ [MPa]	$N_r$ [cycles to failure]	Specimen	$S_a$ [MPa]	$N_r$ [cycles to failure]
2E	80	39	3B	88	2 081 850
2C	50	7 549	3E	70	861 858
2A	35	176 481	3A	65	74
2B	30	1 751 395	3C	60	844 393
2D	25	40 179	3D	60	5 271
4C	80	41	5E	165	36
4D	50	104 655	5B	74	962 505
4E	40	97	5A	65	439 338
4A	35	12 463 211	5C	56	99
4B	30	2 360 844	5D	43	670 789
6E	80	60	7E	80	49
6D	50	41	7B	50	2 956
6B	35	1 259	7C	35	380 467
6C	25	487	7D	30	54 957
6A	20	40	7A	30	45 187

### 3.4 Fractographic analysis of the fatigue fracture surfaces

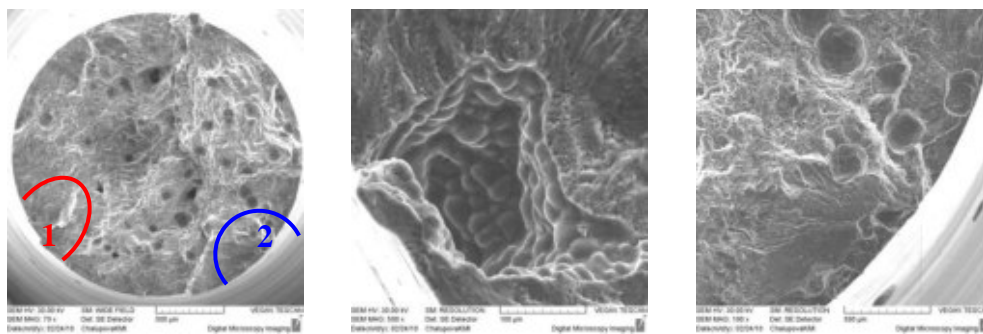
After the fatigue tests due to the initiation places identification the fracture surfaces of the broken specimens on the SEM VEGA Tescan were examined.

Because of the casting process the defects on the fracture surfaces were found. The defects were present in the entire broken surface of the specimens and also on the specimens' free surface. Defects located on the specimen's free surface and close to the specimen's free surface were in the case of the rotating bending loading the initiating places for the fatigue cracks what is in agreement with [13, 14, 15, 18, 19].

The defects on the surface act like stress concentrators and the defects in the specimens weaken the specimen cross sections.

The fracture surfaces of examined specimens consist from the fatigue fracture area and the final fracture area, **Fig. 5a**. The fatigue fracture area corresponds to the fatigue crack stable growth. The final fracture region corresponds to the unstable crack growth. In the case of the examined specimens the fatigue fracture region is eccentric due to the position and number of the fatigue crack initiation defects. In all the cases the fatigue cracks were initiated on the specimens' free surfaces and in the fatigue cracks initiation places the casting defects were present, **Fig. 5b - c**.

The defects that caused the fatigue crack initiation were compared with the predicted defect sizes identified by the  $\text{area}^{1/2}$  and the max. Ferret diameter sizes. The sizes of the defects observed on the fracture surfaces were larger compare to the predicted values, but the relation was retained, i.e. the defects in the initiation places were smaller in the case of the specimens with smaller predicted largest defect sizes and in case of the specimens with the larger predicted defects size the fatigue crack initiating defects were larger. A dependence of the fatigue life to the number of the fatigue crack initiation places was also found [16-20].



a) fatigue fracture surface with two initiation places

b) defect in the fatigue crack initiation place 1

c) defect in the fatigue crack initiation place 2

**Fig. 5** Specimen 7C (cast after the modification by Sr and gassing by the Begaser tablets),  $S_a = 35$  MPa,  $N_f = 380\,467$  cycles to failure, SEM

#### 4 Conclusions

This study was aimed at the evaluation of the influence of the used modifier and the casting process on porosity and fatigue behavior using the casting pore size description of the LEVD theory and a limited number of specimens. The fatigue tests of different batches of cast AlSi7Mg were performed after the metallographic evaluation of the specimens and the detailed study of their porosity. The following conclusions were reached:

- microshrinkages were observed in all of the specimens;
- in the case of the batch 7 the gas pores originated due to the gassing of the liquid metal before casting;
- the fatigue test results correlated to the largest defects sizes predictions, i.e. the fatigue life increased by the predicted largest defects size decreasing for a given stress amplitude;
- the best fatigue performance was for the specimens cast after the subsiding effect of the modification by pure Na (batch 3);
- the specimens cast after the modification by pure Na (batch 2) and cast after the modification by Sr and gassing by the Begaser tablets (batch 3) had comparable fatigue properties;
- the fatigue behavior depends on size, number and position of pores and not on their shape (microshrinkage or gas pore);
- although the amount of the tested specimens was limited, the correlation of pore sizes and the fatigue behaviour was confirmed.

#### References

- [1] Q. G. Wang, P. E. Jones: The Minerals, Metals and Materials Society and ASM International, Vol. 38, 2007, No. 4, p. 615-621
- [2] J-Y. Buffière, S. Savellib, P. H. Jouneau, E. Maire, R. Fougères: Materials Science and Engineering, Vol. 316, 2001, No. 1, p. 115-126
- [3] Q. G. Wang, D. Apelian, D. A Lados: Journal of Light Metals. Vol. 1, 2001, Issue 1, p. 73-84
- [4] J.Z. Yi, Y.X. Gao, P.D. Lee, T.C. Lindley: Materials Science and Engineering A, Vol. 386, 2004, Issues 1-2, p. 396-407

- [5] P. Li, D.M. Maijer, T.C. Lindley, P.D. Lee: *Materials Science and Engineering A*, Vol. 460, 2007, p. 20-30
- [6] H. R. Ammar, A. M. Samuel, F. H. Samuel: *International Journal of Fatigue*, Vol. 30, 2008, Issue 6, p. 1024-1035
- [7] H. R. Ammar, A. M. Samuel, F. H. Samuel: *Materials Science Engineering A*, Vol. 437, 2008, Issue 1-2, p. 65-75
- [8] Y. Murakami: *Metal Fatigue: Effects of Small Defects and Nonmetallic Inclusions*, first ed., Elsevier, Oxford, 2002
- [9] Y.X. Gao, J.Z. Yi, P.D. Lee, T.C. Lindley: *Acta Materialia*, Vol. 52, 2004, No. 19, p. 5435-5449
- [10] R. Konečná, S. Fintová, G. Nicoletto: *Key Engineering Materials*, Vol. 465, 2011, p. 354 - 357
- [11] S. Fintová, R. Konečná, G. Nicoletto: *Materials Engineering*, Vol. 16, 2009, No. 3, p. 24-28
- [12] J. P. Anson, J. E. Gruzleski: *Materials Characterization*, Vol. 43, 1999, Issue 5, p. 319-335
- [13] H. R. Ammar, A.M. Samuela, F.H. Samuel: *Materials Science and Engineering A*, Vol. 473, 2008, Issues 1-2, p. 65-75
- [14] M. Avalle, G. Belingardi, M. P. Cavatorta, R. Doglione: *International Journal of Fatigue*, Vol. 24, 2002, Issue 1, p. 1-9
- [15] H. Arami, R. Khalifehzadeh, M. Akbari, F. Khomamizadeh: *Materials Science and Engineering A*, Vol. 472, 2008, Issues 1-2, p. 107-114
- [16] S. Fintová, V. Konstantová, R. Konečná, G. Nicoletto: *Experimental study of porosity and fatigue behavior*, In.: 17th International Metallurgical & Materials Conference, Hradec nad Moravicí, TANGER Ostrava, CD-ROM (no. 54), 2008
- [17] R. Konečná, G. Nicoletto, S. Fintová: *Statistical description of largest pore sizes in cast Al-Si alloys*, In.: 25th Danubia-Adria Symposium on Advances in Experimental Mechanics, ČVUT Praha, Powerprint, 2008, p. 123-124
- [18] R. Konečná, G. Nicoletto, S. Fintová: *Acta Metallurgica Slovaca Conference*, Vol. 1, 2010, No. 2, p. 8-15
- [19] R. Konečná, G. Nicoletto, S. Fintová: *Fractographic characterization of fatigue crack initiation from casting defects in AlSiMg*, In.: *Fractography 2009*, Košice: Institute of Materials Research of the Slovak Academy of Sciences, CD-Rom, 2009
- [20] G. Nicoletto, R. Konečná, S. Fintová: *International Journal of Fatigue*, Vol. 41, 2012, p. 39-46

### Acknowledgements

*Authors thank the support of experimental research by national project VEGA 1/0196/12.*

XVII. [41] F. Stanislava, K. Radomila, ná, N. Gianni, Statistical description of largest pore size in midified Al-Si alloys, *Materiálové Inžinierstvo*, 16 (2009) 24-28.



## STATISTICAL DESCRIPTION OF LARGEST PORE SIZE IN MODIFIED AL-SI ALLOYS

Stanislava Fintová<sup>1</sup>, Radomila Konečná<sup>1</sup>, Gianni Nicoletto<sup>2</sup>

Received 8<sup>th</sup> May 2009; accepted in revised form 8<sup>th</sup> June 2009

### Abstract

*Casting defects in AlSi7Mg alloys are owing to the processing technology inseparable features of final products. The porosity consisting of gas pores or microshrinkages is the most decisive factor influencing the fatigue life of castings. Extreme value statistic method has been shown a suitable procedure for prediction of a size of the largest defects, which can occur in real castings, which are substantially larger than the area of a control specimen prepared for defect distribution analysis. In this contribution application of Murakami's statistical method based on the description of the largest extreme value distribution to the evaluation of porosity in AlSi7Mg alloy prepared by casting technologies with two types of modifiers, namely Sr and Na is presented. The results of statistical analysis are compared with the fatigue performance of specimens manufactured from particular materials.*

**Keywords:** Cast AlSi7Mg alloy, Porosity, Murakami's statistical method

### 1. Introduction

Fatigue properties of aluminum castings are sensitive to the defect size. In recent years, the maximum defect size has been recognized as the most important parameter determining the fatigue properties of aluminum castings. The larger the maximum defect size, the lower the fatigue strength. In the presence of imperfections the fatigue strength is primarily affected by them, the effects of chemical composition, heat treatment or solidification time, as reflected by dendrite arm spacing and the sizes of eutectic silicon and intermetallic particles are relatively low [1].

A cast AlSi7Mg alloy with two different modifiers was analysed in this study. The choice between sodium or strontium as modifier is determined by many factors. Sodium is accepted as the more potent modifier, but the rapid fade, fume evolution and low controllability of sodium additions has led to its gradual replacement by strontium in the majority of foundries [2].

One of the roles of modifier is a control of porosity dispersion in casting, whether caused by gas or shrinkage, [2]. The mechanism of porosity redistribution is not precisely understood. The increased freezing range of

modified alloy due to the reduced eutectic temperature leads to large semi-solid regions in the casting. This leads to longer feeding paths to counteract shrinkage and to the possibility that it becomes blocked. This results in lower porosity in the feeders/risers and higher in the bulk of the casting. There are also arguments for easier pore nucleation due to the reduced surface tension of modified melts. If pores are easier to form, then they will occur earlier during solidification and thus be more numerous, smaller and better dispersing in the casting [2].

Modified AlSi alloys were produced and examined metallographically in this work. Two definitions of equivalent pore size, namely in terms of area<sup>1/2</sup> and in terms of Maximum Feret Diameter (MFD), were used in the evaluation of pore severity observed on polished cross-sections. The statistical description of the largest pore size uses the Murakami's method based on the Largest Extreme Value Distribution (LEVD) [1, 3]. The implication on the role of pores in fatigue is discussed.

### 2. Experimental material and methods

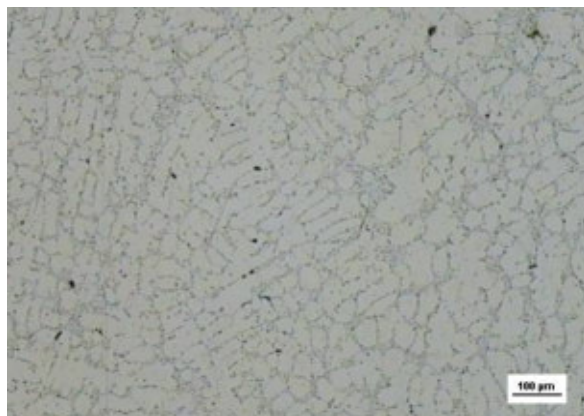
Three sets of cast AlSi7Mg alloy were used in the experiments. The same basic material was used for production of sets A and B. Set A was modified with pure

<sup>1</sup> S. Fintová, Ing.; R. Konečná, prof. Ing. PhD. – Department of Materials Engineering, Faculty of Mechanical Engineering, University of Žilina, Univerzitná 1, 010 26 Žilina, Slovak Republic.

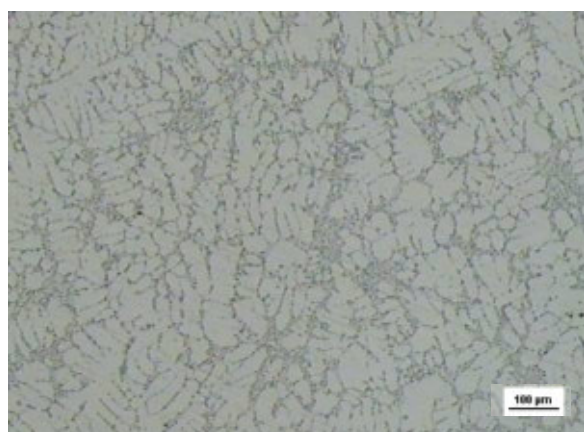
\*Corresponding author, e-mail address: stanislava.fintova@fstroj.uniza.sk

<sup>2</sup> G. Nicoletto, prof. Ing. - Department of Industrial Engineering, University of Parma, Viale G.P. Usberti, 181/A, 43100 Parma, Italy

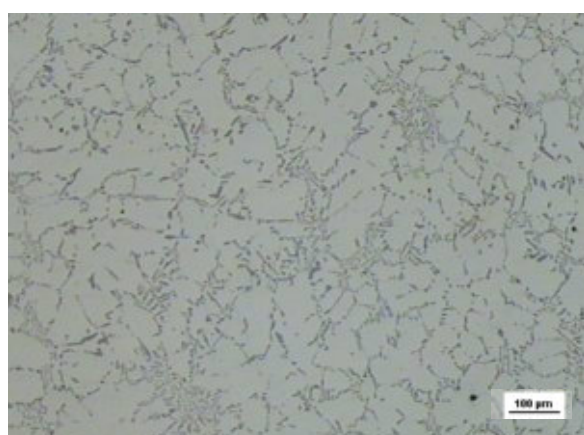
Na and set B modified with pure Sr and cast in a steel shell mold. Set C was produced using AlSi7Mg with Sr modification and the sand casting process.



a) set A, modified by pure Na, cast to steel mold



b) set B, modified by pure Sr, cast to steel mold



c) set C, modified by pure Sr, sand cast

Fig. 1 Typical microstructure of AlSi7Mg, unetched

Five bars for the sets A and B and three bars for the set C were separately cast. All the specimens were heat treated to the T6 regime. Metallographic specimens were

extracted from the cast bars. The structural analysis applying metallographic techniques on polished cross sections was carried out. Typical microstructures are shown in Fig. 1.

The microstructure is characterized by primary dendrites of  $\alpha$ -phase (solid solution Si in Al with maximal solubility limit 1.59 % at eutectic temperature 577 °C) together with an eutectic structural compound  $E = (\alpha + Si)$  located between the secondary dendrite arms. The silicon as eutectic phase grew as thin, interconnected rods in  $\alpha$ -phase because Na or Sr modifiers to the liquid metal were used. The modified silicon rods appeared as round particles on the metallographic section, Fig.1. The structure and secondary dendrite arm spacing (SDAS) were similar in cases of steel shell mould cast specimens regardless of the modifier. The SDAS value for the sand cast specimens was larger than that for the shell molding, Tab. 1.

Casting porosity was studied on metallographic specimens using a light microscope. However, random 2-D sections through pores cannot provide good estimates of the largest defect size without further data analysis. Furthermore, pores originating fatigue fractures observed on fracture surfaces are significantly larger than pores observed on the metallographic sections regardless of the alloy [1, 4]. Therefore, the largest pore size expected in a cast component has to be estimated by extrapolation of the statistical description of the equivalent pore sizes obtained by metallography [1]. Here, the Murakami's method for the characterization of the pore size population according the LEVD method, [5], based on the evaluation of the largest defect size in many fields of view was applied. The image analysis program NIS Elements 3.0 for extensive and detailed measurement of pore features was used.

Because the shape of casting defects is not the same in all cases, according to the defect origin (gas pores, microshrinkages), different definitions of pore severity (or equivalent pore size), namely in terms of  $area^{1/2}$  and Maximum Feret Diameter, in the investigation of polished cross sections were used, [1, 3]. The scheme of measurement of defects is shown in Fig. 2. For the largest pore sizes evaluation the 50 x magnification was used. The control area of metallographic measurements was  $S_0 = 1.86 \text{ mm}^2$ .

The equivalent defect size,  $area^{1/2}$ , was obtained from measured area by the image analysis software; examples of such determination are shown in Fig. 2. The Maximum Feret Diameter was measured as the maximum distance between pairs of parallel lines tangent to the two-dimensional outline of a defect, shown in Fig. 2, too.

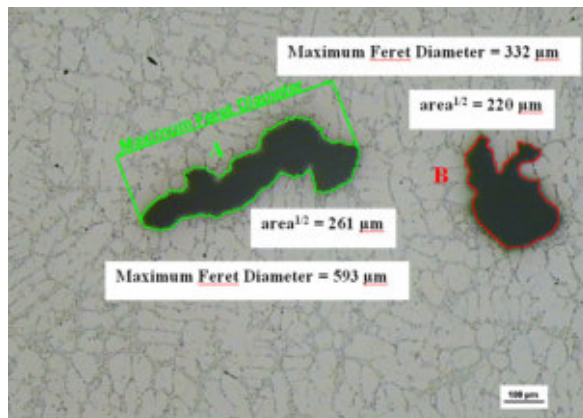


Fig. 2 Scheme of defects sizes measurement

Fig. 2 shows that the two definitions of equivalent pore size give quite different results when applied to the two pores, one rounded and the other elongated. Pore A yields the value of  $\text{area}^{1/2} = 261 \mu\text{m}$  and Maximal Feret Diameter =  $593 \mu\text{m}$ ; pore B is characterized by  $\text{area}^{1/2} = 220 \mu\text{m}$  and Maximal Feret Diameter =  $332 \mu\text{m}$ . Although the shape of defects is different, the  $\text{area}^{1/2}$  is quite similar for both of them. The difference between values of Maximum Feret Diameter characterizing measured defects is substantial.

### 3. Porosity evaluation and LEVD plots

The results of the largest pore size characterization according to the LEVD method, [5], are plotted in Fig. 3. Since all data in the LEVD plots fulfill the linear dependence, the Gumbel statistical distribution describes all data sets. The LEVD plots using the  $\text{area}^{1/2}$  parameter are shown in Fig. 3a and the plots using the Maximum Feret Diameter parameter in Fig. 3b. Although the same largest defects were measured, the use of different parameters characterizing the pore size give different results because of the role of defects shape as explained in Fig. 2.

The slope of the regression line is an indicator of the defect distribution. Inspection of Fig. 3 shows that set A has the largest scatter among the three materials while set B and C have similar and reduced scatter. As far as the influence of the modifier, defect average size and scatter of measured values were smaller in the Sr-modified specimens than in the Na-modified specimens. The sand cast method involved pores that are smaller and less scattered than the steel shell mold casting.

Generally, set A modified by pure Na has the largest pores. The smallest sizes of the largest defects were measured for the set C modified by Sr and obtained by sand casting. In the case of specimens cast to steel shell mold, smaller defects sizes on specimens from set B, modified by Sr, were measured.

The comparison of plots in Fig.3 shows also in absolute values differences between defects sizes predicted from measurements on cross sections of metallographic specimens using the  $\text{area}^{1/2}$  values.

The differences between porosity measured on metallographic specimens, described by LEVD plots, shown in Fig. 3b, where the MFD values were used, have similar trend as in case of LEVD plot for  $\text{area}^{1/2}$  values. In addition, in this case, the smallest defects sizes on the Sr modified specimens were measured. In this case, the largest defects obtained on sand cast specimens compared to defects sizes on steel shell molding specimens were smaller and the scatter in data was smaller too.

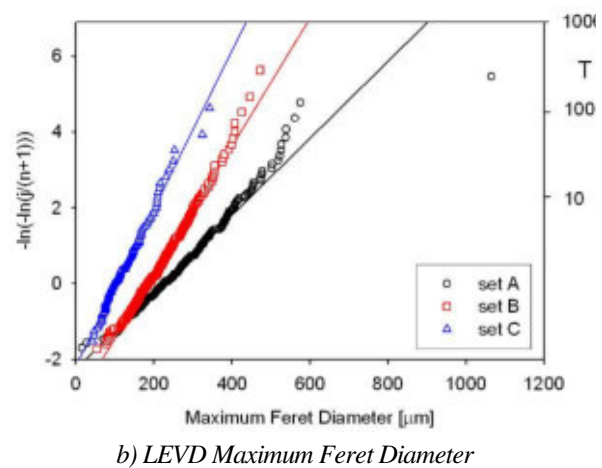
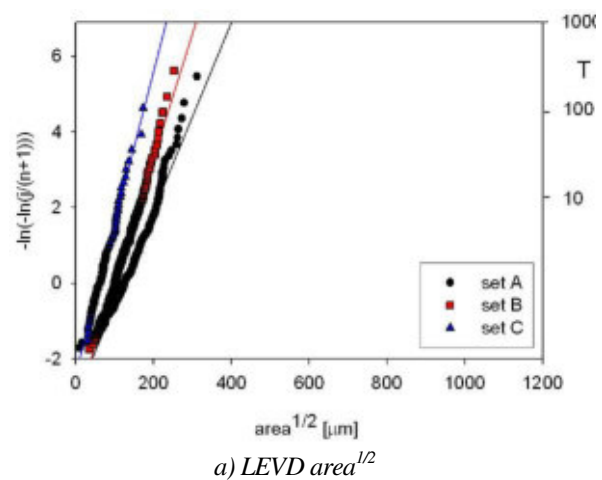


Fig. 3. LEVD plots

### 4. Porosity prediction and implication for fatigue

The largest defects sizes expected in a given area  $S$  was used to compare the influence of modifiers on porosity, Na for the set A and Sr for the sets B and C, and the influence of production technology on porosity size population. In order to correlate the largest values of defects with fatigue properties of studied alloys extrapolated values of the largest pores expected in areas responsible for fatigue damage were obtained from the LEVD description of the

different sets of materials. The predicted largest defects sizes for two different cross-sectional areas, i.e.  $S = 10 \text{ mm}^2$ , which is representative of the highly stressed cross section of a rotating bending specimen, and  $S = 100 \text{ mm}^2$ , representative of a small casting, are shown in Tab. 1.

Tab. 1

*Predicted largest defect sizes*

Prediction of the largest defect size for:		$S = 10 \text{ mm}^2$		$S = 100 \text{ mm}^2$	
Set	SDAS [ $\mu\text{m}$ ]	area <sup>1/2</sup> [ $\mu\text{m}$ ]	Max. Feret Diameter [ $\mu\text{m}$ ]	area <sup>1/2</sup> [ $\mu\text{m}$ ]	Max. Feret Diameter [ $\mu\text{m}$ ]
set A	32	186	377	283	612
set B	30	148	279	221	421
set C	40	99	180	159	295

In all cases the predicted largest defects sizes expressed in terms of area<sup>1/2</sup> are larger than the critical defect size for fatigue crack initiation (in Sr modified cast A356 alloy, the critical defect size at the fatigue limit is in the range of 25-50  $\mu\text{m}$ , [6]). However, not only the size of casting defects influences fatigue lives of castings, but also their shape and localisation towards the free surface of casting, porosity population and its their occurrence in clusters can play a role and, last but not least, also the defects origin can be of significance [1, 4, 7].

A final comment to the results presented in Tab. 1 relates to the observation that predicted MFDs values of the largest pores are about twice of these derived from area<sup>1/2</sup> equivalent sizes. Naturally, a significant influence has to be expected on predicted residual life calculations in fatigue as they are assumed to be the initial crack size.

To assess and rank the influence of largest pore size both in terms of MFD and area<sup>1/2</sup>, the AFGROW structural life prediction program was used [8]. The input data needed to run AFGROW include: i) crack growth data:  $\Delta K_{th}$ ; empirical Paris law coefficient and exponent,  $C$  and  $m$  plane strain fracture toughness,  $K_{IC}$ , and plane stress fracture toughness,  $K_C$ ; ii) maximum applied load, stress ratio, constant amplitude in the case of interest; iii) geometry and dimensions of the component, initial flaw geometry, size, and location.

The material data were taken from [9]; the loading conditions from testing performed at University of Parma on similar cast material, [4]. Information related to iii) are: rotating bending geometry  $R=-1$ , smooth 6-mm-dia section, initial surface crack size equal to the largest pore size.

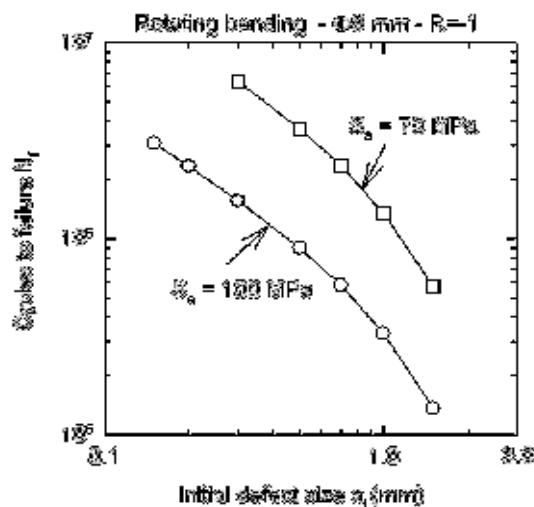


Fig. 4 Predicted influence of the largest pore size on the fatigue life of rotating bending specimens of AlSi7Mg at two applied stress levels.

Fig. 4 shows the results of the simulations of lifetime for two stress levels and different initial crack sizes. The influence of the largest pore size prediction on fatigue life is immediately determined entering in the plot with the data of Tab. 1 and selecting the applied maximum stress. An example is given in Tab. 2 for a stress amplitude  $S_a = 100 \text{ MPa}$  and a reference area  $S = 10 \text{ mm}^2$ . Data in Tab. 2 demonstrate an approximately factor-of-two influence on calculated fatigue life in dependence of material set. Similarly, a factor-of-two is found comparing the life predictions based on either the area<sup>1/2</sup> or the Maximum Feret Diameter.

Tab. 2

*Number of cycles for predicted largest defect sizes*

Predicted number of cycles for stress amplitude $S_a = 100 \text{ MPa}$ and reference area $S = 10 \text{ mm}^2$				
Set	area <sup>1/2</sup> [ $\mu\text{m}$ ]	$N_f$ [cycles]	Max. Feret Diameter [ $\mu\text{m}$ ]	$N_f$ [cycles]
set A	186	$2.3 \cdot 10^6$	377	$1.1 \cdot 10^6$
set B	148	$3 \cdot 10^6$	279	$1.6 \cdot 10^6$
set C	99	$4 \cdot 10^6$	180	$2.3 \cdot 10^6$

### 5. Conclusions

The casting porosity has a strong influence on fatigue properties of castings produced from Al-Si alloys. Therefore, the largest pore size prediction is a suitable tool for fatigue life prediction and for comparison of different materials. In this study the same base alloy, AlSi7Mg, modified with Na or Sr, was used for production of specimens using either steel shell mold casting or sand casting. The following conclusions can be drawn from this study:

- Murakami's statistical method for the porosity description and the largest defects sizes prediction can be applied for studied alloys, because all values in LEVD plots fulfill a linear dependence,
- Two parameters were used for defect characterization, namely Maximum Feret Diameter and area<sup>1/2</sup> parameter,
- AlSi7Mg modified with Na contains defects of larger size than the Sr modified alloy,
- Use of a simple fracture mechanics model demonstrated the important role of the initial crack size estimate, which is assumed to be equal to the largest pore size expected in a reference volume, on the predicted fatigue life of a material,
- Predicted fatigue lives, based on the Maximum Feret Diameter, are larger than the predicted fatigue life based on the area<sup>1/2</sup> parameter.

#### Acknowledgements

*This work was done as a part of the KEGA grant No.3/6110/08 and VEGA grant No.1/0208/08. It is also consistent with the objectives of MATMEC, an Emilia-Romagna regional net-lab (<http://www.matmec.it/>).*

#### References

- [1] Wang, Q. G., Jones, P. E.: Prediction of Fatigue Performance in Aluminum Shape Castings Containing Defects. The Minerals, Metals & Materials Society and ASM International 2007, doi: 10.1007/s11663-007-9051-4.
- [2] [http://www.metallurgicalaluminium.com/Downloads/tech\\_paper\\_pdfs/Guide\\_Modif\\_AlSi\\_Alloys.pdf](http://www.metallurgicalaluminium.com/Downloads/tech_paper_pdfs/Guide_Modif_AlSi_Alloys.pdf); Modification of Aluminium-Silicon Foundry Alloys. Dr. Ray Cook, (LSM), 1998. (cited 25.3.2009)
- [3] Konečná, R., Nicoletto, G., Majerová, V.: Largest extreme value determination of defect size with application to cast Al-Si alloys porosity. In: METAL, Hradec nad Moravicí, CZ, 2007, p. 94, ISBN 978-80-86840-33-8. (+ CD ROM).
- [4] Fintová, S., Konstantová, V., Konečná, R., Nicoletto, G.: Experimental study of porosity and fatigue behavior. In: METAL, Hradec nad Moravicí, CZ, 2008, p. 70, ISBN 978-80-254-1987-8. (+ CD ROM).
- [5] Murakami, Y.: Metal Fatigue: Effects of Small Defects and Nonmetallic Inclusions, Elsevier, Oxford, 2002, pp. 320.
- [6] Wang, Q. G., Apelian, D., Lados, D. A.: Fatigue behavior of A356-T6 aluminum cast alloys. Part I: Effect of casting defects. Journal of Light Metals 1, 2001, pp. 73-84.
- [7] Fintová, S., Konečná, R., Nicoletto, G.: Predicted largest defect sizes vs. Fatigue crack initiation defects sizes in cast Al-Si alloys, In: SEMDOK 2009, 2009. - ISBN 978-80-8070-959-4, pp. 22-25.
- [8] <http://afgrow.wpafb.af.mil/>
- [9] Lados, D.A., Apelian, D.: Fatigue crack growth characteristics in cast Al-Si-Mg alloys, Part II. Life predictions using fatigue crack growth data, Materials Science and Engineering A 385 (2004) 187-199.



- XVIII. [42] S. Fintová, G. Anzelotti, R. Konečná, G. Nicoletto, Casting Pore Characterization by X-Ray Computed Tomography and Metallography, in: *Archive of Mechanical Engineering*, 2010, pp. 263.

STANISLAVA FINTOVÁ \*, GIANCARLO ANZELOTTI \*\*, RADOMILA KONEČNÁ \*  
GIANNI NICOLETTO \*\*

## CASTING PORE CHARACTERIZATION BY X-RAY COMPUTED TOMOGRAPHY AND METALLOGRAPHY

Casting porosity is the main factor influencing the fatigue properties of Al-Si alloys. Due to the increasing use of aluminum castings, porosity characterization is useful for estimating their fatigue strength. In principle, a combination of metallographic techniques and statistical pore analysis is a suitable approach for predicting the largest defect size that is critical for the casting. Here, the influence of modifiers and casting technology on the largest pore size population in AlSi7Mg alloy specimens is obtained and discussed adopting the Murakami's approach. However, porosity evaluation is a challenge in the case of microshrinkage pores, which are frequently found in industrial castings. Their complicated morphology prevents a reliable definition of an equivalent defect size based on metallographic techniques. This contribution reports the application of X-ray tomography to the 3D reconstruction of real pores in cast Al-Si alloys and provides insight into the complication of microshrinkage pore sizing by metallography.

### 1. Introduction

Cast Al-Si alloys are widely used in automotive applications for their excellent combination of mechanical and technological properties. Fatigue properties of aluminum castings are, however, sensitive to the casting defects [1]. Fatigue properties of aluminum shape castings are sensitive to the defect size. In recent years, the maximum defect size has been recognized as the most important parameter in determining the fatigue properties of aluminum shape castings. The larger the maximum defect size, the lower the fatigue strength. In the presence of imperfections, fatigue strength is little affected

---

\* University of Žilina, Dept. of Materials Engineering, Žilina, Slovakia; E-mail: stanislava.fintova@fstroj.uniza.sk

\*\* University of Parma, Dept. of Industrial Engineering, 43100 Parma, Italy; E-mail: gianni.nicoletto@unipr.it

by chemical composition, heat treatment, or solidification time, as reflected by dendrite arm spacing and the sizes of eutectic silicon and intermetallic particles [2]. Casting defects have a detrimental effect on fatigue life by shortening not only fatigue crack propagation, but also the initiation period. The decrease in fatigue life is directly correlated to the increase of defect size [1].

In this paper, a method of statistical pore size characterization by metallography is initially considered. Two definitions of equivalent pore size, namely in terms of area  $^{1/2}$  and in terms of Maximum Feret Diameter, in the evaluation of pore severities observed on polished cross-sections were used. The statistical description of the largest pore size uses the Murakami's method based on the Largest Extreme Value Distribution (LEVD) [2]. Then, X-ray computed tomography (XCT) for the 3D shapes and distribution of casting defects in AlSi7Mg reconstruction was used. Special interest is devoted to microshrinkage pores irregular in shape. The XCT results to discuss metallographic issues in equivalent pore sizing criteria were used.

## 2. Experimental material

Three sets (A, B and C) of specimens of AlSi7Mg alloy were used in the experiments. The specimens for fatigue testing were prepared by machining from separately cast bars. The difference between bars depended on modifier used and casting process. Specimens of set A were modified by pure Na and cast in a steel mold, specimens of set B were modified by Sr and cast in steel mold while specimens from set C were modified by Sr and sand cast. All the specimens were heat-treated according to the heat treatment regime T6.

The structural analysis was carried out applying metallographic techniques and digital image analysis software NIS Element 5 on polished metallographic cross sections according to the Slovak standard STN 42 0491. Typical microstructures of the three sets of cast AlSi7Mg are shown in Fig. 1. The microstructure consists of primary dendrites of  $\alpha$ -phase (solid solution of Si in Al) and eutectics ( $\alpha$ -phase + Si particles). Si particles on the metallographic section were observed as round particles due to the optimal modification of the cast alloy.

The microstructure was also characterized determining the Secondary Dendrite Arm Spacing (SDAS) factor. Evaluation of SDAS was performed according to the line method (i.e. line length = 120  $\mu\text{m}$ ) [3]. The SDAS factor for the set A and B, both cast in steel mold, showed similar values (i.e. SDAS = 30  $\mu\text{m}$  for the set A and 32  $\mu\text{m}$  for the set B). For the sand cast set C, the measured SDAS value was 40  $\mu\text{m}$ , Tab. 1.

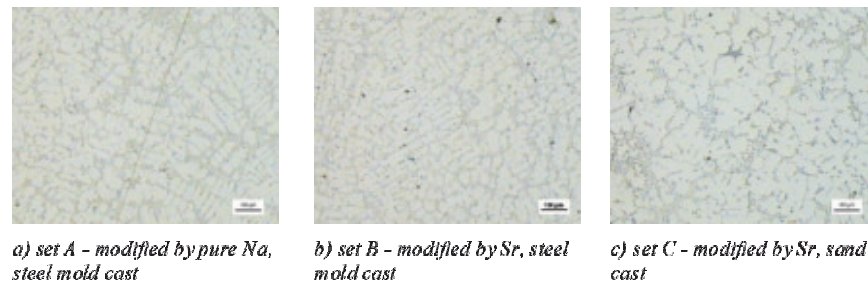


Fig. 1. Typical microstructure of AlSi7Mg aluminum cast alloy

### 3. Results and discussion

#### 3.1. Pore sizing by metallography

Comparison of different materials in terms of porosity suggests material ranking with respect to fatigue performance. Knowledge of the expected largest pore size and its location is a suitable information and can be obtained by metallography. Previous experiments used for correlation between the predicted largest defect sizes and actual sizes of defects responsible for the fatigue crack initiation used alternatively two equivalent parameters: the pore area<sup>1/2</sup> and the max. Feret diameter, [2, 4]. Those two parameters characterize the defect size population in different ways. But this is not unexpected because the equivalent defect size definition is complex in the case of microshrinkage pores of complicated morphology and interconnected shape.

##### 3.1.1. Metallographic evaluation

Metallography can be routinely used to study porosity in Al-Si castings. Typical porosity observed on the metallographic section of specimens is shown in the Fig. 2. The defects are different in the shape, size, amount and relative location among themselves and with respect to the free specimen surface. Casting porosity was extensively studied on the metallographic specimens using a light microscope. However, random 2D sections through pores cannot provide good estimates of the expected largest defect size without further data analysis. Furthermore, pores that originated fatigue fractures are significantly larger when observed on the fracture surface than pores measured on the metallographic sections regardless of the alloy. Therefore, the largest pore size expected in a cast component has to be estimated by extrapolation of the statistical description of the equivalent pore sizes obtained by metallography [2].

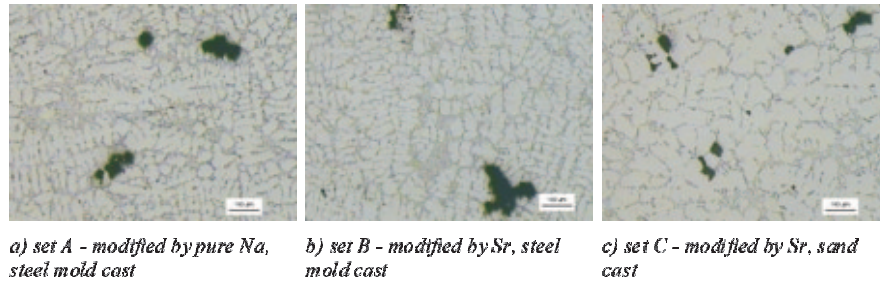
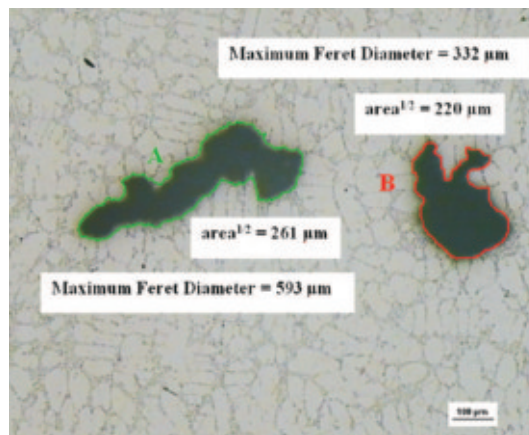
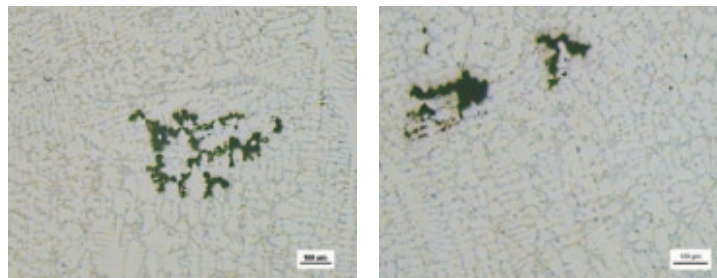


Fig. 2. Typical porosity of AlSi7Mg cast alloy

Fig. 3a shows two casting pores in AlSi7Mg alloy and the difference between two definitions of the equivalent pore size, namely the maximum Feret diameter (i.e. maximum distance between two points on the pore surface), [2], and  $\text{area}^{1/2}$ , [4], to define pore severity in fatigue. Quite different equivalent sizes are obtained because one pore in Fig. 3a is more rounded and another one is more elongated.



a) characteristic defect sizes measurement scheme



b) typical microshrinkage pores morphology

Fig. 3. Casting pores in AlSi7Mg observed by metallography



In some cases, there are difficulties to identify the real defect shape in the volume and corresponding characteristic defect size, which should be measured and used for the largest defect size prediction. Although cast defects on metallographic sections are observed as disconnected areas, they are probably branches of a single microshrinkage pore, Fig. 3b, sectioned during the metallographic specimen preparation. The casting defects observed in the present metallographic investigation were microshrinkage pores in all cases. Some of the observed defects were more rounded, i.e. Fig. 3a, but not as much as typical gas pores, [6].

There is no unique model how to measure and define the defect size of those microshrinkage defects observed in our case and typical for the Al-Si castings. Their presence is caused by the casting solidification. As different regions of a casting freeze, the shrinkage is compensated for by drawing liquid from neighboring areas, a process known as feeding. In long freezing-range alloys, feeding through the mushy zone is via small interdendritic channels. As solidification progresses, the ability to feed becomes more and more difficult due to the decreasing size of the channels. Eventually the channels freeze completely, isolating small areas from a supply of fresh metal. At this point any shrinkage occurring in these isolated areas causes a tension within the liquid, and voids may form to relieve this tension. These shrinkage pores may continue to grow into the interdendritic channels with the aid of any additional shrinkage. As a consequence of their growth mechanism, shrinkage pores tend to be composed of many long and irregular "arms", [6].

### 3.1.2. Largest defect size prediction

The Murakami's statistical method for the pore size evaluation was used, [4]. The method is based on the selection of the largest defect size present in a large number,  $n$ , of fields of view (i.e. controlled area  $S_0$  dependent on image magnification) of polished metallographic sections. The equivalent size,  $\text{area}^{1/2}$ , of the largest pore within each region is recorded. The set of  $n$  observations of maximum sizes  $\text{area}^{1/2}$ , or  $x_1, \dots, x_n$ , is used to determine whether the Gumbel distribution [4] gives a good fit. In a Gumbel plot ( $y_j = -\ln(-\ln(j/(n+1)))$ ) vs.  $x_{(j)}$ ) the data should lie close to a line. The fitted distribution is then used to estimate the size of the largest defect size in a given region  $S$  larger than the control area  $S_0$ , through the return period  $T = S/S_0$ , or to compare largest defects from control areas of different sizes [4].

Examples of largest pore size data sets entered into the Gumbel plot are shown in Fig. 4. Since each data set appreciably fulfills the linearity condition, the Gumbel statistical distribution can be used for fitting, extrapolation

and comparison. The slope of the regression line is an indicator of the data scatter. Inspection of Fig. 4 shows that the set A (modified with Na and cast in steel mold) has the largest scatter among the three materials while the set B (modified with Sr and cast in steel mold) and the set C (modified with Sr and sand cast) have similar and reduced scatter. The results were analogous when we used either  $\text{area}^{1/2}$  as an equivalent pore size or maximum Feret diameter. Estimates of the largest defects size expected in a given area  $S$  can be used to compare the influence of the modifiers, i.e. Na for the set A and Sr for the sets B and C, and production technology on porosity and fatigue.

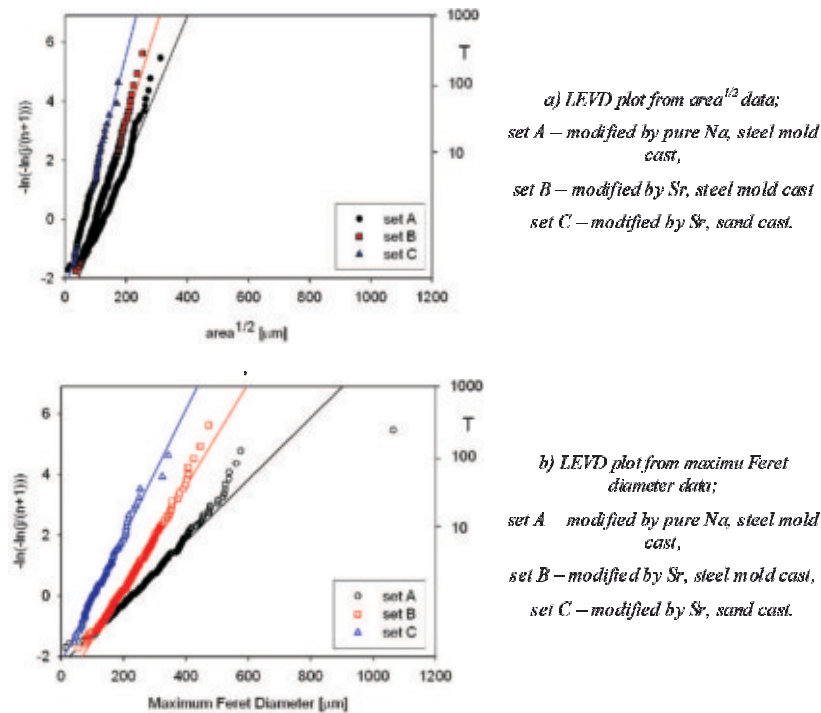


Fig. 4. Largest pore sizes in AlSi7Mg alloy according to the LEVD theory

In order to correlate the largest values of defects with fatigue properties of the studied AlSi7Mg alloy, the extrapolated values of the largest pores expected in areas responsible for fatigue damage were obtained from the Gumbel description of the different sets of materials. The largest defects sizes for two different cross-sectional areas were predicted; i.e. for the area  $S = 10 \text{ mm}^2$ , which is representative of the highly stressed cross section of a rotating bending specimen, and area  $S = 100 \text{ mm}^2$ , representative for a small castings, Tab. 1. In all cases, the predicted largest defects sizes expressed in terms of  $\text{area}^{1/2}$  are larger than the critical defect size for the fatigue

crack initiation (in Sr modified cast A356 alloy, the critical defect size at the fatigue limit is in the range of 25-50  $\mu\text{m}$ , [1]). When the casting defect size is larger than this critical defect size for the fatigue crack initiation, [2], other microstructural features will play only the minor role in the fatigue crack initiation and the crack will be initiated preferentially on the casting pore.

Table 1.

Predicted largest defect sizes for AlSi7Mg alloy

Prediction of the largest defect size for:		S = 10 mm <sup>2</sup>		S = 100 mm <sup>2</sup>	
Set	SDAS [ $\mu\text{m}$ ]	area <sup>1/2</sup> [ $\mu\text{m}$ ]	Max. Feret Diameter [ $\mu\text{m}$ ]	area <sup>1/2</sup> [ $\mu\text{m}$ ]	Max. Feret Diameter [ $\mu\text{m}$ ]
set A	32	186	377	283	612
set B	30	148	279	221	421
set C	40	99	180	159	295

### 3.3. Pore reconstruction by XCT

However, not only the size of casting defects does influence the fatigue life of castings. Their shape, origin and localisation with respect of the free surface can play a role, [1, 2, 8]. To obtain realistic information of actual pore shape, distribution within a material volume, a technique such as X-ray tomography (XCT), which is finding many applications in material science, [5], could be used. XCT exploits the penetrating power of a high density focused x-ray beam and it is based on a two-step procedure.

In the first step, a large number of XCT scans of a material volume are acquired. These scans are “front photos” of the specimen, representing pixel by pixel the absorption coefficient of the material crossed by x-rays. From these scans, cross-section images (i.e. slices) of the material volume are obtained with a back-projection algorithm. The second step of the procedure is the 3D reconstruction of pores from the series of slices. Original software has been developed to obtain all the pores inside the volume under investigation (i.e. a cylinder 4 mm in diameter and 1 mm in length shown in Fig. 5). Only the outer surface of each pore is stored as non-structured triangular surfaces according to the STL standard and finally smoothed.

The 3D shapes of cast defects found in Al-Si depend on the generation mechanism. Gas pores are usually approximately spherical in shape because they exist first as bubbles within the liquid. On the other hand, microshrinkage pores tend to be composed of many long and irregular “arms” as a consequence of their growth mechanism, [6]. The high spatial resolution of the

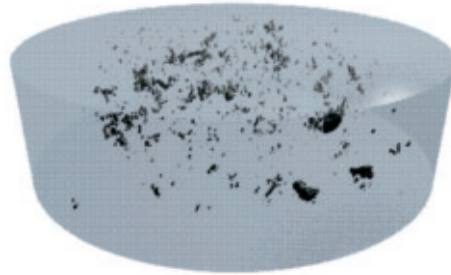


Fig. 5. Reconstruction of the porosity in a cylindrical volume of the specimen from AlSi7Mg cast alloy

present XCT equipment allows the reconstruction of the intricate geometry of microshrinkage pore, see Fig. 6, and of the defect distribution in the volume, see Fig. 5. By this method, not only the shape and size of defects can be reconstructed, but also their location to the free surface of specimen and also their mutual location can be controlled. Also the clusters of defect and spaces without defects can be detected.

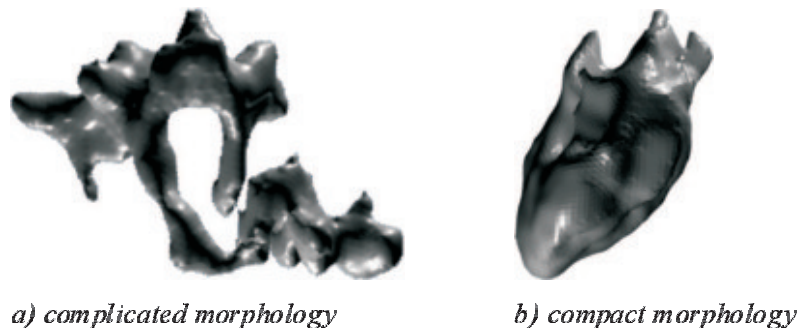


Fig. 6. 3D models of casting defects identified by the X-ray tomography

Although not presented here, [7], the reconstructed pores can be embedded into a finite element model of the material volume to investigate the influence of parameters such as shape, size, vicinity, etc., on the internal stress distribution. For example, the complex, branched shape of the shrinkage pores can lead to larger stress concentration compares to the rounded gas pores.

### 3.4. Sectioning a microshrinkage pore

The branched appearance of microshrinkage pores poses a challenge to the metallographic characterization of largest pore sizes for fatigue model development. Metallographic methods were originally developed to quantify

the role of inclusions, which are typically compact in shape, [2]. Since metallography observes a random material section under high magnification, it is unlikely that sectioning a pore exposes the largest pore dimension. However, in the case of a compact pore, i.e. gas pore, the largest size in a given area can be obtained by extrapolation of measured sizes if they fit a statistical distribution. On the other hand, clusters of observed defects such as in Fig. 2 and 3 cannot readily be classified as a group of gas pores or as the result of sectioning through branches of one complicated microshrinkage pore. An example of a microshrinkage pore sectioning is visualized in Fig. 7, where isolated neighboring cavities are found. None of these pseudo-pores, even the largest one, has a size comparable to the size of the original pore. Therefore, guidelines for estimating representative pore sizes based on coalescence conditions of neighboring pores are needed. The scheme of Fig. 7 explains why the determination of the actual equivalent size of pores shown in Fig. 2 and 3 is not straightforward and criteria for pore vicinity and coalescence should be defined and which equivalent size parameter should be used (i.e. area  $\frac{1}{2}$  or max Feret diameter). An on-going FEM investigation of the effective stresses near pores of different kinds, [7], demonstrates that gas and microshrinkage pores of similar size in terms of max. Feret diameter give comparable stress concentration with negligible influence of pore morphology.

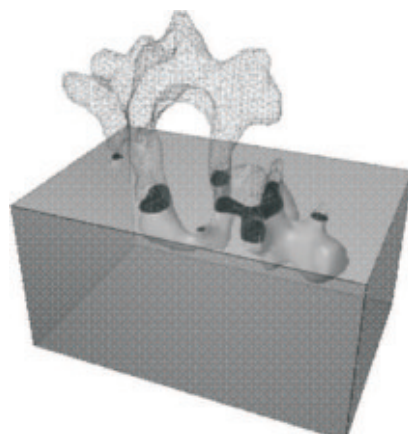


Fig. 7. Cross-section through 3D model of a microshrinkage pore and in black the resulting cluster of pores in the metallographic section

#### 4. Conclusions

In this study, the same base alloy, AlSi7Mg, modified with Na or Sr, was used for the production of specimens using either steel die casting or sand



casting. Metallography and X-ray tomography were used to characterize the cast porosity and its dependence from the technological parameters. Production technology and modifiers influence mainly the pore size distribution not the typical shape.

The following conclusions can be drawn from this study:

Murakami's statistical method for the pore size description and the largest defect size prediction can be applied to the present alloys, because data fulfill a linear dependence in the Gumbel plot.

Two alternative parameters for the equivalent defect size definition, i.e. maximum Feret diameter and  $\text{area}^{1/2}$ , gave similar relative statistical descriptions for the different production methods of AlSi7Mg.

AlSi7Mg specimens modified by pure Na contains larger defects than the Sr modified specimens.

X-ray tomography gave a detailed and accurate description of casting porosity in terms of pore size, shape and distribution.

3D modeling of defects observed by x-ray tomography can be used to understand the influence of the complex shrinkage pore shape on metallographic technique of pore size characterization to be used for the fatigue life prediction.

### Acknowledgements

The authors wish to thank Dr. Dreossi and the staff of the Tomolab (Sincrotrone Trieste) for their contribution to XCT image acquisition and analysis. This work was done as a part of the KEGA grant No.3/6110/08 and PRIN 2008.

Manuscript received by Editorial Board, March 29, 2010;

### REFERENCES

- [1] Q.G. Wang, D. Apelian, D.A. Lados: Fatigue behavior of A356-T6 aluminum cast alloys. Part I. Effect of casting defects, *Journal of Light Metals*, **1**, 1, 2001, pp. 73-84.
- [2] Q.G. Wang, P.E. Jones: Prediction of fatigue performance in aluminum shape castings containing defects, *Metallurgical and Materials Transactions B*, 2007, **38B**, pp. 615-621.
- [3] Anon.: Atlas métalographique des alliages d'aluminium. CTIF, Paris, 1980.
- [4] Y. Murakami: *Metal Fatigue: Effects of small defects and nonmetallic inclusions*, Elsevier, 2002.
- [5] P. Powazka, et al.: 3D computed tomography – an alternative for traditional metallographic investigations of porosity in cast aluminium, *Proc. Leoben Fatigue Symposium*, 2008, pp.
- [6] J.P. Anson, J. E. Gruzleski: The quantitative discrimination between microshrinkage and gas microporosity in cast aluminum alloys using spatial data analysis, *Acta Materialia* **57**, 2009, pp. 3539-3548.

- [7] A. Vincenzi, et al.: Comparison of local stresses at microshrinkage and gas pores in cast Al-Si alloys, Proc. DAS 2009 Leoben, 2009, pp. 239-240.
- [8] S. Fintová, V. Konstantová, R. Konečná, G. Nicoletto: Experimental study of porosity and fatigue behavior. In: METAL, Hradec nad Moravicí, CZ, 2008, p. 70, ISBN 978-80-254-1987-8. (+ CD ROM)

### **Charakteryzacja porów odlewniczych metodami rentgenowskiej tomografii komputerowej i metalografii**

#### **Streszczenie**

Porowatość odlewów jest głównym czynnikiem wpływającym na właściwości wytrzymałościowe stopów Al-Si. Z uwagi na rosnące zastosowanie odlewów aluminiowych, charakteryzacja ich porowatości nabiera znaczenia dla oceny wytrzymałości zmęczeniowej. Uważa się, że właściwym podejściem jest zastosowanie kombinacji technik metalograficznych i statystycznej analizy porów, co umożliwi przewidywanie największego, krytycznego dla odlewu, rozmiaru defektów. W tej pracy wyznaczano i dyskutowano wpływ modyfikatorów i technologii odlewania na największy rozmiar populacji porów w próbkach stopu AlSi7Mg, przyjmując podejście Mirakami'ego. Ocena porowatości staje się jednak wyzwaniem w przypadku porów związanych z mikrokurczliwością, które występują często w odlewach przemysłowych. Ich skomplikowana morfologia powoduje, że trudno jest wiarygodnie zdefiniować równoważny rozmiar defektu w oparciu techniki metalograficzne. Przedstawione doniesienie zawiera opis zastosowania rentgenowskiej tomografii komputerowej do trójwymiarowej rekonstrukcji rzeczywistych porów w odlewie ze stopu AlSi i daje pogląd na temat komplikacji w wymiarowaniu porów związanych z mikrokurczliwością metodami metalograficznymi.

- XIX. [43] L. Kunz, P. Lukáš, R. Konečná, S. Fintová, Casting defects and high temperature fatigue life of IN 713LC superalloy, *International Journal of Fatigue*, 41 (2012) 47-51.



## Casting defects and high temperature fatigue life of IN 713LC superalloy

Ludvík Kunz<sup>a,\*</sup>, Petr Lukáš<sup>a</sup>, Radomila Konečná<sup>b</sup>, Stanislava Fintová<sup>b</sup>

<sup>a</sup> Institute of Physics of Materials, Academy of Sciences of the Czech Republic, Žitkova 22, 616 62 Brno, Czech Republic

<sup>b</sup> University of Žilina, Univerzitná 1, 010 26 Žilina, Slovak Republic

### ARTICLE INFO

#### Article history:

Received 22 April 2011

Received in revised form 31 October 2011

Accepted 7 December 2011

Available online 16 December 2011

#### Keywords:

IN 713LC

High-cycle fatigue

Casting defects

Hot isostatic pressing

Extreme value statistics

### ABSTRACT

High-cycle high temperature fatigue life of a superalloy IN 713LC in as cast state and after hot isostatic pressing was experimentally determined for symmetrical cycling and cycling with tensile mean stress of 300 MPa. Fatigue tests were conducted at 800 °C in laboratory air. It has been found that the hot isostatic pressing improves the fatigue life. Large casting defects are sites of fatigue crack initiation in both states of the alloy. The hot isostatic pressing reduces the size of casting defects, however the broad scatter band of the lifetime data remains. Determination of casting defects size by optical microscopy on metallographic sections and an analysis of the size distribution by extreme value statistics indicates two types of defects: (i) small isolated defects and (ii) defect clusters consisting of complicated interconnected shrinkages in the three-dimensional space. The size distribution of both types of defects follows the extreme value statistics. This enables to estimate the maximum size of a defect likely to occur in a defined volume. The predicted maximum defect size in a volume of a fatigue specimen reasonable corresponds to the size of defect observed on the fracture surface of failed specimen.

© 2011 Elsevier Ltd. All rights reserved.

### 1. Introduction

A cast IN 713LC superalloy is a low carbon variant of IN 713, which has been used since a long time for high temperature applications like integral wheels of turbine engines or in the mass-production of turbocharger wheels. It possesses qualifications for good casting properties, no heat treatment is required and it has relatively low cost. On the other hand its grain size is often large and castings contain porosity, microshrinkages and other inhomogeneities. The fatigue life exhibits a large scatter, which is substantially higher in the high-cycle fatigue region (HCF) than in the low-cycle fatigue region (LCF). This is evidently a weak point for the application of this alloy in cyclically loaded components where good HCF fatigue strength is required.

There are several methods for minimizing casting defects. None of them is able to eliminate defects completely. Hot isostatic pressing (HIP) technology was found to have beneficial effect on creep/fatigue performance of IN 713 [1]. Namely in comparison with the as cast materials the HIP led to an increase of material strength under creep/fatigue conditions and moreover narrowed the scatter of creep data. Tensile strength and strength in bending tests of IN 713 was also positively affected by HIP [2]. Beneficial effect was found also for fatigue lifetime both in LCF and HCF regions [3]. Nevertheless in all the mentioned cases the materials after HIP procedure were not defect-free. A fine-grain casting processes resulting in

improvement of mechanical properties also do not guarantee the defect free products. The microporosity observed after centrifugal casting in IN 713LC causes an early fracture and leads to a drop of tensile stress [4].

The fracture mechanics enables the defect tolerant approach to fatigue design, however the basic premise here is that the size, shape and the distribution of the pre-existing defects is known. Though various non-destructive methods of defect detection are available, like visual, X-ray, ultrasonic magnetic or acoustic, the reliable prediction of fatigue strength or lifetime of components with defects remains a serious problem for engineering practice.

The studies of internal dislocation structure and development of surface relief of fatigued IN 713 in LCF region at elevated and high temperatures performed by Petrevec et al. [5] and Obrtlík et al. [6] show that highly inhomogeneous dislocation structure develops. Formation of dislocation rich slabs in the form of thin bands and ladder like bands was observed. These bands play an important role in often observed long Stage I fatigue crack propagation in Ni-base superalloys [7–9]. Fatigue cracks propagate crystallographically along the {111} crystallographic planes and form mutually inclined facets on the fracture surface. It is believed that the crystallographic propagation in early stages of fatigue cracks in coarse-grained structure contributes to the generally high scatter of fatigue life data of cast superalloys [10,11]. The initiation of fatigue cracks in IN 713 takes place predominantly on microshrinkages and pores, seldom on carbides [12].

The aim of this paper is to quantitatively evaluate the effect of HIP procedure on high-cycle fatigue life of IN 713LC and on casting

\* Corresponding author.

E-mail address: [kunz@ipm.cz](mailto:kunz@ipm.cz) (L. Kunz).

defect reduction. Attention is focused on size distribution of casting defects and prediction of maximum defect size.

## 2. Material and specimens

Specimens for fatigue testing were machined from conventionally cast rods of 20 mm in diameter and 100 mm in length. Specimens were manufactured from three, from the point of view of casting technology, nominally identical batches cast in one foundry subsequently within some months. All rods were controlled by conventional X-ray non-destructive defectoscopy and were found “defect free”, which means that the defect size should be below the resolution limit of the method, which is about 0.5 mm. The gauge length of cylindrical specimens with button end heads was 35 mm and the diameter of the gauge length was 5 mm, Fig. 1. The final operation of specimen machining was fine grinding. The surface roughness was  $R_a = 0.4$ .

Twenty-five specimens from the batch 3 were processed by HIP. The finally machined specimens were heated at the temperature 1160 °C at a pressure of 1000 bar for 3 h. The cooling rate was 10 °C/min and the process was performed under Ar atmosphere down the 900 °C, later on the cooling was conducted on air.

## 3. Experiments

A 100 kN resonant testing system Amsler 10HFP®1478 with VibroVin® controlling software operating under controlled load was used for fatigue testing in HCF region at a temperature of 800 °C. Two sets of fatigue tests were performed: load symmetrical tests characterized by mean stress of 0 MPa and tests with tensile mean stress of 300 MPa. During the start-up of the tests the mean load was kept zero as long as the specimen was not at the desired temperature 800 °C for at least 2 h. Then the resonant system was switched on in the case of the stress symmetrical testing. In the case of non-zero mean stress the mean load was applied during several seconds and without a delay the cycling was started. The full load amplitude was reached by a ramp during several hundreds of loading cycles. The frequency of loading was of about 115 Hz. Tests were run in laboratory air. The heating was performed in an electric furnace. The long-term stability of temperature of specimen gauge length was within  $\pm 1$  °C. The temperature gradient at the central part of the gauge length was smaller than 3 °C/cm.

The size and the distribution of casting defects were analyzed by an extreme value statistics. The method, originally applied to

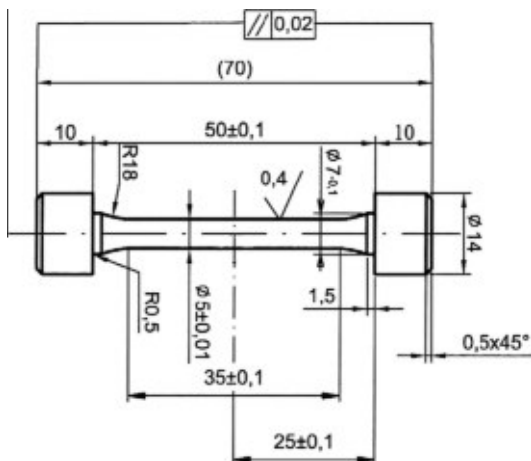


Fig. 1. Specimen for fatigue tests.

very small defects in high strength steels by Murakami [13], was shown to be applicable also for large casting defects in light materials, e.g. [14,15]. The casting defects in IN 713LC were observed on metallographically prepared axial sections of the specimen gauge length of  $5 \times 20$  mm in dimension or on transversal sections of 5 mm in diameter. Altogether 25 different places of the area  $S_0 = 1.83$  mm<sup>2</sup> located on several sections were analyzed. The size of defects was evaluated in terms of their square root area by means of image analysis software and finally treated by statistical method based on extreme value theory.

## 4. Results

The HCF fatigue life at 800 °C of as cast specimens is shown in Fig. 2. Data for load symmetrical cycling, i.e. with the mean stress zero are shown together with data characterizing the fatigue life at the tensile mean stress of 300 MPa. The S–N data exhibit substantial scatter, which is obviously higher for the symmetrical fatigue loading. The lines in the figure represent the power law best fit of the experimental points corresponding to the specimens failed for  $N_f \leq 10^7$ . Arrows denote the run-out specimens. As expected, the S–N curve for fatigue loading with the tensile mean stress is shifted towards lower stress values. The shift makes nearly 100 MPa for the lifetime of the order of  $10^4$  cycles to failure and slightly decreases with increasing number of cycles.

Fractographic observation of fatigue fracture surfaces shows that in all cases the fracture was initiated on large casting defects, nearly always in the specimen interior. An example of the initiation site in as cast material can be seen in Fig. 3. A large casting defect is encircled by an ellipse. The arrows indicate the boundary of a fish eye.

The results of the experimental determination of fatigue life of specimens processed by HIP are shown in Fig. 4 for load symmetrical cycling and cycling with the tensile mean stress of 300 MPa. The experimental points exhibit similar scatter like the data of the as cast material. The full and the dashed lines in Fig. 4 represent the best fits of S–N points of failed specimens. The limit for run-out specimens was again  $10^7$  cycles.

The coefficients of the power law fit  $\sigma_a = AN_f^{-b}$  and the coefficients of determination  $R^2$  for as cast material and material after HIP are summarized in Table 1. Further, there are also the fatigue limits determined by power law fits for  $N = 10^7$  cycles there.

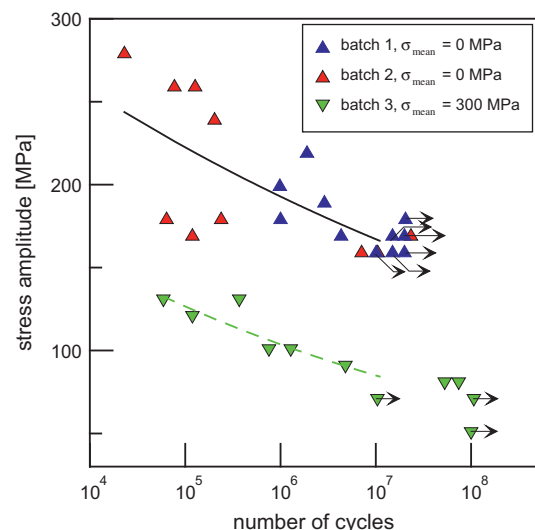


Fig. 2. High-cycle S–N data of IN 713LC in as cast state. Stress symmetrical loading and cycling with tensile mean stress of 300 MPa.



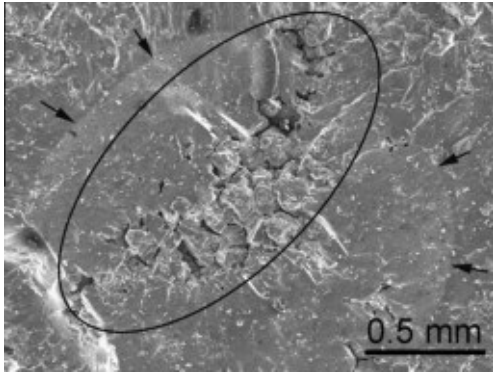


Fig. 3. Fatigue crack initiation on a large casting defect in as cast IN 713LC superalloy.

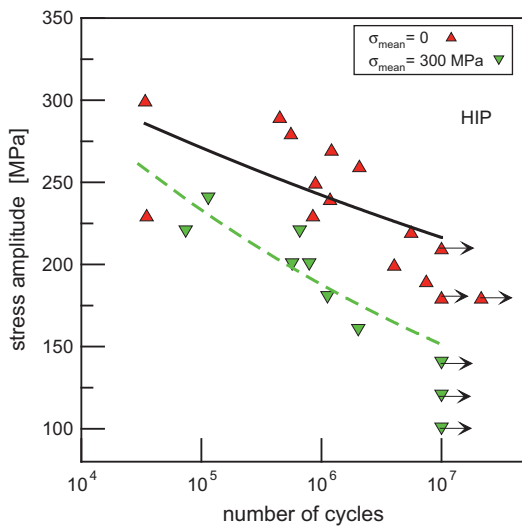


Fig. 4. High-cycle S–N data of IN 713LC processed by HIP, stress symmetrical loading and cycling with tensile mean stress of 300 MPa.

Table 1  
Parameters of S–N curves, fatigue limits and coefficients of determination.

	Mean stress (MPa)	A (MPa)	b	Fatigue limit $\sigma_c$ (MPa)	$R^2$
As cast	0	455	0.062	167	0.36
As cast	300	343	0.087	84	0.79
HIP	0	476	0.049	216	0.35
HIP	300	687	0.094	151	0.69

Fractographic observation of fracture surfaces of specimens processed by HIP revealed that the fatigue crack initiation took place in the same manner as in the as cast material. Cracks initiated internally on casting defects. An example of a fracture surface corresponding to the specimen loaded at the stress amplitude 250 MPa, which failed after  $10^6$  cycles, is shown in Fig. 5. The site of the crack initiation is shown in Fig. 6 at higher magnification. The cluster consisting of a complicated three-dimensional shrinkage, which initiated the crack, is encircled. Arrows indicate the isolated defects.

Casting defects both in as cast and in HIP processed materials were observed by light microscopy at polished metallographic sections. An example of such micrograph is presented in Fig. 7. The defects can be classified into two groups. There are isolated defects in the structure; arrows in the figure mark them. Besides iso-

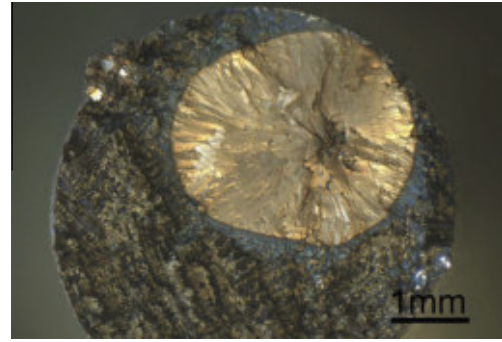


Fig. 5. Internal fatigue crack initiation on a casting defect in HIP processed IN 713LC.

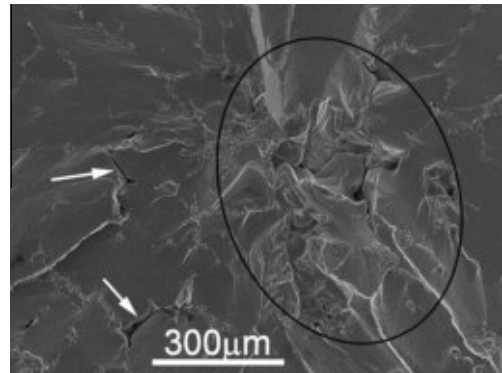


Fig. 6. Fatigue crack initiation site from Fig. 5 at higher magnification.

lated defects a clusters of defects can be often recognized. They represent apparently sections of large, in three-dimensional space interconnected shrinkages located in interdendritic regions. A cluster of defects is encircled in Fig. 7 by an ellipse.

The evaluation of the area of isolated defects was performed by means of image analysis software. More complicated is the evaluation of the size of clusters of defects. One of the possible ways is to define a cluster as a complex apparently belonging to a shrinkage, which has been cut by the metallographic section. For purposes of further evaluation by means of extreme value statistics the area of a cluster was determined as an area of the ellipse circumscribed as close as possible to the cluster. Though this conventional definition of a cluster size is not exact, this simple treatment yields quite reasonable results. This point will be gone through in more detail in Section 5.

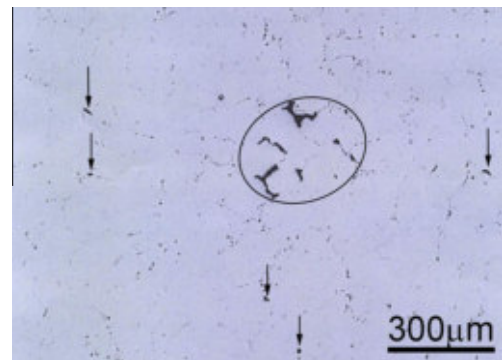


Fig. 7. Casting defects as observed on metallographic sections. As cast material.

The results of the determination of the size of isolated defects and clusters of defects in as cast and HIP processed superalloy are shown in Fig. 8 in the representation of a Gumbel plot [13]. Four distinct sets of experimental points can be seen here. Straight lines fitting well the particular data sets witness for the fact that the size of both types of defects obeys the extreme value statistics. The mutual shift of lines for isolated defects indicates that the HIP process reduces their size. Similar conclusion can be drawn for clusters.

## 5. Discussion

The available literature data indicate, that the HIP procedure results in an improvement of fatigue life data of cast Ni-base superalloys, but the results often fail of expectations [3]. The experimental S–N data obtained in this work for load symmetrical cycle and cycling with tensile mean stress of 300 MPa show the significant improvement of high temperature performance of IN 713LC in the range of number of cycles to failure from  $10^4$  to  $10^7$ . Fig. 9 summarizes the best fits of S–N data. It can be seen that for fatigue limit defined by these dependences for  $10^7$  cycles the improvement due to HIP makes 30% for the symmetrical loading and 80% for the loading with the tensile mean stress, see also Table 1. On the other hand, the large scatter of the experimentally determined S–N data remains. The coefficient of determination  $R^2$  is for symmetrical cycling of as cast and HIP processed material 0.36 and 0.35. To the similar conclusion leads the comparison of  $R^2$  values for tests with the men stress tests. The improvement due to HIP has to be considered insignificant. The narrowing of the scatter band due to HIP procedure reported for creep data of IN 713 [1] was not observed in the case of fatigue life.

The HIP procedure, though heaving a beneficial effect on the fatigue lifetime, is not able to get rid of casting defects and porosity completely. The distribution both of isolated defects and their clusters describes Fig. 8. There are two pairs of straight lines there. The fact that the experimental points can be well fitted with straight lines in the given representation means that the defect distribution follows the extreme value statistics. This holds both for the isolated defects and for clusters. Important is that under this condition the extreme value statistics enables estimation of the maximum size of a defect likely to occur in a defined volume.

The prediction of the largest defect likely to occur in the fatigue specimen volume,  $S_{\text{spec}}$ , was performed in the following way. In the

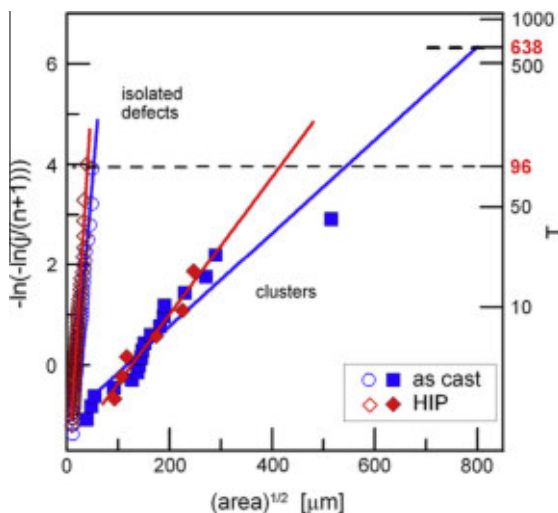


Fig. 8. Gumbel plot for isolated defects and clusters for as cast and HIP processed IN 713LC superalloy.

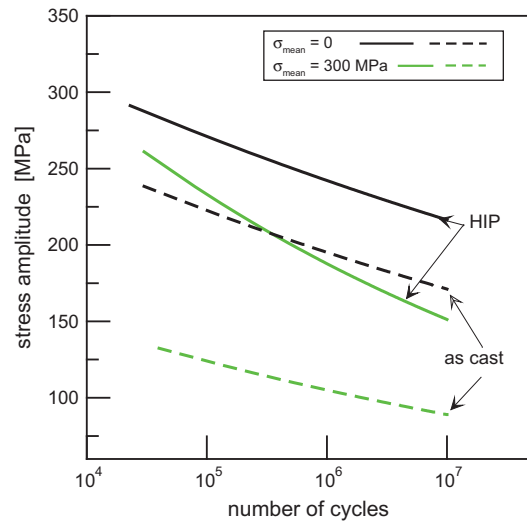
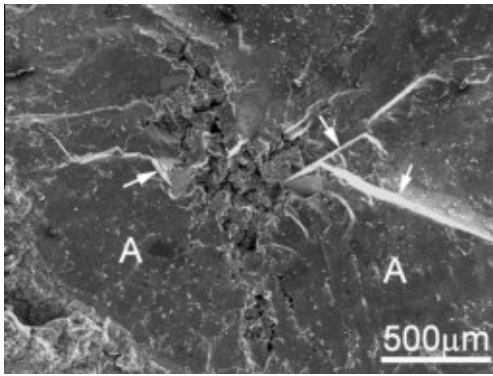


Fig. 9. Comparison of S–N curves for as cast and HIP processed IN 713LC.

first step the maximum defect size (in terms of the  $(\text{area})^{1/2}$ ) was determined for a reference area  $S_{\text{ref}} = 5 \times 35$  mm, which is equal to the area of the axial section of the fatigue specimen gauge length. This was done by an extrapolation of plots in Fig. 8 to the value  $T = 96$ , which is the return period of  $S_{\text{ref}}$  to  $S_0 = 1.83$  mm<sup>2</sup>. The maximum defect size likely to occur in this area is  $D_{T=96} = 43, 56, 446, 591$  μm for isolated defects in HIP processed material, for isolated defects in as cast material, for clusters in HIP processed material and clusters in as cast material, respectively. Indeed, the defects are in reality three-dimensional. Provided that their dimension is the same in the longitudinal and transversal sections, it can be expected that the three-dimensional defects of these sizes can be found in a cuboids having volumes  $S_{\text{ref}} D_{T=96}$ . The number of these volumes in the specimen gauge volume  $S_{\text{spec}}$  is  $N = S_{\text{spec}} / S_{\text{ref}} D_{T=96}$ . Then the return period for the whole specimen volume can be defined as  $T_{\text{spec}} = TN$ . This procedure yields for clusters in as cast material the return period  $T = 638$ , which defines the maximum defect size of 800 μm, Fig. 8. This predicted value was compared with the real defect, which resulted in final failure of the particular specimen. The defect is shown in Fig. 3. The defect, similarly to the procedure used for determination of clusters on metallographic sections, is circumscribed by the ellipse. Its area is 1.180 mm<sup>2</sup>, which yields the value  $(\text{area})^{1/2} = 1086$  μm. The agreement of both values can be taken as fair, especially taking into account the inaccuracy in the determination of the area of clusters. Analogical procedure for the clusters in HIP processed material yields the maximum defect size of 620 μm; the defect size on the fracture surface in Fig. 6 is  $(\text{area})^{1/2} = 550$  μm, which is again in reasonable agreement with the predicted value. It is also smaller than the value found for as cast material. From Fig. 8 and fractographic observation of defects, which initiated cracks, it follows that only large clusters are jeopardizing. Small isolated defects seem to be harmless, see defects indicated by arrows in Fig. 6.

In relation to the above-described results the problem of the metallographic determination of the largest defects in material is worthwhile to discuss. The metallographic procedure for the determination of defect size is not fully precise, due to the fact that the metallographic section of the measured defect reveals necessarily not its largest size. Murakami [13] analyses this problem in detail with the conclusion that the procedure, despite of this limitation, is useful for practical applications. In our case, the real shape of defects, especially of clusters, is much more complicated than the shape of small defects, which are usually treated by this



**Fig. 10.** Non-crystallographic and crystallographic fatigue crack propagation from casting defect. As cast material.

procedure. Our results indicate that the predicted defect size in terms of the inscribed ellipse (which is again an approximation) reasonably corresponds to the fractographic observation of the defect size on the fracture surface of a specimen. This means that the metallographic procedure can be reasonable used for prediction of the largest defects in bulky castings.

Another issue, which should be discussed, is the fact that the number of experimental points in Fig. 8 is low for the case of clusters. There are only six points for clusters in HIPed material in the figure. The procedure consisted in analysis of the 25 places having the area of 1.83 mm<sup>2</sup> on the section with area of 100 mm<sup>2</sup> separated from the specimen gauge length. There is a lot of small isolated defects at this area, but the frequency of large clusters is low. To increase their number means to increase the inspected area. The analysis was performed for several specimens. Though the number of experimental points for clusters was in all cases low, the observed trend was the same and the predictions for particular specimens were reasonable.

The fatigue crack propagation in the vicinity of defects was both non-crystallographic and crystallographic. There is a general agreement that crystallographic Stage I and non-crystallographic Stage II take place in Ni-base alloys. Fig. 10 shows the fracture surface created mainly by non-crystallographic crack growth (marked by A). The fracture surface is macroscopically perpendicular to the principal stress. In the vicinity of the defect some crystallographic facets can be observed. Arrows in the figure denote them. The facets are often inclined at high angles to the prevailing non-crystallographic macroscopic fracture surface. The mechanism of facet formation consists in development of highly localized slip in slip bands along {111} crystallographic planes [5]. Their length is in cast material large; they often terminate at the grain boundaries and represent planes along which the material separates due to cyclic slip on non-coplanar slip systems in neighboring grains [11]. The stress concentration effect of large casting defects promotes the slip and contributes to decohesion process. The casting defects are variable in size and differ also in shape, which means that they have different

stress concentration factor. This variety also contributes to the observed high scatter of the S–N data.

## 6. Conclusions

Hot isostatic pressing improves the fatigue performance of cast IN 713LC superalloy at 800 °C in air. A shift of S–N curves towards higher stress amplitudes for given number of cycles was observed for HIP processed material both for load symmetrical cycling and cycling with tensile mean stress of 300 MPa. The high scatter of S–N data, which is caused by large casting defects resulting in crack initiation, however, remains. The extreme value statistics applied to the metallographic determination of casting defect size yields reasonable prediction of the maximum defect size likely to occur in a given volume. The prediction was verified by fractographic analysis of fatigue fracture surfaces.

## Acknowledgements

The Ministry of Industry and Trade of the Czech Republic under the Contract FR-T13/055 and the project “CEITEC – Central European Institute of Technology” CZ.1.05/1.1.00/02.0068 financed by European Regional Development Fund supported this work. This support is gratefully acknowledged.

## References

- [1] Persson C, Persson PO, Ostensson HIP. A way to increase lifetime of cast Inconel 713 C. In: Proceedings of the 1988 int powder metallurgy conf, Orlando, June, 1988. Princeton, USA: American Powder Metallurgy Inst.; 1988.
- [2] Chang SH. Optimization of pressure and soaking time of HIP treatment on IN 713LC cast superalloy. Mater Trans 2009;50:909–16.
- [3] Donachie MJ, Donachie SJ. Superalloys. A technical guide. 2nd ed. ASM International; 2002. p. 266.
- [4] Wei CN, Bor HY, Ma CY, Lee TS. A study of IN-713LC superalloy grain refinement effects on microstructure and tensile properties. Mater Chem Phys 2003;80:89–93.
- [5] Petreňec M, Obrtlík K, Polák J. Inhomogeneous dislocation structure in fatigued Inconel 713LC superalloy at room and elevated temperatures. Mater Sci Eng 2005;A400–401:485–8.
- [6] Obrtlík K, Man J, Polák J. Room and high temperature low cycle fatigue of Inconel 713LC. In: Proc of Euromat 2001 conference, Rimini, June 10–14, 2001. AIM Milano; 2001.
- [7] Antolovich BF. In: ASM handbook fatigue and fracture, vol. 19. ASM Int.; 1996. p. 854.
- [8] Duquette DJ, Gell M. The effect of environment on the mechanism of Stage I fatigue fracture. Met Trans 1971;2:1325–31.
- [9] Kunz L, Lukáš P, Mintách R, Hrbáček K. Effect of mean stress on high-cycle fatigue strength of IN 713LC superalloy. Kovove Mater 2006;44:275–81.
- [10] Kunz L, Lukáš P, Konečná R. Initiation a propagation of fatigue cracks in cast IN 713LC superalloy. Eng Fract Mech 2010;77:2008–15.
- [11] Kunz L, Lukáš P, Konečná R. High-cycle fatigue of Ni-base superalloy Inconel 713LC. Int J Fatigue 2010;32:908–13.
- [12] Sonsino CM, Brandt U, Bergmann J. Fatigue and short crack propagation behaviour of cast nickel base alloys IN 713C and MAR-M-247 LC at high temperatures. In: Rie KT ed. Low cycle fatigue and elasto-plastic behaviour of materials – 3. Elsevier; 1992. p. 262–8.
- [13] Murakami Y. Metal fatigue: effects of small defects and nonmetallic inclusions. Elsevier; 2002.
- [14] Nicoletto G, Konečná R, Baicchi P, Majerová V. Casting porosity and long-life fatigue strength of cast Al-alloy. Mater Sci Forum 2008;567–568:393–6.
- [15] Konečná R, Fintová S, Nicoletto G. Shrinkage pores and fatigue behaviour of cast Al–Si alloys. Key Eng Mater 2011;465:354–7.

XX. [44] M. Šmíd, S. Fintová, L. Kunz, P. Hutař, Role of defects in fatigue damage mechanisms of cast polycrystalline superalloy MAR-M 247, MATEC Web of Conferences, 12 (2014) 03005.

## Role of defects in fatigue damage mechanisms of cast polycrystalline superalloy MAR-M 247

Miroslav Šmíd, Stanislava Fintová, Ludvík Kunz and Pavel Hutař

Institute of Physics of Materials, AS CR, Žitkova 22, Brno 616 62, Czech Republic

**Abstract.** High-cycle fatigue life of nickel-based superalloy MAR-M 247 was experimentally determined for as-cast material and material processed by hot isostatic pressing (HIP). Fatigue testing was conducted at temperatures 650, 800, 900 °C in laboratory air. HIP was done at the following conditions: 1200 °C/100 MPa/240 min. It has been found that HIP significantly improves the fatigue life. Obtained results indicate that main factors which determine the fatigue strength of material in both conditions are grain size, grain orientation and size and distribution of casting defects. The distribution and size of the casting defects were evaluated by light microscopy on metallographic sections. The data were processed by the extreme value statistics, which enables to estimate the maximum size of a defect likely to occur in a defined volume. Light and scanning electron microscopy were used for fractographic investigation of fracture surfaces and fatigue crack initiation sites. Focused ion beam technique and transmission electron microscopy were applied with the aim to reveal the microstructure in the nearest vicinity of the early cracks. The mechanism of crack initiation, early crack propagation and the role of casting defects were described and discussed.

The alloy MAR-M 247 is cast polycrystalline nickel-base superalloy developed by Martin Marietta Corporation. The alloy belongs among advanced cast superalloys with exceptionally high temperature strength, corrosion and oxidation resistance. Thanks to balanced chemical composition the alloy exhibits very good microstructural and mechanical stability up to temperatures of 1000 °C.

Chemical composition of the alloy was following (in wt. %): 0.15 C, 8.37 Cr, 0.67 Mo, 5.42 Al, 1.01 Ti, 3.05 Ta, 9.92W, 9.91 Co, 0.04 Nb, 0.015 Br, 1.37 Hf, bal. Ni. HIP procedure is used for cast materials with the aim to close or at least minimize casting porosity. Therefore one batch of the material underwent HIP procedure while second one was left in as-cast state. Subsequently, both batches were heat treated by solution annealing (1200 °C/2 hours) and then by precipitation annealing (870 °C/24 hours). The structure of the MAR-M 247 alloy is dendritic with coarse grains of average size 0.8 mm. Casting defects were detected in the structure. Their typical size was around 400  $\mu\text{m}$  measured in alloy after HIP, while pores over 1 mm were found in the alloy without HIP. High volume fraction (approximately 60%) of strengthening phase  $\gamma'$  is heterogeneously distributed in  $\gamma$  matrix. Areas of fine  $\gamma'$  precipitates with mostly cuboidal shape (edge size 0.4  $\mu\text{m}$ ) are often surrounded by areas of coarse  $\gamma'$  precipitates (1.6  $\mu\text{m}$  in diameter) of spherical or more complicated morphologies. Numerous carbides and eutectics  $\gamma/\gamma'$  were found in interdendritic and grain boundary areas.

This is an Open Access article distributed under the terms of the Creative Commons Attribution License 4.0, which permits unrestricted use, distribution, and reproduction in any medium, provided the original work is properly cited.



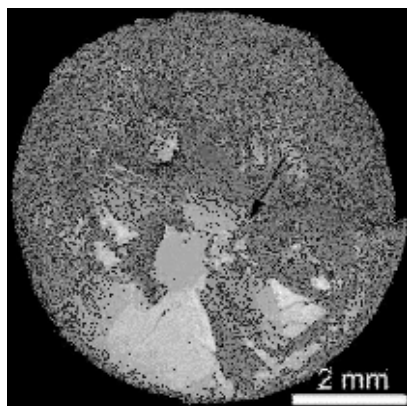


**Figure 1.** Crystallographic fatigue fracture surface of specimen cycled at 650 °C, ( $\sigma_a = 220$  MPa,  $N_f = 2.0 \times 10^6$ ). The fatigue crack initiation site is marked by arrow.

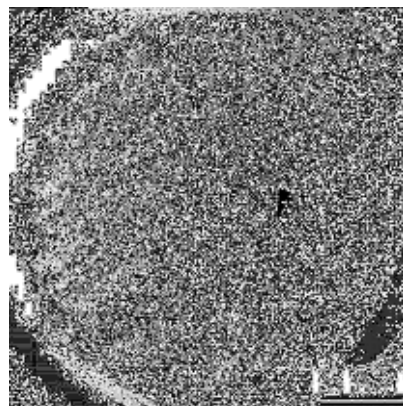


**Figure 2.** Non-crystallographic fatigue fracture surface of specimen cycled at 900 °C, ( $\sigma_a = 220$  MPa,  $N_f = 6.51 \times 10^5$ ). The fatigue crack initiation site is marked by arrow.

Resonant testing machine with 100 kN force range was used for fatigue tests under load control regime in fully reversed loading ( $R = -1$ ). The frequency of loading was around 122 Hz. Cylindrical specimens with cylindrical gauge (8 mm in diameter and 23 mm in length) were used in the study. The experimental temperature was provided by electric furnace with resistance heating. All tests were done in laboratory air.

The fracture surfaces and specimens cross-sections were observed by scanning electron microscopy (SEM) equipped by electron back scatter diffraction (EBSD) detector and also by light microscope (LM) with image analysis software.

The S-N curves in high cycle fatigue region were obtained for the alloy which underwent HIP procedure as well as for the alloy without HIP. The test temperatures were 650, 800 and 900 °C. The results clearly show that HIP has significant influence on the fatigue performance of the alloy. The material without HIP procedure had significantly worse high fatigue resistance than the alloy after this procedure.

Fractographic analysis revealed that shrinkage pores are main fatigue crack initiation sites in the most cases. The size and distribution of the pores is strongly heterogeneous and fluctuate significantly. Therefore numerous specimen sections were metallographically analysed and processed by extreme value statistics.

The fatigue fracture surfaces revealed changes in appearance due to the increase of the test temperature. Crystallographic fatigue crack propagation with characteristic facets on the surface was dominant for tests at 650 °C (see Fig. 1). Observation of longitudinal cross-sections of specimens revealed intensive cyclic slip activity along the activated shear planes. EBSD analysis confirmed that these planes are of (111) type. Extend of crystallographic crack propagation was significantly lower at temperature 800 °C. The facets appeared just in the vicinity of the crack initiation sites and from a certain distance the fatigue crack propagated by non-crystallographic mode macroscopically perpendicularly to the loading axis. This mode of fatigue damage was dominant even in areas around crack initiation site at temperature 900 °C (see Fig. 2). This change of the fracture surface appearance is mainly caused by emergence of thermally activated processes in structure like diffusion and dislocation climb and cross-slip.

SEM observations, focused ion beam technique and transmission electron microscopy were used to analyze areas in front of the crack tip. Strong cyclic slip activity going across matrix channels as well as  $\gamma'$  precipitates was observed.

This research was financially supported by the project FR-TI4/030 of the Ministry of Industry and Trade of the Czech Republic.

- XXI. [45] M. Šmíd, S. Fintová, L. Kunz, P. Hutař, K. Hrbáček, Prediction of maximum casting defect size in MAR-M 247 alloy processed by hot isostatic pressing, *Materials Engineering - Materiálové inžinierstvo*, 22 (2015).



# PREDICTION OF MAXIMUM CASTING DEFECT SIZE IN MAR-M 247 ALLOY PROCESSED BY HOT ISOSTATIC PRESSING

Miroslav Šmíd<sup>1,\*</sup>, Stanislava Fintová<sup>1,2</sup>, Ludvík Kunz<sup>1</sup>, Pavel Hutař<sup>1</sup>, Karel Hrbáček<sup>3</sup>

<sup>1</sup> Institute of Physics of Materials Academy of Sciences of the Czech Republic v. v. i., Žižkova 22, 616 62 Brno, Czech Republic

<sup>2</sup> Brno University of Technology, CEITEC BUT – Central European Institute of Technology, Technická 3058/10, 616 00 Brno, Czech Republic

<sup>3</sup> První brněnská strojírna Velká Bíteš a.s., Vlkovská 279, 595 12 Velká Bíteš, Czech Republic

\*corresponding author: tel.: +420 532 290 362, fax: +420 541218 657, e-mail: [smid@ipm.cz](mailto:smid@ipm.cz)

## Resume

Nickel based MAR-M 247 superalloy treated by hot isostatic pressing was investigated with the aim to identify the influence of casting defect size on fatigue life. Two testing temperatures of 650 and 800 °C and one stress amplitude were chosen for fatigue tests. The Murakami approach and the largest extreme value distribution theory were applied. It has been found that the maximum size of casting defects in a specimen can be satisfactorily predicted. Fatigue life of specimens was in good agreement with assumptions based on the evaluation and prediction of the casting defect size.

## Article info

### Article history:

Received 25 August 2014

Accepted 4 February 2015

Online 17 February 2015

### Keywords:

MAR-M 247;

Superalloys;

Fatigue;

Casting defects;

Elevated temperatures.

Available online: <http://fstroj.uniza.sk/journal-mi/PDF/2015/04-2015.pdf>

ISSN 1335-0803 (print version)

ISSN 1338-6174 (online version)

## 1. Introduction

Nickel based superalloys has been one of the most essential class of materials in aerospace, power generation and automotive industries since many decades. These alloys are irreplaceable in many applications despite lot of new materials were developed [1]. Their combination of mechanical properties and corrosion and oxidation resistance is still unique. That is why superalloys are commonly used for the most critical parts of turbines [2 – 4].

MAR-M 247 is a well-known advanced superalloy suitable for investment casting. Mechanical properties are mainly determined by the structure of the material. Superalloys typically consist of a  $\gamma$  matrix, coherently embedded strengthening precipitates of a  $\gamma'$  ordered intermetallic phase and carbides.

The MAR-M 247 alloy contains about 60 %  $\gamma'$  phase volume fraction which provides very good high temperature mechanical properties [5]. Solid solution alloying of the  $\gamma$  matrix by W, Ta, Mo and other elements enhances strength and thermal stability while carbides are beneficial for grain boundary strength. A special feature of this alloy is the addition of Hf which has an enhancing effect on tensile strength and temperature retention of  $\gamma'$  [6]. While processed under optimal casting conditions and with well-chosen heat treatment, the alloy exhibits high tensile strength and creep resistance at high temperatures along with excellent oxidation resistance. Thanks to the mentioned combination of properties the MAR-M 247 alloy is used in turbine components subjected

to various loading and high temperatures [7 – 9].

Casting defects like shrinkage pores and gas pores are an inevitable feature of every cast material. Their size and distribution is strongly dependent on casting conditions. These irregularities act as stress concentrators and fatigue crack initiation sites. Hot Isostatic Pressing (HIP), which can diminish pores and casting defects, improves the mechanical properties [10]. However, this process can be accompanied by coarsening of the  $\gamma'$  phase which can cause a decrease of the yield strength [11] or in some cases coarsening of dangerous carbide particles [12]. Despite the shrinkage pore size is usually in the range of tenths or hundreds of micrometers they are difficult to detect by non-destructive defectoscopy. Therefore these material defects can cause significant scatter in service life-time [13] and also unexpected failures of turbine components. This serious material issue has been studied for decades and it is still of great interest for the engineering and scientific community. Therefore investigation focused on relationship of the fatigue life and the porosity of material is very desirable.

Statistical analysis of casting defects present in the structure has been shown [14] to be an useful tool in the procedure of the fatigue life prediction. This method was used for fatigue life prediction of different materials and in some cases a quite good agreement with fatigue test results [13, 15 – 17] was demonstrated.

The present paper is focused on the statistical analysis of the casting defects of Ni-based superalloy MAR-M 247 after HIP. The analysis of casting defects was performed according to Murakami's statistical method using Largest Extreme Distribution theory (LEVD).

This theory enables to predict the largest defects which can occur in a given volume. The predicted largest defect sizes were compared to the sizes of the defects observed on the fracture surface of the failed specimens. Proposed fatigue life according to the statistical evaluation and prediction of casting defects was found to be in agreement with the number of cycles reached by fatigue tests conducted at 650 °C and 800 °C.

## 2. Experimental material and methods

Experimental material was provided by PBS Velká Bíteš, a.s. as pre-casted specimens. Final machining of the cylindrical specimens was done to obtain the gauge length diameter of 8 mm. The chemical composition of MAR-M 247 guaranteed by the producer is shown in the Table 1.

Pre-casted specimens were subjected to HIP treatment at 1 200 °C at 100 MPa for 4 hours before final machining in order to reduce the extent of casting defects. Subsequently, the alloy was heat treated by homogenizing annealing at 1 200 °C for 2 hours and following precipitation annealing at 870 °C for 24 hours.

Fatigue tests were performed under controlled load in symmetrical tension-compression loading (load ratio  $R = -1$ ). A resonant fatigue machine Roell Amsler equipped with VibroWin electronics was used for fatigue tests. The full load amplitude was reached by a ramp during several hundreds of loading cycles. The test frequency was  $120 \pm 3$  Hz. Fatigue tests were held until final failure of the specimen or decrease of test frequency higher than 5 Hz. The heating to the desired experimental temperature was provided by an electric furnace with temperature stability on gauge length within  $\pm 1$  °C.

Table 1

Chemical composition of MAR-M 247 alloy (wt. %).

C	Cr	Mo	Al	Ti	Ta	W	Co	O	N	Nb	B	Hf	Ni
0.15	8.37	0.67	5.42	1.01	3.05	9.92	9.91	5 ppm	6 ppm	0.04	0.015	1.37	rest



The fatigue tests in this study were performed at two temperatures, 650 °C and 800 °C. For identification of the influence of casting defects and temperature all tests were performed at one stress amplitude, namely at 240 MPa.

Metallographic specimens for microstructural observations and the statistical analysis of casting defects were machined from fatigued specimens by electroerosion cutting. The cutting of the gauge length of all specimens was parallel to the loading direction. Subsequently, the surface of the sections was carefully prepared by mechanical grinding with grind papers and polishing with diamond paste. The last finalizing step was done by vibration polishing. Observation of the metallographic samples and fracture surfaces of fatigued specimens was performed using Scanning Electron Microscope (SEM) Tescan LYRA 3 XMU. The size of the casting defects was determined by light microscopy (LM) using confocal microscope Olympus LEXT OLS3100.

For the analysis of defects the LEVD theory proposed by Murakami [14] was used. The theory is based on the evaluation of the size of the largest defects on the controlled area  $S_0$  (field of view). The defect size was characterized in terms of the square root of its area,  $area^{1/2}$ . The measurement was done on  $n$  number of the controlled areas. The number of the controlled areas has to be sufficient for reasonable statistical description. On each metallographic specimen at least 30 measurements were done. The number of the measurements is dependent on specimen size and on chosen magnification. For this paper a magnification of 480× was used. According to the return period  $T = S/S_0$  which is based on measured sizes of the largest defects found on the controlled area, it is possible to predict defect sizes on areas larger than the controlled area.

### 3. Results

#### 3.1 Microstructural analysis

Metallographic specimens were prepared from the specimens used for the high temperature fatigue testing. Typical microstructure of the examined MAR-M 247 superalloy is shown in Fig. 1. The alloy exhibits coarse dendritic structure from the macroscopic point of view.

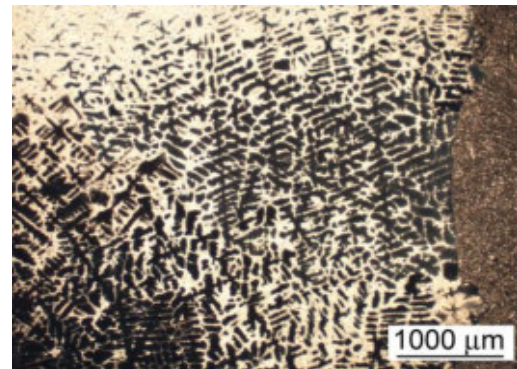


Fig. 1. Typical microstructure of MAR-M 247, LM, etch. 40 ml  $HNO_3$  + 30 ml  $HF$ , dark field. (full colour version available online)

The microstructure of the alloy is significantly heterogeneous in terms of size and morphology of  $\gamma'$  strengthening precipitates (see Fig. 2).

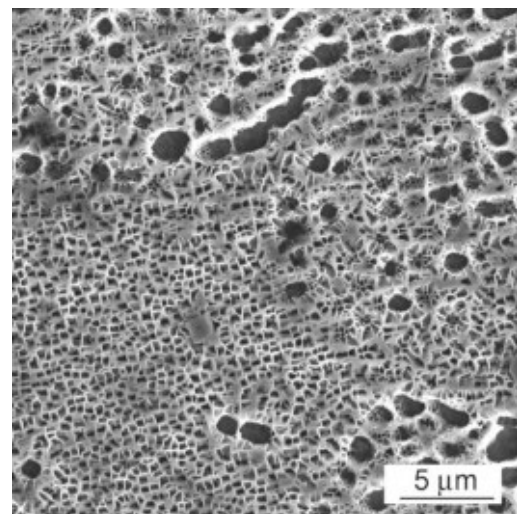


Fig. 2. Size and shape of the strengthening  $\gamma'$  precipitates, SEM, etch. 40 ml  $HNO_3$  + 30 ml  $HF$ .

Areas of fine cubic  $\gamma'$  and coarse  $\gamma'$  phase with irregular shape were found to be characteristic for this material. Average edge size of the cubic precipitates was  $0.4\ \mu\text{m}$  and the average diameter of coarse precipitates was  $1.6\ \mu\text{m}$ .

The structure contains numerous casting defects. The characteristic size and morphology of the defects is documented in Fig. 3. The defects have mostly spherical shape; however, some irregularly shaped shrinkage pores were present in the structure even after HIP.

### 3.2 Fatigue test results

All specimens were tested at stress amplitude  $\sigma_a = 240\ \text{MPa}$ . Results of the performed fatigue tests are shown in Table 2. The specimens were arranged in the table according to the number of cycles till fracture. Range of reached number of cycles to fracture in case of the specimens tested at  $650\ ^\circ\text{C}$  was from  $7.83 \times 10^5$  to  $1.3 \times 10^6$  cycles. Fatigue tests conducted at  $800\ ^\circ\text{C}$  revealed an increase in scatter

of fatigue life data while the range of number of cycles to fracture was  $4.65 \times 10^5$  to  $8.3 \times 10^6$  cycles. It should be noted that the average fatigue life increased with higher experimental temperature.

Fractographic observation revealed the presence of casting defects on all fracture surfaces.

### 3.3 Analysis of casting defect distribution

The evaluation of defect size and distribution was performed on metallographic sections prepared from the cross-section of the gauge length of specimens after fatigue testing. The predictions of the largest defect size which can occur on an area  $S$ , which is equivalent to the area of the cross section of gauge length of the fatigued specimen ( $S = 50\ \text{mm}^2$ ), were carried out. The results were compared with defects responsible for the fatigue crack initiation in particular specimens. The size of these defects was evaluated on fracture surfaces of failed specimens.

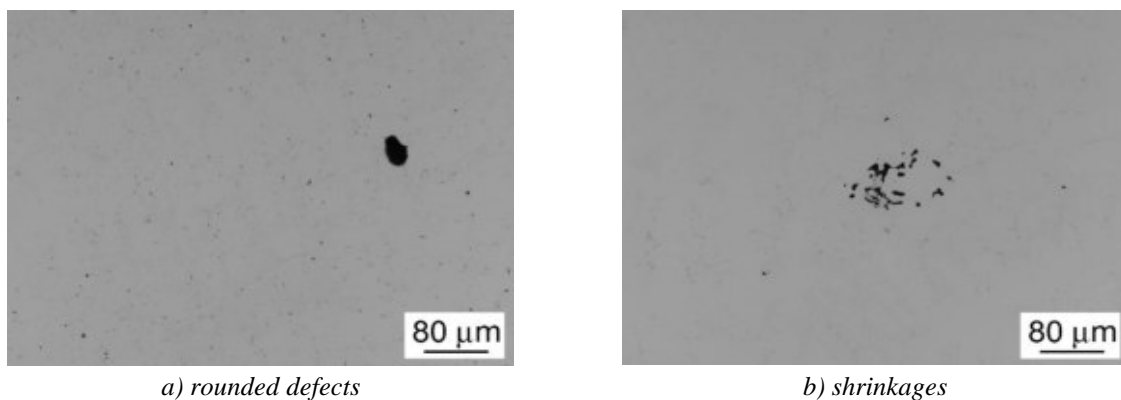


Fig. 3. Typical casting defects present in the microstructure, LM.

Table 2

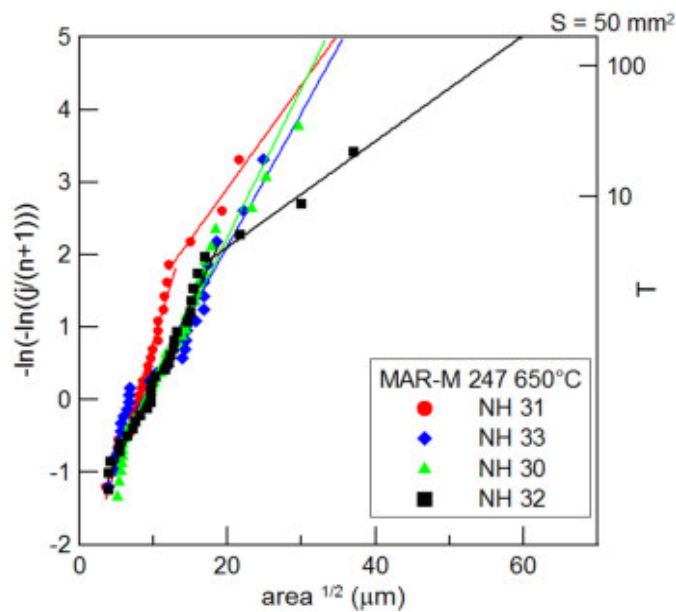
Fatigue tests results.

650 °C specimen	$\sigma_a = 240\ \text{MPa}$ $N_f$ (cycles)	800 °C specimen	$\sigma_a = 240\ \text{MPa}$ $N_f$ (cycles)
NH 31	1 301 000	NH 24	8 309 000
NH 33	1 132 000	NH 27	1 991 000
NH 30	987 000	NH 28	1 078 000
NH 32	783 000	NH 34	465 000

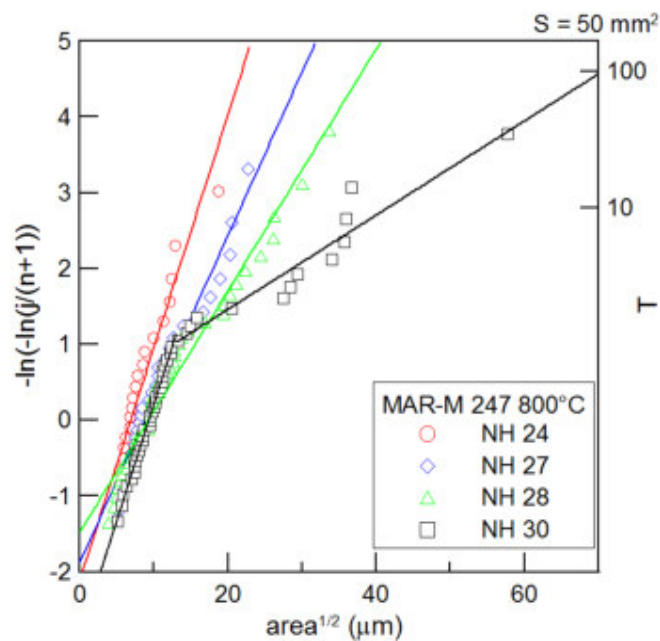
The results of analysis using the LEVD theory are shown in Fig. 4. The size of the largest defects measured on evaluated specimens is presented as a Gumbel plot. The data were extrapolated for the values corresponding to the largest defects which could occur in area of  $S = 50 \text{ mm}^2$  marked on the T axis. The ratio between the projected area

and the controlled area is  $T = S/S_0 = 163$  in this study.

The results of the prediction of the largest size of defects which can occur on the cross section of the gauge length and experimentally determined areas of defects observed on the fracture surface of particular specimens are shown in Table 3. The size is presented in terms of area of the defect.



a) specimens tested at 650 °C



b) specimens tested at 800 °C

Fig. 4. LEVD plots of porosity.  
(full colour version available online)

Table 3

Values of the average defect size, the predicted largest defect size and real defect size found on fracture surface of fatigued specimens.

650 °C			800 °C				
specimen	average defect size ( $\mu\text{m}^2$ )	predicted largest defect size ( $\mu\text{m}^2$ )	real defect size on the fracture surface ( $\mu\text{m}^2$ )	specimen	average defect size ( $\mu\text{m}^2$ )	predicted largest defect size ( $\mu\text{m}^2$ )	real defect size on the fracture surface ( $\mu\text{m}^2$ )
NH 31	107	1 100	1 200	NH 24	84	550	560
NH 33	162	1 142	740	NH 27	149	1 044	3 940
NH 30	169	1 145	490	NH 28	211	1 700	1 160
NH 32	199	3 884	40	NH 34	342	5 608	4 870

In Table 3 are further given the values of the average size of the largest defects measured directly on the metallographic specimens.

#### 4. Discussion

Cast materials, like the MAR-M 247 examined in this study, contain inevitable casting defects in some extent. The size of the defects can be minimized by the HIP process. However, it is not possible to completely eliminate some shrinkage pores which are too large. Even after HIP they can be larger than the size of intermetallic phases and detrimental for fatigue strength of the material.

As it was mentioned above, Murakami's statistical LEVD theory (for more details see [14]) was used in this study. The porosity of fatigued specimens was evaluated and the largest size of defects which could occur in the area larger than the examined area was predicted. The average defect size for examined metallographical specimens was in the range from 84 to 342  $\mu\text{m}^2$  (see Table 3). Measured defect sizes are smaller than the size of defects observed by Roskosz et al. [19] who examined the porosity in precision cast blades of aircraft engine from the MAR-M 247 alloy. The size of defects range observed in their study was from 135 to 2745  $\mu\text{m}^2$ . The difference in the average defect size can be explained by the applied HIP process. While Roskosz et al.

in [19] observed mostly defects of shrinkage shape in this study while the majority of them were predominantly rounded.

The porosity evaluation was conducted on metallographical specimens taken from each fatigued specimen. Characteristic values of the defect size were subsequently compared with the fatigue test results obtained at 650 °C and 800 °C. The number of cycles reached by the fatigued specimens is in good agreement with the porosity of the individual metallographic specimens and with the predicted largest defect sizes for the area of the cross section of the specimens (see Table 2 and 3). Also the scatter of the obtained number of cycles to fracture at the same stress amplitude at chosen temperatures correlates well with the different porosity of individual specimens. It should be noted that specimens were prepared by the same technology and are different only in the size and density of defects. Just these differences were the reason for the various fatigue life of individual specimens. Fig. 5 summarizes obtained relationship of the predicted largest defect sizes of the area with obtained fatigue life-times. Especially at 800 °C very good agreement in these 2 parameters is clearly visible. The correlation of the results is worse at temperature 650 °C which is caused by low number of examined specimens and also by different fatigue crack propagation mechanisms observed at this temperature.

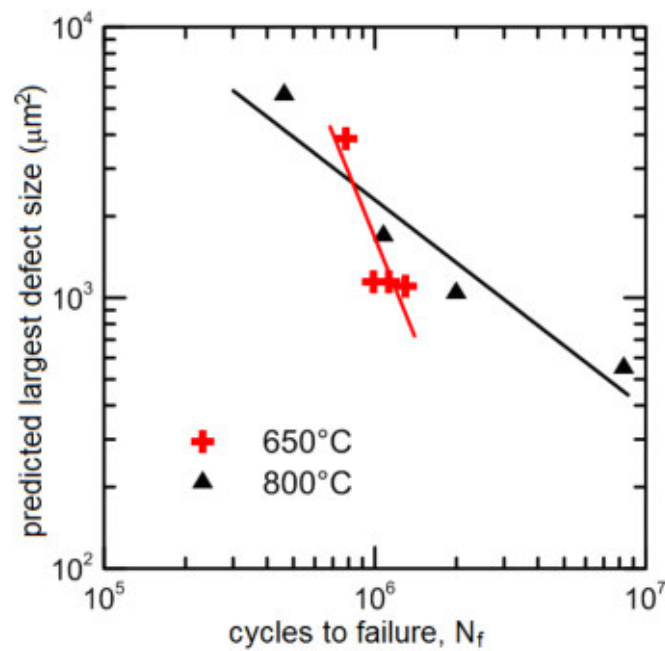


Fig. 5. Relation between predicted largest defect size and obtained fatigue life-time for given specimen. (full colour version available online)

Despite these facts, good agreement would be reached even on this temperature with reasonably higher number of observations.

The prediction and the largest defect size was not in agreement in the case of the specimens NH31 tested at 650 °C and NH27 tested at 800 °C. The reason for this discrepancy can be in difficult distinguishing of the real size of shrinkage pore. However, also in these cases the number of cycles to fracture is in reasonable correlation with the predicted largest defect sizes for cross section area of the fatigue specimen.

Metallographic sections on which the analysis of defects was performed are showing just 2D information about structure and porosity. On the other hand, especially the shrinkage pores are complicated 3D objects and therefore a metallographic specimen describing one cross section is not sufficient to fully represent the observed 3D structure. Therefore, for more accurate results it would be necessary to investigate a sufficient number of metallographical specimens with different orientation. The influence of cutting of the shrinkages when the metallographic specimen is prepared was studied in [16].

Nevertheless, the presented paper shows that also the used simplified procedure brings reasonable and useful results.

The performed study confirms that the approach by Murakami, [14], based just on the metallographic analysis and the prediction of the largest defect size seems to be a suitable treatment for prediction of fatigue life of the MAR-M 247 superalloy.

## 5. Conclusion

Maximum size of casting defects in a specimen from the MAR-M 247 alloy was satisfactorily predicted on the basis of an analysis of defect distribution on small metallographic sections detracted from the specimen gage length. It has been shown that the fatigue lives of tested specimens are in good agreement with the predicted largest defect size. The specimens with the largest predicted defect size had the shortest fatigue lives and vice versa.

## Acknowledgements

This research was financially supported by the project FR-TI4/030 of the Ministry



*of Industry and Trade of the Czech Republic and by the grants No. CZ.1.07/2.3.00/20.0214 and CZ.1.07/2.3.00/30.0039 of the Ministry of Education, Youth and Sports of the Czech Republic.*

### References

- [1] M. Ashby: *Materials Selection in Mechanical Design*, 3rd edition, Butterworth-Heinemann, Oxford 2005.
- [2] M.J. Donachie, S.J. Donachie: *Superalloys – A Technical Guide*, 2nd edition, ASM International, USA 2002.
- [3] R.C. Reed: *The Superalloys, Fundamentals and Applications*, 2nd edition, Cambridge University Press, New York 2008.
- [4] A. Pineau, S.D. Antalovich: *Eng. Fail. Anal.* 16(8) (2009) 2668-2697.
- [5] C.M. Sonsino, U. Brandt, J. Bergmann: In: 3rd International Conference on Low Cycle Fatigue and Elasto-Plastic Behaviour of Materials, Ed.: K.T. Rie et al., Berlin 1992, pp. 262-268.
- [6] N. Baluc, R. Schäublin.: *Philos. Mag. A.* 20(1) (1996) 113-136.
- [7] C.A. MacIntyre, P. N. Agarwal: In: *Aerospace Congress and Exposition*, Warrendale, Long Beach, California 1984, paper 841515, pp. 35-45.
- [8] I.R. Delgado, G.R. Halford, B.M. Steinetz, C.M. Rinnac: In: *Proceedings of the ASME Turbo Expo Vol. 5*, Montreal, Canada 2007, pp. 583-597.
- [9] M. Kaufman: In: *Superalloys 1984*, Ed.: M. Gel et al., Metallurgical Society of AIME, Warrendale, 1984, pp. 43-52.
- [10] H.V. Atkinson, S. Davies: *Metall. Mater. Trans. A* 31A(12) (2000) 2981-3000.
- [11] H.Y. Bor, C. Hsub, C.N. Wie: *Mater. Chem. Phys.* 84 (2004) 284–290.
- [12] K.C. Antony, J.F. Radavich: In: *Superalloys 1980*, 4th Int. Symp. on Superalloys, Ed.: J.K. Tien et al., Metal Park, Ohio 1980, pp. 257-265.
- [13] L. Kunz, P. Lukáš, R. Konečná: *Int. J. Fatigue* 32(6) (2010) 908-913.
- [14] Y. Murakami: *Metal Fatigue: Effects of Small Defects and Nonmetallic Inclusions*, 1st edition, Elsevier, Oxford 2002.
- [15] L. Kunz, P. Lukáš, R. Konečná, S. Fintová: *Int. J. Fatigue* 41 (2012) 47-51.
- [16] G. Nicoletto, R. Konečná, S. Fintová: *Int. J. Fatigue* 41 (2012) 39–46.
- [17] M. Filippini, S. Beretta, L. Patriarca, G. Pasquero, S. Sabbadini: *J. ASTM Int.* 9(5) (2012) 279-295.
- [18] L. Kunz, P. Lukáš, R. Konečná: *Eng. Fract. Mech.* 77 (11) (2010) 2008-2015.
- [19] S. Roskosz, M. Staszewski, J. Cwajna: *Mat. Charact.* 56(4-5) (2006) 405–413.